UNIVERSIDAD AUTÓNOMA DE MADRID
Facultad de Ciencias Físicas
Departamento de Física Teórica

RADIO ASTRONOMICAL STUDY OF THE PHYSICAL CONDITIONS, KINEMATICS, AND CHEMISTRY OF THE ENVIRONMENT SURROUNDING LOW-MASS YOUNG STELLAR OBJECTS

Itziar de Gregorio Monsalvo
Madrid, 2006

UNIVERSIDAD AUTÓNOMA DE MADRID
Facultad de Ciencias Físicas
(Departamento de Física Teórica)

RADIO ASTRONOMICAL STUDY OF THE PHYSICAL CONDITIONS, KINEMATICS, AND CHEMISTRY OF THE ENVIRONMENT SURROUNDING LOW-MASS YOUNG STELLAR OBJECTS

Dirigido por el **Dr. José Francisco Gómez Rivero**
en el
Laboratorio de Astrofísica Espacial y Física Fundamental
(INSTITUTO NACIONAL DE TÉCNICA AEROESPACIAL)

Memoria presentada por
Itziar de Gregorio Monsalvo
para aspirar al grado de
Doctora en Ciencias Físicas

Madrid, Abril 2006

A mis padres y a David,
por estar siempre a mi lado.

Agradecimientos

El comienzo de este libro tuvo lugar con mis primeras clases de matemáticas y con la primera vez que contemplé el cielo con mi abuela, por ello son muchas las personas a las que tengo que agraceder el haber podido acabar la última página de esta tesis.

En primer lugar, quiero expresar mi agradecimiento a mis padres, por haberme apoyado con tanta ilusión desde el día en que les pedí como regalo de cumpleaños un libro de Astronomía y un telescopio. Igualmente agradezco al resto de mi familia y a los Martínez y Pernía el apoyo y la curiosidad con la que me preguntan siempre sobre mi trabajo.

Agradezco al Instituto Nacional de Técnica Aeroespacial el haberme concedido una beca para la realización de esta tesis y al personal de la estación espacial de Robledo de Chavela la ayuda prestada durante las observaciones. Mi más sincero agradecimiento a mi director de tesis, José Francisco Gómez Rivero, por haberme transmitido tanto conocimiento y por su manera de trabajar. Agradezco a mi tutor, Carlos Eiroa, la ayuda con el papeleo de la tesis. Quiero dar las gracias a todas las personas que han colaborado conmigo y de las que tanto he aprendido, en especial a Guillem Anglada, Claire Chandler, Paola D'Alessio, Yolanda Gómez, Tom Kuiper, Luis Felipe Miranda, Nimesh Patel, Luis Felipe Rodríguez y José María Torrelles.

Gracias a la gente del Centro de Radioastronomía y Astrofísica de la UNAM, por haberme hecho sentir como en casa durante mi estancia en Morelia. Estoy especialmente agradecida a Paola D'Alessio y a Javier Ballesteros, por la cálida acogida y por haber sido tan cariñosos conmigo.

Quisiera agradecer al Array Operators Center del NRAO la buena acogida y el soporte dado durante mi estancia como summer student en Socorro. I am specially grateful to Claire Chandler for be at the other side of the Atlantic, helping and supporting me.

Thanks to Tom Kuiper, for helping me with technical and scientific questions, and for providing a different point of view to all my papers. I also would like to express my gratefulness to Nimesh Patel, for being so kind and for his help with the VLBA observations.

Gracias a todos mis compañeros del LAEFF, con los que tantas risas he pasado y de los que tantas cosas he aprendido. Gracias a todos mis amigos, por estar siempre ahí, y a mis chicas VLBI (Rebeca y Raquel) por los buenos ratos pasados. Gracias a todos mis compañeros de viaje, amigos que he hecho alrededor de todo el mundo, que han hecho de esta bonita aventura algo inolvidable.

Por último, gracias a David, mi gran tesoro, por darme tanto aliento y tanta luz, por quererme tanto y por ser mi eterno compañero.

Itziar de Gregorio Monsalvo,
2 de Abril de 2006

List of contents

List of Figures

List of Tables

Resumen

En esta tesis presentamos un estudio detallado de la interacción de los objetos estelares jóvenes de baja masa con su medio circundante, mediante la caracterización de las condiciones físicas, la cinemática y la química de su entorno. Estos estudios se han realizado utilizando como herramienta fundamental la información proporcionada por las líneas moleculares de emisión en radio, a través de observaciones con antena única de alta sensibilidad complementadas con observaciones interferométricas. Para ello, se han puesto a punto los equipos de espectroscopía de la antena de 70 metros (DSS-63) situada en el complejo espacial de NASA en Robledo de Chavela, Madrid.

Presentamos la búsqueda sistemática de más alta sensibilidad de máseres de H_2O en glóbulos de Bok, utilizando la antena DSS-63. Como criterio de selección elegimos indicadores de formación estelar, como fuentes de radiocontinuo, centros de flujos moleculares, picos de trazadores moleculares de alta densidad y fuentes IRAS. Hemos observado 207 posiciones y detectamos emisión máser de H_2O en siete glóbulos de Bok (CB 3, CB 34, CB 54, CB 65, CB 101, CB 199 y CB 232). Todas excepto CB 3 son detecciones nuevas, con lo que incrementamos de tres a nueve el número de glóbulos de Bok con emisión máser conocida. Este estudio se complementa con las primeras observaciones interferométricas, usando el VLA, en algunos de los glóbulos de Bok que presentan máser de H_2O, hallando las posiciones precisas de dichos máseres. En el caso de CB 3, CB 54, CB 101 y CB 232 identificamos sus fuentes excitadoras.

Realizamos una búsqueda de emisión de CCS y amoniaco a 1 cm en objetos estelares jóvenes con presencia de máseres de H_2O como signo de formación estelar. Esta búqueda se ha realizado con la antena DSS-63, para estudiar las propiedades físicas, la cinemática y la edad de dichas regiones. Detectamos emisión de CCS en seis fuentes (L1448C, L1448-IRS3, B1-IRS, NGC2071-North, GF9-2 y L1251A). Todas estas regiones, excepto B1-IRS, son mostradas aquí por primera vez emitiendo a 1 cm. Hemos buscado la relación entre la presencia de CCS y las propiedades físicas de los objetos centrales, sus flujos moleculares y la emisión de NH_3. Encontramos que en las regiones emisoras de CCS, el NH_3 presenta máximos de emisión significativamente más intensos que en regiones sin emisión de CCS, pero intensidades integradas similares, lo que sugiere un medio menos turbulento, es decir, más joven, en el primer grupo. Además, obtenemos buenos candidatos para posteriores estudios con alta resolución de la cinemática y las propiedas físicas del medio.

Este estudio se completa con observaciones interferométricas, usando el VLA, en CCS, NH_3 y máseres de H_2O en la región que rodea el objeto joven B1-IRS. Estudiamos la cinemática de la región y la relación entre el objeto central y el medio circundante. Obtenemos una distribución de CCS en distintos "grumos", con un patrón de velocidad

que indica una fuerte interacción del gas trazado por esta molécula con el flujo molecular existente en la región. Esto sugiere la posibilidad de un aumento local de la abundancia de CCS mediante química inducida por choques. Además observamos por primera vez una anticorrelación espacial entre el CCS y el NH_3 a escalas de $\simeq 5''$.

Intentamos utilizar por primera vez la técnica de calibración cruzada aplicada a líneas espectrales térmicas con el VLA, observando simultáneamente la emisión en CCS y máser de H_2O a 1 cm en torno a la fuente IRAS 16293$-$2422 y usando la emisión intensa de los máseres de H_2O para trazar las variaciones atmosféricas a 1 cm. Si bien no se detecta emisión de CCS, el radiocontinuo a la frecuencia de esta línea mejora claramente su relación señal-ruido al aplicar esta técnica.

Por último, presentamos un prometedor método estadístico para estimar las características observacionales que pueden ser más relevantes en la obtención de los parámetros físicos de discos protoplanetarios. Con este fin, hemos desarrollado una red de modelos de emisión de la línea $C^{17}O(3-2)$ en discos protoplanetarios con distintas propiedades físicas. Como resultado preliminar, este método permite distinguir relativamente bien entre discos con distintos radios y en menor medida entre diferentes tasas de acrecimiento de masa. Además, presentamos un estudio de detectabilidad de nuestros discos modelados con los interferómetros SMA y ALMA, todos los cuales podrán ser detectados con ALMA en una hora de tiempo de integración.

Abstract

In this thesis we present a detailed study of the interaction of low-mass young stellar objects (YSOs) with their surrounding medium, by means of a characterization of the physical conditions, kinematics, and chemistry of their environment. These studies have been performed using as our main tool the information from molecular emission lines at radio wavelengths, via high sensitivity single-dish observations complemented with interferometric observations. With this purpose, we have set up and calibrated the spectroscopy equipment of 70 meter antenna (DSS-63) located at NASA's Deep Space Complex in Robledo de Chavela, Madrid (Spain).

We show the most systematic and sensitive survey of H_2O masers towards Bok globules, using the DSS-63 antenna. As selection criteria for targets, we have chosen indicators of star formation such as radio continuum sources, centers of molecular outflows, peaks of high-density molecular tracers, and IRAS sources. We have observed 207 target positions, and we have detected H_2O maser emission in seven Bok globules (CB 3, CB 34, CB 54, CB 65, CB 101, CB 199, and CB 232). All of them, except CB 3 are new detections, increasing from three to nine the number of Bok globules known to emit H_2O masers. This study is complemented with the first VLA interferometric observations towards some of the globules associated with H_2O masers, and we have located accurate positions of the masers. We identify their exciting sources in the case of CB 3, CB 54, CB 101, and CB 232.

We have performed a search for CCS and ammonia emission at 1 cm towards YSOs that show H_2O maser emission, as a sign of star formation. This search was done with the DSS-63 antenna, to study the physical properties, kinematics, and age of those regions. We detected CCS emission towards six sources (L1448C, L1448-IRS3, B1-IRS, NGC2071-North, GF9-2, and L1251A). All of these regions, except B1-IRS, are reported here to emit CCS at 1 cm for the first time. We have studied the possible relationship between the presence of CCS emission and the physical properties of the central objects, their molecular outflows, and the NH_3 emission. We found that ammonia shows higher peak intensities in regions with CCS emission than in those without it, but the ammonia integrated intensities are similar. This suggests a less turbulent medium, i.e., younger in CCS-emitting regions. In addition, we found good candidates for future high-resolution studies of their kinematics and physical properties.

This study is completed with VLA interferometric observations in CCS, NH_3, and H_2O masers in the region surrounding the YSO B1-IRS. We studied the kinematics of this region and the relationship between the central object with the surrounding medium. We detected a clumpy CCS distribution, with a velocity pattern that indicates a strong interaction of the gas traced by this molecule with the molecular outflow. This suggests the

possibility of a local enhancement of the CCS abundance via shocked-induced chemistry. Moreover, we observed for the first time a spatial anticorrelation between CCS and NH_3 at scales of $\simeq 5''$.

We tried for the first time a cross-calibration technique for thermal spectral lines, observing simultaneously with the VLA CCS and H_2O maser emission at 1 cm towards the source IRAS 16293−2422. We have used the intense H_2O maser emission to trace and correct the atmospheric fluctuations at 1 cm. Although we failed to detect CCS emission, the radio continuum at the frequency of this line improved significantly its signal to noise ratio after applying this technique.

Finally, we show a promising statistical method to infer which observational characteristics could be more relevant to obtain information about the physical parameters of protoplanetary disks. With this aim, we have developed a grid of emission models for the $C^{17}O(3-2)$ transition in protoplanetary disks with different physical properties. As a preliminary result, this method allows us to discriminate relatively well between disks with different radii, and to a lesser degree it provides information on their mass accretion rates. In addition, we show a detectability study of our modeled disks with the interferometers SMA and ALMA. All of them could be detected using ALMA with one hour of integration time.

Chapter 1

Introduction

1.1 Star formation theory

The formation of stars and planetary systems constitutes one of the basic problems of modern Astrophysics. The development of new instrumentation and observational techniques has provided a large body of observational data, which allowed us a deeper understanding of the earlier stages of the evolution of stars and planets. Nevertheless, there still remain many open questions.

Our present understanding of star formation is primarily based on the observations of low-mass stars ($L_{bol} < 100\ L_\odot$), because these objects are more numerous than high-mass stars, their formation phase is longer, and their parent molecular clouds are closer to us. In addition, low-mass stars sometimes form in isolation and are easier to be studied individually.

In the current paradigm, stars are born within molecular clouds, which are accumulations of gas and dust mainly composed of H_2. These clouds are initially supported against gravitational collapse by a combination of thermal, magnetic, and turbulent pressures (Shu et al. 1987; Mouschovias 1991). Nevertheless, molecular clouds can fragment in smaller and denser cores, where the presence of gravitational instabilities yields a collapse of the cloud material (Shu et al. 1987, and references therein). The mechanisms responsible for the fragmentation and instabilities are still poorly understood. Impulsive events like a shock wave produced by a supernova explosion (Mueller & Arnett 1976; Jungwiert & Palous 1994; Bottema 2003), an expanding HII region (Elmegreen & Lada 1977; Clark & Porter 2004; Hester & Desch 2005), or a collision between clouds or clumps (Loren 1976; Vallée 1995; Wang et al. 2004), or other kind of mechanisms involving gradual processes like ambipolar diffusion (Shu et al. 1987; Mouschovias 1991; Frank et al. 1999; Hosking & Whitworth 2004) or dissipation of turbulence (Nakano 1998; Myers 1999) have been suggested as responsible for such instabilities.

The processes that take place after the initial gravitational collapse are very likely to depend on the mass of the system. While these processes are still largely unknown for high-mass stars, there is a widespread consensus about what happens for low-mass ones, and we will focus on them in what follows. The gas of molecular clouds contains an initial amount of angular momentum (Goodman et al. 1993), which must be conserved during the collapse of the core. Due to this conservative phenomenon, the infalling matter encounters a centrifugal barrier in a plane perpendicular to the angular momentum vector, and the cloud material tends to be deposited on a that plane, yielding the formation of a rotating disk and a central protostar (Terebey et al. 1984; Shu et al. 1987). After the collapse phase, where most of the infalling material is deposited onto the disk, an accretion phase begin, in which part of the disk mass is accreted onto the central protostar. This step requires both, the transfer of mechanical energy (to keep the stability in a Keplerian disk when material fall onto the protostar), and the transfer of angular momentum (to make possible that disk material falls onto orbits located closer to the protostar). See an schematic overview of the complete process of formation of low-mass stars and a time scale estimation of the different phases in Fig. 1.1.

One of the proposed theories for transferring mechanical energy within the disk is through turbulent viscosity (Ruden & Lin 1986; D'Alessio et al. 1998), which also produces a momentum transfer (Shakura & Sunyaev 1973). Another good candidate to liberate angular momentum are winds. Some theoretical models postulate a magnetohydrodynamic origin for winds, which are connected to the disk by magnetic fields (Shu et al. 1994; Pudritz & Norman 1983, 1986). This possibility is specially interesting due to the observation of mass-loss phenomena in star forming regions (see section 1.4).

The disk that was formed around the young stellar object (YSOs) is the structure from which a new planetary system may form. This is the reason why this kind of structures are usually referred to as "protoplanetary disks". In the conventional model, the first stage of planetary formation begins when microscopic dust grains in protoplanetary disks grow via collisions induced by electrostatic forces during settling towards the midplane of the disk, yielding kilometer-sized solid bodies called "planetesimals" (Lissauer 1993). At this stage, gravitational forces induce inelastic collisions between planetesimals, producing a rapid build-up of solid cores, precursors of rocky planets and cores of giant planet, in timescales of $\sim 10^6$ years (Wetherill & Stewart 1989; Aarseth et al. 1993). Nevertheless, there has been some controversy about the formation of giant planets. In the core-accretion model (Pollack et al. 1996), when a rocky core reaches ~ 10 $M_\oplus$ via the process described above, the accretion of considerable amount of nebular gas would be possible (Mizuno 1980). The problem with this model arises from the time necessary to accrete a the atmosphere of a giant planet, with ~ 300 $M_\oplus$, which is estimated to be $\sim 10^7$ years (Pollack et al. 1996). These timescales fall at the upper end of disk lifetimes ($10^5 - 10^7$ years; Strom et al. 1989). Some authors have proposed and alternative model based on gravitational instabilities in protoplanetary disks (Kuiper 1951; Boss 1998), which produce self-graviting clumps of gas and dust (giant gaseous protoplanets) in timescales $<10^3$ years, followed by a fast gas contraction in $\sim 10^5$ years (Boss 1998).

This thesis will focus in the study of some of the processes related to the formation of low-mass stars.

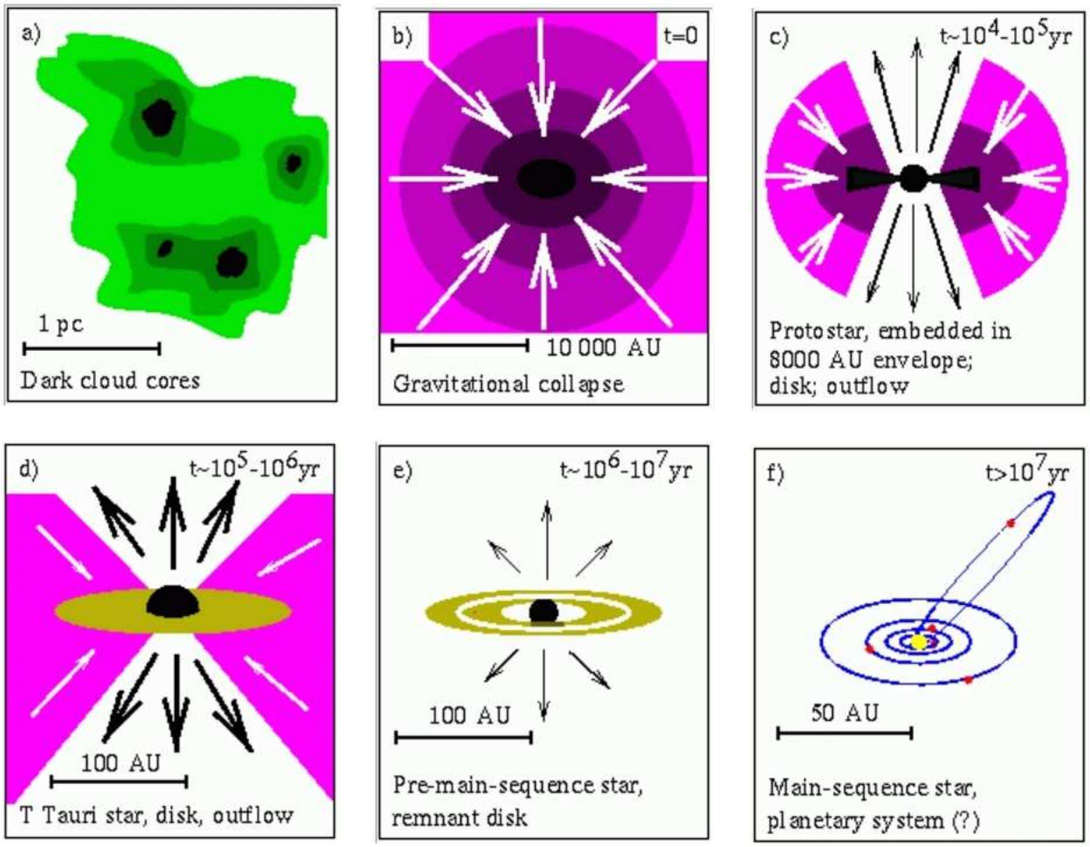

Figure 1.1: Schematic overview of the current theory of the formation of a low-mass star (Hogerheijde 1998, after Shu et al. 1987).

1.2 Stellar nurseries: GMCs and Bok globules

Most stars form in clusters, embedded in dense cores within Giant Molecular clouds (GMCs) (Lada 1992; McCaughrean & Stauffer 1994; Lada & Lada 2003), which are massive (10^4–10^5 M$_\odot$) and large (50–100 pc in their longest dimension) complexes of molecular material (see Fig. 1.2). These GMCs are sites of both, low- and high-mass star formation. In this environment, the influence of close neighbors competing for the same cloud material, the interaction between mass-loss phenomenon of nearby protostars, and the ultraviolet radiation from relatively close massive stars that ionize and disrupt the surrounding molecular gas, somewhat complicate the study of the processes related to the formation of low-mass stars.

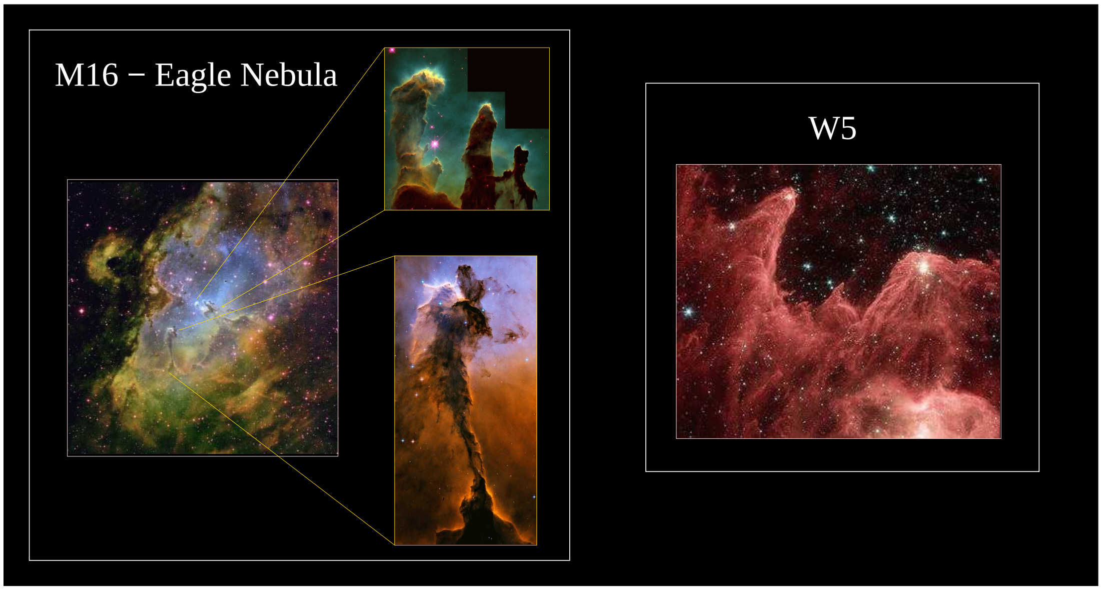

Figure 1.2: Examples of sites of star formation within giant molecular clouds. Left panel: Optical image taken with 0.9 m telescope on Kitt Peak. Courtesy and Copyright: T.A.Rector & B.A. Wolpa, NOAO/AURA/NSF; Close up from the Hubble Space Telescope (HST). Courtesy NASA. Right panel: Infrared image of W5 (IC 1848), taken by the Infrared Array Camera (IRAC) on Spitzer. Courtesy NASA/JPL-Caltech.

On the other hand, low-mass star formation can also take place in relative isolation from each other, inside smaller dark molecular clouds such us the Taurus-Auriga clouds or inside some Bok globules (Bok & Reilly 1947), which are small (projected size $\leq 20'$), isolated, and relatively simple molecular clouds, with typical masses of $\simeq 5 - 50$ M$_\odot$ (Martin & Barrett 1978; Clemens et al. 1991, see Fig. 1.3). These globules are usually identified and cataloged as dark patches in optical images (e.g., Clemens & Barvainis 1988, hereafter CB). The reference catalogs of Bok globules compiled by CB and Bourke et al.

(1995a, hereafter BHR) in the north and south hemispheres, respectively, focused on the group of smaller Bok globules, using a size of $< 10'$ as a selection criterion. Under the assumption that they are nearby clouds ($d \leq 500$ pc), as suggested by the small number of foreground stars, the globules in the CB and BHR catalogs would in general have linear sizes ≤ 1 pc.

Some Bok globules are sites of low- and intermediate-mass star formation (e.g., Yun & Clemens 1991, 1992; Reipurth et al. 1992). Since they are identified from optical images, without any selection criterion related to possible star-forming activity, catalogs of Bok globules may span a wide range of evolutionary stages, from quiescent dark cores to clusters of Herbig Ae/Be or T-Tauri stars. Therefore, systematic studies of these globules are potentially useful to study the evolution of phenomena related to star formation, like collapse, fragmentation, mass-loss, or formation of protoplanetary disks. Moreover, being small and relatively simple molecular clouds, one can study these phenomena with a lower chance of contamination from multiple generations of young stellar objects (YSOs) within the same region. For these reasons, they are interesting laboratories in the study of the star-formation processes and its evolution.

Another important reason to study star formation in Bok globules is that field stars in the solar neighborhood, and the Sun itself, may have formed in this kind of clouds. Moreover, some T Tauri stars apparently not related to known molecular clouds, may have originated in Bok globules which have been dispersed, leaving isolated pre-main-sequence objects (Launhardt & Henning 1997).

Taking advantage of the mentioned properties of Bok globules, part of this thesis, in particular Chapters 3 and 4, will concentrate in the study of the environment of these regions.

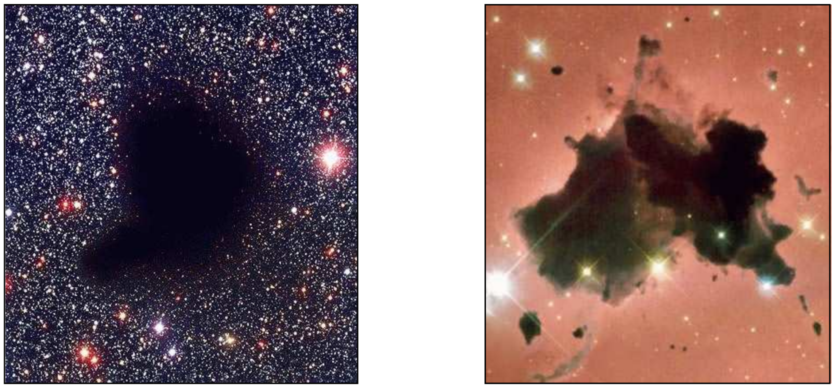

Figure 1.3: Pictures of Bok globules. Left panel represents an optical image of CB 68, observed with the Very Large Telescope (VLT; Courtesy ESO) Right panel represents an optical picture of the source IC 2944, observed with the HST (Courtesy NASA).

1.3 Evolutionary classification of YSOs

The first attempt to empirically study the nature of embedded low-mass YSOs was performed via infrared observations. Objects in the embedded phase emit a significant fraction of their luminosity in the infrared, since dust of the surrounding envelope reprocess the energy emitted by the central pre-stellar object. Lada (1987) and Adams et al. (1987) proposed a classification scheme of low-mass YSOs based on the morphology of their spectral energy distributions (SEDs), focusing on their infrared excess (between λ=2.2 and 100 μm) with respect to stellar blackbodies. The values of their slope $\alpha_{IR} = d\ \log(\lambda F_\lambda)/d\ \log\lambda$ in this range (see below) were interpreted in terms of an evolutionary sequence: Class I (deeply embedded objects), Class II (classical T Tauri stars), and Class III objects (young- or pre-main sequence stars). Later, André et al. (1993) proposed an age ordering of embedded YSOs based on the relation of submillimeter and millimeter continuum emission compared with their bolometric luminosity (i.e., L_{smm}/L_{bol} and L_{mm}/L_{bol}), which seem to be rough approximations to the ratio M_{env}/M_* (envelope to stellar mass), a quantity that decreases with protostellar age. They added a new category to the Lada classification, the Class 0 sources, which show strong submillimeter emission, and would correspond to the youngest protostars.

This evolutionary sequence can be parameterized by the bolometric temperature (T_{bol}), defined by Myers & Ladd (1993) as the temperature of a blackbody having the same mean frequency as the observed SED, and that was suggested as another measure of the circumstellar obscuration and evolutionary development of a YSO. These authors proposed for the first time the use of a log-log plot of L_{bol} vs T_{bol} as an evolutionary diagram for embedded objects. Later Chen et al. (1995) limited the ranges of T_{bol} for different evolutionary stages (see below).

The main properties for different evolutionary stages, attending to their observational characteristics, ordered from youngest pre-stellar cores to more evolved Class III sources, are summarized below:

- **Pre-stellar cores:**

  They are dense and cold condensations whose mass is of the order of or larger than the Jeans mass ($\sim$0.3$-$1.6 $M_\odot$; Larson 1985), needed for the collapse to occur. In this phase, there is no evidence of the presence of a central object or outflow activity. Pre-stellar cores are undetected in the near- to far-IR, no compact radio-continuum sources are observed, and the submillimeter dust emission shows an extended envelope without compact peaks (André et al. 1993, 2000). These objects represent the phase just before the collapse begins, or collapsing condensations without central protostars (André et al. 2000, and references therein).

- **Class 0 sources:**

  They are the best candidates for real protostars (before nuclear reactions take place), so deeply embedded that they remain undetected in the near-IR. These objects show submillimeter emission with a central peak (at the position of the star), surrounded by extended emission that traces the presence of a spheroidal circumstellar dust envelope (André et al. 1993, 2000). Their high ratio of submillimeter to bolometric luminosity ($L_{smm}/L_{bol} > 0.005$, where L_{smm} is the luminosity radiated longward of 350 μm; André et al. 1993, 2000) implies an envelope mass larger than the central stellar mass. Their spectral energy distributions are well-fitted by a single blackbody at a low dust temperature (15−30 K; André et al. 1993, 2000), and their typical T_{bol} are <70 K (Chen et al. 1995). This evolutionary stage is characterized by the presence of powerful and collimated molecular outflows (Margulis et al. 1989; Bontemps et al. 1996) and compact centimeter radiocontinuum emission, interpreted as free-free emission arising from the strong interaction between the wind/outflow and the cloud material or from an accretion shocks closer to the central object, which also constitutes indirect evidence for the presence of the central protostar (e.g. Anglada et al. 1998; Rodríguez et al. 1995; Torrelles et al. 1998b). All these properties suggest that Class 0 sources represent young accreting central objects still surrounded by a dense and cold envelope of the initial cloud material (André et al. 1993). The lifetime of this protostellar phase is $\sim 10^4$ years (André & Montmerle 1994).

- **Class I sources:**

  These objects show IR SEDs broader than blackbody energy distributions, with steeply rising spectra longward of 2μm (spectral index $0 < \alpha_{IR} \leq 3$; Lada 1987). They are still deeply embedded in the parental cloud, since this IR excess is mostly attributed to large amounts of circumstellar dust. Nevertheless, submillimeter continuum emission is more diffuse and fainter than in Class 0 stage, indicating less massive circumstellar structures (André et al. 1993, 2000). Class I sources are invisible in optical, but they usually show faint near-IR emission associated to hotter dust closer to the central protostar. Centimeter radio continuum emission is also detected towards them (e.g. Anglada et al. 1998). In this phase, molecular outflows tend to be much less powerful and less collimated than those from Class 0 sources (Bontemps et al. 1996). Bolometric temperatures in these objects range between $70 < T_{bol} < 650$ K (Chen et al. 1995), and the duration of this stage is $\sim 10^5$ years (André & Montmerle 1994). In the current star-formation theory, this phase would correspond to a central object surrounded by a circumstellar disk ∼10-100 AU in radius, embedded in an infalling envelope of $\sim 10^4$ AU in size (Adams et al. 1987;

Shu et al. 1987), which shows a moderate accretion/infall rate ($\dot{M} \simeq 2 \times 10^{-6}$ $M_\odot$ yr^{-1} for a cloud temperature of $\simeq$10 K; Shu et al. 1987; André et al. 2000).

- **Class II sources:**

  These objects also exhibit IR excess, but more moderate than in the objects previously mentioned, showing flat or decreasing SEDs longward of 2 μm ($-2 < \alpha_{IR} \leq 0$; Lada 1987). At this stage, winds and jets have swept up most of the neighboring cloud material, revealing the protoplanetary disk that surrounds the central star. These sources usually show near-IR emission and Hα optical lines (e.g. Hartigan & Kenyon 2003; Lyo et al. 2003), and they are interpreted as embedded T Tauri stars whose IR excess arises from circumstellar disks of $\sim$100 AU size (Adams et al. 1987). Class II sources show a T_{bol} that ranges between 650 to 2800 K (Chen et al. 1995), and their duration is estimated to be $\sim$10^6 years (André & Montmerle 1994).

- **Class III sources:**

  They are objects that display little or no IR excess, although most of them display optical emission (Lada 1987). Their SED resembles that of a black body reddened by foreground extinction, with $-3 < \alpha_{IR} \leq -2$ (Lada 1987). This stage corresponds to post-T Tauri stars, where the gas of the circumstellar disk is almost dissipated. The associated time scale for these sources is $\sim$10^7 yr (André & Montmerle 1994).

Figure 1.4 shows an scheme of the geometry of low-mass stars from Class 0 to Class III stages, as well as a representation of their typical associated SEDs.

The majority of the existing studies agree that all these classes represent an evolutionary sequence, although there is not a total consensus in this interpretation. Jayawardhana et al. (2001) argue that differences between Class 0 and I sources could be due to the initial conditions of their clouds, rather than to their relative ages. In this scenario, denser clouds would provide Class 0 sources with larger envelopes, mass accretion rates, and more powerful outflows, while Class I objects would be born in less dense clouds. In addition, Masunaga & Inutsuka (2000) suggested that some Class I objects viewed at high inclinations may appear as "Class 0$-$like Class I" sources, because of the high optical depth associated with observing a protoplanetary disk nearly edge-on. Probably the debate arises from how little is known to date about the structure, dynamics, and chemistry of these objects. Thus, it is clear that more studies of the most embedded phases are needed. Part of this thesis will focus on searching for the youngest protostars and studying the kinematics, chemistry, and physical conditions of some of them (see Chapters 5, 6, and 7).

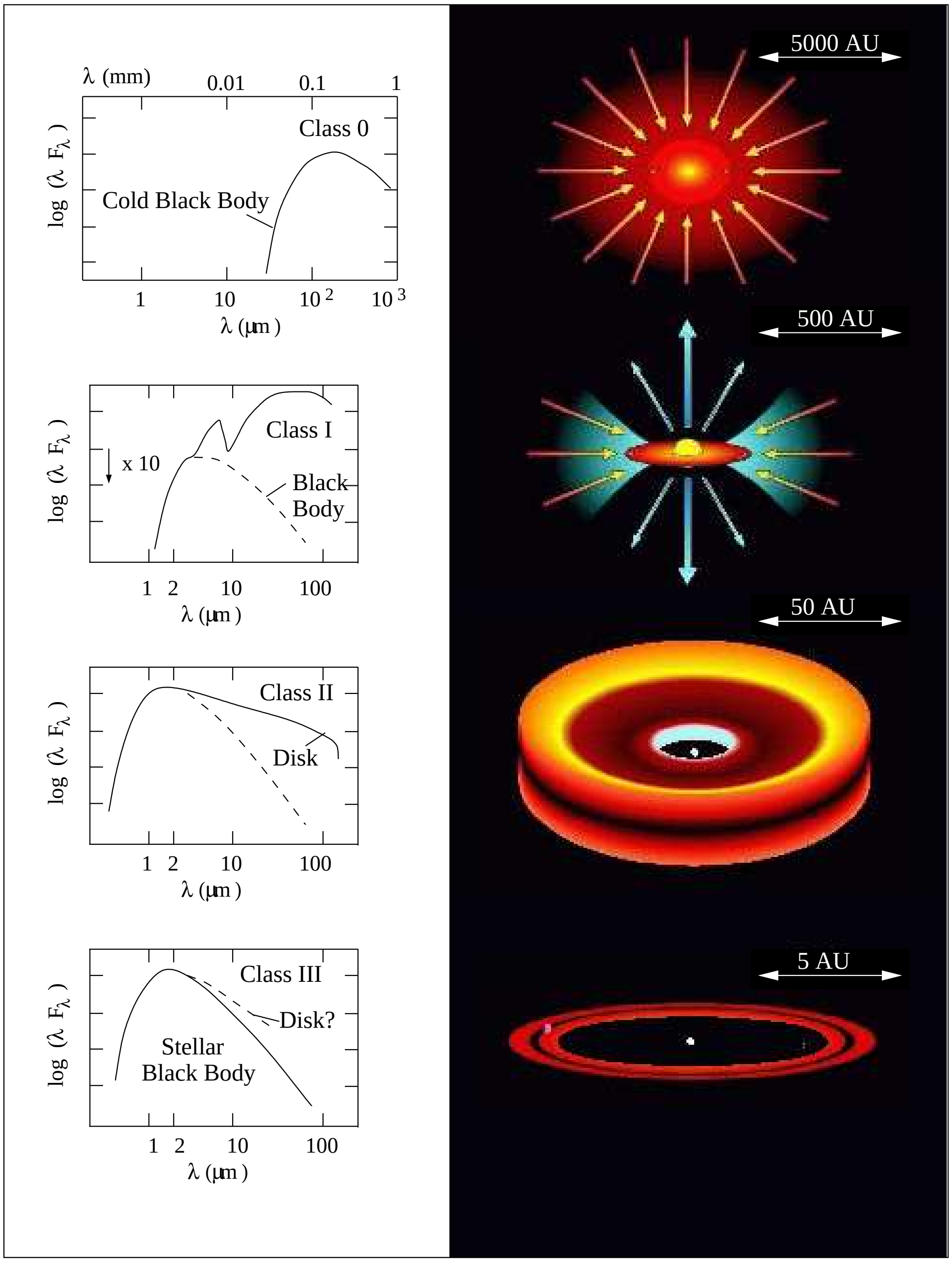

Figure 1.4: Evolution from Class 0 to Class III sources. Left panels represent the SED of the objects at different stages of its evolution (Lada 1987; André 1994). Right panels are artistic representations of the geometry of the sources at different evolutionary stages (courtesy of R. van Boekel, based on figures by A. Natta, M. McCaughrean, C. Dominik and V. Icke).

1.4 Mass-loss phenomena in star-forming regions

It is generally accepted, and supported by observational data, that stars undergo a phase of mass-loss phenomena and strong interaction with their surrounding medium during the earliest stages of their formation. This phase is characterized by the occurrence of intimately related phenomena, like powerful molecular outflows, collimated jets, Herbig-Haro objects and shocked regions (Lada 1985; Shu et al. 1987; Konigl & Pudritz 2000). In this subsection, we are going to thread through some of the manifestations of these mass-loss phenomena.

1.4.1 Molecular outflows

Outflows of cold molecular gas from young stars were observed for the first time by Zuckerman et al. (1976) and Kwan & Scoville (1976), as broad low-intensity wings in lines of rotational transitions of the CO molecule in the Orion A molecular cloud, which were readily interpreted as emission from gas moving at high velocities. Later, they were also detected in low-mass star-forming regions (Snell et al. 1980). Molecular outflows show a wide variety of shapes and sizes. Most of them exhibit a bipolar geometry (two spatially separate lobes of emission, with one lobe containing predominantly blueshifted gas and other predominantly redshifted gas, more or less symmetrically situated from an embedded infrared source or young star (Rodríguez et al. 1980a; Snell et al. 1980; Bally & Lada 1983; Edwards & Snell 1984; Lada 1985), although some monopolar ones are also observed (Lada 1985; Bally & Lada 1983), and even multipolar ones, which could be due to the superposition of several bipolar outflows (Chen et al. 1997; Lee et al. 2002), or to the influence of the interstellar environment (Torrelles et al. 1993b). The typical scales of molecular outflows are 0.1−5 pc, the kinetic energies range between 10^{43}−10^{47} erg, and the dynamical age from 10^3−10^5 years (Lada 1985; Bachiller & Gómez-González 1992; Wu et al. 2004). Molecular outflows typically exhibit moderate velocity ($\lesssim$25 km s^{-1}) and moderate collimated (length-to-width ratio < 10) lobes (Lada 1985), although several highly collimated molecular outflows (with collimation factors $>$10) are also observed, and they exhibit extremely high velocities ($>$40 km s^{-1}) near the outflow axis (Bachiller et al. 1990b; Bachiller & Gómez-González 1992; Zapata et al. 2005).

Observational studies show that the most powerful and best collimated outflows are related to the youngest protostars (Bontemps et al. 1996; Gueth & Guilloteau 1999; Wu et al. 2004; Beuther & Shepherd 2005). This fact suggests that, although molecular outflows are present through much of the embedded phase of protostars, outflow activity decline over time.

1.4.2 Circumstellar jets

In addition to molecular outflows, bipolar mass-loss phenomena are also observed as collimated optical, infrared, and radio jets, all of them being manifestations of collimated ejections at circumstellar scales ($\simeq 100 - 1000$ AU):

- **Optical jets** are observed mainly with [OI]$\lambda\lambda$6300,6363, Hα, [NII]$\lambda\lambda$6548,6584 and [SII]$\lambda\lambda$6716,6731 emission lines from ionized and shocked excited gas (Bacciotti & Eislöffel 1999). They represent ejections of highly collimated gas from the vicinity of the stars (Kepner et al. 1993; Burrows et al. 1996), with speeds that reach hundreds of km s^{-1} (Buehrke et al. 1988; Hartigan et al. 2005; Yusef-Zadeh et al. 2005).

- **Infrared jets** are traced by the emission of atomic near-IR lines such as those of [FeII], Paβ, [SII], and [NI], as well as highly-excited H_2 molecules (Allen & Burton 1993; Reipurth et al. 2000; Lorenzetti et al. 2002; Nisini et al. 2005). They are originated in regions of high temperature (thousands of K) and follow the bipolar structure of molecular outflows at interstellar scales, but tracing shocked gas. In particular, H_2 emission may trace the terminating shocks of optical jets (Garden et al. 1986; Richer et al. 1992; Davis et al. 1997b).

- **Radio jets** are detected in continuum emission at centimeter wavelengths and appear elongated in the same direction as the larger-scale molecular outflows, tracing well-collimated ejections of material emerging from YSOs at scales of $\sim$100 AU (Rodríguez & Reipurth 1989; Anglada et al. 1996b; Rodríguez et al. 2003). In many cases, this centimeter emission can be interpreted as free-free emission from a thermal jet (Reynolds 1986).

1.4.3 Herbig-Haro objects

Another manifestation of mass-loss phenomena, intimately related to jets, are Herbig-Haro (HH) objects, discovered by Herbig (1951) and Haro (1952). They are optical emission nebulae that tend to be distributed bipolarly with respect to a central exciting source. HH objects are observed at highly-excited H_2, optical forbidden lines, hydrogen Balmer emission lines and radiocontinuum emission (Torrelles 1991; Gómez et al. 2003; Wang et al. 2005). Proper motion studies of these objects revealed high expansion velocities, reaching values as high as 200-350 km s^{-1}, which indicate that these objects are related to mass-loss phenomena (e.g., Bally et al. 2002; Yusef-Zadeh et al. 2005). Nowadays it is believed that Herbig-Haro objects are created when highly collimated jets ejected by young stars collide with the surrounding cloud material, generating strong shock waves that heat and ionize the gas (Reipurth & Bally 2001).

Unified models propose that all the mass-loss phenomena summarized in this section are intimately related, and accept that molecular outflows represent ambient molecular gas swept by stellar jets emanating from the central star/disk system (Richer et al. 1992; Raga et al. 1993). Nevertheless, there is also evidence for momentum being deposited into the flows by wider stellar winds (e.g. Bence et al. 1998). Thus, nowadays there are the still some open questions about the origin, collimation mechanism, and evolution of molecular outflows.

1.5 Protoplanetary disks

Direct observational evidence of protoplanetary disks has been difficult to obtain. By comparing with our Solar System, we can expect a typical radius of ∼100 AU for protoplanetary disks in low-mass YSOs, which is also the size predicted by theoretical calculations (Shu et al. 1987; Rodríguez et al. 1989). These structures substend $\sim 0\farcs7$ at 140 pc (the distance to the Taurus molecular cloud, one the closest star forming regions). Therefore, we need subarsecond resolution to image them, and nowadays this can only be achieved by the Hubble Space Telescope or with radio interferometers. In addition, protoplanetary disks are cold, typically with temperatures of the order of 100 K (Beckwith et al. 1990), which means that high-sensitivity telescopes are also needed for their detection.

Most studies on protoplanetary disks have been performed towards T Tauri stars, since most of them show indirect evidence of harboring these structures (Strom 1995), which therefore can evolve toward planetary systems similar to our own. Before the first images were available, many indications and indirect pieces of evidence of the existence of protoplanetary disks around young stars had been collected. The most important piece of evidence is probably the mentioned infrared excess from interstellar dust thermal emission (Strom 1995), but we can also mention the preferentially blueshifted profiles observed in optical forbidden emission lines (coming from stellar winds, with the redshifted emission hidden by an obscuring disk; Appenzeller et al. 1984; Edwards et al. 1987), the polarization patterns of optical scattered light (perpendicular to the jets and outflows in the regions closer to the central protostar and produced by the disk; Bastien & Menard 1988, 1990), or interestellar toroidal structures of $\sim 0.1-1$ pc detected in molecular line studies (Torrelles et al. 1983, 1994). Molecular lines studies have also played an important role in providing observational evidence of the existence of protoplanetary disks, although spectroscopy observations with radio telescopes have only allowed to obtain information of the global disk line emission (e.g., Kenyon & Hartmann 1987; Beckwith & Sargent 1993; Koerner & Sargent 1995), without being able to resolve it.

Nevertheless, images from the HST have been the definitive proof of the existence of protoplanetary disks, with examples like the HH 30 region, which shows a edge-on disk of ∼250 AU perpendicular to a jet structure (Burrows et al. 1996), or the protoplanetary disks silhouettes observed in the Orion nebula against a bright reflection nebula, or ionized by the ultraviolet radiation from a near high mass star (O'Dell et al. 1993; O'Dell & Wen 1994). See Fig. 1.5 for these and other examples.

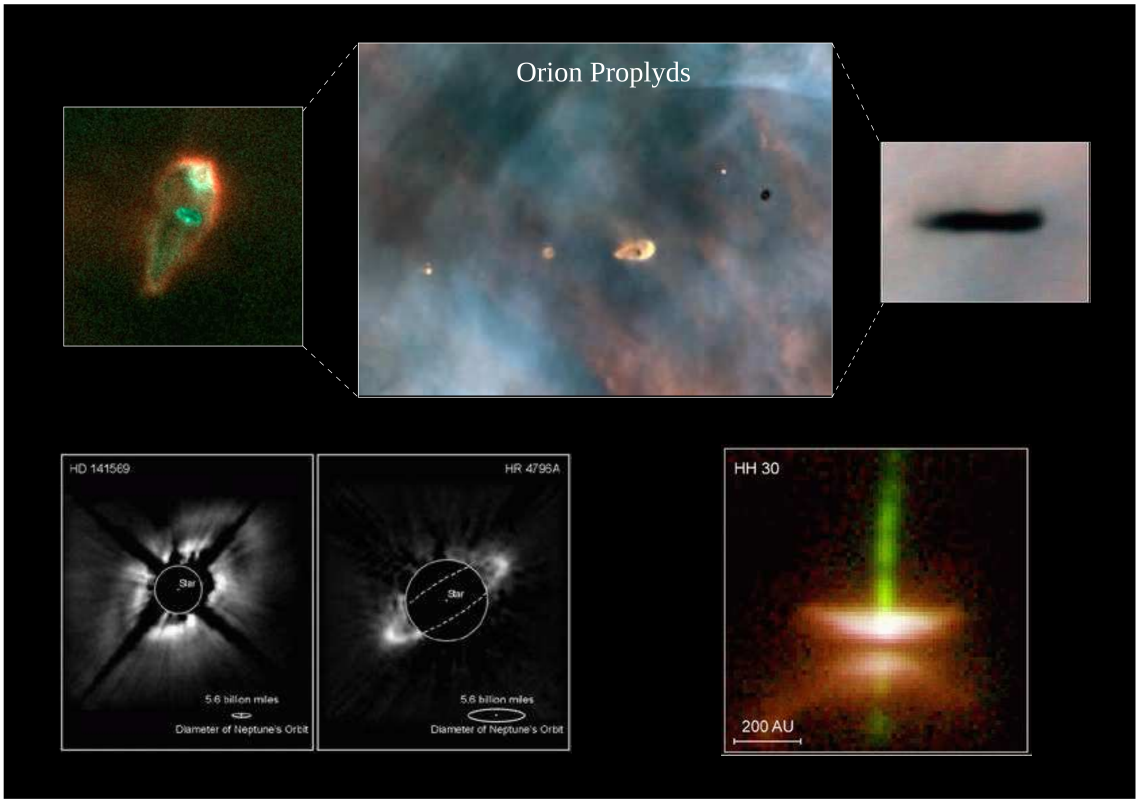

Figure 1.5: Protoplanetary disks observed with the HST. Courtesy NASA.

The development of the new generation of millimeter and submillimeter interferometers will play an important role in the study of protoplanetary disks. Currently, the first results of observations of protoplanetary disks in low-mass YSOs with the Submillimeter Array are being reported, (e.g. Jørgensen et al. 2005; Qi et al. 2006). This instrument has also recently provided the first resolved image of a protoplanetary disk in a high-mass YSOs (Patel et al. 2005). Undoubtedly, ALMA[1] will be the most powerful interferometer to perform molecular line studies in protoplanetary disks. Nevertheless, even when disks are resolved, a considerable amount of assumptions will probably be needed to derive their physical parameters. In this thesis we present a statistical and theoretical study to try to derive which observational characteristics yield more information about the physical properties of disks (see Chapter 8).

---

[1] Atacama Large Millimeter Array

1.6 Molecular lines as diagnosis tools

Molecular spectral lines studies are very useful tools to diagnose the physical properties, chemistry and the kinematics of the interstellar medium. Molecules can experiment three different kind of transitions (Townes & Schawlow 1975; Rohlfs & Wilson 2000): **electronic** (with typical energies of a few eV, which correspond to lines in the visual or ultraviolet range), **vibrational** (caused by oscillations of the nuclei with respect to their equilibrium positions. They show typical energies of 10^{-1}–10^{-2} eV and provide lines in infrared range), and **rotational** (due to rotation of the molecule. Typical energies are 10^{-3}–10^{-4} eV, corresponding to lines at radio wavelengths, i.e., mm and cm wavelengths).

Spectral line emissions from molecules can be produced by thermal and non-thermal mechanisms. Thermal emission involves equilibrium processes, while non-thermal mechanisms are related to processes far from equilibrium. Astronomical masers are one of the most common sources of non-thermal radiation in star forming regions. Since thermal and maser emission lines are extremely useful for deriving physical and kinematical characteristics in molecular clouds, we describe below some of the main properties of these processes.

1.6.1 Thermal emission lines

Molecules can be excited to higher energy levels via collision with other molecules (most of them H_2) or by a radiation field. Therefore, the population of energy levels will be determined by the kinetic temperature (T_K), density of particles in the medium (n_{H_2}), and the characteristics of the radiation field. The dependence of the excitation conditions on the temperature and density of the medium makes intensities of thermal molecular lines from different transitions a powerful tool for deriving information about the physical conditions of the molecular gas.

Molecular clouds provide appropriate conditions to excite the lowest rotational transitions of most molecules. The typical kinetic temperatures inside dark clouds ($T_K \simeq$ 10 K) provide the energy required to excite rotational levels ($E_{rot} \simeq k\ T_K$) and on the other hand their typical densities ($n_{H_2} \simeq 10^3$–10^4 cm^{-3}) are higher than critical densities (n_{crit}) of the lowest transitions of many molecular species (Rohlfs & Wilson 2000). This situation ($n_{H_2}>>n_{crit}$) implies that the excitation will be dominated by collisions, i.e., the transition will be nearly thermalized and local thermodynamic equilibrium (LTE) can be used as a first approximation. In LTE conditions, the population ratio between different levels is a function of the excitation temperature, T_{ex} ($\simeq T_K$), and follows the Boltzmann distribution. For thermal transitions of different molecular species studied in this thesis (NH_3, CCS, CO and isotopes) LTE is a valid approximation. Under LTE conditions, the intensity of an optically thick line allow the determination of T_{ex} ($\simeq T_K$), while for an optically thin line, measurements of its intensity make possible to derive information about the optical depth (τ) of the transition. The optical depth can also be obtained through the ratio of the intensities of the same transition observed in two different isotopes (assuming a known abundance ratio between them). Once the T_{ex} and τ are obtained for a particular line, the column density of the energy levels connected by the transition can be easily derived. To obtain the total column density, it is common to assume that all the energy levels are populated following the Boltzmann law with the same T_{ex} in the calculation of the partition function.

Spectral linewidths and shapes of molecular lines are also a good diagnosis of the kinematics of molecular clouds. The random motions of molecules and the turbulent motions in the gas, produce a line broadening with a Gaussian shape (if molecules follow a Maxwell velocity distribution). Moreover, systemic motions of the gas, such as collapse, expansion or rotation, also leave characteristic signatures in the shape of the spectral lines (e.g., the wings of the CO spectra in molecular outflows; Kwan & Scoville 1976; Zuckerman et al. 1976; Yun & Clemens 1994a).

In addition, molecules can inform about the stage of evolution of a YSO, since the spatial distribution of emission from various molecules tracers in star forming clouds depends not only on the physical conditions within the clouds but also on the (time-dependent) chemistry. That is the case of CCS (dicarbon sulfide) and NH_3 (ammonia), where a pronounced spatial anticorrelation in their emission was reported for starless cores (Hirahara et al. 1992; Kuiper et al. 1996; Lai et al. 2003). The spatial anticorrelation between these two molecules has been explained in terms of chemical and dynamical evolution in protostellar cores, and their relative abundance ratio has been considered as a "clock" to date the age of YSOs (Suzuki et al. 1992).

In studies of the densest regions of a molecular cloud, where stars are formed, high density gas tracers (i.e., molecules with high critical density, like ammonia and CCS) are useful tools to derive physical properties. This thesis will use the properties of some thermal molecular line transitions at 1 cm wavelength, mainly CCS (J_N=2_1-1_0) and NH_3(1,1), in order to derive information about the dynamics, morphology, physical conditions and evolutionary stage of a wide sample of low-mass YSOs. In addition, the mentioned theoretical study of protoplanetary disks in chapter 8, makes use of the $C^{17}O(3-2)$ rotational transition.

1.6.2 Maser emission lines

Maser emission arises when molecules collide, or are radiatively pumped, occurring a population inversion of the energy levels involved in a molecular transition. In this situation, the stimulated emission may easily occur. The overpopulation of a higher energy state formally implies a negative value of T_{ex} in the Boltzmann law, producing an exponential amplification of the radiation as it passes through the gas (see Reid & Moran 1981 for a review).

The most common maser molecules in star forming region are OH (hydroxil), CH_3OH (methanol) and H_2O (water)(e.g. Reid & Moran 1981; Booth & Diamond 2004). All of them are excellent signpost of high-mass star forming processes (Hunter et al. 1998; Szymczak & Gérard 2004; De Buizer et al. 2005; Ellingsen 2006), where methanol and water masers represent the very earliest stages of stellar birth, preceding the OH maser phase (Szymczak et al. 2005). In addition, maser emission from H_2CO (Araya et al. 2005), NH_3 (Hofner et al. 1994; Kraemer & Jackson 1995; Zhang & Ho 1995) and SiO (Morita et al. 1992; Doeleman et al. 1999) has also been observed towards a high-mass YSOs.

Although water masers are more intense and widespread in high-mass star forming regions, they are also present around low-mass YSOs (e.g. Wilking & Claussen 1987; Terebey et al. 1992). Water can show maser emission in different transitions, ranging in frequency from 22 GHz up to at least 906 GHz (Menten & Melnick 1989; Menten et al. 1990; Cernicharo et al. 1990; Melnick 1993; Melnick et al. 1993; Menten & Young 1995). Nevertheless the case of water masers at 22 GHz is specially interesting because they show the highest luminosities, the most compact sizes, the most rapid variability and the widest velocity ranges (Booth & Diamond 2004).

Water maser emission at 22 GHz is fairly common in star forming regions, and constitutes a good tracer of mass-loss activity in young stars of all masses (Rodríguez et al. 1980b; Felli et al. 1992; Xiang & Turner 1995; De Buizer et al. 2005). Their spectra range from simple ones containing a single feature to very complex ones showing different velocity components, some of them accelerated to high velocities (hundreds of km s^{-1}; Comoretto et al. 1990; Furuya et al. 2003). VLBI[2] has proven to be an important tool for studying the structure and dynamics of masers. The maps obtained with this technique have revealed the water maser features to be associated with compact condensations (10-100 AU; e.g., Torrelles et al. 2001a; Patel et al. 2000). Their relative positions can be measured with precisions of milliarcseconds, making possible proper motions measurements, which provide very useful information on the structure and kinematics of the gas close to the central exciting source (see Torrelles et al. 2005 for a review). Recently, this technique has revealed intriguing mass-loss phenomena with isotropic/spherical distributions in the high-mass sources Cepheus A and W75N (Torrelles et al. 2001b, 2003). This phenomenon of uncollimated mass-loss has never been observed in any low-mass YSOs and moreover, we do not know whether it is present in all high-mass stars during some phase of their evolution.

Several water maser surveys towards low-mass YSOs have shown that these

---

[2] Very Long Baseline Interferometry

masers tend to be located close (within several hundred AU) from their powering source (Chernin 1995; Claussen et al. 1998; Furuya et al. 2000, 2003) and revealed them as highly variable on short timescales (< 1 month) (Haschick et al. 1983; Wilking et al. 1994a; Claussen et al. 1996; Furuya et al. 2003).

Highly localized conditions are needed to pump the maser emission, since water masers are activated in regions that are warmer (hundreds of K) and denser ($n_{H_2} \simeq 10^7 - 10^{11}$ cm^{-3}) than the general physical conditions of the environment of YSOs, and a large column density of velocity-coherent water molecules is needed to make maser emission possible (Goldreich & Kwan 1974; Reid & Moran 1981; Elitzur et al. 1989). Theoretical models predict that conditions to pump the water maser emission can be reached in shocked regions in the star forming environment (Elitzur et al. 1989, 1992). These conditions can be originated in the shocked gas compressed by winds (Chernin 1995; Torrelles et al. 1997; Furuya et al. 2000; Moscadelli et al. 2000), as well as in circumstellar disks (Fiebig et al. 1996; Torrelles et al. 1996, 1998b; Seth et al. 2002; Brand et al. 2003), although most of the observations show water masers associated to outflowing material. This dichotomy has also suggested to be a possible evolutionary sequence, with water masers tracing gravitationally bound material (e.g., circumstellar disks) in the youngest sources, and outflows in more evolved YSOs (Torrelles et al. 1997, 1998b). Recently, the hot dense infalling gas after the accretion shock has also been proposed as good environment to pump the maser emission (Menten & van der Tak 2004).

Several studies have shown that water masers provide a good characterization of the age of low-mass YSOs (e.g. Furuya et al. 2001), with Class 0 sources being the most probable candidates to harbor water maser emission, due to the interaction of powerful bipolar outflows with a larger amount of circumstellar material. In their survey of water maser emission towards low-mass YSOs, Furuya et al. (2001) obtained a detection rate of 40% on Class 0 sources, 4% on Class I and 0% on Class II. This fact makes sources that host water maser emission good candidates to be in a very early stage of its evolution.

The newest generation of millimeter and submillimeter interferometers (e.g., SMA[3], CARMA[4], or ALMA) may provide the necessary sensitivity and resolution to clarify some of the still open questions in the star formation processes. While these instruments yield their expected important results, we have used water maser emission as an essential tool to study, not only the physical conditions and kinematics of the innermost regions of low-mass YSOs, but also their stage of evolution and the location of their central YSOs. An important part of this thesis will be dedicated to detect and observe the water maser emission in low-mass YSOs with both single-dish and interferometric techniques.

---

[3] Submillimeter Array

[4] Combined Array for Research in Millimeter-wave Astronomy

1.7 Motivation, methodology, and work scheme

1.7.1 Motivation and methodology of this thesis

The presentation of this thesis has taken place just at the time previous to the development of the next generation interferometers like EVLA[5], eSMA[6], CARMA, SKA[7], or ALMA. These instruments will play a crucial role in solving some of the questions still open today about the formation of stars and planetary systems, since critical scales for most of the star forming processes mentioned above are of the order of $1''-10''$ for nearby low-mass molecular clouds, and in most cases subarsecond resolution is needed to resolve some of these phenomena, specially the protoplanetary disks.

While we wait for these next-generation instruments, we have pressed to their limits the capabilities of some of the currently available radio telescopes in order to contribute to our understanding of some phenomena related to the star formation processes in the low-mass star formation framework. Some of the aspects treated in this work are related to some basic questions like:

1. Which are the youngest protostars?
2. What are the best predictors for the presence of water masers and what characterize their pumping sources?
3. Where is the location of the central engine of the mass-loss phenomena observed in SFRs?
4. What are the chemical, kinematical, and physical properties of the gas surrounding the innermost regions in YSOs?
5. What kind of observations will allow us to extract information about the physical parameters of disks?
6. How are all these phenomena related?
7. How can we obtain the best quality maps in thermal molecular line observations?

In order to answer these questions, we have used the emission of various thermal molecular lines and water masers (see section 1.6) as tools to derive information about the physics, kinematics and stage of evolution of YSOs.

The **methodology** applied in this thesis has been to perform spectroscopic single-dish observations to obtain the most interesting candidates to be observed at higher resolution with interferometric techniques. The synergy between single-dish and interferometric observations allows a more efficient use of both kind of instruments. In this thesis we have mainly used the Robledo-70m antenna to perform single dish surveys, and later we have carried out VLA[8] observations in our most interesting detections.

---

[5] Expanded Very Large Array

[6] Expanded Submillimeter Array

[7] Square Kilometer Array

[8] Very Large Array

With this purpose, we have set-up NASA's 70 m antenna located at the Madrid Deep Space Communication Complex, in Robledo de Chavela, to make possible spectroscopy Radio Astronomy observations. This radio telescope is one of the most sensitive in the world (see section 2.2), but it had been scientifically underused in recent years. Nevertheless, the results obtained in this thesis show the usefulness of the Robledo-70m antenna to perform Radio Astronomy observations and to obtain high-quality data.

We have carried out the first spectroscopic observations with this antenna and this thesis presents some these pioneering results. In total, our work has already yielded six papers either published or accepted in refereed astronomical journals during 2004 and 2005, and the first months of 2006 (de Gregorio-Monsalvo et al. 2004, 2005a,b; Gómez et al. 2005; Kondratko et al. 2006; de Gregorio-Monsalvo et al. 2006). Among these results, it is worth mentioning two projects in which the author of this thesis has been actively involved, using the 70 m antenna, although they fall beyond the scope of the work we present here:

- Search for water maser emission toward planetary nebulae. This survey was done with the Robledo-70m and the Medicina-32m antennas, as well as the VLA, and it provided the second detection of a water maser in a planetary nebula: IRAS 17347−3139 (de Gregorio-Monsalvo et al. 2004). In addition, this study has been complemented with radio continuum observations using the ATCA[9] interferometer (Gómez et al. 2005).
- Smithsonian Astronomical Maser Black hole All-Sky Survey. This project aims to search for H_2O maser emission in the vicinity of supermassive black holes at the nuclei of distant galaxies. It is led by the Smithsonian Astrophysical Observatory, which so far has provided 15 detections out of 630 AGNs observed, using NASA's 70 m antennas in Spain and Australia, and complemented with GBT[10] and VLA observations (Greenhill et al. 2003; Kondratko et al. 2006).

In addition, this thesis is the first one whose results are mainly based on spectroscopic observations with the Robledo-70m antenna. Due to the importance of the set-up and tests of the Robledo-70m antenna equipment for the development of this thesis, in Chapter 2 we will present a detailed description of the technical characteristics and of the observation and calibration procedures.

---

[9] Australia Telescope Compact Array

[10] Green Bank Telescope

1.7.2 Work scheme

This thesis is structured as follows:

- In **chapter 2** we describe the procedures and technical work carried out at the Madrid Deep Space Communication Complex to make possible the spectroscopy observations with the Robledo-70m antenna. That chapter is also intended as a reference for prospective users of this facility.

- In **chapter 3** we present the most extensive and sensitive survey of water masers towards Bok globules to date, in order to derive the better predictors for the presence of water maser emission. This work is complemented in **chapter 4** with high-resolution interferometric studies using the VLA to accurately determine the spatial distribution of the maser emission, interaction with the surrounding medium, and information about the exciting source.

- In **chapter 5**, we show a survey of CCS and NH_3 in low mass YSOs with the presence of water maser emission. Our main goals were to search for indicators of cloud evolution and find the best candidates to make interferometric studies applying a new technique of cross-calibration in spectral line, which would allow us to obtain high-quality and high-resolution maps. This study is complemented in **chapters 6** and **7** with a detailed interferometric multimolecular study of the kinematics, physics, and chemistry of the region surrounding the infrared sources B1-IRS and IRAS 16293−2422.

- **Chapter 8** is centered on a theoretical study of protoplanetary disks. We perform a novel statistical approach to study the molecular line emission of protoplanetary disks. In preparation of future observations with instruments such as ALMA, we calculated the expected emission from disk with different physical parameters parameters, and we try to predict which observational characteristics yield more information about those physical parameters. We also present prospects for molecular line observations of protoplanetary disks, using millimeter and submillimeter interferometers, based on our results.

- In **chapter 9** we summarize the conclusions of this thesis and we expose future lines of work.

Chapter 2

Radio Astronomy at the Madrid Deep Space Communication Complex

In this chapter we give an introduction to the Radio Astronomy at the Madrid Deep Space Communication Complex (MDSCC), in particular about the spectroscopic observations with the 70 m antenna, on which an important part of this thesis is based. We show the setup used in our observations and how these were performed. We also describe our determination of the antenna parameters needed for a proper calibration of the Radio Astronomy data.

2.1 The Deep Space Network and Radio Astronomy

The NASA's Deep Space Network (DSN) is an international collection of antennas that support earth-orbiting and interplanetary spacecraft missions, as well as radio and radar astronomy observations for the exploration of the Solar System and the Universe. The DSN is managed by the Jet Propulsion Laboratory (JPL).

The current structure of the DSN consists of three Deep Space Communication Complexes (DSCCs) located in different continents, and separated approximately by 120 degrees in longitude to allow continuous observations of spacecraft as the Earth rotates (see Fig. 2.1). There is a complex at Goldstone, in California, USA (GDSCC), another one at Tidbinbilla, near Canberra, Australia (CDSCC), and the third one at Robledo de Chavela, near Madrid, Spain (MDSCC). The complexes host several receiving and transmitting stations equipped with steerable parabolic dish antennas of different diameter and ultrasensitive receiving systems. There are at least four stations in each complex:

- One **26-meter** diameter antenna: originally built to support the Apollo missions to the Moon, it is used for communicating with Earth-orbiting satellite spacecraft.
- One **34-meter** diameter high efficiency antenna (HEF): it contains a precision-shaped reflector, for maximum signal-gathering capability.
- One **34-meter** diameter beam waveguide antenna (BWG): based on the HEF design, it hosts five mirrors that reflect radio signals along a beam-waveguide tube from the vertex of the antenna to the pedestal equipment room, making the access easier for maintenance and modification.
- One **70-meter** diameter antenna: the largest and most sensitive antenna of the complexes, capable of tracking the deepest space missions.

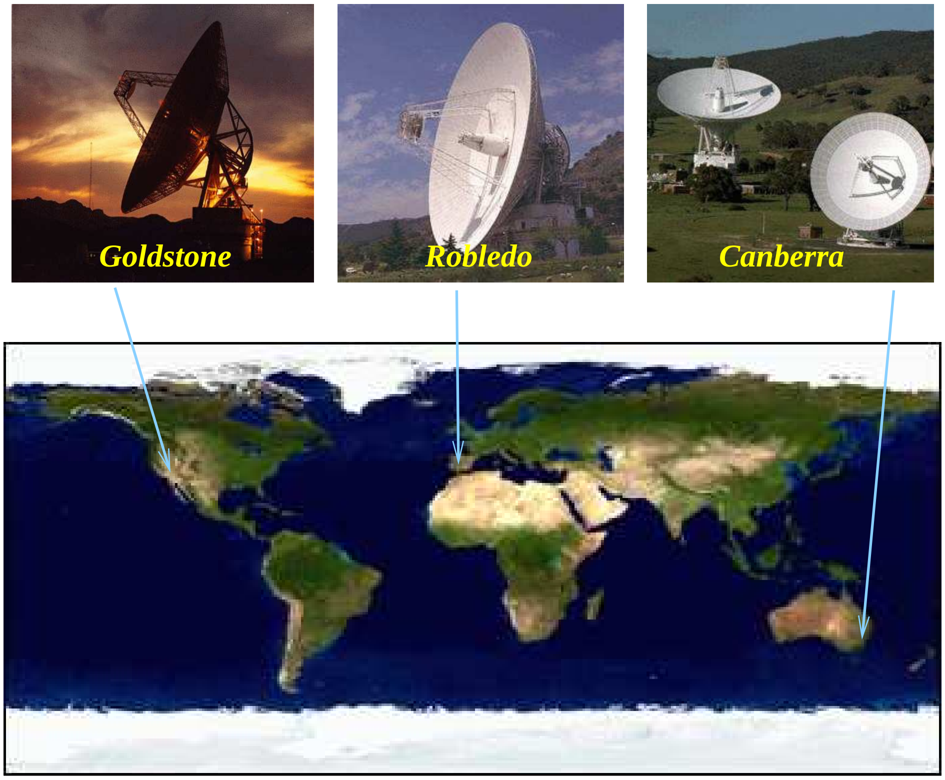

Figure 2.1: NASA's Deep Space Communication Complexes around the world. Credits: NASA

2.1.1 The Deep Space Network functions

The Deep Space Network serves as a communication instrument in space exploration, as well as a facility for science research. The main functions of the DSN antennas are:

- Reception of telemetry data from spacecraft missions, and transmission of commands to spacecraft.
- Radiometric tracking of the position and velocity of spacecraft.
- Very Long Baseline Interferometry (VLBI) observations to measure positions of radio sources, DSN stations, interstation time and frequency offsets, and Earth orientation parameters.
- Monitoring and control of the performance of the DSN.
- Science:

  - *Radio Science data*: Recording of changes in the radio signal sent by a spacecraft as it passes through a planetary atmosphere or the Solar corona. This method provides information about the atmosphere, surface, gravity, and rings of the planets, as well as interplanetary plasma, planetary gravity, and mass of the Solar System bodies.

  - *Radar Astronomy*: extraction of information from the echoes of radio emission reflected from Solar System bodies.

  - *Earth Dynamics*: measurement of geodetic positions via Global Position System satellites.

  - *Interferometric Radio Astronomy observations*: They include global observations with the European VLBI Network (EVN), the Very Large Baseline Array (VLBA), and other ground-based radio telescopes, as well as past space VLBI observations carried out with the space antenna HALCA of the VLBI Space Observatory Program (Hirabayashi & Hirosawa 2000; Hirabayashi et al. 2000; Smith et al. 2000). Moreover, the Goldstone 70 m antenna has been used in combination with the Very Large Array (VLA) interferometer as a radar science instrument (Bolton et al. 2001).

  - *Single Dish Radio Astronomy Observations*: interestellar microwave spectroscopy and continuum single-dish observations.

Nowadays, there are three antennas available for Radio Astronomy observations at the Robledo DSN complex: a 70 m antenna (DSS-63) dedicated to perform spectroscopy observations at centimeter wavelengths, and two 34 m antennas: DSS-61, dedicated exclusively to the educational project PARTNeR (Proyecto Académico con el Radio Telescopio de NASA en Robledo), and the HEF DSS-65, mainly used for VLBI observations. In the near future the BWG antenna DSS-55, will be equipped with a Q-band receiver to perform Radio Astronomy observations at 7 mm.

In addition to Jet Propulsion Laboratory (JPL) allocated time, DSN facilities can be used by "Host Country" scientists for independent Radio Astronomy observations. The "Host Country" observing time allocation is managed by the Commonwealth Scientific and Industrial Research Organization (CSIRO) in Australia, and the Laboratorio de Astrofísica Espacial y Física Fundamental (LAEFF) of the Instituto Nacional de Técnica Aeroespacial (INTA), in Spain.

2.1.2 Host Country observations at MDSCC

About 260 hours per year and per available antenna are reserved for Spanish astronomers at the Robledo station. Spanish "Host Country" observations at MDSCC began in the 70's 80's with radio continuum observations at X and S bands using the Cebreros and Robledo facilities (see, e.g., Estalella et al. 1983; Paredes et al. 1987, 1990). These pioneering observations represented the starting point of Radio Astronomy in Spain. Our group started the spectroscopic observations with the Robledo-70m antenna (DSS-63) in the year 2001, after several years of installation, optimization, software development, and testing. Since then, we have carried out several single-dish surveys of molecular lines, searching for high-density tracers (CCS and NH_3) in young stellar objects, water maser emission in AGNs, evolved stars, and star forming regions, as well as methanol masers around evolved objects. Some of these surveys have been carried out for this thesis work (see Chapters 3 and 5).

2.2 Spectroscopy with the 70 m antenna DSS-63

2.2.1 General characteristics

Nowadays, Host Country time at MDSCC is dedicated to perform spectroscopic Radio Astronomy observations at K-band (wavelengths $\simeq 1$ cm), with the 70 m antenna DSS-63. In Table 2.1 we present a summary of the general properties of the antenna and radiometry system at K-band frequencies, that will be extensively explained in next section.

2.2.2 DSS-63 in the international Radio Astronomy context

The DSS-63 antenna is one of the most sensitive radio telescopes in the world, and can be compared with the K-band capabilities of the largest and most sensitive radio telescopes: the 100-m Effelsberg antenna and the Green Bank Telescope (see Table 2.2).

Table 2.1: Characteristics of the DSS-63 Spectroscopy System

Antenna System	K-band receiver	Spectrometer
Name: Deep Space Station 63 **Diameter**: 70 m **Type**: parabolic cassegrain **Mount**: azimuth/elevation **Latitude**: $40^{\rm o}25'52''$ N **Longitude**: $04^{\rm o}14'53''$ W **Altitude**: 865.5 m [1]**HPBW (22 GHz, el=$40^{\rm o}$)**: $42''$ [2]η **(22 GHz; el=$40^{\rm o}$)**: 49% maximum **Sensitivity (22 GHz, $40^{\rm o}$)**: 0.7 K/Jy **Pointing accuracy**: $\leq 10''$	**Amplifier type**: cooled HEMT **Frequency range**: 18−26 GHz **Polarization**: LCP or RCP [3]$\mathbf{T}_{\rm sys}$: 50 K (winter) 75 K (summer)	[4]**Spectra-Data** **Type**: Digital autocorrelator **BW**: 1, 2.5, 5, and 10 MHz **N. channels**: 256 **Observing mode**: frequency switching [5]**Spaceborne-500** **Type**: Digital autocorrelator **BW**: 2, 4, 8, and 16 MHz **N. channels**: 384 **Observing mode**: position switching [6]**SAO4K** **Type**: Digital autocorrelator **BW**: 400 MHz **N. channels**: 4096 **Observing mode**: position switching

Notes to Table 2.1

[1] Half Power Beam Width.

[2] Aperture efficiency.

[3] System temperature at zenith, in good weather conditions.

[4] This spectrometer was used from 2001 to 2003. Now it is not working any longer.

[5] This is the autocorrelator currently used.

[6] This spectrometer belongs to the Smithsonian Astrophysical Observatory and it is used in the SAMBA survey.

Table 2.2: DSS-63 vs other antennas[1]

Telescope	Diameter (m)	Aperture efficiency(η_a)	Resolution	Sensitivity(K/Jy)
Effelsberg	100	29%	$40''$	0.8
GBT	100-110	55%	$34''$	1.5
Robledo DSS-63	70	49%	$42''$	0.7

Note to Table 2.2

[1] Values at 22 GHz

2.3 DSS-63 radio frequency signal pathway

In this section, we present a sketch of the pathway that the incoming radio signal follows, from the first reflection onto the antenna surface, until its arrival to the spectrometer.

2.3.1 The first encounter: The big dish

DSS-63 is a Cassegrain-focus antenna composed of a large 70 m diameter collecting surface that focuses the incoming radio frequency (RF) onto a subreflector, which in its turn sends the RF into the feed horns, located on the main dish (see example of a Cassegrain focus antenna in Fig 2.2). These primary and secondary reflectors are shaped as modified paraboloids to allow a more uniform illumination of one reflector by the other. The subreflector is adjustable in both axial and angular position, to actively correct for gravitational deformations of the antenna as it moves between zenith and horizon.

There are two K-band feed horns (on- and off-axis, see Fig. 2.3). For the time being, the off-axis feed is not used in spectroscopy observations.

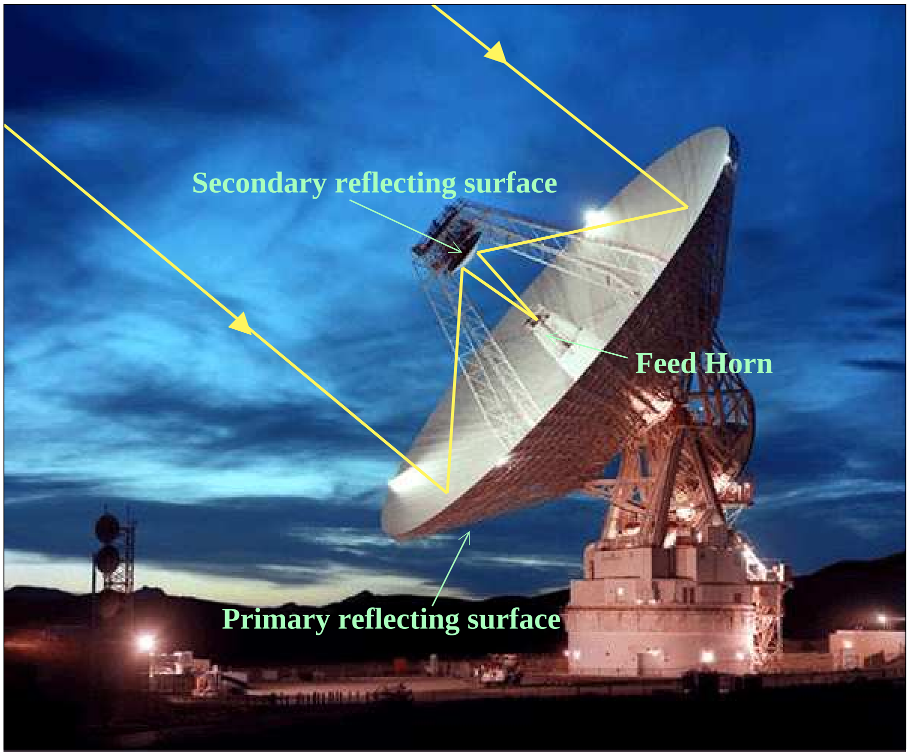

Figure 2.2: Example of Cassegrainian antenna. Credits: NASA

2.3.2 The next step: The receiving system

The function of a radio telescope receiver is to detect, filter, and measure the incoming radio emission. In most cases, the radio emission from celestial sources is extremely weak incoherent radiation whose statistical properties do not differ much either from the background radiation coupled to the receiver by the antenna or from the noise originated in the receiver itself. For this reason, signal amplification is required to reach a detectable level. On the other hand, the transmission of high-frequency signals is difficult, due to the high attenuation of these signals through cables, which makes a transformation to lower frequencies necessary.

The DSS-63 K-band receiving system is a superheterodyne receiver that filters, amplifies, and transforms the incoming high signal frequency from 18−26 GHz to an intermediate frequency (IF) of 321.4 MHz. For clarity, we have divided this system in two modules: the K-band front-end, and the down-converter system.

- **K-band front-end**

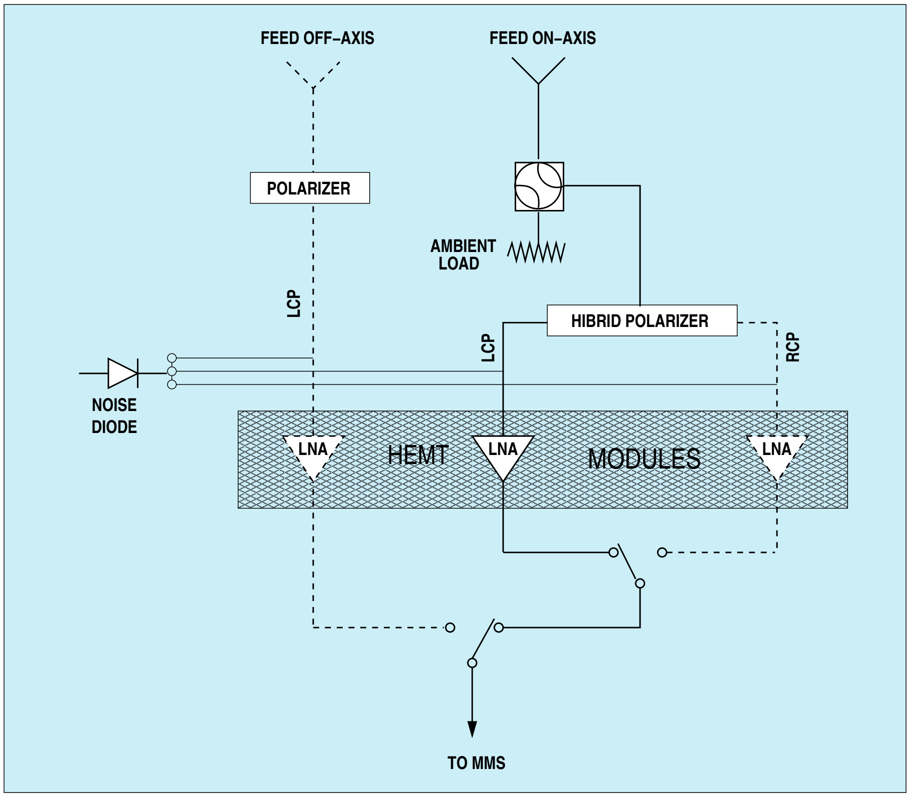

Figure 2.3: K-band front-end diagram. Dashed lines represent components not used in K-band spectroscopy.

The first stage of the receiving system used in K-band spectroscopy is composed of an on-axis feed, a load at ambient temperature ("ambient load"), and a noise diode for calibration, and a polarizer that allows us to observe in either left or right circular polarization (see Fig. 2.3). Currently (as of 2005 September), we only observe in left circular polarization (LCP). Alternatively, the observations could be performed in RCP, but not in both polarizations simultaneously.

The next component is a cooled High Electron Mobility Transistor (HEMT), which is a low-noise amplifier (LNA) under cryogenic cooling conditions (using liquid helium). This equipment amplifies the weak radio signals minimizing the noise temperature (see Fig 2.3).

- **Down-Converters (Modular Measurement System)**

The DSS-63 antenna contains two independent Modular Measurement System (MMS) downconverters, but only one of them is used in spectroscopy observations. The MMS consist of two amplifiers, a bandpass filter of $\simeq$ 50 MHz bandwidth, a local oscillator, and a mixer. After this stage, an intermediate frequency (IF) of 321.4 MHz is obtained (See Fig. 2.4).

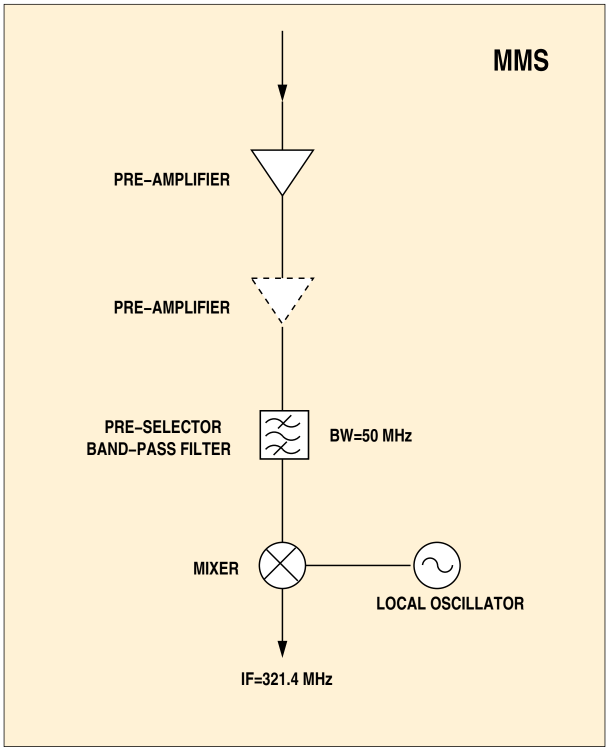

Figure 2.4: Modular Measurement System diagram. Dashed lines represent components not used in K-band spectroscopy.

2.3.3 The final step: The back-end system

The IF frequency at 321.4 MHz from the receiving system, passes throughout an IF distributor, which sends the radio signal to both, a power meter (used for calibration) and a spectrometer. Three different spectrometers have been used in Host Country observations:

- **Spectrada-data (SDS)**: This was the first spectrometer used in Host Country Radio Astronomy observations at DSS-63, and was operative at MDSCC from 2001 to 2003. It was a 256-channel digital autocorrelator, with four different bandwidths available of 1, 2.5, 5, and 10 MHz.

  The IF from the receiving system was mixed with the signal from two successive local oscillators at 271.4, and 50 MHz respectively, obtaining an output signal at baseband (0 MHz). Bandpass filters divided the signal into two half-bandwidth signals, that were transformed by an analog-to-digital converter into a digital signal with the desired bandwidth, ready to be measured by the SDS (see Fig. 2.5, left panel).

- **Spaceborne-500 (SPB500)**: This is is the new spectrometer available for spectroscopy observations. It is a 512-channel digital autocorrelator, although only 383 are usable at the bandwidths used in our observations: 2, 4, 8, and 16 MHz.

  In this case, the IF passes through a video converter that filters the signal into the desired bandwidth and mixes it with a local oscillator of 321.4−1/2 BW MHz frequency, which centers the tunned radio frequency at the chosen bandpass. An output to a second power meter is available at this stage, also used for calibration (see Fig. 2.5, right panel).

- **SAO4K**: This spectrometer belongs to the Smithsonian Astrophysical Observatory and it is used in the SAMBA survey project (see section 1.7), to search for new maser sources within the nuclei of galaxies (Greenhill et al. 2003; Kondratko et al. 2006). It is a portable spectrometer available generally during the local winter at Robledo de Chavela and Tidbindilla complexes, by special arrangement with the principal investigator of the project. SAO4K is a 4096-channel digital autocorrelator with bandwidths up to 400 MHz. We have used this spectrometer for a few days in which SDS was not operational (see section 3.2).

We summarize the total signal pathway in Fig. 2.6.

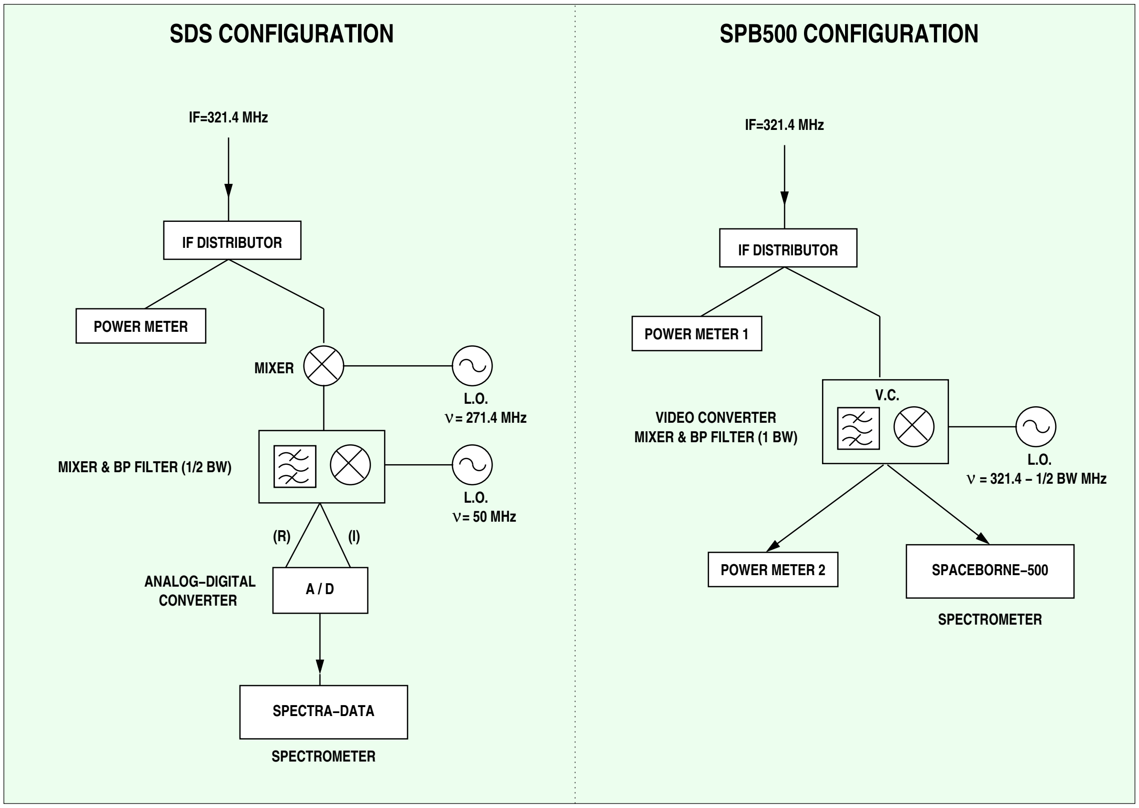

Figure 2.5: Backend signal pathway. Left and right panel show the SDS and the SPB500 configurations, respectively.

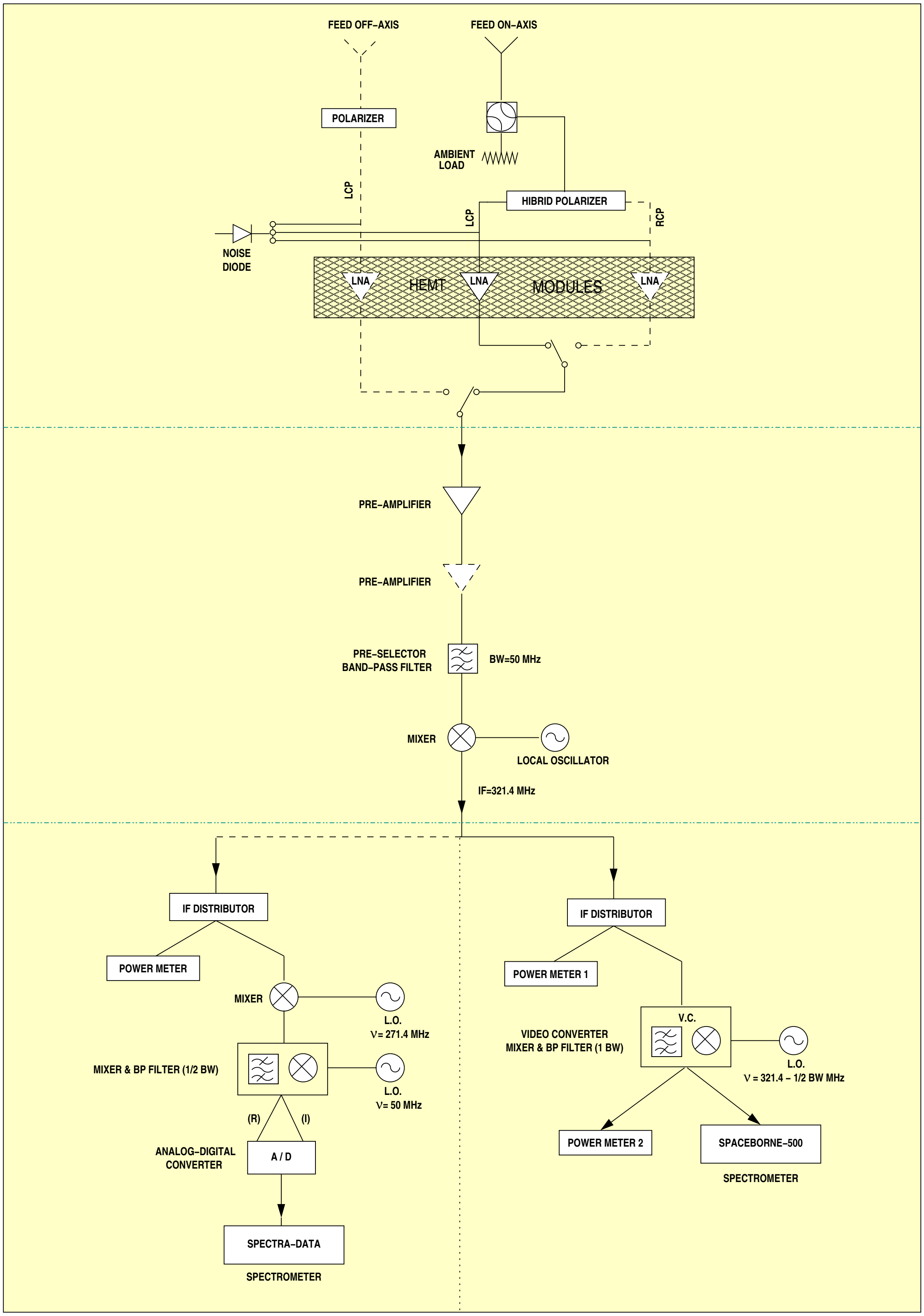

Figure 2.6: Radio frequency signal path at DSS-63. Dotted lines represent components not currently used in K-band spectroscopy (as of 2005 September).

2.4 From the observations to the Physics

A typical spectroscopy observing session at the Robledo de Chavela station consists of several procedures for system configuration, line calibration, pointing check, and data acquisition. For almost four years, astronomers had to be present at the MDSCC to perform spectroscopy observations, although remote observations were implemented at the beginning of 2005. In this section, we will go over the most important concepts and equations that are used in the calibration process. We will also summarize the different steps necessary to carry out a spectroscopy observation, from the initial system configuration to the final data acquisition.

2.4.1 Some basic equations and definitions

2.4.1.1 Brightness temperature: The Rayleigh-Jeans approximation

The brightness or intensity emitted by a blackbody at a temperature T and a frequency ν, is given by the Planck function:

$$I_\nu(T) = \frac{2h\nu^3}{c^2}\frac{1}{e^{h\nu/kT}-1} \ , \tag{2.1}$$

where h is the Planck's constant, k is the Boltzmann's constant and c is the velocity of light. At radio wavelengths $h\nu \ll kT$, an the expansion of the exponential $e^{h\nu/KT} \simeq 1 + \frac{h\nu}{KT} + ...$ results in the Rayleigh-Jeans law:

$$I_\nu(T) = \frac{2\nu^2}{c^2}kT = \frac{2}{\lambda^2}kT \tag{2.2}$$

in which the brightness emitted by a blackbody is proportional to its thermodynamic temperature. From the Rayleigh-Jeans law we can define the brightness temperature, T_b, as the temperature of a black body that emits the same intensity as the observed object:

$$T_b = \frac{\lambda^2}{2k}I_\nu(T) \ . \tag{2.3}$$

The flux density of a source is defined as

$$S_\nu \equiv \iint_{source} I_\nu \ d\Omega \ . \tag{2.4}$$

Then, the flux density of a source of uniform brightness temperature $T_{\rm const}$ that subtends a solid angle Ω_s is, in the Rayleigh-Jeans regime:

$$S_\nu(T) = \iint_{source} I_\nu(T) \ d\Omega = \frac{2k}{\lambda^2}T_{\rm const}\Omega_s \ . \tag{2.5}$$

2.4.1.2 Efficiency parameters

Beam pattern [$\mathbf{P}_n(\theta,\phi)$]

The normalized beam pattern, $P_n(\theta,\phi)$, is the normalized response of the antenna to radiation, as a function of the angles θ and ϕ (see Fig 2.7).

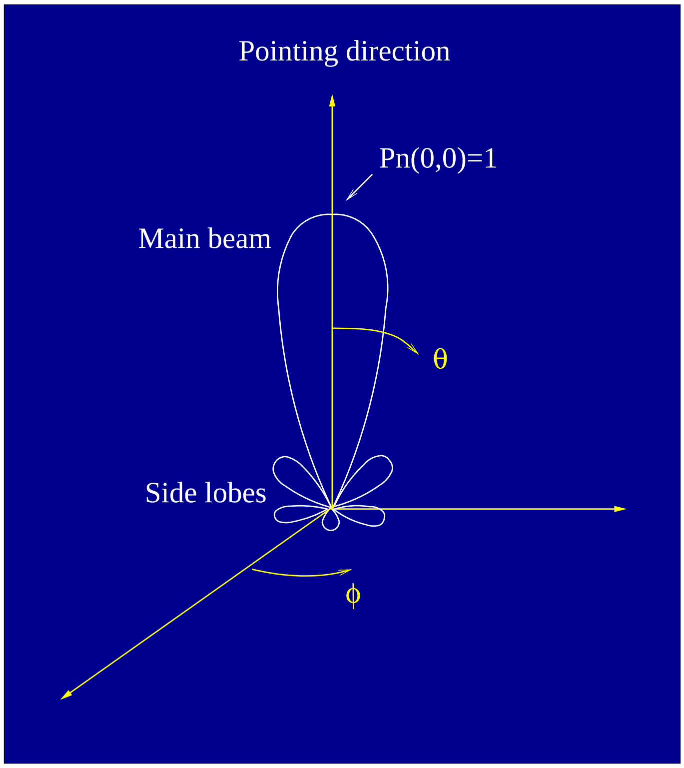

Figure 2.7: Diagram of a normalized beam pattern of an antenna in spherical coordinates.

Beam solid angle (Ω_a)

The beam solid angle, Ω_a, is the integration of the beam pattern over the whole sky (4π radian), i.e., the whole beam including sidelobes:

$$\Omega_a = \iint_{4\pi} P_n(\theta,\phi)\ d\Omega\ . \tag{2.6}$$

Main beam solid angle (Ω_{mb})

This parameter is the integration of the beam pattern over the main lobe of the beam (see fig 2.7):

$$\Omega_{mb} = \iint_{Main\ lobe} P_n(\theta,\phi)\ d\Omega\ . \tag{2.7}$$

Main beam efficiency (η_{mb})

It is the ratio between the main beam solid angle and the total beam solid angle:

$$\eta_{mb} = \frac{\Omega_{mb}}{\Omega_a} \ . \tag{2.8}$$

This efficiency indicates what fraction of the total power that an antenna can receive actually enters through the main lobe of the beam. Its complementary, the stray factor $(1 - \eta_{mb})$, reflects the contribution of the sidelobes.

Effective aperture ($\mathbf{A}_e$)

It is the area of a perfect (100% efficiency) antenna that would receive the same power as the one observed in our real antenna. The antenna theorem (Stanimirovic et al. 2002) states that:

$$A_e \Omega_a = \lambda^2 \ . \tag{2.9}$$

Geometric aperture ($\mathbf{A}_p$)

It is the physical area of the antenna:

$$A_p = \pi \left(\frac{Diameter}{2} \right)^2 \ . \tag{2.10}$$

Aperture efficiency (η_a)

This is a parameter that we need to determine for the calibration of our data. It is the ratio between the effective and the geometric aperture:

$$\eta_a = \frac{A_e}{A_p} \ . \tag{2.11}$$

2.4.1.3 Antenna temperature: The Nyquist theorem

The spectral power w available at the terminal of a resistor of temperature T is $w = k \ T$ (Nyquist 1928). Therefore, if we receive a power w with an antenna, we can define the temperature of a resistor that yields the same power:

$$w = k \ T_A \ , \tag{2.12}$$

where this equivalent temperature, T_A, is called "antenna temperature". The antenna temperature is often used as the intensity scale for Radio Astronomy observations.

2.4.1.4 The measured antenna temperature

The power per unit bandwidth received by an antenna of effective area A_e and beam pattern $P_n(\theta,\phi)$, from a source with brightness distriburion $I_\nu(\theta,\phi)$ is:

$$w = \frac{1}{2}\, A_e \iint I_\nu(\theta,\phi)\ P_n(\theta,\phi)\ d\Omega\ . \tag{2.13}$$

The *observed* flux density of the source with such an antenna is:

$$S_{\rm obs} = \iint_{source} I_\nu(\theta,\phi)\ P_n(\theta,\phi)\ d\Omega\ , \tag{2.14}$$

while the *real* flux density of the source is defined in 2.4. When the source is much smaller than the antenna main beam, then $P_n \simeq 1$ for the whole source extent, and the flux density of the source (S_ν) would be equal to the flux density observed ($S_{\rm obs}$). From equations 2.12, 2.13, and 2.14, we derive:

$$S_\nu = \frac{2k}{A_e} T_A \quad \text{(for a point source).} \tag{2.15}$$

From equations 2.12 and 2.13 we can obtain a general expression for the antenna temperature of the source:

$$T_A = \frac{1}{2k} A_e \iint_{source} I_\nu(\theta,\phi)\ P_n(\theta,\phi)\ d\Omega \tag{2.16}$$

Considering the Rayleigh-Jeans approximation and the antenna theorem, i.e., equations 2.3 and 2.9:

$$T_A = \frac{1}{\Omega_a} \iint_{source} T_b(\theta,\phi)\ P_n(\theta,\phi)\ d\Omega\ , \tag{2.17}$$

where T_b is the brightness temperature of the source.

- For a **point source**, $P_n(\theta,\phi) \simeq 1$, then

  $$T_A = \frac{1}{\Omega_a} \iint_{source} T_b(\theta,\phi)\ d\Omega\ \simeq\ \frac{\Omega_{source}}{\Omega_a}\ T_{avg}\ , \tag{2.18}$$

  where T_{avg} is the *average* brightness temperature of the source. The factor Ω_{source}/Ω_a is often referred to as the “filling factor” of the source.

- For an **extended source** that fills the main beam (i.e., $\Omega_s \simeq \Omega_{mb}$), and its brightness temperature is constant (T_{const}), then:

  $$T_A = \frac{T_{const}}{\Omega_a} \iint_{source} P_n(\theta,\phi)\ d\Omega\ =\ T_{const}\frac{\Omega_{mb}}{\Omega_a}\ =\ T_{const}\ \eta_{mb}\ . \tag{2.19}$$

  Therefore, the main beam brightness temperature, defined as

  $$T_{mb} \equiv \frac{T_A}{\eta_{mb}} \tag{2.20}$$

  can be considered as a good approximation to the brightness temperature of extended sources, assuming that this temperature does not change much within the main lobe of the beam.

2.4.2 System configuration

Before a spectroscopy track at DSS-63 starts, astronomers have to configure the system for K-band observations. This procedure consists of the following steps:

- Calibrate the zero-point of the power meters: These instruments have a good linear response with input power. However, the reading at zero input power has to be reset regularly.

- Configure and check the front-end for K-band: This includes checking the temperature of the receiver, activating the amplifier, and checking the antenna signal using the power meter readings. The program "CRDE Menu", developed in the Tcl/Tk language by JPL staff, makes these operations possible (see Fig 2.8).

- Configure the MMS downconverters: Selecting the desired preamplifiers, preselector filter, and initial sky frequency. CRDE Menu has a submenu to perform these activities (see Fig 2.8).

- Configure the back-end system: This step includes setting the appropriate mixer frequency and filters, activating the A/D converter, and launching the spectrometer control program (for the old SDS spectrometer), or configuring the video converters, setting the desired bandwidth, and launching the spectrometer control program (for the new SPB500 spectrometer).

- Configure the DSS-63 antenna for K-band: This activity is carried out by the station operators and consists of moving the subrefrector to send the signal to the K-band feed, loading the pointing correction model and the information of the first source, and activating the antenna motors to move the antenna towards the chosen position.

Once everything is configured, the astronomer is ready to launch the observing program: the "Experiment Control". This program, also developed at JPL in Tcl/Tk language, reports and controls every element needed during a spectroscopy observation. It provides control over the front-end and MMS elements, as well as over the antenna motion. It implements procedures for calibration, pointing, and data gathering with any attached spectrometer. See a snapshot of the Experiment Control program in Figure 2.9.

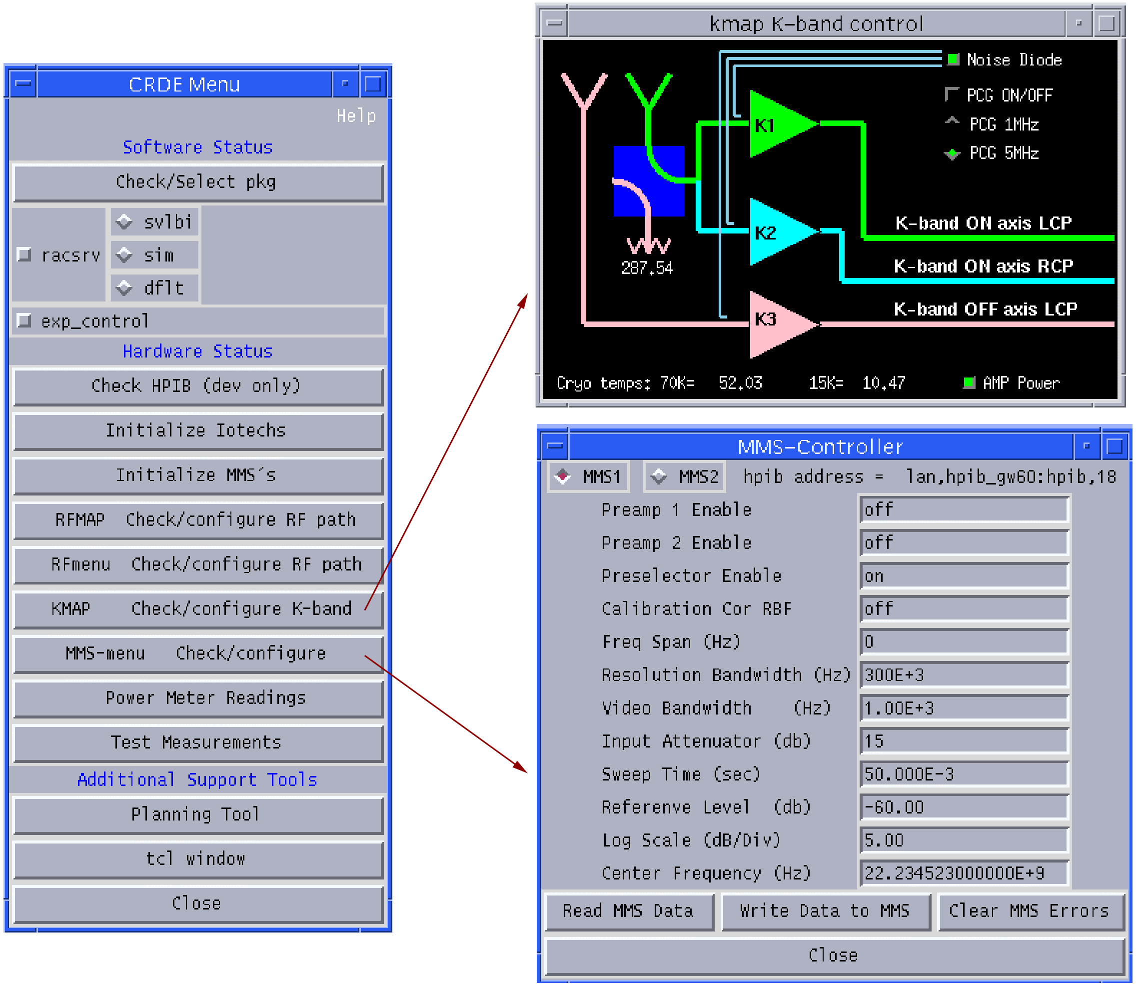

Cryo temps: 70K= 52.03 15K= 10.47

◆ MMS1 ◇ MMS2 hpib address = lan,hpib_gw60:hpib,18

Preamp 1 Enable off
Preamp 2 Enable off
Preselector Enable on
Calibration Cor RBF off
Freq Span (Hz) 0
Resolution Bandwidth (Hz) 300E+3
Video Bandwidth (Hz) 1.00E+3
Input Attenuator (db) 15
Sweep Time (sec) 50.000E-3
Referenve Level (db) -60.00
Log Scale (dB/Div) 5.00
Center Frequency (Hz) 22.234523000000E+9

Figure 2.8: CRDE Menu program for the system configuration

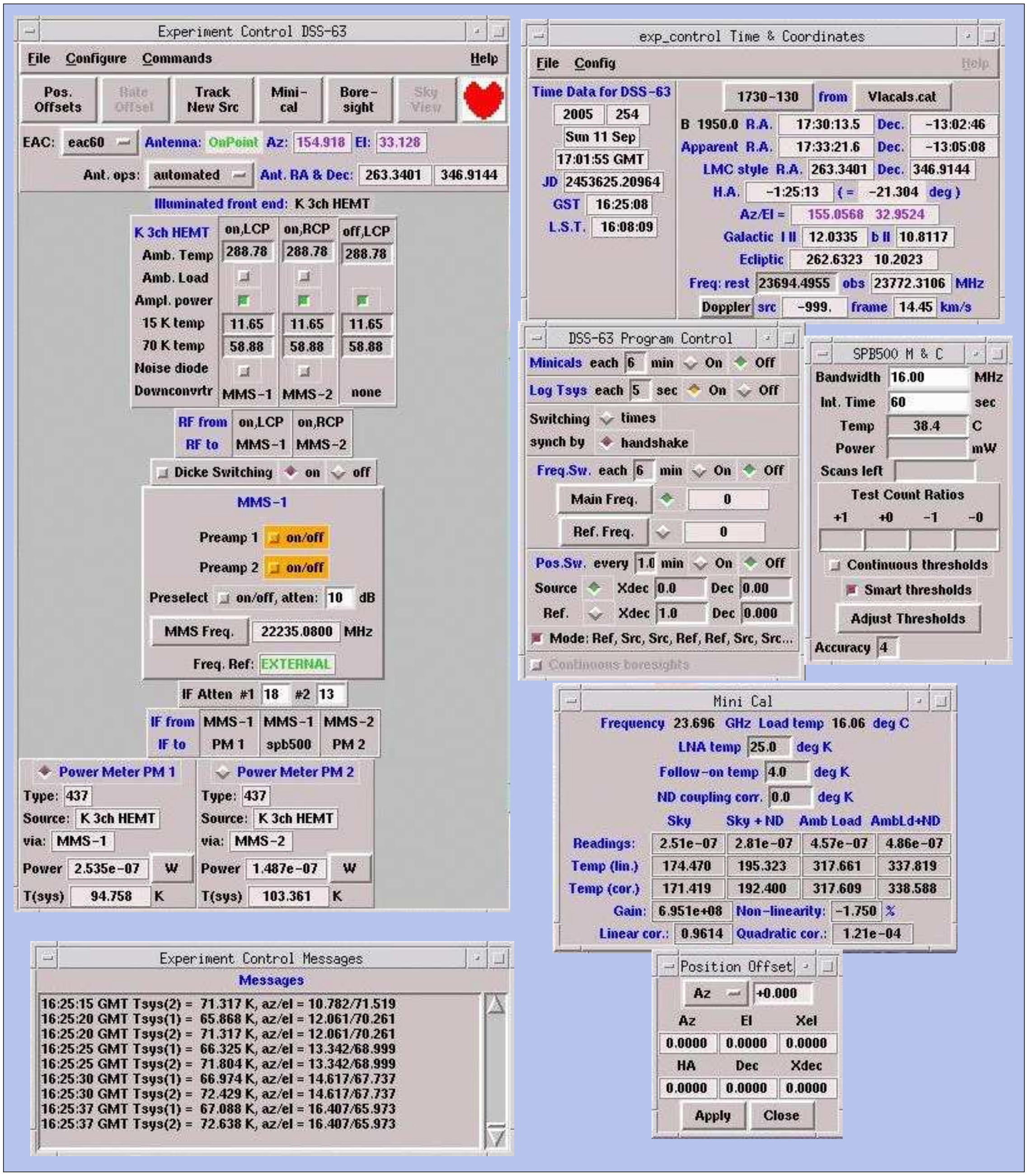

EAC: eac60 Antenna: OnPoint Az: 154.918 El: 33.128

Ant. ops: automated Ant. RA & Dec: 263.3401 346.9144

Illuminated front end: K 3ch HEMT

K 3ch HEMT	on,LCP	on,RCP	off,LCP
Amb. Temp	288.78	288.78	288.78
Amb. Load	☐	☐	
Ampl. power	☑	☑	☑
15 K temp	11.65	11.65	11.65
70 K temp	58.88	58.88	58.88
Noise diode	☐	☐	
Downconvrtr	MMS-1	MMS-2	none

RF from	on,LCP	on,RCP
RF to	MMS-1	MMS-2

☐ Dicke Switching ● on ○ off

MMS-1

Preamp 1 ☐ on/off

Preamp 2 ☐ on/off

Preselect ☐ on/off, atten: 10 dB

MMS Freq. 22235.0800 MHz

Freq. Ref: EXTERNAL

IF Atten #1 18 #2 13

IF from	MMS-1	MMS-1	MMS-2
IF to	PM 1	spb500	PM 2

● Power Meter PM 1
Type: 437
Source: K 3ch HEMT
via: MMS-1
Power 2.535e-07 W
T(sys) 94.758 K

○ Power Meter PM 2
Type: 437
Source: K 3ch HEMT
via: MMS-2
Power 1.487e-07 W
T(sys) 103.361 K

Time Data for DSS-63
2005 254
Sun 11 Sep
17:01:55 GMT
JD 2453625.20964
GST 16:25:08
L.S.T. 16:08:09

1730-130 from Vlacals.cat
B 1950.0 R.A. 17:30:13.5 Dec. -13:02:46
Apparent R.A. 17:33:21.6 Dec. -13:05:08
LMC style R.A. 263.3401 Dec. 346.9144
H.A. -1:25:13 (= -21.304 deg)
Az/El = 155.0568 32.9524
Galactic l II 12.0335 b II 10.8117
Ecliptic 262.6323 10.2023
Freq: rest 23694.4955 obs 23772.3106 MHz
Doppler src -999. frame 14.45 km/s

Minicals each 6 min ○ On ● Off
Log Tsys each 5 sec ● On ○ Off
Switching ○ times
synch by ● handshake
Freq.Sw. each 6 min ○ On ● Off
Main Freq. ● 0
Ref. Freq. ○ 0
Pos.Sw. every 1.0 min ○ On ● Off
Source ● Xdec 0.0 Dec 0.00
Ref. ○ Xdec 1.0 Dec 0.000
☑ Mode: Ref, Src, Src, Ref, Ref, Src, Src...
☐ Continuous boresights

Bandwidth 16.00 MHz
Int. Time 60 sec
Temp 38.4 C
Power mW
Scans left

Test Count Ratios

+1	+0	-1	-0

☐ Continuous thresholds
☑ Smart thresholds
Adjust Thresholds
Accuracy 4

Frequency 23.696 GHz Load temp 16.06 deg C
LNA temp 25.0 deg K
Follow-on temp 4.0 deg K
ND coupling corr. 0.0 deg K

	Sky	Sky + ND	Amb Load	AmbLd+ND
Readings:	2.51e-07	2.81e-07	4.57e-07	4.86e-07
Temp (lin.)	174.470	195.323	317.661	337.819
Temp (cor.)	171.419	192.400	317.609	338.588

Gain: 6.951e+08 Non-linearity: -1.750 %
Linear cor.: 0.9614 Quadratic cor.: 1.21e-04

Az +0.000

Az	El	Xel
0.0000	0.0000	0.0000

HA	Dec	Xdec
0.0000	0.0000	0.0000

Messages

```
16:25:15 GMT Tsys(2) =  71.317 K, az/el = 10.782/71.519
16:25:20 GMT Tsys(1) =  65.868 K, az/el = 12.061/70.261
16:25:20 GMT Tsys(2) =  71.317 K, az/el = 12.061/70.261
16:25:25 GMT Tsys(1) =  66.325 K, az/el = 13.342/68.999
16:25:25 GMT Tsys(2) =  71.804 K, az/el = 13.342/68.999
16:25:30 GMT Tsys(1) =  66.974 K, az/el = 14.617/67.737
16:25:30 GMT Tsys(2) =  72.429 K, az/el = 14.617/67.737
16:25:37 GMT Tsys(1) =  67.088 K, az/el = 16.407/65.973
16:25:37 GMT Tsys(2) =  72.638 K, az/el = 16.407/65.973
```

Figure 2.9: Observing program for spectroscopy observations (Experiment Control)

2.4.3 Antenna temperature calibration

The first step in the data calibration is to know the correspondence between the readings of the power meter (in Watt) and the equivalent antenna temperature (in Kelvin). Our power meters show a good linear behavior, and the antenna temperature (T_A) calibration could be easily obtained with a linear fit between the power (P_1 and P_2) received from two black bodies of known temperature (T_1 and T$_2$):

$$T_1 = mP_1 + n \tag{2.21}$$

$$T_2 = mP_2 + n \tag{2.22}$$

The antenna temperature calibration problem is solved by calculating the slope (m) and the intercept (n) of the linear fit:

$$m = \frac{T_1 - T_2}{P_1 - P_2} \tag{2.23}$$

$$n = T_1 - P_1 \frac{T_1 - T_2}{1 - P_2/P_1} \tag{2.24}$$

The calibration procedures we used in our observations assume that, besides a linear behavior of the power meters, their zero-power point is correctly set up, so that the intercept n equals 0. A linearity check (see below) is implemented to confirm that the calibration is correct.

In DSS-63 K-band observations, calibration has been performed using a "noise diode" and/or an "ambient load" with known equivalent temperature (T_{diode} and T_{amb} respectively), located at the entry of the receiving system (see Fig. 2.3). Spectroscopy data have been calibrated in two different ways, depending on the spectrometer used:

- **Old calibration system**, used in observations performed with the SDS spectrometer, it was performed by means of two measurements of the sky, the first one with the diode turned off, and the second one with the diode turned on, so that (see Fig. 2.10, left panel):

  $$T_1 = T_{sky} + T_{rec} \tag{2.25}$$

  $$T_2 = T_{sky} + T_{rec} + T_{diode} \tag{2.26}$$

  Where T_{rec} is the temperature of the receiving system, that is composed of the contribution of the different components (e.g., cables, mixers, amplifiers) located before the input to the spectrometer. T_{rec} is considered measurable and known, and it does not vary much with either time or frequency. Then, the factor of the power-temperature conversion is:

$$m = \frac{-T_{diode}}{P_1 - P_2} \tag{2.27}$$

These calculations were performed internally by the control program of the SDS spectrometer.

- **New calibration system**, for observations made with the SPB500 spectrometer, we make use of the known equivalent temperature of the ambient load. Then, under the assumption of zero intercept for the power meter readings, the calibration is performed with only one measurement of antenna temperature, that includes the contribution of the ambient load and the receiving system:

  $$T_1 = T_{rec} + T_{amb} \tag{2.28}$$

  Then the conversion factor to obtain antenna temperatures is:

  $$m = \frac{T_{rec} + T_{amb}}{P_1} \tag{2.29}$$

  This calibration process is performed by the task "minical", within the "Experiment Control" program. In addition, in each minical the system tests the linearity of the power meter, by measuring the power for three more antenna temperature points (T_2, T_3, and T_4, see Fig. 2.10, right panel):

  $$T_2 = T_{rec} + T_{amb} + T_{diode} \tag{2.30}$$

  $$T_3 = T_{rec} + T_{sky} + T_{diode} \tag{2.31}$$

  $$T_4 = T_{rec} + T_{sky}\ . \tag{2.32}$$

The program then compares the noise diode temperature obtained in the high-power regime ($T_2 - T_1$) with that of the low-power regime ($T_4 - T_3$) that, ideally, should be identical. We usually obtain values of non-linearity better than 2%.

In the calibration system of SPB500, it is usually enough to obtain the calibration factor m only once per frequency during an observing session, since the power meter response is known to be stable on timescales larger than the typical durations of our observing tracks ($\simeq 8$ h). The power meter readings are recorded every few seconds, and a system temperature can easily be assigned to each spectrum.

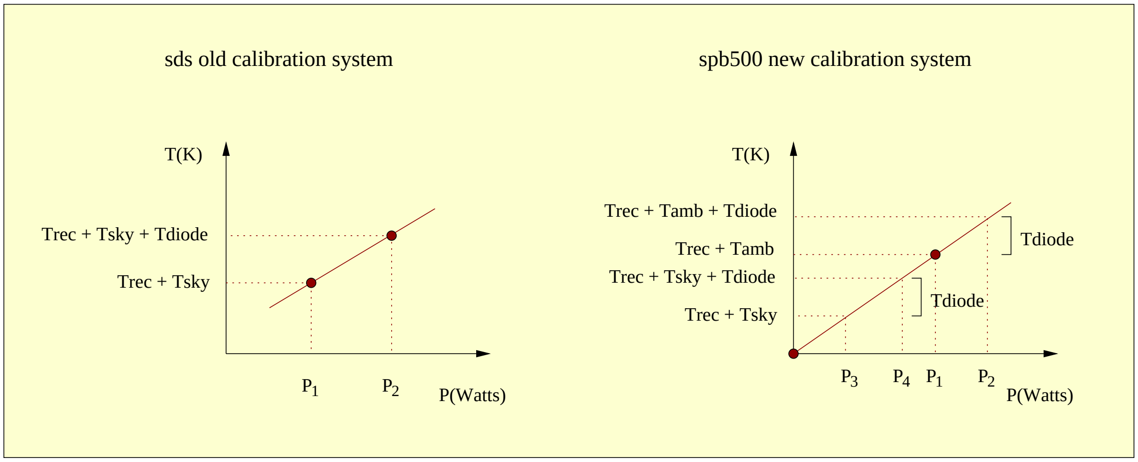

Figure 2.10: Calibration schemes to obtain antenna temperatures

2.4.4 Pointing

In K-band spectroscopy at DSS-63 we use a pointing model that provides corrections to systematic pointing errors for different values of azimuth and elevation. This model is built by making scans in both elevation and cross-elevation (the direction of a major circle perpendicular to the local meridian at the source position) over strong continuum calibrators, for a wide range of azimuth an elevation. Pointing corrections are estimated by calculating the deviation of the peak of a Gaussian fit to the data with respect to the actual pointing position of the antenna. This model is checked and revised periodically by MDSCC staff.

In addition to those first-order corrections, before we observe a source, and in order to further improve the observing position, it is necessary to make a pointing check (which we will call “boresight”) over a strong continuum source near our target. This procedure can be made by the task “boresight” in the “Experiment Control” program, and consists of performing cross-scans in elevation and cross-elevation across the calibrator, measuring the T_A at the nominal pointing positions, points at half-beam distance, and points completely off-source (Fig. 2.11). From these measurements, and assuming that the beam is a Gaussian, we derive the pointing correction.

We usually get rms pointing accuracies better than $5''$ in our observing sessions. In the worst conditions, the pointing accuracy is always better than $10''$. Once we have a good pointing estimate, we are already prepared to carry out the next step: observe an interesting source.

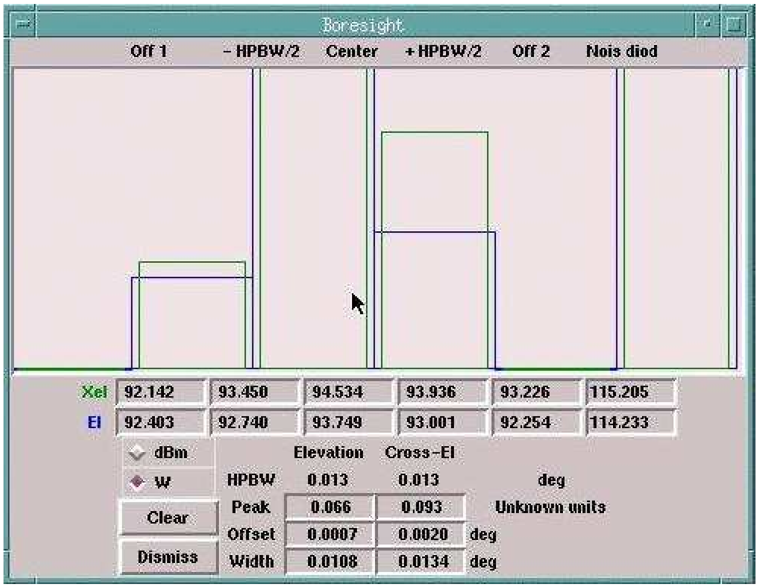

	Off 1	- HPBW/2	Center	+ HPBW/2	Off 2	Nois diod
Xel	92.142	93.450	94.534	93.936	93.226	115.205
El	92.403	92.740	93.749	93.001	92.254	114.233

	Elevation	Cross-El	
HPBW	0.013	0.013	deg
Peak	0.066	0.093	Unknown units
Offset	0.0007	0.0020	deg
Width	0.0108	0.0134	deg

Figure 2.11: Experiment Control boresight

2.4.5 System temperature and atmospheric corrections

The antenna temperature measured toward a source is the sum of the system temperature (T_{sys}) and the source temperature (T_s) attenuated by the atmosphere.

$$T_A = T_{sys} + T_s\ e^{-\tau_0 A}\ , \tag{2.33}$$

where τ_0 is the opacity at zenith, A is the air mass $[1/\sin(h)]$, and h is the antenna elevation. The system temperature is the contribution of the noise produced by the antenna components located before the input to the spectrometer (T_{rec}) plus and the atmospheric emission (T_{atm}), and therefore:

$$T_A = T_{rec} + T_{atm} + T_s\ e^{-\tau_0 A}\ . \tag{2.34}$$

The atmospheric contribution is $T_{atm} = T_{eq}(1-\ \mathrm{e}^{-\tau_0 A})$, where T_{eq} is the mean equivalent temperature of the atmosphere ($\simeq$ 265 K):

$$T_A = T_{rec} + T_{eq}(1 - e^{-\tau_0 A}) + T_s\ e^{-\tau_0 A}\ . \tag{2.35}$$

To determine the source temperature, we have to substract the system temperature and derive the value of τ_0. In practice, the source temperature can be separated from the system temperature by making two observations: one of them ON source (i.e., including the source within the beam), and the other one OFF source (i.e., without including the source), then:

$$T_{ON} = T_{sys} + T_s\ e^{-\tau_0 A}\ , \tag{2.36}$$

$$T_{OFF} = T_{sys} \ , \tag{2.37}$$

The value of the source temperature attenuated by the atmosphere will be given by:

$$T_s \ e^{-\tau_0 A} = \left[\frac{T_{ON}}{T_{OFF}} - 1 \right] T_{sys} \ , \tag{2.38}$$

which is the algorithm we used to calibrate our spectra.

2.4.5.1 System temperature substraction

The value of the system temperature can be easily eliminated in spectroscopic observations using two basic observing modes:

- **Position switching**: This technique involves observing the source of interest and then moving the telescope to a region in the sky close to our source and taking another spectrum. Then the spectra are divided and the equation 2.4.5 is applied, obtaining the value of $T_s \ e^{-\tau_0 A}$. This is the mode used in observations with the new spectrometer SPB500.
- **Frequency switching**: This technique obtains the sky information by keeping the telescope pointed at the source of interest, but switching the center frequency of the measurements. Assuming that the system emission does not change much within the applied frequency shift, the two sets of data are divided and the equation 2.4.5 is applied, obtaining the value of $T_s \ e^{-\tau_0 A}$. This was the mode used in observations with the old spectrometer SDS.

2.4.5.2 Atmospheric corrections

At centimeter wavelengths, water vapor is the major contributor to atmospheric opacity. To correct for atmospheric absorption we must know the value of the atmospheric opacity at the zenith (τ_0) and the elevation where the source was observed. In Robledo K-band spectroscopy the τ_0 is obtained by observing the blank sky at different elevations, from zenith to horizon, and by building a curve of system temperature versus elevation:

$$T_A = T_{sys} = T_{rec} + 265 \ (1 - e^{-\tau_0 A}) \ . \tag{2.39}$$

This procedure is made by the task “tipping curve”, implemented in “Experiment Control”. It assumes an optically thin atmosphere, which transforms equation 2.39 in:

$$T_{sys} = T_{rec} + 265 \ (\tau_0 A) \tag{2.40}$$

Then, performing a linear fit, both values, τ_0 and T_{rec}, are obtained. Tipping curves are obtained at least once per observing session and per frequency observed. If weather conditions drastically change during an observation, this procedure has to be repeated. Typical zenith opacities were $\simeq 0.08$.

2.4.6 Scale conversion

2.4.6.1 Aperture efficiency

To estimate the relationship between the antenna temperature and the flux density of a point source, we need an estimate of the aperture efficiency of the antenna. From equations 2.11 and 2.15:

$$S_\nu = \frac{T_A}{A_e/2k} = \frac{2kT_A}{\eta_a A_p} \, . \tag{2.41}$$

This equation indicates that the aperture efficiency η_a can be estimated by measuring the antenna temperature of a source of known flux density, at different elevations. For the DSS-63 antenna, and as an example, we will show how we have proceeded to determine the aperture efficiency for data taken after 2004 April:

- We measured the antenna temperature of a strong continuum calibrator visible in a wide range of elevations and at a frequency of 22340.1372 MHz. To do this, we made cross-scans at different elevations of the source 3C84 ($S_{22\mathrm{GHz}} \gtrsim 10$ Jy), which culminates near zenith at Robledo. The peaks of Gaussian fit to these scans provided the source antenna temperature, which was then corrected for atmospheric opacity (see Fig. 2.12). We made a 4-degree polynomial fit to compute the shape of the aperture efficiency curve as a function of the elevation. Since 3C84 is not a primary calibrator, we also made observations at the same frequency toward the fainter ($S_{22\mathrm{GHz}} \simeq 2.6$ Jy) flux density calibrator 3C286 (see Fig. 2.12).

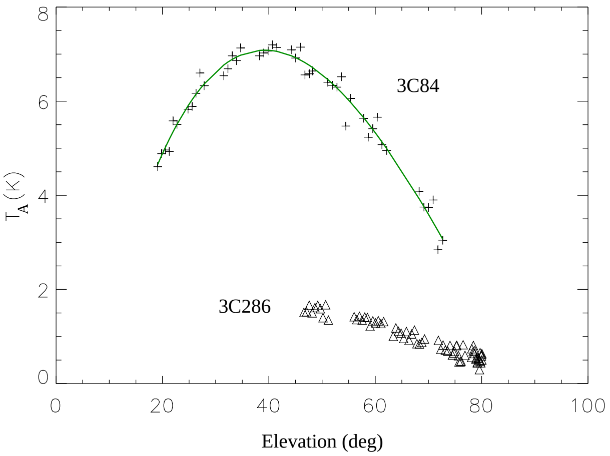

Figure 2.12: Antenna temperature of sources 3C84 and 3C286 as a function of elevation, after correction by atmospheric opacity. Crosses and triangles represent the data for 3C84 and 3C286, respectively. The green curve is the 4-degree polynomial fit to the 3C84 data.

- We rescaled the polynomial obtained for 3C84, to get the best least-square fit to the antenna temperature data of 3C286 (see Fig. 2.13) for the elevations in which both datasets overlap.

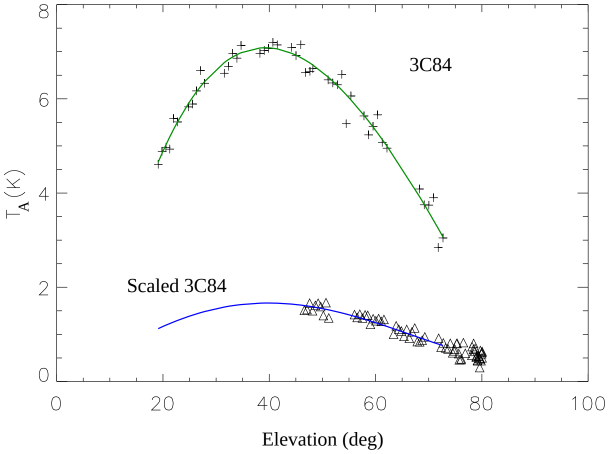

Figure 2.13: The blue curve is the rescaled 4-degree polynomial fit to the 3C84 data. Symbols and green curve have the same meaning as in Fig. 2.12

- We multiplied the source antenna temperature data of 3C84 by the factor obtained to scale the polynomial, in order to scale 3C84 to the flux density of 3C286. We then made a new 4-degree polynomial fit to the scaled 3C84 data together with the 3C286 data (see Fig. 2.14). This provides a fit to the antenna temperature of 3C286 as a function of elevation, valid for elevations between 19.°1 and 80.°0.

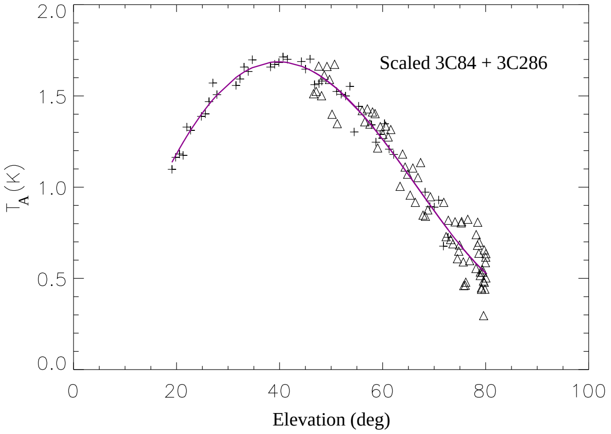

Figure 2.14: Final shape of the antenna efficiency curve. The violet curve is a 4-degree polynomial fitting to the scaled 3C84 data and the 3C86 data. Symbols have the same meaning as in Fig. 2.12

- Finally, we estimated the aperture efficiency curve considering the physical area of the antenna ($\pi\ [70m/2]^2$), and the flux density of 3C286 at the frequency studied, derived from[1]:

  $$\log\ S_\nu = 1.23734 - 0.43276\ \log\ \nu - 0.14223\ (\log\ \nu)^2 + 0.00345\ (\log\ \nu)^3\ ,$$

  where S_ν is the flux density in Jansky and ν is the observed frequency in GHz. Then using the linear fit to T_A as a function of elevation that we obtained, and eq. 2.41, the resulting aperture efficiency curve at 22340.1372 MHz (see Fig. 2.15), is given by:

  $$\eta_a = -0.068 + 0.024\ h - (1.17 \times 10^{-4})\ h^2 - (5.6 \times 10^{-06})\ h^3 + (4.7 \times 10^{-08})\ h^4\ ,$$

  with h measured in degrees. This curve is valid for elevations between $19\overset{\circ}{.}1$ and $80\overset{\circ}{.}0$, and peaks at $39\overset{\circ}{.}8$, with a value of $\eta_a = 0.477$.

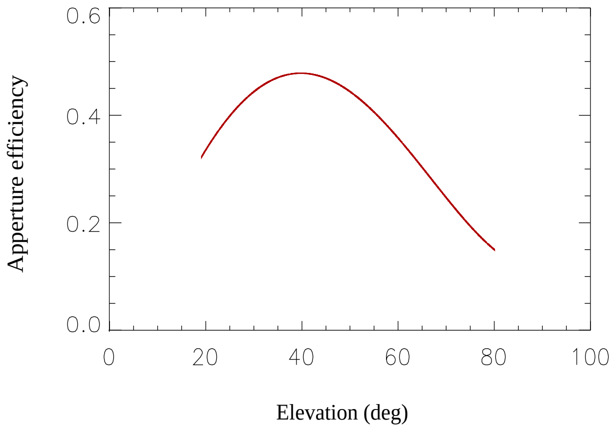

Figure 2.15: Aperture efficiency curve at 22340.1372 MHz, as a function of the elevation.

In order to calculate the aperture efficiency curve at frequencies other than 22340.1372 MHz, we estimated the rms surface accuracy from Ruze's formula:

$$\eta_a = \eta_0\ \exp\left[-\left(\frac{4\pi\sigma}{\lambda}\right)^2\right] \tag{2.42}$$

Where η_0 is the aperture efficiency of a perfect paraboloid reflector with the given illumination properties, which we will assume to be equal to 1, and σ is the rms of surface deviations of our antenna from a perfect paraboloid shape. Using this formula, we derived a peak value of $\sigma \simeq 0.9$ mm, similar to the value of $\simeq 0.8$ mm obtained by holographic

---

[1] http://www.aoc.nrao.edu/~gtaylor/calman/baars.html

measurements, a consistency that gives support to the results of our calculations. Then, we can derive the aperture efficiency for any frequency within the observing K-band as:

$$\eta_a(\nu) = \exp\left[-\left(\frac{\nu}{\nu_0}(\sqrt{-\ln[\eta_a(\nu_0)]}\right)\right]^2 \tag{2.43}$$

with $\nu_0 = 22340.1372$ MHz.

Each time the position of the subreflector changes for optimization, a new aperture efficiency curve must be obtained, since the illumination parameters may change. During the four years of spectroscopy observations for this thesis, the subreflector position has been moved twice, thus resulting in three different setups. The values reported here are valid for the current position (as of 2005 September). Aperture efficiencies for all subreflector positions we used are of similar values.

2.4.6.2 Main beam efficiency

As mentioned in sec. 2.4.1.4 to estimate the main beam brightness temperature of an extended source, we need the value of the main beam efficiency:

$$T_{mb} = \frac{T_A}{\eta_{mb}} \, . \tag{2.44}$$

The main beam efficiency is the ratio between the main beam solid angle Ω_{mb} and the beam solid angle Ω_a (see equation 2.8). The latter can be derived using equations 2.9, 2.10, and 2.11, which, for the particular case of a 70 m antenna, yield:

$$\Omega_a = \frac{\lambda^2}{\eta_a \ \pi \ \left(\frac{70m}{2}\right)^2} \, . \tag{2.45}$$

On the other hand, we estimated the value of the main beam solid angle of DSS-63, proceeding as follows:

- We carried out cross-scans on strong continuum point-like sources at different elevations, to derive the beam pattern response, at a frequency of 23694.5 MHz . See an example of these observations towards the calibrator 3C84 in Fig 2.16.

- For each scan, we substracted a linear baseline. Then, we normalized both the elevation and cross-elevation profiles and applied a polynomial fit to them, keeping as the main beam the curve between the first zeros.

- We computed the main beam solid angle by means of a bidimensional numerical integration of the main beam pattern profile (see eq. 2.7). The numerical program calculates the bidimensional main beam pattern considering that a cut-off of the beam at a particular height is an ellipse whose axes are equal to the width of the cross-scans at that height (see Fig. 2.17).

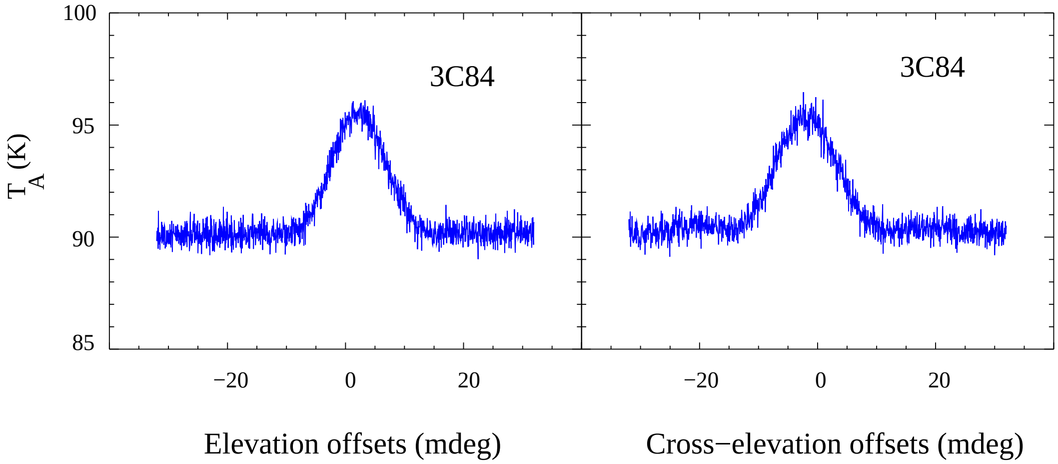

Figure 2.16: Observation of the beam pattern response using the source 3C84 at a frequency of 23694.5 MHz, at elevation = 48°.

- This numerical calculation provided us with the main beam solid angle at different elevations. Then, we made a 2-degree polynomial fit to the results, obtaining the main beam solid angle as a function of elevation and at a frequency of 23694.5 MHz (see Fig. 2.18, upper panel):

$$\Omega_{mb} = 6.3751744 \times 10^{-8} - (1.1772181 \times 10^{-9})\ h + (1.4366759 \times 10^{-11})\ h^2\ .$$

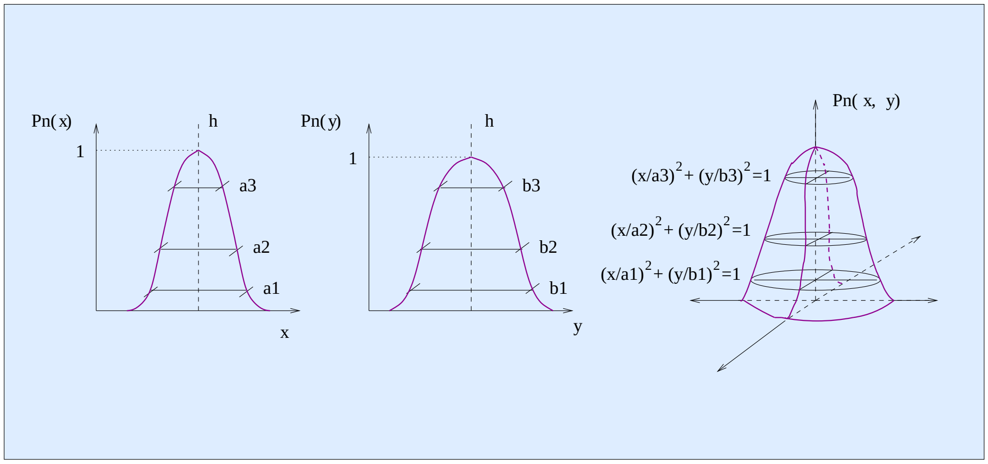

Figure 2.17: Main beam construction. Left and central plot represent the observed cross-scans (Fig. 2.16). Right plot represents the numerical procedure for building the main beam pattern, which is then integrated to obtain the main beam solid angle

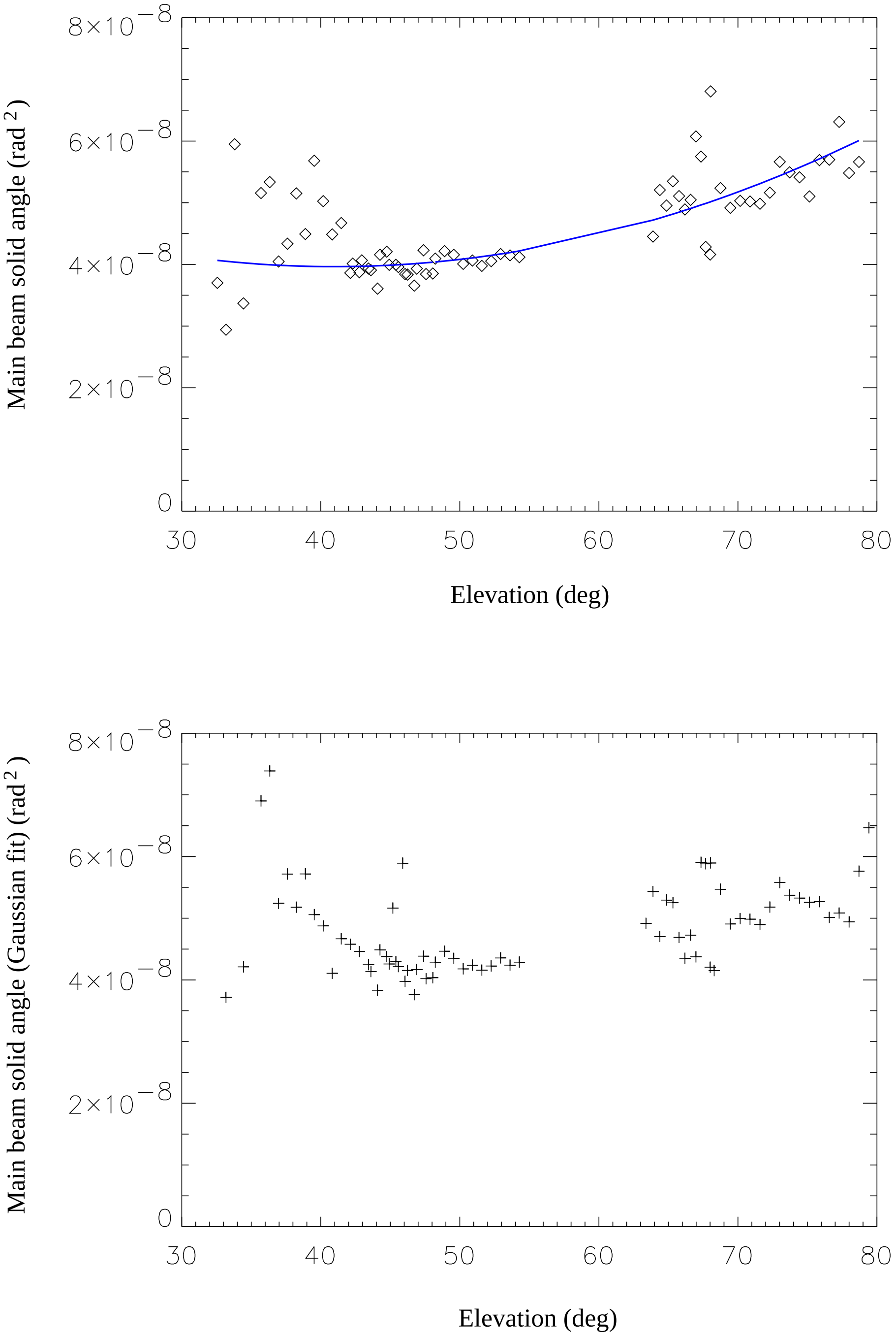

Figure 2.18: Upper panel: main beam solid angle derived from numerical calculations. Lower panel: main beam solid angle derived from Gaussian fits. The solid lines represent a polynomial fit to beam solid angle data. Note that, for clarity, we plotted points corresponding to data taken on a single day, while the fitted line was built with more data.

The method above uses the measured beam profiles, without assuming a Gaussian shape for them. In order to test the deviation from a Gaussian main beam, we made Gaussian fits to the profiles obtained in the cross-scans, and we calculated the full angular width between the half power points of the resulting fits (θ_{FWHM}, the angular resolution of the telescope). For an elliptical Gaussian with major and minor FWHM θ_M and θ_m, respectively, the main beam solid angle would be (Stanimirovic et al. 2002):

$$\Omega_{mb} = \frac{\pi}{4\ ln2}\ \theta_M\ \theta_m = 1.133\ \theta_M\ \theta_m\ . \tag{2.46}$$

The values obtained with Gaussian fits (Fig. 2.18, lower panel) are consistent with the values obtained in the numerical calculations.
The angular resolution θ is limited by the diffraction pattern of the radio telescope. For a circular aperture, the angular resolution is $\theta \simeq 1.22\lambda/D$, with D the diameter of the aperture and, in general:

$$\theta\ \alpha\ \frac{1}{\nu} \tag{2.47}$$

Then:

$$\Omega_{mb}\ \alpha\ \frac{1}{\nu^2} \tag{2.48}$$

and the main beam as a function of elevation and frequency would be:

$$\Omega_{mb}(\nu) = \Omega_{mb}(\nu_0)\ \left[\frac{\nu_0}{\nu}\right]^2 \tag{2.49}$$

with ν_0=23694.5 MHz. Then, from eq. 2.8, 2.45, and 2.49, we derive a general expression for the main beam efficiency as a function of the frequency:

$$\eta_{mb}(\nu) = \Omega_{mb}(\nu_0)\ \eta_a(\nu)\ \pi\ \left[\frac{\nu_0 D}{2c}\right]^2 \tag{2.50}$$

with D=70 m, in our case.

We compared ammonia spectra corrected by main beam efficiency of some sources taken with with both, the Robledo-70m antenna and Effelsberg (e.g., Estalella et al. 1993) and the results are compatible, within $\simeq$ 10%. Therefore, our estimates seem good enough for the purposes of this thesis.

Chapter 3

A sensitive survey for water maser emission towards Bok globules.

In this chapter we report the most sensitive water maser survey towards Bok globules to date, using NASA's 70 m antenna in Robledo de Chavela (Spain). We observed 207 positions within the Clemens & Barvainis (1988) catalog with a higher possibility of harboring a young star, using as selection criteria the presence of radio continuum emission (from submillimeter to centimeter wavelengths), geometrical centers of molecular outflows, peaks in maps of high-density tracers (NH_3 or CS), and IRAS point sources. We also present a statistical study of our selection criteria as predictors for the presence of maser emission.

3.1 Motivation

Bok globules have traditionally been considered important laboratories for the study of phenomena related to star formation, mainly due to their small size ($\leq 20'$) and relatively simplicity, which make the star forming processes less likely to be affected by confusion from different generations of YSOs (see section 1.2).

An important phenomenon related to star formation is the occurrence of water maser emission at 22 GHz. This emission provides a good characterization of the age of low-mass YSOs, where sources that host water masers emission are good candidates to be in a very early stage of its evolution (Furuya et al. 2001). In addition, several works (Torrelles et al. 1997, 1998b) have suggested a possible evolutionary sequence, with masers tracing circumstellar disks in the youngest sources, and outflows in more evolved YSOs (see section 1.6.2).

Since there are several evolutionary aspects related to water maser emission, it is interesting to study this emission in Bok globules, where we can find YSOs in different evolutionary stages. However, there are very few studies of water masers towards Bok globules. Only Scappini et al. (1991) intended a search for water masers specifically in Bok globules. These authors observed 80 globules, and obtained a detection towards CB 3 (LBN 594), with a peak flux density of $\simeq 77.6$ Jy. However, their detection threshold ($\sim 4.4 - 15.7$ Jy) would miss a high fraction of masers around low-mass YSOs.

Other surveys included among their targets some objects within the globules in the CB catalog (Felli et al. 1992; Palla & Prusti 1993; Wouterloot et al. 1993; Persi et al. 1994; Codella & Felli 1995). To our knowledge, only three Bok globules of the CB catalog have been reported to harbor a water maser: the mentioned one in CB 3 (Scappini et al. 1991), a detection of $\simeq 1-2$ Jy towards the Herbig Be star HD 250550 in CB 39 (Schwartz & Buhl 1975), and another one of $\simeq 7.5$ Jy in CB 205 (LDN 810) obtained by Neckel et al. (1985). We are not aware of any water masers in the southern Bok globules of the BHR catalog.

In this chapter, we have searched for water maser emission towards the positions within the globules in the CB catalog with the highest probability of harboring a YSOs. This survey aims to be nearly complete for possible star-forming regions in Bok globules north of declination $\simeq -36^\circ$, to study the conditions and characteristics of maser emission in these isolated globules. This work is complemented by high-resolution interferometric studies of the detections in this survey, to accurately determine their spacial and velocity distribution (see Chapter 4). This chapter is structured as follows: In §3.2 we describe the technical details of the observations, in §3.3 we explain the criteria used to select the target sources, we present our results in §3.4, which are further discussed in §3.5. We summarize our conclusions in §3.6.

3.2 Observations

We observed the $6_{16} \rightarrow 5_{23}$ transition of the water molecule (rest frequency 22235.080 MHz) using the NASA 70 m antenna (DSS-63) at Robledo de Chavela (See Chapter 2 for technical details). Water maser observations were carried out using three different backends depending on the observing dates: From 2002 March 13 to 2002 April 10, we used the 4096 channel spectrometer (SAO4K) covering a bandwidth of 400 MHz ($\simeq 5398$ km s^{-1}), which provided a velocity resolution of $\simeq 1.3$ km s^{-1}. From 2002 April 14 to 2003 July 18, we used the 256-channel autocorrelation spectrometer (SDS), covering a bandwidth of 10 MHz, which provided a velocity resolution of $\simeq 0.5$ km s^{-1}. From 2004 July 6 to 2005 October 16, we used the 384-channel spectrometer (SPB500), covering a bandwidth of 16 MHz ($\simeq 216$ km s^{-1} with $\simeq 0.6$ km s^{-1} resolution). Spectra were taken in position-switching mode with the SAO4K and SPB500 spectrometers, and in frequency switching mode, with a switch of 5 MHz, when using SDS, thus providing in the latter case an effective velocity coverage of $\simeq 202$ km s^{-1} (15 MHz) centered at the $V_{\rm LSR}$ of each source. System temperatures ranged between 45 and 135 K, and the total integration time was typically 20 min per source in frequency-switching mode and 30 min (on+off) in position-switching mode. The rms pointing accuracy was better than $10''$. The data reduction was performed using the CLASS package, which is part of the GAG software package developed at IRAM and Observatoire de Grenoble.

3.3 Source Sample. Selection criteria

The target positions in our survey are those within the Bok globules cataloged by CB that show indications of possible star formation, or with higher probability of harboring a YSO. We used four selection criteria for those targets:

1. **Radio continuum sources (submillimeter to centimeter wavelengths).**
   Low-mass stars undergoing mass-loss can show radio continuum emission from ionized winds (Anglada et al. 1992), which at cm wavelengths is not likely to be significantly contaminated by dust emission from envelopes and disks. For the mm and submm emission, the youngest protostars (deeply embedded class 0 sources) show prominent emission at those wavelengths (André et al. 1993; Saraceno et al. 1996). The radio continuum sources were taken mainly from Anglada et al. (1992, 1998), Yun et al. (1996), and Moreira et al. (1999) at cm wavelengths, Launhardt & Henning (1997) at mm, and Launhardt et al. (1997), Huard et al. (1999), Huard et al. (2000), and Visser et al. (2002) at submm ones. We selected those sources located within the optical boundaries of the cloud and which were not suspected to be extragalactic objects due to their negative spectral indices (see e.g., Anglada et al. 1998).

2. **Center of molecular outflows.**
   Molecular outflows driven by low-mass YSOs are specially powerful during the earlier evolutionary phases (Bontemps et al. 1996), which in their turn, are more likely to show water maser emission Furuya et al. (2001). We have chosen the position of the geometrical center of the outflow (i.e. between the red- and blue shifted lobes), since we expect the driving source of the outflow to be near that position. In the case of outflows with only one lobe, we selected the position of the proposed powering source. Most molecular outflows known in Bok globules of the CB catalog have been reported by Yun & Clemens (1992, 1994a).

3. **Peak of high-density molecular tracers.**
   YSOs form in the densest part of molecular clouds. The maxima in maps of high-

density tracers like NH_3 have been found to pinpoint the location of the driving sources of molecular outflows (Anglada et al. 1989; Gómez et al. 1994). For this survey we have used the peaks of NH_3 maps compiled by Jijina et al. (1999), most of them observed by Lemme et al. (1996) in these globules, and peaks of CS maps published by Launhardt et al. (1998).

4. **IRAS sources.**
   Many globules have been scarcely studied, if at all, so the previous observational signs of possible star formation are not always available. Therefore, we have also used the position of IRAS sources as possible locations of YSOs. We considered as target positions all IRAS sources listed by CB as associated with the globules in their catalog. Most of these IRAS sources show rising IRAS fluxes at longer wavelengths, which is expected for class 0 and class I objects (Wilking et al. 1989b; André et al. 1993), but our search was not restricted based on their far infrared spectra.

These criteria are ordered by decreasing preference given to the observations of sources selected by each of them. After compiling the initial set of target positions (all located north of $\delta = -36^\circ$) we dropped from the list most sources lying within a distance of $\sim 21''$ from another source with equal or higher preference, since they would be within the beam of Robledo radio telescope, although we observed some positions that would have been left out by this proximity filter, specially for the ones that would fall closer to the edge of the telescope beam. With these selection criteria, the previously reported masers in CB 39 and CB 205 are within the beam of one of the positions in our survey (see notes to Table 3.1). This is not the case for the maser reported in CB 3 by (Scappini et al. 1991), but our interferometric data (Chapter 4) provided a more accurate position, which lies $5''$ from the position of CB3-mm, a source that is included in our target list. Therefore, we see that our selection criteria seem appropriate to locate water maser emission that may exist in Bok globules of the CB catalog.

Using the final list of target sources, we searched for water masers around all radio continuum sources, centers of outflows, and peak of high-density tracers, with a total of 100 observed positions. In addition to that, we also observed 107 IRAS sources with no known nearby source falling into the other three categories. The observed sources are shown in Table 3.1.

Considering the sources lying within a distance of $\sim 21''$ from each observed position, and therefore, which fell within the telescope beam for at least one of the observations, our survey covered 34 centimeter sources, 20 millimeter sources, 30 submillimeter sources, 16 centers of outflows, 18 peaks of CS maps, 18 peaks of NH_3 maps, and 132 IRAS sources.

3.4 Results

3.4.1 Survey results

Tables 3.2 and 3.3 show the results of our survey of water maser emission in Bok globules. We have obtained seven detections (Table 3.2), six of which (the ones in CB 34, CB 54, CB 65, CB 101, CB 199, and CB 232) are reported for the first time here. Of the previously known masers, only CB3-mm was detected by us. We did not detect the masers in either CB 39 or CB 205. In Figs. 3.1 to 3.7 we show the spectra of the detected masers.

With these detections, we have increased the number of sources in Bok globules known to emit water maser emission from 3 to 9. However, we note that some of the new detections are not likely to be related to their respective globules, and they could be background or foreground objects projected against the clouds (see Sec. 3.4.2). The ones which are most likely to be associated to YSOs in these globules are the masers in CB 34, CB 54, and CB 232 (and probably CB 199).

With respect to our selection criteria, considering the sources that fall within the beam of the telescope of a position with water maser detected, we have detected water maser emission around 2 centimeter sources (6%), 2 millimeter sources (10%), 4 submillimeter sources (13%), 3 centers of molecular outflows (19%), 3 peaks of CS (17%), no peak of NH_3 (0%), and 5 IRAS sources (4%), 2 of them without association with any of the other criteria (2%).

3.4.2 Detections: individual sources

3.4.2.1 CB 3 (CB3-mm)

CB 3 is located at a distance of $\simeq$ 2.5 kpc (Launhardt & Henning 1997). This large distance (and thus, large physical size, $\simeq$ 4.5 pc, see CB), and the presence of intermediate-mass star formation (it hosts a source of $L_{\rm bol} \simeq 930$ $M_\odot$; Launhardt et al. 1997) distinguish it from the rest of the globules in the CB catalog.

We detected water maser emission towards the millimeter source CB3-mm detected by Launhardt & Henning (1997). This source is believed to be the powering source of a powerful bipolar molecular outflow (Yun & Clemens 1992, 1994a; Codella & Bachiller 1999). The maser probably corresponds to the one detected by Scappini et al. (1991), although they reported a position $\sim 1'$ from CB3-mm. We took spectra towards their position, but we did not detect any emission (3σ upper limit of 0.5 Jy on 2004 August 19, between $V_{\rm LSR} = -146.2$ and 69.5 km s^{-1}), which is compatible with beam response if the emission is actually related to CB3-mm (see Chapter 4). Within the beam of the Robledo telescope from CB3-mm, there is also submillimeter emission (Launhardt et al.

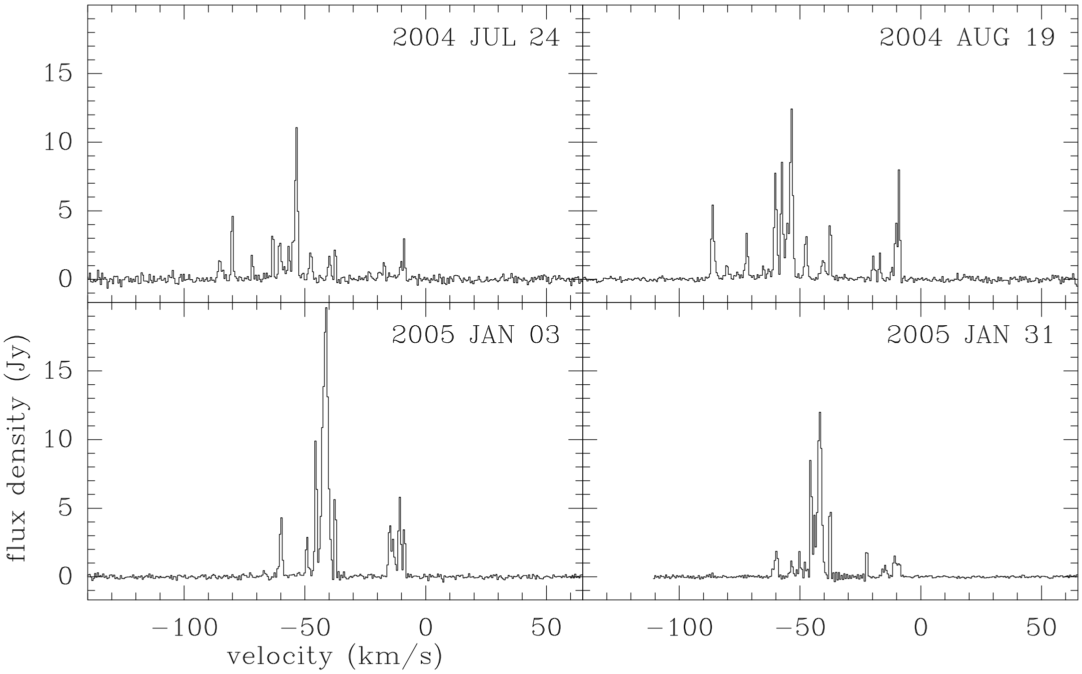

Figure 3.1: Water maser spectra towards CB3-mm detected with the Robledo-70m antenna

1997; Huard et al. 2000), the peak of a CS map (Launhardt et al. 1998), and the source IRAS 00259+5625 (Table 3.1).

The maser emission is relatively strong (10 − 20 Jy), and shows variations of a factor of ∼ 2 (Table 3.2). The spectra are very rich in maser components at different velocities (Fig. 3.1), with variations in the velocity distribution and in the ratio between different components. The data taken in 2004 show maser emission over a wider range of velocities (from −85 to −10 km s^{-1}), while those taken in 2005 do not show emission more blueshifted than −60 km s^{-1}. The centroid velocity of the maser emission ($V_{\rm LSR} = -37.5$ to -52.8 km s^{-1}, depending on the observing date) is within 15 km s^{-1} from the cloud velocity ($V_{\rm LSR} \simeq -38.3$ km s^{-1}, CB).

3.4.2.2 CB 34 ([HSW99] CB 34 SMM 3/SMM 4)

CB 34 is a globule with multiple star formation (Alves & Yun 1995), located at 1.5 kpc (Launhardt & Henning 1997). We detected water maser emission towards the submillimeter source CB 34 SMM 3 (Huard et al. 2000). The maser emission was detected in August 2003 (Fig. 3.2), with two main components (at ≃ 1 and 8 km s^{-1}, respectively) close to the cloud velocity ($V_{\rm LSR} \simeq 0.7$ km s^{-1}, CB). Several months later, the emission dropped below the detection threshold of the telescope.

In the vicinity of CB 34 SMM 3 there are several Herbig-Haro objects (HH 290N1,

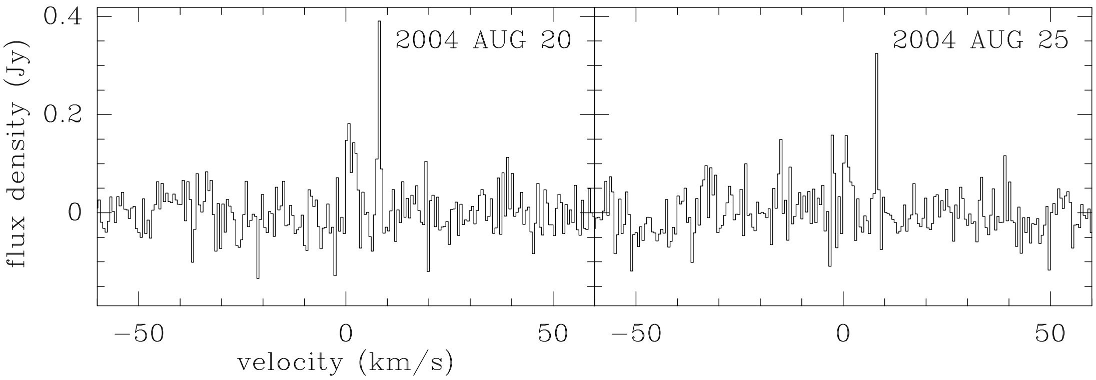

Figure 3.2: Water maser spectra towards [HSW99] CB 34 SMM 3 detected with the Robledo-70m antenna

HH 290N2, HH290S, and HH291) and H_2 knots, all forming at least three highly collimated jets in different directions (Moreira & Yun 1995; Khanzadyan et al. 2002). Within the Robledo beam from CB 34 SMM 3 also lies the submillimeter source CB 34 SMM 4 (Huard et al. 2000), and the geometrical center of the bipolar outflow reported by Yun & Clemens (1992), oriented NE-SW, although higher-resolution observations (Khanzadyan et al. 2002) seem to locate its center closer to the position of CB 34 SMM 1. Although CB 34 SMM 4 was not in our original list of targets, given that it was within the beam when observing at CB 34 SMM 3, we took an additional spectrum at its position $[\alpha(J2000) = 05^h47^m05\overset{s}{.}2$, $\delta(J2000) = +21°00'25'']$ on 2004 August 25, to try to determine with which source the maser emission was more likely to be related to. However, the spectrum was similar (peak intensity $\simeq 0.32 \pm 0.13$ mJy at 7.7 km s^{-1}) to the one obtained at CB 34 SMM 3 the same day (Table 3.2). Therefore, it is not possible to ascertain the association of the maser with either submillimeter source, and since the signal-to-noise ratio of the spectra was relatively low, any other attempt to determine a more precise position would have been subject to high uncertainties. The water maser may in fact be pumped by a source lying roughly at the same distance from SMM 3 and SMM 4. A good candidate could be source Q, also lying within the telescope beam from both submillimeter sources (at $\sim 13''$ from them), and which Moreira & Yun (1995) suggested to be the powering source of one of the jet-like chains of H_2 knots (Q knots). Interestingly, this jet is the one whose orientation is closer to that of the molecular outflow. Therefore, this Q-jet could trace the dominant mass-loss process in CB 34. No interferometric observations of the maser emission have been carried out so far. Such observations would be useful to determine the excitation source of the maser and to relate the water maser distribution with that of the jets in the region.

3.4.2.3 CB 54 ([YMT96] CB 54 2)

CB 54 (LBN 1042), located at 1.5 kpc (Launhardt & Henning 1997), is an active site of star formation, with multiple jets (Khanzadyan 2003) and a bipolar outflow (Yun & Clemens 1992, 1994a). We detected water maser emission towards the centimeter source [YMT96] CB 54 2 (Yun et al. 1996; Moreira et al. 1997). Within the beam of the Robledo telescope also fall the infrared object IRAS 07020-1618, a mm source (Launhardt & Henning 1997), a submillimeter source (Launhardt et al. 1997), the peak of a CS map (Launhardt et al. 1998), and the geometrical center of the molecular outflow (Yun & Clemens 1992, 1994a). This radio continuum source is associated with the near-infrared object CB54YC1 (Yun & Clemens 1994b, 1995), a possible protobinary system. This object has been classified by Yun & Clemens (1995) as a class I YSOs.

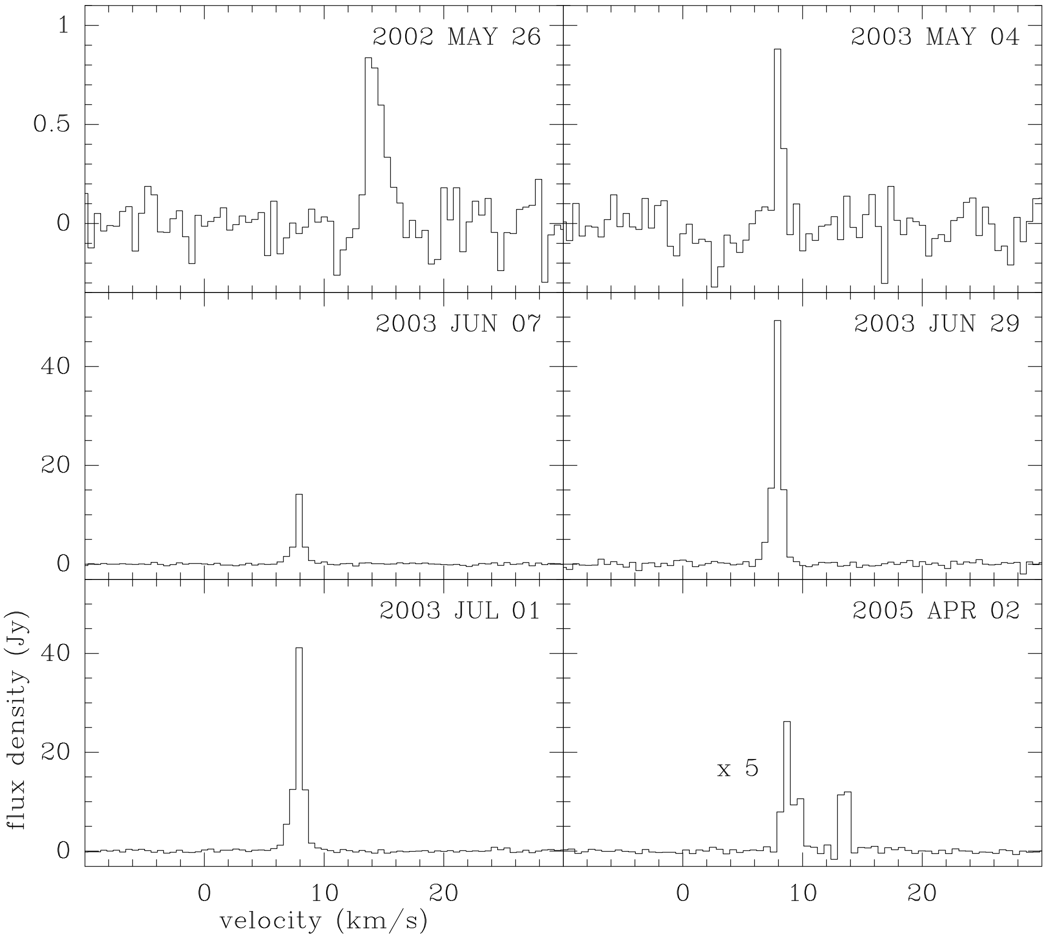

Figure 3.3: Water maser spectra towards [YMT96] CB 54 2 detected with the Robledo-70m antenna. Note that the scale of the top panels is different from the rest. The spectrum taken on 2005 April 02 (bottom right) has been multiplied by a factor of 5 to show it more clearly

The maser emission is highly variable. On 2002 May and 2003 May, the flux density was below 1 Jy. However, a component at $\simeq 7.9$ km s^{-1}, undetected on 2002 May, suffered an outburst in 2003 June-July, reaching a flux density of $\simeq 50$ Jy. This component was again undetected (or very weak and blended with a component at 8.7 km s) on 2005 April. Such high variability in a water maser is typical of a low-mass YSO (Haschick et al. 1983; Wilking et al. 1994a; Claussen et al. 1996; Furuya et al. 2003). The velocity of the maser emission is within 15 km s^{-1} from the cloud velocity ($V_{\rm LSR} \simeq 19.5$ km s^{-1}, CB).

3.4.2.4 CB 65 (IRAS 16277-2332)

CB 65 (LDN 1704) is at a distance of ~ 160 pc (Visser et al. 2002), which makes it the nearest cloud among our detections. We detected maser emission towards IRAS 16277-2332. There is no other source complying our selection criteria within the Robledo beam around this IRAS source. Moreover, there is not much known about IRAS 16277-2332, apart from its non-detection in the submillimeter (Visser et al. 2002), and that Parker (1988) does not include it as associated with CB 65. Therefore, we cannot say much about the nature of this source.

The maser was detected in 2002 June, with a velocity ($V_{\rm LSR} \simeq 1.2$ km s^{-1}, Table 3.2), close to the velocity of the cloud ($V_{\rm LSR} \simeq 2.3$ km s^{-1}, CB), which would be very unlikely if the object is completely unrelated to the globule. The maser was not visible in later in observations with the Robledo radio telescope (Table 3.2).

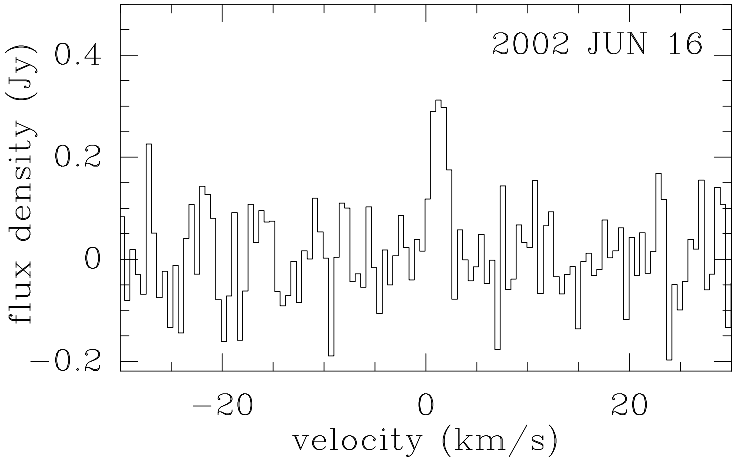

Figure 3.4: Water maser spectrum towards IRAS 16277-2332, in CB 65, detected with the Robledo-70m antenna.

3.4.2.5 CB 101 (IRAS 17503-0833)

CB 101 (LDN 392) is a globule located at 200 pc (Lee & Myers 1999). Lee & Myers (1999) and Lee et al. (1999) cataloged it as a starless core.

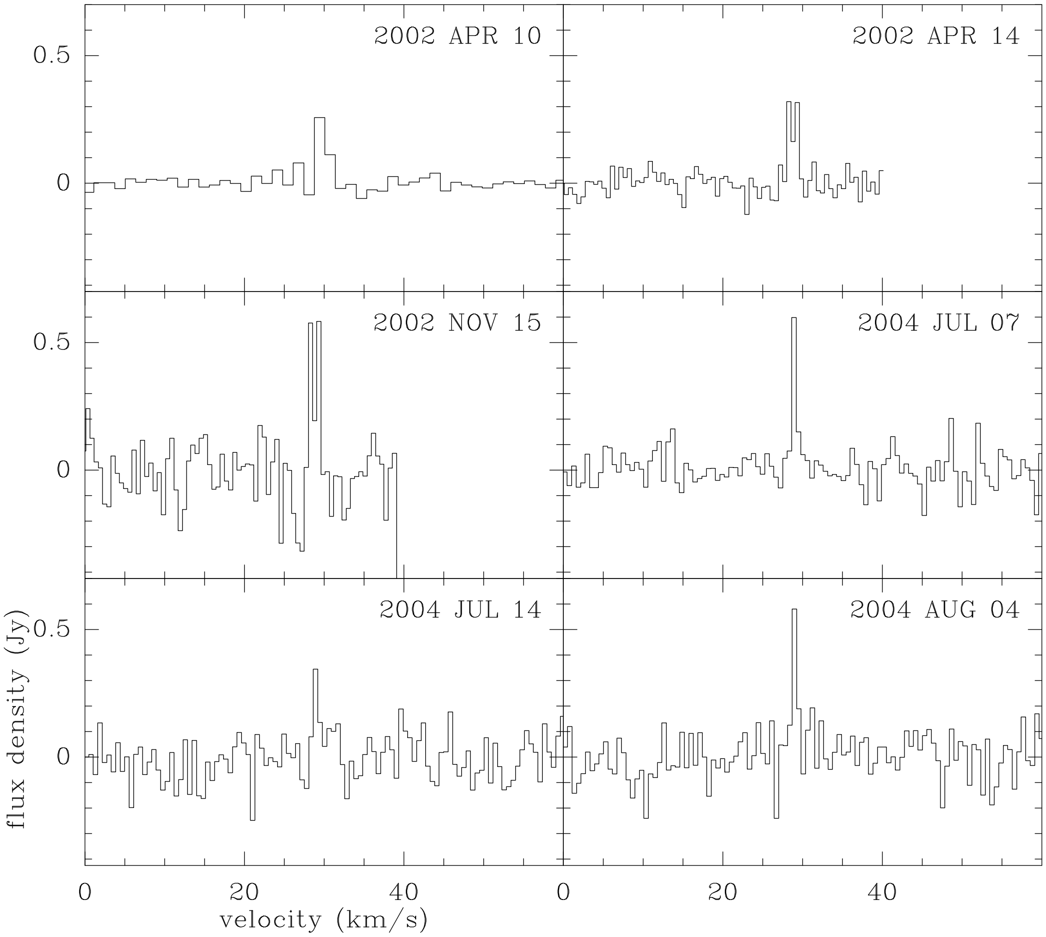

Figure 3.5: Water maser spectra towards IRAS 17503-0833, in CB 101, detected with the Robledo-70m antenna

We detected maser emission towards IRAS 17503-0833. No other source with our selection criteria is found around this IRAS source. The maser does not show strong variations in flux density, although it showed a double-peaked profile in 2002, of which only one component was visible in 2004. The maser emission, at $V_{\rm LSR} \simeq 29$ km s^{-1} (Table 3.2), is $\gtrsim 20$ km s^{-1} away from the cloud velocity ($\simeq 6.7$ km s^{-1}, CB). We note that the centroid velocities of water maser emission from YSOs, specially for low-mass sources, is usually found within $\simeq 15$ km s^{-1} from the cloud velocity (Wilking et al 1994; Anglada et al. 1996a; Brand et al. 2003). The high relative velocity of the masers in this source suggests that IRAS 17503-0833 may not be related to the CB 101 globule. By inspecting the optical images of the Digital Sky Survey, we noted that IRAS 17503-0833 is out of the optical limit of CB 101, and it should probably not have been included in the list of IRAS sources of CB.

3.4.2.6 CB 199 ([ARC2001] HH 119 VLA 3)

CB 199 (B335), located at 250 pc (Tomita et al. 1979) is an extensively studied site of recent star formation, which has also be the subject of spectral line studies of protostellar collapse (Zhou et al. 1993; Choi et al. 1995).

There is a bipolar molecular outflow in the region (Frerking & Langer 1982; Goldsmith et al. 1984), as well as the jet-like structure of Herbig-Haro objects HH 199A, B, and C (Vrba et al. 1986; Reipurth et al. 1992). Both the molecular outflow and the optical jet are thought to be powered by a far-infrared and submillimeter source (Keene et al. 1983; Chandler et al. 1990), which is probably the same object as IRAS 19345+0727. A total of 13 centimeter sources were detected around this IRAS source (Anglada et al. 1992, 1998; Avila et al. 2001) of which at least 4 are probably background objects due to their non-thermal, negative spectral index at radio wavelengths (Anglada et al. 1998).

We detected maser emission towards [ARC2001] HH 119 VLA 3, a radio continuum source of $\simeq 0.55$ mJy detected by Avila et al. (2001), but undetected in the previous observations by Anglada et al. (1992) and Anglada et al. (1998) (upper limit of ~ 0.15 mJy), which suggested source variability. No other source with our selection criteria was known within the beam of Robledo from this source. The other radio continuum sources in the region are more than $2'$ away from this one. The radio continuum source [ARC92] Barn 335 4 (Anglada et al. 1992), associated with IRAS 19345+0727, the powering source of the outflow, lies $\simeq 3\farcm5$ from [ARC2001] HH 119 VLA 3. Therefore, the water maser seems not to be related to either this outflow or the HH 199 jet. The lack of infrared counterpart for [ARC2001] HH 119 VLA 3 in the IRAS point source and 2MASS catalogs would suggest that this object is deeply embedded, and thus, very young.

Only one maser component at $\simeq 37.9$ km s^{-1} is clearly visible in our spectra. This is ~ 30 km s^{-1} from the cloud velocity (8.4 km s^{-1}), i.e., a shift for the centroid velocity much larger than expected for masers in YSOs (Wilking et al 1994; Anglada et al. 1996a; Brand et al. 2003). Although they are rare, there are some known cases of sources with large velocity shifts (up to $\simeq 80$ km s^{-1}) between water masers and cloud, specially around HH and GGD objects Rodríguez et al. (1978, 1980b), but they are generally associated with high-mass YSOs. Large velocity shifts are even rarer in low-mass objects. If the maser is associated to a YSOs in the globule CB 199, this would be one of the cases with the largest velocity offset between maser emission and cloud velocity know to date for a low-mass star-forming region. A similar, unusual shift of $\simeq 30$ km s^{-1} is also found in the low-mass YSOs SVS13 (Claussen et al. 1996), while values $\simeq 45$ km s^{-1} have been seen

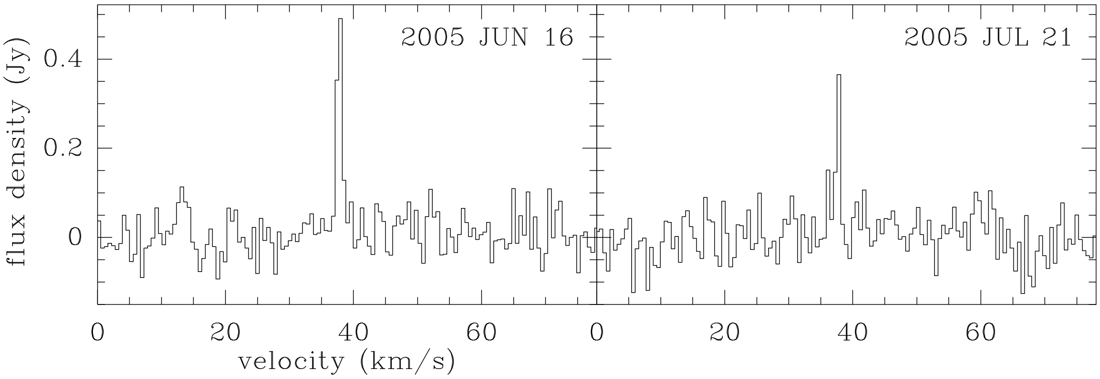

Figure 3.6: Water maser spectra towards [ARC2001] HH 119 VLA 3, in CB 199, detected with the Robledo-70m antenna.

in Cep E-mm (Furuya et al. 2003), although the latter is probably an intermediate-mass YSOs ($\sim$ 3 $M_{\odot}$; Moro-Martín et al 2001; Froebrich et al. 2003). Both SVS13 and Cep E-mm seem to be close binaries, with separations of $\simeq$ 65 AU (Eislöffel et al 1996; Anglada et al. 2000). In the case SVS13, Rodríguez et al. (2002) showed that the high-velocity masers seem to be associated with one of the components, although the maser velocities do not seem to mark the orbital motions in the binary, given the low-mass of the system. On the other hand, it has been proposed that gravitational interactions within binaries or multiple systems give rise to mass-loss outbursts that show up as Herbig Haro jets or FU Ori phenomena (Reipurth 2000; Reipurt & Aspin 2004), and we could speculate that these outbursts could also show up as high-velocity masers. However, it is not possible at this point to determine whether high-velocity masers are favored in low-mass binary systems, given the scarce number of objects we are dealing with. Obviously, it would be interesting to determine whether the source [ARC2001] HH 119 VLA 3 is indeed a binary.

An alternative possibility to explain this high-velocity feature is that [ARC2001] HH 119 VLA 3 is associated to an evolved star. If this is true, and the source [ARC2001] HH 119 VLA 3 is the one pumping the maser, the presence of radio continuum emission would indicate that it is a protoplanetary or a young planetary nebula, located behind the CB 199 globule. It is not likely that it is an evolved object in the foreground (i.e., closer than 250 pc), given the lack of an infrared counterpart.

Given the proximity of CB 199, and the abnormal velocity pattern of its maser emission, such interferometric observations would be useful to confirm its association with the radio continuum source and the spatio-kinematical distribution of the maser emission.

3.4.2.7 CB 232 (IRAS 21352+4307)

CB 232 is a globule located at 600 pc (Launhardt & Henning 1997). We detected a maser towards IRAS 21352+4307. From the nominal position of this source, within the beam of Robledo fall two submm sources ([HSW99] CB 232 SMM 1 and SMM 2, Huard et al. 1999), the peak of a CS map (Launhardt et al. 1998), and the center of a molecular outflow (Yun & Clemens 1992, 1994a).

The maser emission shows a varying velocity pattern. The maximum emission was at $\simeq 12.1$ km s^{-1} in 2003 May, although a weaker component at $\simeq 10$ km s^{-1} was also present. This weaker component was the dominant one in later spectra, while the one at 12.1 km s^{-1} was absent. The detected maser components are close to the cloud velocity ($\simeq 12.6$ km s^{-1}, CB).

The variation of the maser spectrum and the presence of other signs of star formation indicates that the maser emission is pumped by a low-mass YSOs.

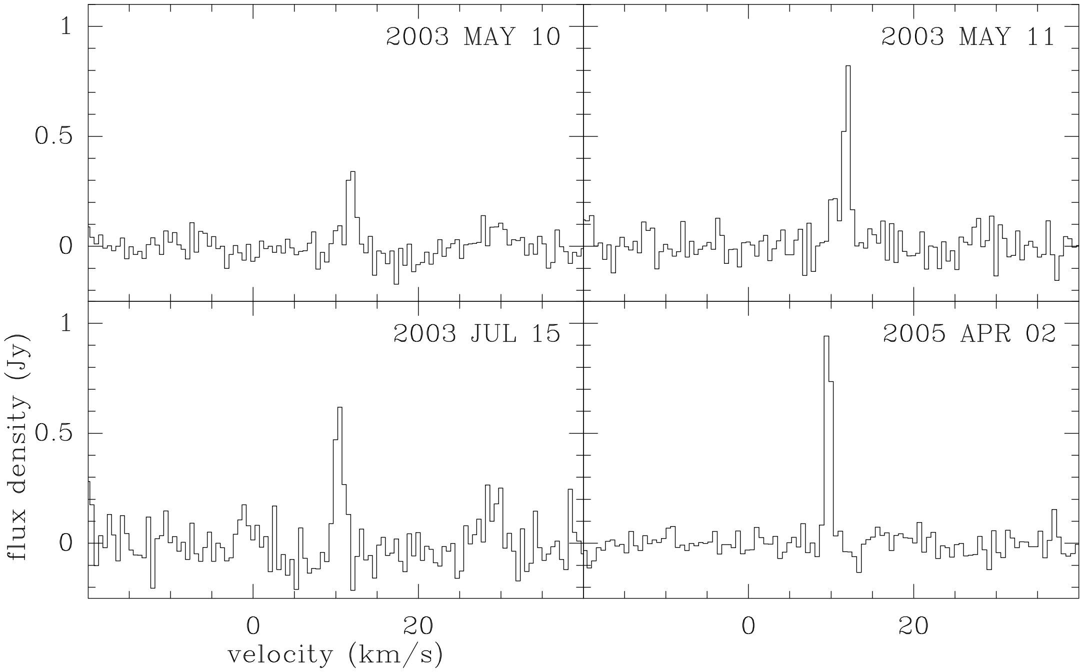

Figure 3.7: Water maser spectra towards IRAS 21352+4307, in CB 232, detected with the Robledo-70m antenna.

3.5 Discussion

Of the selection criteria used to select our target sources, the highest detection rates of masers are those related to the presence of molecular outflows or the peak in maps of the high-density tracer CS. We performed a statistical study to try to determine whether any of the selection criteria is a better predictor for the presence of water maser emission. For this, we used a Fisher's Exact test and a confidence level of 95%[1]. This test indicates that the presence of a submillimeter source, of a peak of CS, or of a molecular outflow are all a better predictor of the existence of water maser emission than the presence of an IRAS source, which is reasonable, since the latter was the less restrictive of all our criteria in the identification of YSOs candidates. Apart from IRAS sources, the detection rates for all other selection criteria (even the 0% rate for peaks of NH_3 maps) are all statistically compatible.

Another relevant fact is that most of the globules in the CB catalog which are known to be associated with water masers (CB 3, CB 34, CB 39, CB 54, CB 205) are located at distances ≥ 1 kpc. Therefore, they tend to be larger than probably intended by CB in their catalog, which tried to select "small" (size ≤ 1.5 pc) globules, using a criterion of $< 10'$ assuming distances ≤ 500 pc. So the globules mentioned above belong to a class of "large" Bok globules. Large, massive globules are obviously more likely to be sites of (multiple) star formation. In our survey we have identified the smallest Bok globules known to harbor water maser emission. In particular, CB 232, whose maser is most likely associated with a YSO, has a size of $\simeq 0.6$ pc ($5\rlap{.}'6 \times 2\rlap{.}'2$ at 600 pc; CB; Launhardt & Henning 1997). The cases of CB 65 ($\simeq 0.3$ pc size) and CB 199 ($\simeq 0.5$ pc size) need further investigation to determine the nature of their pumping sources, but these three sources seem to be the best candidates for further use of water masers as a tool to study star formation in small Bok globules.

---

[1] We have used this confidence level for all the statistical tests in this thesis

3.6 Conclusions

In this chapter, we present the most sensitive survey for water maser emission towards Bok globules to date, using NASA's 70 m antenna in Robledo de Chavela (Spain). A total of 207 target positions within the clouds of the Clemens & Barvainis (1988) catalog were observed. Our main results are as follow:

- We have obtained seven maser detections, six of which (in CB 34, CB 54, CB 65, CB 101, CB 199, and CB 232) are new. Of the previously known masers in the CB catalog, only the one in CB 3 was detected by us. No emission was seen towards the previously reported masers in either CB 39 or CB 205.

- Of our detections, the ones in CB 3, CB 34, CB 54, and CB 232 are most likely associated with YSOs. The nature of CB 65 and CB 101 is uncertain.

- In the case of CB 199, the relatively large shift ($\simeq 30$ km s^{-1}) of the centroid velocity of the maser emission with respect to the cloud velocity is unusual for YSOs, specially for low-mass ones. We speculate that the presence of high-velocity masers in low-mass YSOs might be related to episodes of energetic mass loss in close binaries. Alternatively, the maser in CB 199 could be related to a protoplanetary or a young planetary nebula.

- CB 232 is the smallest Bok globule (size $\simeq 0.6$ pc) known to be associated with water maser emission. However, if their association with YSOs is confirmed, CB 65 (size $\simeq 0.3$ pc) and CB 199 ($\simeq 0.5$ pc) are even smaller globules. These objects are good candidates for the study of relatively isolated star formation with high spacial resolution.

- Of our selection criteria, the more restrictive ones for the identification of YSOs (radio continuum emission, peak of a high-density tracer, and geometrical center of a molecular outflow) show statistically compatible rates of water maser detection. Only the presence of IRAS sources tends to be a somewhat worse predictor for the presence of masers.

3.6.1 Conclusiones

En este capítulo, presentamos la búsqueda de máseres de agua de mayor sensibilidad realizada hasta ahora en glóbulos de Bok, utilizando la antena de 70 metros de NASA situada en Robledo de Chavela (España). Se ha observado un total de 207 posiciones dentro de las nubes del catálogo de Clemens & Barvainis (1988). Nuestros principales resultados son los siguientes:

- Hemos obtenido detecciones de siete máseres, seis de las cuales (en CB 34, CB 54, CB 65, CB 101, CB 199 y CB 232) son nuevas. De los máseres conocidos en el catálogo de CB, sólo detectamos el de CB 3. No se observó la emisión de los máseres previamente publicados ni en CB 39 ni en CB 205.
- De nuestras detecciones, las correspondientes a CB 3, CB 34, CB 54 y CB 232 son las que con mayor probabilidad están asociadas a un objeto estelar joven. La naturaleza de CB 65 y de CB 101 es desconocida.
- En el caso de CB 199, el desplazamiento relativamente grande ($\simeq 30$ km s $^{-1}$) del centroide de velocidad de la emisión máser con respecto a la velocidad de la nube es inusual en objetos estelares jóvenes, especialmente en los de baja masa. Especulamos con la posibilidad de que la presencia de máseres a alta velocidad en objetos estelares jóvenes de baja masa podría estar relacionada con episodios energéticos de pérdida de masa en binarias cercanas. Alternativamente, el máser en CB 199 podría estar asociado a una nebulosa protoplanetaria o planetaria joven.
- CB 232 es el glóbulo de Bok más pequeño (tamaño $\simeq 0.6$ pc) que se conoce como asociado a emisión de máser de agua. Sin embargo, si se confirmara la asociación de CB 65 (tamaño $\simeq 0.3$ pc) y CB 199 ($\simeq 0.5$ pc) con objetos estelares jóvenes, estos glóbulos serían los más pequeños. Estos objetos son buenos candidatos para el estudio a alta resolución espacial de formación estelar relativamente aislada.
- De nuestros criterios de selección, los más restrictivos en la identificación de objetos estelares jóvenes (emisión en radio continuo, picos de trazadores de alta densidad y centros geométricos de flujos moleculares) muestran unas tasas de detección de máser de agua estadísticamente compatibles. La mera presencia de fuentes IRAS tiende a predecir peor la presencia de estos máseres.

Table 3.1: Sources searched for water maser emission

Globule	Source[1]	Right Ascension[2] (J2000)	Declination[2] (J2000)	Included Sources[3]	References[4]
CB 3	[YMT96] CB 3 1	00 28 22.0	+56 41 39		6
	CB3-mm[5]	00 28 42.7	+56 42 06	smm ([HSW99] CB 3 SMM 1), IRAS 00259+5625, outf, cs	1, 2, 3, 4, 5
CB 4	IRAS 00362+5234	00 39 03.5	+52 50 57		
CB 6	IRAS 00465+6028	00 49 25.0	+50 44 45	mm, smm	1, 2
CB 7	IRAS 01078+6409	01 11 03.4	+64 25 24		
	IRAS 01087+6404	01 11 58.0	+64 20 07		
CB 8	IRAS 01202+7406	01 24 12.4	+74 22 03		
CB 11	IRAS 01333+6448	01 36 51.5	+65 03 55		
	IRAS 01334+6442	01 36 59.4	+64 57 39		
	IRAS 01341+6447	01 37 41.3	+65 03 08		
CB 12	CS peak	01 38 32.7	+65 06 02		5
	IRAS 01354+6447	01 38 56.8	+65 03 12		
CB 15	IRAS 03521+5555	03 56 07.9	+56 04 30		
	IRAS 03523+5608	03 56 21.7	+56 17 01		
	IRAS 03535+5555	03 57 30.4	+56 04 15		
CB 16	IRAS 03592-5642	04 03 15.6	+56 50 27		
CB 17	IRAS 04005+5647	04 04 33.7	+56 56 10	mm, smm	1, 2
	NH_3 peak	04 04 38.0	+56 56 11		7
CB 19	IRAS 04233+2529	04 26 21.3	+25 36 22		
	IRAS 04240+2535	04 27 02.7	+25 42 24		
CB 22	NH_3 peak	04 40 33.2	+29 55 04		7
CB 23	NH_3 peak	04 43 30.0	+29 39 01		7
	CB23-cm1	04 43 34.9	+29 38 05		8
	CB23-cm2	04 43 35.0	+29 37 13		8
CB 26	IRAS 04559+5200	04 59 52.4	+52 04 45	mm	1
CB 27	IRAS 05013+3234	05 04 37.2	+32 38 15		
CB 28	IRAS 05036-0359	05 06 08.9	−03 55 16		
	IRAS 05037-0402	05 06 13.7	−03 58 60		
	CS peak	05 06 19.4	−03 56 24	IRAS 05038-0400	
	IRAS 05038-0400	05 06 19.9	−03 56 33	cs	5
	NH_3 peak	05 06 20.2	−03 56 02		7

Table 3.1: (continued).

Globule	Source[1]	Right Ascension[2] (J2000)	Declination[2] (J2000)	Included Sources[3]	References[4]
CB 29	IRAS 05190-0348	05 21 31.5	−03 45 08		
	IRAS 05194-0346	05 21 56.2	−03 44 08		5
	IRAS 05194-0343	05 21 57.5	−03 40 35		
	CS peak	05 22 10.3	−03 41 06		5
	IRAS 05201-0341	05 22 38.5	−03 38 53		
CB 30	[MYT99] CB 30 3	05 29 30.5	+05 43 22		9
	IRAS 05268+0550	05 29 31.7	+05 52 55		
	IRAS 05268+0538	05 29 32.2	+05 40 34	cm ([MYT99] CB30 4), cs	9, 5
	IRAS 05274+0542	05 30 06.7	+05 44 23		
CB 31	[YMT96] CB 31 1	05 33 14.5	−00 35 34		6
	[YMT96] CB 31 2	05 33 15.8	−00 35 20		6
	IRAS 05307-0038	05 33 18.2	−00 36 13		
CB 32	IRAS 05344-0016	05 36 59.7	−00 14 21		
	CS peak	05 38 28.2	−00 17 25		5
CB 33	IRAS 05433+2040	05 46 17.7	+20 41 39		
	IRAS 05437+2045	05 46 41.1	+20 46 10		
CB 34	[HSW99] CB 34 SMM 2	05 47 00.0	+21 00 30		3
	[YMT96] CB 34 3	05 47 01.7	+21 00 25	mm, smm ([HSW99] CB 34 SMM 1), IRAS 05440+2059, outf, cs, nh3	6, 1, 2, 3, 4, 5, 10
	[HSW99] CB 34 SMM 1	05 47 01.9	+21 00 06	cm ([YMT96] CB 34 3), IRAS 05440+2059	3, 6
	[HSW99] CB 34 SMM 3	05 47 05.3	+21 00 42	smm ([HSW99] CB 34 SMM 4)	3
	[HSW99] CB 34 SMM 5	05 47 07.8	+21 00 04		3
CB 37	[MYT99] CB 37 1	06 00 35.6	+31 37 37		11
	NH_3 peak	06 00 37.3	+31 38 50		7
	[MYT99] CB 37 2	06 00 47.6	+31 40 48		11
CB 39	IRAS 05591-1630[6]	06 01 59.5	+16 30 56	outf	
	CS peak	06 01 59.6	+16 31 44		5
	[YMT96] CB 39 2	06 02 04.6	+16 30 06		6
CB 40	IRAS 05589+1638	06 01 53.1	+16 38 35		
	IRAS 05592+1640	06 02 07.2	+16 40 11		
CB 42	IRAS 06000+1644	06 02 55.7	+16 44 36		
CB 43	[MYT99] CB 43 1	06 03 10.6	+16 36 07		11

Table 3.1: (continued).

Globule	Source[1]	Right Ascension[2] (J2000)	Declination[2] (J2000)	Included Sources[3]	References[4]
CB 44	CS peak	06 07 29.3	+19 27 53		5
	[MYT99] CB 44 2	06 07 37.2	+19 25 12		11
	[MYT99] CB 44 3	06 07 37.6	+19 28 35		11
	IRAS 06047+1923	06 07 39.2	+19 22 43		
	IRAS 06048+1934	06 07 47.4	+19 34 18		
CB 45	IRAS 06055+1800	06 08 27.1	+17 59 59		
	NH_3 peak	06 08 56.6	+17 50 19		7
CB 48	IRAS 06175+0711	06 20 15.6	+07 10 14		
CB 50	IRAS 06316+0748	06 34 19.1	+07 45 46		
CB 51	IRAS 06355+0134	06 38 07.3	+01 31 56		
CB 52	[YMT96] CB 52 1	06 48 33.5	−16 50 31		6
	IRAS 06464-1650	06 48 39.2	−16 54 04	mm, smm	1, 2
	IRAS 06464-1644	06 48 41.8	−16 48 06		
	IRAS 06471-1651	06 49 22.2	−16 55 01		
CB 54	[YMT96] CB 54 2	07 04 21.2	−16 23 15	mm, smm, IRAS 07020-1618, outf, cs	6, 1, 2, 4, 5
CB 55	IRAS 07019-1631	07 04 12.6	−16 35 34		
CB 56	IRAS 07125-2507	07 14 36.5	−25 12 57		
	IRAS 07125-2503	07 14 38.9	−25 08 54		
CB 57	IRAS 07154-2304	07 17 32.2	−23 09 42		
	IRAS 07156-2248	07 17 45.5	−22 54 14		
	IRAS 07156-2301	07 17 47.8	−23 07 01		
CB 58	IRAS 07159-2329	07 18 02.5	−23 35 06		
	[YMT96] CB 58 1	07 18 07.6	−23 41 07		6
	IRAS 07161-2336	07 18 15.2	−23 41 42	mm, smm	1, 2
CB 59	IRAS 07171+0359	07 19 44.6	+03 53 48		
CB 60	IRAS 08022-3115	08 04 11.9	−31 24 00		
	IRAS 08026-3122	08 04 36.9	−31 30 44		
	IRAS 08029-3118	08 04 56.4	−31 27 23		
CB 63	IRAS 15486-0350	15 51 16.7	−03 59 41		
CB 65	IRAS 16277-2332	16 30 43.7	−23 39 08		
	[VRC2001] L1704 SMM 1	16 30 50.6	−23 42 08		12
	IRAS 16287-2337	16 31 44.6	−23 43 55		

Table 3.1: (continued).

Globule	Source[1]	Right Ascension[2] (J2000)	Declination[2] (J2000)	Included Sources[3]	References[4]
CB 67	IRAS 16485-1906	16 51 10.3	−19 11 12		
CB 68	CS peak	16 57 16.3	−16 07 40		5
	IRAS 16544-1604[7]	16 57 19.5	−16 09 25	mm, smm ([HSW99] CB 68 SMM 1), outf	1, 3, 13
	NH_3 peak	16 57 20.5	−16 09 02		7
CB 78	IRAS 17147-1821	17 17 38.5	−18 24 14		
CB 81	outflow	17 22 26.5	−27 08 10		4
CB 82	[VRC2001] L57 SMM 1	17 22 38.5	−23 49 57		12
	NH_3 peak	17 22 39.3	−23 49 46		14
	CS peak	17 22 40.7	−23 48 46		5
CB 98	CB98-mm	17 47 00.7	−20 30 29		1
CB 100	IRAS 17490-0258	17 51 38.1	−02 59 07		
	IRAS 17493-0258	17 52 00.4	−02 58 59		
CB 101	IRAS 17503-0833	17 53 05.2	−08 33 41		
	IRAS 17505-0828	17 53 14.1	−08 28 42		
CB 104	IRAS 17526-0815	17 55 21.1	−08 15 38		
	IRAS 17533-0808	17 56 03.7	−08 09 16		
CB 105	IRAS 17561-0349	17 58 44.5	−03 49 52		
CB 106	IRAS 17577-0329	18 00 25.8	−03 29 35		
	IRAS 17580-0330	18 00 41.4	−03 30 30		
	IRAS 17586-0330	18 01 18.3	−03 30 01		
CB 108	[YMT96] CB 108 1	18 03 01.9	−20 49 37		6
CB 118	IRAS 18094-1550	18 12 22.1	−15 49 13		
CB 121	IRAS 18115-0701	18 14 17.6	−07 00 51		
	IRAS 18116-0657	18 14 18.9	−06 56 44		
CB 124	IRAS 18120+0704	18 14 31.4	+07 05 13		
	IRAS 18122+0703	18 14 42.7	+07 04 44		
CB 125	NH_3 peak	18 15 34.7	−18 11 12		7
CB 128	IRAS 18132-0350	18 15 52.5	−03 49 40		
CB 130	CB130-mm	18 16 14.8	−02 32 47	nh3	1, 7
CB 131	CB131-smm	18 17 00.5	−18 02 04		2
CB 137	IRAS 18219-0100	18 24 30.3	−00 58 22		
CB 142	IRAS 18272-1343	18 30 02.0	−13 41 07		

Table 3.1: (continued).

Globule	Source[1]	Right Ascension[2] (J2000)	Declination[2] (J2000)	Included Sources[3]	References[4]
CB 145	IRAS 18296-0911	18 32 21.7	−09 09 25	mm	1
CB 146	IRAS 18293-0906	18 32 08.2	−09 03 57		
	IRAS 18294-0901	18 32 11.1	−08 59 05		
	[HSW99] CB 146 SMM 2	18 32 19.4	−08 53 00		15
	[HSW99] CB 146 SMM 1	18 32 21.3	−08 51 56		15
CB 171	[YMT96] CB 171 2	19 01 33.6	−04 31 48		6
	[YMT96] CB 171 3	19 01 55.8	−04 31 11		6
CB 177	IRAS 18599+1739	19 02 07.7	+17 43 58		
CB 178	IRAS 18595+1812	19 01 44.0	+18 16 29		
	IRAS 19002+1755	19 02 28.0	+17 59 58		
CB 180	NH_3 peak	19 06 08.6	−06 52 47		7
CB 184	IRAS 19116+1623	19 13 56.4	+16 28 27		
CB 187	IRAS 19162-0135	19 18 48.7	−01 29 39		
CB 188	IRAS 19179+1129	19 20 14.9	+11 35 35	mm	1
	Outflow	19 20 16.3	+11 35 57		4
	CS peak	19 20 19.9	+11 35 57		5
	IRAS 19180+1127	19 20 21.0	+11 32 54		
CB 189	IRAS 19180+1116	19 20 22.5	+11 22 07		
	[VRC2001] L673 SMM 7	19 20 23.1	+11 22 50		12
	[VRC2001] L673 SMM 1	19 20 25.2	+11 22 17		12
	IRAS 19180+1114	19 20 25.8	+11 19 52	smm ([VRC2001] L673 SMM 2), outf	12, 15
	IRAS 19183+1123	19 20 44.0	+11 28 55		
	IRAS 19184+1118	19 20 45.6	+11 23 50		
CB 190	IRAS 19186+2325	19 20 46.3	+23 31 31		
CB 194	IRAS 19273+1433	19 29 35.7	+14 39 23		
CB 196	IRAS 19329+1213	19 35 18.0	+12 20 36		
CB 198	IRAS 19342+1213	19 36 37.8	+12 19 59		

Table 3.1: (continued).

Globule	Source[1]	Right Ascension[2] (J2000)	Declination[2] (J2000)	Included Sources[3]	References[4]
CB 199	[ARC92] Barn 335 9	19 36 44.4	+07 36 43		17
	[ARC92] Barn 335 1	19 36 47.6	+07 32 58		17
	IRAS 19343+0727	19 36 48.8	+07 34 29		
	[ARC92] Barn 335 2	19 36 49.5	+07 35 04		17
	NH_3 peak	19 36 59.0	+07 34 17		19
	IRAS 19345+0727	19 37 01.0	+07 34 11	cm ([ARC92] Barn 335 4), smm ([HSW99] B 335 SMM 1), outf	17, 2, 18
	[ARC92] Barn 335 11	19 37 08.8	+07 31 41		17
	[ARC2001] HH 119 VLA 3	19 37 10.2	+07 36 50		20
	IRAS 19347+0729	19 37 10.5	+07 36 26		
	IRAS 19348+0724	19 37 17.0	+07 31 57		
CB 203	IRAS 19413+1902	19 43 33.5	+19 09 52		
CB 205	IRAS 19427+2741	19 44 45.5	+27 48 37		
	[YMT96] CB 205 1	19 45 09.5	+27 51 06		6
	[HSW99] L 810 SMM 2	19 45 21.3	+27 50 40		2
	[YMT96] CB 205 2	19 45 21.9	+27 53 40		6
	IRAS 19433+2743[8]	19 45 23.9	+27 50 58	mm, smm ([HSW99] L 810 SMM 1), outf, nh3	1, 2, 21, 22
	IRAS 19433+2751	19 45 25.2	+27 58 54		
	[YMT96] CB 205 3	19 45 35.1	+27 54 11		6
	IRAS 19438+2757	19 45 51.2	+28 04 23		
	IRAS 19438+2737	19 45 55.5	+27 44 58		
	IRAS 19439+2748	19 45 57.8	+27 56 06		
CB 206	[YMT96] CB 206 2	19 46 30.4	+19 06 06		6
CB 207	IRAS 19437+2108	19 45 53.0	+21 16 15		
CB 208	IRAS 19450+1847	19 47 14.7	+18 55 10		
CB 210	IRAS 19529+3341	19 54 49.1	+33 49 15		
CB 211	IRAS 19576+2447	19 59 46.5	+24 55 35		
CB 214	IRAS 20018+2629	20 03 57.9	+26 38 20	outf	4, 21
CB 216	Outflow	20 05 49.7	+23 27 04		4
	IRAS 20037+2317	20 05 53.6	+23 26 34	cs	5
	CS peak	20 05 54.1	+23 26 16	IRAS 20037+2317	5
CB 217	Outflow	20 07 45.9	+37 07 01		21
	[YMT96] CB 217 4	20 07 51.5	+37 06 55		6

Table 3.1: (continued).

Globule	Source[1]	Right Ascension[2] (J2000)	Declination[2] (J2000)	Included Sources[3]	References[4]
CB 219	IRAS 20176+6343	20 18 23.7	+63 52 30		
CB 222	IRAS 20328+6351	20 33 36.4	+64 02 21		
CB 224	NH_3 peak	20 36 20.3	+63 52 55		7
	IRAS 20355+6343	20 36 22.1	+63 53 39	mm	1
CB 225	IRAS 20365+5607	20 37 48.0	+56 17 56		
CB 230	[YMT96] CB 230 1	21 17 30.9	+68 18 10		
	[YMT96] CB 230 2	21 17 38.5	+68 17 32	mm, smm([HSW99] CB 230 SMM 1), IRAS 21169+6804, outf, cs	6, 1, 2, 15, 4, 21, 5
CB 232	IRAS 21352+4307	21 37 11.3	+43 20 36	smm ([HSW99] CB 232 SMM 1, [HSW99] CB 232 SMM 2), outf, cs	15, 4, 5
CB 233	CS peak	21 40 26.4	+57 48 06		5
CB 235	IRAS 21548+5843	21 56 25.7	+58 57 54		
CB 238	NH_3 peak	22 13 22.6	+41 02 51		7
CB 240	IRAS 22317+5816	22 33 39.3	+58 31 56	mm	1
CB 241	IRAS 23095+6547	23 11 37.0	+66 04 07		
CB 243	IRAS 23228+6320	23 25 05.7	+63 36 34	mm, smm ([VRC2001] L1246 SMM 1), nh3	1, 23, 12, 7
	NH_3 peak	23 25 06.9	+63 36 50	smm ([VRC2001] L1246 SMM 1), IRAS 23228+6320	7, 23, 12
	[VRC2001] L1246 SMM 2	23 25 16.4	+63 36 46		23, 12
	CS peak	23 25 27.0	+63 35 46		5
CB 244	[VRC2001] L1262 SMM 2	23 25 26.0	+74 18 28	nh3	12, 23, 24
	[YMT96] CB 244 1	23 25 46.6	+74 17 40	mm, smm ([VRC2002] L1262 SMM 1), IRAS 23238+7401, outf	6, 1, 2, 12, 4
	IRAS 23249+7406	23 26 53.2	+74 22 34		
CB 246	CB246-mm	23 56 43.6	+58 34 29		1
CB 247	IRAS 23550+6430	23 57 36.4	+64 46 48		

Table 3.1: (continued).

Notes to Table 3.1

[1] Target sources. SIMBAD names were used, where available. Labels [YMT96], [MYT99], [ARC92], and [ARC2001] indicate cm sources

[2] Coordinates of pointing position. Units of right ascension are hours, minutes, and seconds. Units of declination are degrees, arcminutes, and arcseconds

[3] Other sources included within the telescope beam, complying any of the selection criteria mentioned in sec. 3.3. Cm: centimeter source; mm: millimeter source; smm: submillimeter source; outf: center of molecular outflow; nh3: peak of NH_3 map; cs: peak of CS map. Where available, SIMBAD names are given between parentheses

[4] References for the sources complying the selection criteria (except for IRAS sources)

[5] Maser detected by Scappini et al. (1991)

[6] Maser detected by Schwartz & Buhl (1975)

[7] Coordinates used for IRAS 16544-1604 are those in the IRAS Point Source Catalog. SIMBAD reports for this source the coordinates of F16544-1604 in the IRAS Faint Source Catalog, which is also within the Robledo beam from our pointing position

[8] Maser detected by Neckel et al. (1985)

References (1) Launhardt & Henning (1997); (2) Launhardt et al. (1997); (3) Huard et al. (2000); (4) Yun & Clemens (1992); (5) Launhardt et al. (1998); (6) Yun et al. (1996); (7) Lemme et al. (1996); (8) Harvey et al. (2002); (9) Moreira et al. (1999); (10) Codella & Scappini (1998); (11) Moreira et al. (1999); (12) Visser et al. (2002); (13) Vallée et al. (2000); (14) Bourke et al. (1995b); (15) Huard et al. (1999); (16) Armstrong & Winnewisser (1989); (17) Anglada et al. (1992); (18) Frerking & Langer (1982); (19) Benson & Myers (1989); (20) Avila et al. (2001); (21) Yun & Clemens (1994a); (22) Neckel et al. (1985); (23) Visser et al. (2001); (24) Benson et al. (1984)

Table 3.2: Water maser detections

Globule	Source	S_ν[1] (Jy)	$\int S_\nu\, dV$[2] (Jy km s^{-1})	$V_{\rm peak}$[3] (km s^{-1})	Date[4]
CB 3	CB3-mm	11.0 ± 0.4	52 ± 3	-53.4 ± 0.6	2004-JUL-24
		12.9 ± 0.4	80.2 ± 2.4	-53.5 ± 0.6	2004-AUG-19
		19.60 ± 0.22	97 ± 3	-41.1 ± 0.6	2005-JAN-03
		12.00 ± 0.13	56.0 ± 0.7	-41.8 ± 0.6	2005-JAN-31
CB 34	[HSW99] CB 34 SMM 3	0.34 ± 0.08	0.57 ± 0.23	8.1 ± 0.6	2004-AUG-20
		0.33 ± 0.07	0.57 ± 0.20	8.1 ± 0.6	2004-AUG-25
		< 0.14			2005-APR-14
		< 0.14			2005-APR-18
CB 54	[YMT96] CB 54 2	0.84 ± 0.22	1.1 ± 0.5	13.7 ± 0.5	2002-MAY-26
		0.88 ± 0.20	0.7 ± 0.3	7.9 ± 0.5	2003-MAY-04
		14.1 ± 0.4	12.6 ± 0.7	7.9 ± 0.5	2003-JUN-07
		49.3 ± 0.9	45.3 ± 1.8	7.9 ± 0.5	2003-JUN-29
		41.1 ± 0.5	39.9 ± 0.9	7.9 ± 0.5	2003-JUL-01
		5.24 ± 0.11	9.5 ± 0.4	8.7 ± 0.6	2005-APR-02
CB 65	IRAS 16277-2332	0.30 ± 0.19	0.6 ± 0.3	1.2 ± 0.5	2002-JUN-16
		< 0.25			2004-JUL-08
		< 0.18			2004-JUL-14
		< 0.22			2005-JUN-05
CB 101	IRAS 17503-0833	0.26 ± 0.05	0.41 ± 0.13	29.3 ± 1.3	2002-APR-10
		0.32 ± 0.09	0.41 ± 0.15	28.3 ± 0.5	2002-APR-14
		0.55 ± 0.19	0.63 ± 0.25	29.3 ± 0.5	2002-NOV-15
		0.60 ± 0.15	0.52 ± 0.21	28.9 ± 0.6	2004-JUL-07
		0.34 ± 0.17	0.6 ± 0.4	28.9 ± 0.6	2004-JUL-14
		0.58 ± 0.18	0.6 ± 0.3	29.0 ± 0.6	2004-AUG-04
CB 199	[ARC2001] HH 119 VLA 3	0.49 ± 0.06	0.69 ± 0.15	37.9 ± 0.6	2005-JUN-16
		0.36 ± 0.10	0.41 ± 0.18	37.8 ± 0.6	2005-JUL-21
CB 232	IRAS 21352+4307	0.34 ± 0.10	0.46 ± 0.19	12.1 ± 0.5	2003-MAY-10
		0.82 ± 0.13	1.10 ± 0.23	12.1 ± 0.5	2003-MAY-11
		0.62 ± 0.19	0.51 ± 0.24	10.5 ± 0.5	2003-JUL-15
		0.94 ± 0.12	0.95 ± 0.23	9.4 ± 0.6	2005-APR-02

Notes to Table 3.2

[1] Flux density of the strongest maser feature. Uncertainties are 2σ. Upper limits are 3σ

[2] Flux density integrated over the velocity extent of the maser emission. Uncertainties are 2σ.

[3] Velocity of the strongest feature

[4] Date of observation

Table 3.3: Non detections

Globule	Source	V_{min}[1] (km s^{-1})	V_{max}[1] (km s^{-1})	Noise[2] (Jy)	Date[3]
CB 3	[YMT96] CB 3 1	-2696	2698	0.03	2002-APR-09
		-139.4	62.8	0.14	2002-OCT-13
CB 4	IRAS 00362+5234	-112.4	89.8	0.05	2003-MAY-10
CB 6	IRAS 00465+6028	-113.6	88.6	0.06	2003-MAY-10
CB 7	IRAS 01078+6409	-107.8	107.9	0.06	2004-AUG-04
	IRAS 01087+6404	-107.8	107.9	0.08	2004-AUG-04
		-107.7	108.0	0.04	2005-APR-14
CB 8	IRAS 01202+7406	-105.7	110.0	0.05	2004-AUG-04
CB 11	IRAS 01333+6448	-109.8	105.9	0.07	2004-AUG-04
	IRAS 01334+6442	-109.8	106.0	0.05	2004-AUG-04
	IRAS 01341+6447	-109.7	106.0	0.06	2004-AUG-05
CB 12	CS peak	-112.5	89.7	0.09	2003-MAY-09
		-119.4	96.4	0.05	2004-JUL-09
	IRAS 01354+6447	-119.3	96.4	0.05	2004-AUG-20
CB 15	IRAS 03521+5555	-107.2	108.5	0.08	2004-AUG-19
	IRAS 03523+5608	-107.2	108.5	0.10	2004-AUG-19
		-107.1	108.7	0.07	2005-APR-14
	IRAS 03535+5555	-107.2	108.5	0.05	2004-AUG-20
CB 16	IRAS 03592-5642	-2716	2677	0.05	2002-APR-09
		-103.3	98.9	0.10	2002-NOV-15
CB 17	IRAS 04005+5647	-112.8	103.0	0.05	2004-JUL-27
	NH_3 peak	-105.8	96.4	0.05	2003-MAY-09
CB 19	IRAS 04233+2529	-101.5	114.2	0.04	2004-AUG-20
	IRAS 04240+2535	-101.5	114.2	0.04	2004-AUG-20
CB 22	NH_3 peak	-105.6	110.1	0.05	2004-AUG-20
CB 23	NH_3 peak	-105.8	109.9	0.05	2004-AUG-20
	CB23-cm1	-102.6	113.1	0.06	2004-JUL-15
		-102.1	113.7	0.05	2005-APR-14
	CB23-cm2	-102.5	113.2	0.05	2004-JUL-27
CB 26	IRAS 04559+5200	-2722	2671	0.07	2002-APR-09
CB 27	IRAS 05013+3234	-101.2	114.6	0.08	2004-SEP-04
CB 28	IRAS 05036-0359	-99.2	116.5	0.10	2004-SEP-08
	IRAS 05037-0402	-99.3	116.5	0.12	2004-SEP-08
	CS peak	-92.3	109.9	0.3	2002-NOV-17
		-92.3	109.9	0.07	2003-MAY-10
	IRAS 05038-0400	-99.3	116.5	0.07	2004-SEP-08
	NH_3 peak	-92.3	109.9	0.4	2002-NOV-17
		-92.3	109.9	0.11	2003-MAY-09
CB 29	IRAS 05190-0348	-96.8	119.0	0.06	2004-OCT-05
		-96.7	119.1	0.04	2004-OCT-31
	IRAS 05194-0346	-96.8	119.0	0.06	2004-SEP-08
	IRAS 05194-0343	-96.7	119.0	0.06	2004-OCT-05
		-96.7	119.0	0.05	2004-OCT-31
	CS peak	-89.9	112.3	0.4	2002-NOV-17
		-89.9	112.3	0.08	2003-MAY-10
		-96.6	119.1	0.04	2005-APR-14
	IRAS 05201-0341	-96.6	119.1	0.04	2004-OCT-31

Table 3.3: (continued).

Globule	Source	$V_{\rm min}$[1] (km s^{-1})	$V_{\rm max}$[1] (km s^{-1})	Noise[2] (Jy)	Date[3]
CB 30	[MYT99] CB 30 3	-101.2	101.0	0.08	2003-MAY-11
	IRAS 05274+0542	-108.2	107.6	0.06	2004-OCT-05
		-108.1	107.6	0.05	2004-OCT-30
	IRAS 05268+0538	-101.2	101.0	0.11	2003-MAY-08
	IRAS 05268+0550	-108.1	107.6	0.05	2004-OCT-05
		-108.1	107.6	0.05	2004-OCT-29
CB 31	[YMT96] CB 31 1	-108.3	93.9	0.10	2003-MAY-08
	[YMT96] CB 31 2	-108.3	93.9	0.08	2003-MAY-06
	IRAS 05307-0038	-115.0	100.7	0.06	2004-OCT-05
		-115.0	100.8	0.07	2004-OCT-07
		-104.2	111.5	0.04	2004-OCT-26
CB 32	IRAS 05344-0016	-112.9	102.8	0.06	2004-OCT-31
	CS peak	-106.2	96.0	0.14	2003-MAY-09
		-106.2	96.0	0.12	2003-MAY-10
CB 33	IRAS 05433+2040	-107.3	108.4	0.10	2004-SEP-04
	IRAS 05437+2045	-107.3	108.4	0.09	2004-SEP-04
CB 34	[HSW99] CB 34 SMM 2	-107.4	108.3	0.05	2004-AUG-20
	[YMT96] CB 34 3	-100.4	101.8	0.05	2003-MAY-06
	[HSW99] CB 34 SMM 1	-93.9	121.8	0.06	2004-JUL-27
	[HSW99] CB 34 SMM 5	-107.4	108.3	0.06	2005-SEP-23
CB 37	[MYT99] CB 37 1	-99.9	102.3	0.10	2003-JUL-15
		-107.0	108.7	0.07	2004-AUG-27
		-104.4	111.4	0.04	2005-APR-14
	NH_3 peak	-107.0	108.8	0.05	2004-AUG-20
	[MYT99] CB 37 2	-107.0	108.7	0.05	2004-AUG-20
CB 39	IRAS 05591-1630	-98.7	103.5	0.07	2003-MAY-10
	CS peak	-98.7	103.5	0.14	2003-MAY-08
	[YMT96] CB 39 2	-98.7	103.5	0.05	2003-MAY-06
CB 40	IRAS 05589+1638	-118.9	96.9	0.07	2004-SEP-05
	IRAS 05592+1640	-105.4	110.3	0.10	2004-SEP-05
CB 42	IRAS 06000+1644	-105.2	110.6	0.08	2004-OCT-07
		-105.1	110.7	0.06	2004-OCT-26
CB 43	[MYT99] CB 43 1	-101.6	114.2	0.04	2005-OCT-16
CB 44	CS peak	-101.6	100.6	0.06	2003-MAY-07
	[MYT99] CB 44 2	-101.6	100.6	0.06	2003-MAY-11
	[MYT99] CB 44 3	-101.6	100.6	0.07	2003-MAY-11
	IRAS 06047+1923	-108.6	107.2	0.06	2004-OCT-07
		-108.3	107.4	0.10	2004-OCT-26
	IRAS 06048+1934	-101.6	100.6	0.23	2003-MAY-08
CB 45	IRAS 06055+1800	-107.2	108.5	0.07	2004-OCT-07
		-107.2	108.5	0.05	2004-OCT-30
	NH_3 peak	-100.3	101.9	0.10	2003-MAY-07
CB 48	IRAS 06175+0711	-89.4	126.3	0.04	2004-OCT-30
CB 50	IRAS 06316+0748	-107.1	108.6	0.04	2004-OCT-30
CB 51	IRAS 06355+0134	-117.2	98.5	0.06	2004-DEC-01
CB 52	[YMT96] CB 52 1	-91.4	124.3	0.06	2004-OCT-30
	IRAS 06464-1650	-85.6	116.6	0.10	2003-MAY-07
	IRAS 06464-1644	-91.4	124.4	0.04	2005-FEB-19
	IRAS 06471-1651	-91.3	124.5	0.04	2005-FEB-19

Table 3.3: (continued).

Globule	Source	$V_{\rm min}$[1] (km s^{-1})	$V_{\rm max}$[1] (km s^{-1})	Noise[2] (Jy)	Date[3]
CB 55	IRAS 07019-1631	-87.8	127.8	0.03	2005-FEB-19
CB 56	IRAS 07125-2507	-93.3	122.4	0.04	2005-FEB-19
	IRAS 07125-2503	-93.3	122.4	0.04	2005-FEB-19
CB 57	IRAS 07154-2304	-87.6	128.1	0.08	2005-FEB-22
	IRAS 07156-2248	-87.4	128.3	0.21	2004-DEC-01
	IRAS 07156-2301	-87.4	128.4	0.06	2005-FEB-19
CB 58	IRAS 07159-2329	-87.4	128.3	0.07	2005-FEB-22
	[YMT96] CB 58 1	-85.6	116.6	0.18	2003-MAY-04
	IRAS 07161-2336	-85.6	116.6	0.10	2003-MAY-07
CB 59	IRAS 07171+0359	-90.5	111.7	0.05	2002-APR-18
CB 60	IRAS 08022-3115	-93.9	121.8	0.07	2005-FEB-19
	IRAS 08026-3122	-94.0	121.8	0.23	2004-DEC-01
	IRAS 08029-3118	-93.0	121.8	0.11	2004-DEC-30
CB 63	IRAS 15486-0350	-2665	2728	0.02	2002-APR-09
CB 65	[VRC2001] L1704 SMM 1]	-132.6	83.1	0.09	2004-AUG-04
	IRAS 16287-2337	-98.8	103.4	0.16	2002-JUN-16
CB 67	IRAS 16485-1906	-130.3	85.4	0.08	2004-AUG-04
CB 68	CS peak	-102.6	113.1	0.08	2004-JUL-09
		-102.7	113.0	0.05	2005-JUN-06
	IRAS 16544-1604	-102.7	113.0	0.05	2004-JUL-08
	NH_3 peak	-102.8	113.0	0.10	2004-AUG-21
CB 78	IRAS 17147-1821	-2720	2673	0.06	2002-MAR-13
CB 81	outflow	-104.3	111.4	0.15	2004-JUL-04
CB 82	[VRC2001] L57 SMM 1	-104.2	111.5	0.3	2004-JUL-23
		-101.0	114.7	0.06	2005-JUN-06
	NH_3 peak	-104.4	111.3	0.12	2004-AUG-26
	CS peak	-97.5	104.7	0.06	2004-JUL-08
CB 98	CB98-mm	-97.0	118.7	0.14	2004-JUL-23
CB 100	IRAS 17490-0258	-96.5	105.7	0.10	2002-NOV-16
	IRAS 17493-0258	-103.1	112.7	0.05	2004-AUG-21
CB 101	IRAS 17505-0828	-2654	2739	0.02	2002-APR-10
		-101.1	114.6	0.07	2004-AUG-04
CB 104	IRAS 17526-0815	-2654	2738	0.03	2002-APR-10
	IRAS 17533-0808	-97.1	118.6	0.05	2004-AUG-21
CB 105	IRAS 17561-0349	-100.9	114.8	0.09	2004-AUG-21
CB 106	IRAS 17577-0329	-91.5	124.2	0.06	2004-JUL-15
	IRAS 17580-0330	-101.5	114.2	0.05	2004-AUG-26
	IRAS 17586-0330	-101.5	114.3	0.06	2004-AUG-26
CB 108	[YMT96] CB 108 1	-95.5	106.7	0.3	2002-SEP-30
		-102.1	113.6	0.05	2005-JUN-06
CB 118	IRAS 18094-1550	-2654	2739	0.03	2002-APR-08
CB 121	IRAS 18115-0701	-101.9	113.9	0.08	2004-AUG-21
	IRAS 18116-0657	-101.9	113.8	0.09	2004-AUG-26
CB 124	IRAS 18120+0704	-87.2	128.5	0.05	2004-JUL-15
	IRAS 18122+0703	-80.7	121.5	0.20	2002-NOV-15
CB125	NH_3 peak	-94.7	107.5	0.8	2002-OCT-02
CB 128	IRAS 18132-0350	-99.0	116.7	0.06	2004-JUL-07
CB 130	CB130-mm	-97.6	118.1	0.06	2004-JUL-22
CB 131	CB131-smm	-101.0	114.7	0.10	2004-JUL-24
CB 137	IRAS 18219-0100	-98.4	117.3	0.10	2004-AUG-04

Table 3.3: (continued).

Globule	Source	$V_{\rm min}{}^1$ (km s^{-1})	$V_{\rm max}{}^1$ (km s^{-1})	Noise^2 (Jy)	Date^3
CB 142	IRAS 18272-1343	-89.1	126.6	0.06	2004-JUL-08
CB 145	IRAS 18296-0911	-103.1	112.7	0.05	2004-JUL-07
CB 146	IRAS 18293-0906	-103.3	112.4	0.06	2004-JUL-09
	IRAS 18294-0901	-103.3	112.5	0.07	2004-JUL-09
	[HSW99] CB 146 SMM 2	-103.3	112.4	0.05	2004-JUL-08
	[HSW99] CB 146 SMM 1	-103.3	112.4	0.05	2004-JUL-08
CB 171	[YMT96] CB 171 3	-90.9	124.9	0.05	2004-JUL-22
	[YMT96] CB 171 2	-90.9	124.8	0.06	2004-JUL-22
CB 177	IRAS 18599+1739	-91.2	124.5	0.08	2004-SEP-04
CB 178	IRAS 18595+1812	-92.2	123.5	0.13	2004-SEP-05
	IRAS 19002+1755	-92.2	123.5	0.07	2004-AUG-27
CB 180	NH_3 peak	-95.9	119.9	0.04	2004-JUL-09
CB 184	IRAS 19116+1623	-2655	2738	0.03	2002-APR-08
CB 187	IRAS 19162-0135	-101.2	114.5	0.10	2004-SEP-03
CB 188	IRAS 19179+1129	-99.9	115.8	0.07	2004-AUG-25
	Outflow	-100.4	115.3	0.07	2004-JUL-09
	CS peak	-94.0	108.2	0.10	2002-SEP-18
	IRAS 19180+1127	-100.4	115.3	0.05	2004-JUL-09
CB 189	IRAS 19180+1116	-99.9	115.8	0.08	2004-AUG-25
	[VRC2002] L673 SMM 7	-100.1	115.6	0.04	2005-JUN-06
	[VRC2002] L673 SMM 1	-100.0	115.7	0.07	2005-FEB-26
		-100.8	115.0	0.05	2005-JUN-16
	IRAS 19180+1114	-100.0	115.8	0.05	2005-SEP-22
	IRAS 19183+1123	-100.4	115.3	0.06	2004-AUG-22
	IRAS 19184+1118	-100.5	115.3	0.06	2004-AUG-22
CB 190	IRAS 19186+2325	-96.5	119.3	0.09	2004-AUG-22
CB 194	IRAS 19273+1433	-103.7	112.1	0.12	2004-SEP-10
CB 196	IRAS 19329+1213	-97.7	118.0	0.10	2004-SEP-09
CB 198	IRAS 19342+1213	-97.7	118.0	0.06	2004-OCT-25
		-99.0	116.7	0.05	2005-JUN-16
CB 199	[ARC92] Barn 335 9	-99.2	116.5	0.09	2005-FEB-27
	[ARC92] Barn 335 1	-108.9	106.8	0.05	2004-NOV-09
	IRAS 19343+0727	-99.2	116.5	0.08	2004-AUG-18
	[ARC92] Barn 335 2	-108.9	106.8	0.06	2004-NOV-09
		-99.2	116.5	0.10	2005-FEB-22
	NH_3 peak	-99.2	116.5	0.06	2004-AUG-18
		-99.2	116.5	0.12	2005-FEB-22
		-99.3	116.4	0.05	2005-JUN-16
	IRAS 19345+0727	-92.7	109.5	0.13	2003-MAY-16
	[ARC92] Barn 335 11	-99.6	116.1	0.05	2005-JUN-15
	IRAS 19347+0729	-99.1	116.6	0.07	2004-SEP-03
	IRAS 19348+0724	-99.1	116.6	0.07	2004-SEP-04
CB 203	IRAS 19413+1902	-91.7	124.1	0.09	2004-SEP-04
CB 205	IRAS 19427+2741	-93.6	122.1	0.07	2004-AUG-22
		-85.1	117.2	0.06	2005-JUN-16
	[YMT96] CB 205 1	-85.3	116.9	0.07	2002-SEP-03
		-85.3	116.9	0.10	2002-SEP-19
		-85.3	116.9	0.13	2002-NOV-16
	[HSW99] L 810 SMM 2	-91.7	124.0	0.05	2004-JUL-22
	[YMT96] CB 205 2	-2659	2734	0.03	2002-APR-08

Table 3.3: (continued).

Globule	Source	$V_{\rm min}{}^1$ (km s^{-1})	$V_{\rm max}{}^1$ (km s^{-1})	Noise^2 (Jy)	Date^3
	IRAS 19433+2743	-85.3	116.9	0.25	2003-JUL-11
		-91.7	124.0	0.05	2004-JUL-22
		-91.8	124.0	0.05	2005-JUN-16
	IRAS 19433+2751	-91.7	124.1	0.07	2004-AUG-25
	[YMT96] CB 205 3	-85.3	116.9	0.08	2002-SEP-03
		-85.3	116.9	0.17	2002-NOV-16
		-91.7	124.0	0.05	2004-JUL-15
	IRAS 19438+2757	-91.6	124.1	0.07	2004-AUG-25
	IRAS 19438+2737	-91.7	124.0	0.10	2004-AUG-25
	IRAS 19439+2748	-91.7	124.1	0.07	2004-SEP-05
CB 206	[YMT96] CB 206 2	-92.2	123.5	0.07	2004-JUL-22
		-92.3	123.4	0.05	2004-AUG-05
CB 207	IRAS 19437+2108	-99.9	115.9	0.06	2004-AUG-05
CB 208	IRAS 19450+1847	-92.1	123.6	0.11	2004-SEP-10
CB 210	IRAS 19529+3341	-97.8	118.0	0.09	2004-SEP-04
CB 211	IRAS 19576+2447	-100.5	115.2	0.10	2004-SEP-04
CB 214	IRAS 20018+2629	-91.2	111.0	0.14	2003-JUL-11
CB 216	Outflow	-88.5	113.7	0.14	2002-SEP-17
	IRAS 20037+2317	-94.8	120.9	0.10	2004-SEP-05
	CS peak	-2659	2734	0.03	2002-APR-08
		-88.5	113.7	0.13	2002-SEP-17
CB 217	Outflow	-100.6	101.6	0.12	2003-JUL-11
	[YMT96] CB 217 4	-107.0	108.7	0.06	2004-JUL-24
CB 219	IRAS 20176+6343	-2680	2713	0.03	2002-APR-08
CB 222	IRAS 20328+6351	-101.0	101.2	0.04	2002-APR-19
CB 224	IRAS 20355+6343	-103.8	98.4	0.19	2003-JUN-07
		-110.3	105.3	0.04	2004-OCT-29
		-110.7	105.0	0.04	2005-JUN-05
	NH_3 peak	-2681	2713	0.04	2003-APR-08
CB 225	IRAS 20365+5607	-103.6	98.6	0.06	2002-APR-18
		-103.6	98.6	0.13	2002-AUG-14
CB 230	[YMT96] CB 230 1	-98.2	104.0	0.04	2002-APR-19
	[YMT96] CB 230 2	-2685	2708	0.05	2002-APR-07
CB 233	CS peak	-108.5	107.3	0.10	2004-AUG-19
		-109.3	106.4	0.05	2005-APR-14
CB 235	IRAS 21548+5843	-108.0	107.8	0.10	2004-AUG-19
CB 238	NH_3 peak	-107.3	108.4	0.05	2004-AUG-22
CB 240	IRAS 22317+5816	-111.5	104.3	0.08	2004-JUL-30
CB 241	IRAS 23095+6547	-115.5	100.3	0.08	2004-JUL-30
CB 243	IRAS 23228+6320	-112.2	90.0	0.09	2003-MAY-11
	NH_3 peak	-112.2	90.0	0.20	2002-OCT-13
	[VRC2001] L1246 SMM 2	-119.0	96.8	0.07	2004-JUL-24
	CS peak	-119.0	96.8	0.06	2004-JUL-24
CB 244	[VRC2001] L1246 SMM 2	-104.0	111.8	0.08	2004-JUL-30
	[YMT96] CB 244 1	-2694	2699	0.04	2002-APR-07
	IRAS 23249+7406	-97.2	105.0	0.12	2003-JUN-07
CB 246	CB246-mm	-103.6	112.2	0.08	2004-JUL-24
CB 247	IRAS 23550+6430	-104.8	97.4	0.06	2003-MAY-12

Notes to Table 3.3

[1] Velocity range covered by the observational bandwidth

[2] Noise level, 1σ

[3] Date of observation

Chapter 4

High-resolution observations of water masers in Bok globules

In this chapter we present VLA observations at 1.3 cm of several water maser detections obtained by previous single-dish studies of Bok globules in the Clemens & Barvainis (1988; CB) catalog. These include our new detections obtained before 2003 May among those presented Chapter 3, i.e., those in CB 54, CB 65, CB 101, and CB 232, as well as the masers in CB 3 (Scappini et al. 1991 and Chapter 3) and CB 205 (Neckel et al. 1985). We also present single-dish observations of millimeter and centimeter spectral lines towards CB 101 (IRAS 17503−0833) and CB 65 (IRAS 16277−2332) in order to study the nature of these sources. We have used the accurate positions of the maser emission to derive information about the powering source of the masers, their relation with molecular outflows, and the kinematical properties of the region.

4.1 Motivation

As we mentioned in the introduction of this thesis (Chapter 1), water maser emission is a very useful tool for deriving information about the physical conditions and kinematics of the gas surrounding the most embedded YSOs at high-resolution ($\leq$1 mas), due to the highly localized conditions to pump the maser emission and the high intensity of this phenomenon.

Until now, all the reported studies of water masers in Bok globules of the CB catalog present single-dish data (Scappini et al. 1991; Felli et al. 1992; Palla & Prusti 1993; Wouterloot et al. 1993; Persi et al. 1994; Codella & Felli 1995 and Chapter 3). However, interferometric observations are necessary to accurately pinpoint the pumping source of water maser emission, among several candidates, and to determine whether maser emission in these Bok globules tend to trace collimated jets or circumstellar disks.

In this chapter we present for the first time interferometric, high-angular resolution observations using the VLA of some of these water masers in Bok globules. The globules included comprise those in which water masers were detected in the survey reported in Chapter 3, between 2002 April and 2003 May (i.e., CB 54, CB 65, CB 101, and CB 232), as well as CB 3 (Scappini et al. 1991) and CB 205 (Neckel et al. 1985). The interferometric data have been complemented with a multimolecular single-dish study at millimeter and centimeter wavelengths using the IRAM-30m and Robledo-70m antenna of CB101 (IRAS 17503−0833) and CB65 (IRAS 16277−2332), in order to better understand the nature of these sources, and determine the internal structure of their surrounding region.

This chapter is structured as follows: in §4.2 we describe our observations and data processing. In §4.3 we present our observational results and we discuss them. We summarize our conclusions in §4.4.

4.2 Observations and data processing

4.2.1 VLA observations

We observed simultaneously the 6_{16}-5_{23} transition of H_2O and continuum at 1.3 cm with the VLA, toward the Bok globules CB 54, CB 65, CB 101, CB 205, and CB 232. Observations of CB 54, CB 101, CB 205, and CB 232 were carried out on 2004 February 2 and 3 using the VLA in its CnB configuration, while CB 65 was observed on 2005 February 12 in the BnA configuration. We selected the four IF spectral line mode to observe line and continuum simultaneously, processing both right and left circular polarizations. Two IFs were used to observe the water maser transition, sampled on 64 channels over a bandwidth of 3.125 MHz, with a velocity resolution of 0.66 km s^{-1}. The other two IFs were used for radio continuum observations at 1.3 cm, covering a 25 MHz bandwidth on 8 channels, and centered 50 MHz above the central frequency used for line observations. The central velocity of the bands for line observations, the coordinates of the phase centers and the synthesized beam information are listed in Table 4.1 for each source. The primary calibrators were 3C48 (adopted flux density of 1.132 Jy) for observations on 2004 February 2, and 3C286 (adopted flux density of 2.539 Jy) for observations on 2004 February 3 and 2005 February 12. The phase calibrators and their bootstrapped flux densities are given in Table 4.1. We used J0609-157, J1743-038, and 3C286 as bandpass calibrators. Calibration and data reduction were performed with the Astronomical Image Processing System (AIPS) of NRAO. We detected water maser emission on CB 54, CB 101, and CB 232 (see Table 4.2), but we did not detect any emission towards either CB 65 or CB 205.

Table 4.1: Setup of VLA observations

Source	Right Ascension[a] (J2000)	Declination[a] (J2000)	V_0[b] (km s^{-1})	Beam Size ($''$)	Beam P.A. (deg)	Phase calibrator	$S_{\rm cal}$[c] (Jy)	Date[d]
CB 3[e]	00 28 43.5075	+56 41 56.868	−60.0	0.55×0.25	81	J0136+478	5.8±1.2	95/10/28
CB 54	07 04 21.2170	−16 23 15.000	7.9	0.93×0.44	73	J0609−157	4.55±0.17	04/02/02
CB 65	16 30 43.7109	−23 39 07.736	2.3	0.28×0.18	86	J1626−298	2.00±0.03	05/02/12
CB 101	17 53 05.2300	−08 33 41.170	28.8	0.99×0.39	68	J1743−038	7.04±0.05	04/02/03
CB 205	19 45 23.8630	27 50 57.840	13.2	0.86×0.79	48	J2015+371	3.06±0.05	04/02/03
CB 232	21 37 11.3100	43 20 36.260	12.1	1.08×0.67	53	J2202+422	2.50±0.04	04/02/03

Notes to Table 4.1

[a] Coordinates of the phase center. Units of right ascension are hours, minutes, and seconds. Units of declination are degrees, arcminutes, and arcseconds.

[b] Local standard of rest velocity of the center of the bandwidth.

[c] Bootstrapped flux densities of phase calibrators at 22 GHz.

[d] Observation date, YY/MM/DD

[e] Archive data

In the case of CB 101 and CB 232, maser data were self-calibrated, and spectral Hanning smoothing was applied (to alleviate ringing in the bandpass), which provides a final velocity resolution of ~ 1.3 km s^{-1}. The continuum data of these two sources were cross-calibrated using the self-calibration solutions obtained for the stronger maser lines. None of the sources surveyed show radio continuum emission at our sensitivity level (see Table 4.3).

We have also processed water maser data on source CB 3, taken from the VLA archive. The observations were carried out on 1995 October 28, in the B configuration. These observations were made in the 1IF spectral line mode, in right circular polarization only, with a bandwidth of 6.25 MHz sampled over 128 channels (velocity resolution of 0.66 km s^{-1}). The velocity of the center of the bandwidth, coordinates of the phase center, and synthesized beam size are also listed in Table 4.1. The source 3C48 was used as primary flux calibrator, with an assumed flux density of 1.131 Jy, while J0136+478 was used as phase and bandpass calibrator (Table 4.1). Water maser emission was detected toward CB 3 (see Table 4.2). The data were self-calibrated and spectral Hanning smoothing was applied, with a final velocity resolution of ~ 1.3 km s^{-1}.

Table 4.2: Water maser features detected with the VLA.

Source	Offset R.A.[1] ($''$)	Offset Dec[1] ($''$)	Position[2] uncertainty ($''$)	Flux density[3] (Jy)	$V_{\rm LSR}$[4] (km s^{-1})
CB 3 (A)	−0.063	−0.065	0.007	1.4±0.6	−37.0
CB 3 (B)	0	0	....[5]	68±27	−51.4
CB 3 (C)	−0.013	−0.014	0.003	2.8±0.6	−57.4
CB 3 (D)	−0.0226	−0.0207	0.0006	14±6	−67.2
CB 3 (E)	0.003	−0.003	0.003	2.3±0.9	−78.4
CB 54	−6.49	−6.30	0.03	0.091±0.013	17.8
	−6.467	−6.293	0.018	0.124±0.014	15.8
CB 101	0	0	....[5]	0.492±0.011	29.5
CB 232	0	0	....[5]	46.6±1.5	10.1

Notes to Table 4.2

[1] Position offsets of the peak of each distinct water maser feature with respect to the reference feature used for self-calibration ($[\alpha,\delta]_{J2000.0}$ = [$00^h28^m42\overset{s}{.}612$, $+56^\circ42'01\overset{''}{.}17$] for CB 3, [$17^h53^m05\overset{s}{.}882$, $-08^\circ33'38\overset{''}{.}17$] for CB 101 and [$21^h37^m11\overset{s}{.}402$, $+43^\circ20'38\overset{''}{.}26$] for CB 232), or with respect to the phase center ($07^h04^m21\overset{s}{.}217$, $-16^\circ23'15\overset{''}{.}00$) for CB 54.

[2] Relative position errors with respect to the reference positions. The absolute position uncertainty of the reference position is $\simeq 0\overset{''}{.}19$ for CB 3, $\simeq 0\overset{''}{.}05$ for CB 101, and $\simeq 0\overset{''}{.}12$ for CB 232 and CB 54. Uncertainties are 2σ.

[3] Uncertainties are 2σ.

[4] LSR velocity of the spectral channel where maser emission is detected. Velocity resolution $\sim$1.3 km s^{-1}.

[5] Reference feature.

Table 4.3: VLA continuum data at 1.3 cm

Source	Flux density[1] (mJy)
CB 54	<0.4
CB 65	<2.7
CB 101	<0.4
CB 205	<0.5
CB 232	<0.5

Notes to Table 4.3

[1] Upper limits are 3σ.

4.2.2 Single-dish observations

4.2.2.1 IRAM 30 m

Millimeter single-dish observations were carried out towards CB 65 (IRAS 16277−2332) and CB 101 (IRAS 17503−0833) with the IRAM-30m telescope at Pico Veleta (Spain), in 2004 July-August. We have used Superconductor-Insulator-Superconductor (SIS) heterodyne receivers to observe nine different transitions at ~ 1.3, ~ 2.7, and ~ 3 mm. We observed the ^{13}CO(1-0), ^{13}CO(2-1), C^{18}O(1-0), C^{18}O(2-1), CO(1-0), CO(2-1), SiO(2-1), CS(2-1), and CS(5-4) lines towards CB 101. In the case of CB 65, only the CO(1-0) and CO(2-1) lines were observed. In Table 4.4 we have summarized the rest frequencies of the different molecular species observed, the typical system temperature ($T_{\rm sys}$), the half power beam width, the main beam efficiency for each transition, averaging area, and parameters of the lines. Pointing was checked every hour by observing J1743−038, giving a pointing accuracy better that $2''$. The observations were made by wobbling the secondary mirror to a distance of $220''$ from the source for CO(1-0), CO(2-1), and CS(5-4) transitions, and in frequency switching mode for C^{18}O(1-0), C^{18}O(2-1), ^{13}CO(1-0), ^{13}CO(2-1), CS(2-1), and SiO(2-1) transitions. In addition, we observed CO(1-0) and CO(2-1) in frequency switching mode at one selected position to better estimate the excitation conditions. The data were taken with the versatile spectrometer assembly (VESPA) autocorrelator, split into two or three parts (depending on the lines), to observe simultaneously two or three different frequencies. This provided resolutions between 0.05 and 0.4 km s^{-1} at 1.3 mm, between 0.05 and 0.8 km s^{-1} at 2.7 mm, and $\simeq 0.06$ km s^{-1} at 3 mm. Moreover, we used a 1 MHz filter bank split into two parts of 256 channels each, in combination with VESPA. It provided a velocity resolution of 1.3 and 2.6 km s^{-1} at 1.3 and 2.7 mm, respectively. The calibration was made using the chopper wheel technique and the line intensities are reported as main beam brightness temperatures. With this setup, in some cases the same transition was observed with different velocity resolutions. The values shown in Table 4.4 correspond to the data with best rms.

4.2.2.2 Robledo de Chavela 70 m

Centimeter single-dish spectral line observations of CB 101 were obtained with NASA's 70 m antenna (DSS-63) at Robledo de Chavela, Spain, for both CCS J_N=2_1-1_0 and NH_3(1,1) transitions. Rest frequencies, typical system temperatures, half power beam widths, main beam efficiencies, and averaging region for calculations are given in Table 4.4. The rms pointing accuracy of the telescope was better than $6''$ and $11''$ for CCS and ammonia observations, respectively. Observations were made in frequency switching mode, using the SDS 256-channel spectrometer. The CCS observations were performed on 2002 May with a bandwidth of 1 MHz (velocity resolution $\simeq$ 0.05 km s^{-1}), while the NH_3 observations were carried out during 2003 July with a bandwidth of 10 MHz (velocity resolution $\simeq$ 0.5 km s^{-1}). All the single-dish data reduction was carried out using the CLASS package.

Table 4.4: Single-dish observations towards CB 101 and CB 65

Molecule	Transition	Rest ν (MHz)	Telescope	δv^1 (km s^{-1})	$T_{\rm sys}{}^2$ (K)	HPBW^3 ($''$)	$\eta_{\rm MB}{}^4$	$T_{\rm MB}{}^5$ (K)	Averaging^6 area ($'$)	Δv^7 (km s^{-1})	$\int T_{\rm MB} dv^8$ (K km s^{-1})
CB 65											
CO	J=1-0	115271.2018	IRAM-30m	2.60	400	21	0.73	<0.03	(0,0)	...	...
	J=2-1	230538.0000	IRAM-30m	1.30	600	11	0.52	<0.3	(0,0)	...	...
CB 101											
^{13}CO	J=1-0	110201.3541	IRAM-30m	0.05	270	22	0.74	1.51±0.23	(0,0)	0.44±0.04	0.61±0.16
	J=2-1	220398.6765	IRAM-30m	0.05	2700	11	0.54	1.1±0.5	2×2	0.24±0.09	0.27±0.21
C^{18}O	J=1-0	109782.1734	IRAM-30m	0.05	290	22	0.74	<0.10	2×2	...	...
	J=2-1	219560.3568	IRAM-30m	0.05	1300	11	0.54	<0.4	2×2	...	...
CO	J=1-0	115271.2018	IRAM-30m	0.05	400	21	0.73	6.3±0.6	(0,0)	0.86±0.03	5.7±0.7
	J=2-1	230538.0000	IRAM-30m	0.05	600	11	0.52	6.6±1.0	(0,0)	0.95±0.05	6.4±1.5
SiO	J=2-1	86846.9600	IRAM-30m	0.07	700	28	0.77	<0.7	(0,0)	...	...
CS	J=2-1	97980.9500	IRAM-30m	0.06	270	25	0.76	<0.11	2×2	...	...
	J=5-4	244935.6435	IRAM-30m	1.22	500	10	0.49	<0.4	(0,0)	...	...
CCS	$J_N=2_1$-1_0	22344.0330	Robledo-70m	0.05	60	41	0.38	<0.5	(0,0)	...	...
NH$_3$	(J,K)=(1,1)	23694.4955	Robledo-70m	0.50	90	39	0.35	<0.14	1.7×1.7	...	...

Notes to Table 4.4

[1] Velocity resolution for each transition.

[2] Typical system temperature.

[3] Half power beam width of the telescope.

[4] Main beam efficiency.

[5] Main beam brightness temperature of the emission peak. Uncertainties are 2 σ. Upper limits are 3 σ.

[6] Area over which data were averaged to obtain the quoted $T_{\rm MB}$, centered at IRAS 16277−2332 for CB 65 and at IRAS 17503−0833 for CB 101. (0,0) means that only the central spectrum was used. This averaging area coincides with the mapped area in the molecular transitions CO(1-0) and CO(2-1) for CB 65 and ^{13}CO(2-1), C^{18}O(1-0), C^{18}O(2-1), SiO(2-1), CS(2-1), CS(5-4), CCS(2_1-1_0) and NH$_3$(1,1) for CB 101. The transition ^{13}CO(1-0) was mapped in a region of $2'\times2'$ (see Fig 4.5) and the transitions CO(1-0) and CO(2-1) where mapped over an area of $40''\times40''$ in CB 101 (see subsection 4.3.4).

[7] Line width of the emission peak, obtained from a Gaussian fit to the line transition. Uncertainties are 2 σ, and represent the error in the Gaussian fit.

[8] Velocity integrated mean brightness temperature of the emission peak. Uncertainties are 2 σ.

4.3 Results and discussion

4.3.1 CB 3

Several sources in different stages of evolution have been identified in CB 3: the young stellar object CB 3/YC1, which corresponds to the IRAS PSC source IRAS 00259+5625 (Yun & Clemens 1994a), a near-infrared source, CB 3 YC1-I, that was proposed to be a Class II source (Yun & Clemens 1995), and a millimeter source, CB 3-mm (Launhardt & Henning 1997), cataloged by Codella & Bachiller (1999) as a probable class 0 object, which also shows submillimeter emission (Launhardt et al. 1997). As we commented in Chapter 3, this Bok globule is associated with a bipolar molecular outflow elongated in the north-south direction (Yun & Clemens 1994a; Codella & Bachiller 1999), of which CB 3-mm was proposed to be the driving source (Codella & Bachiller 1999). The outflow reveals different CO clumps along its main axis, which suggest episodic mass loss (Codella & Bachiller 1999). There are four H_2 emission knots, projected towards the blueshifted lobe of the outflow, and whose distribution does not follow a straight line (see Fig. 4.1), probably due to precession of the outflow axis (Massi et al. 2004).

The water maser position reported by Scappini et al. (1991), with single-dish observations is shifted $\simeq$ ($30''$, $-60''$) from our VLA detection. At least five distinct spectral features are evident in the maser spectrum. (Fig. 4.1), which we designated as A, B, C, D, and E on Table 4.2, and show velocities of $\simeq -37.0$, -51.4, -57.4, -67.2, and -78.4 km s^{-1} respectively. Component D may in its turn be composed of two individual features, but they are blended with our spectral resolution. All except component A are blueshifted with respect to the cloud velocity (V_{LSR}=-38.3 km s^{-1}, Clemens & Barvainis 1988). There is some inner space-kinematical structure in these maser features. A plot of the centroids of the maser emission for each velocity channel shows a structure of $\simeq 0\rlap{.}''1$, elongated from northeast to southwest (see Fig. 4.1). The overall elongated structure is real, since the relative positional uncertainty of the emission for most individual velocity channels is smaller than the total size of the structure and the well-differentiated velocity components (Fig. 4.1). The emission corresponding the velocity closest to that of the cloud (feature A) occupies the southern part of the structure, while the most blueshifted one (E) is located at the north.

The maser emission is aligned in the direction where the blueshifted molecular outflow extends, and it is located $\simeq$ 5" south of the position of CB3-mm reported by Launhardt & Henning (1997), between this source and the northernmost H_2 knot observed by Massi et al. (2004) (see Fig. 4.1). However, the mm observations were made with a beamsize of $\simeq 12''$, so it is possible that both mm and water maser emission actually come from the same location, which would be more accurately traced by the maser. The proximity of the masers to the mm source is consistent with the idea that this source is powering the molecular outflow.

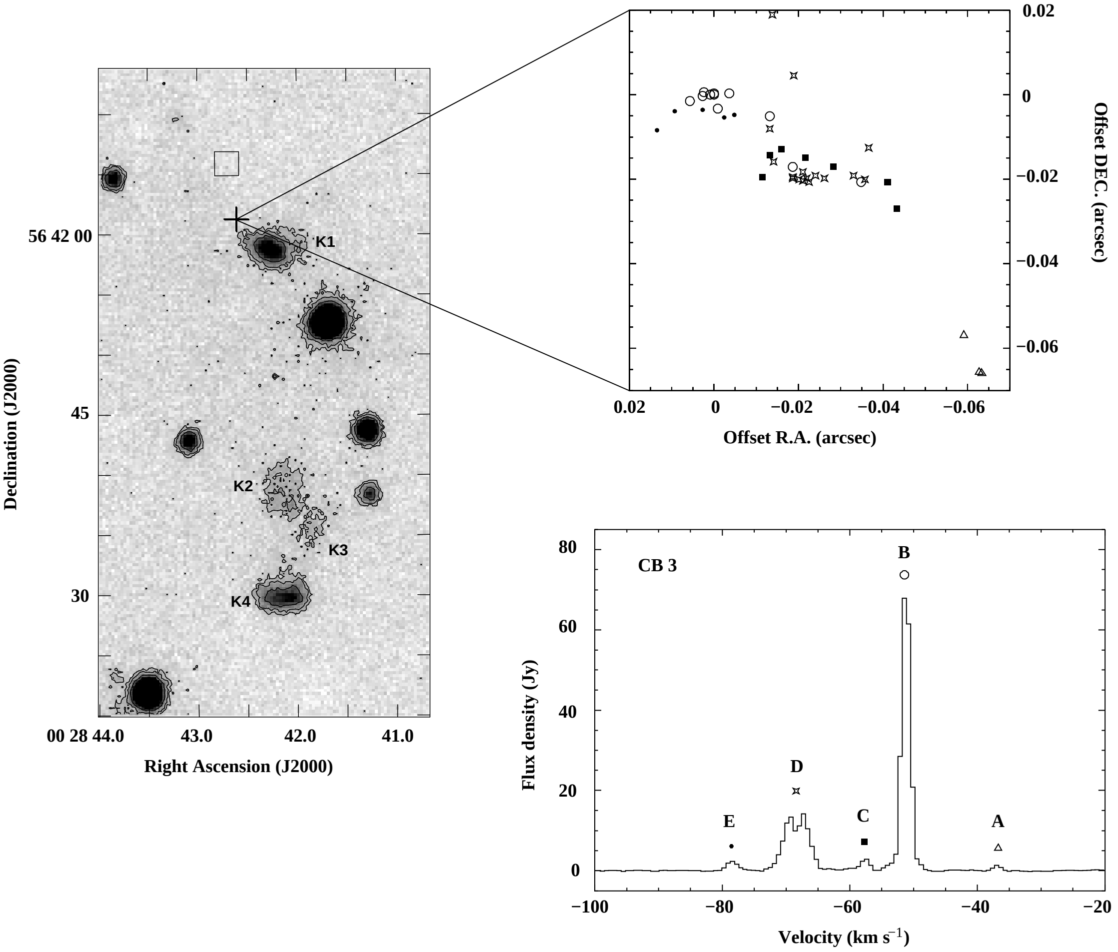

Figure 4.1: (Left) H_2 image (grey scale; Massi et al. 2004. Positional error $\simeq 1''$) of CB 3. K1, K2, K3, and K4 represent the H_2 knots detected by Massi et al. 2004. The square marks the position of CB3-mm (Launhardt & Henning 1997). The cross marks the centroid position of the water maser emission detected with the VLA. (Lower right) Water maser spectrum of CB 3 obtained with the VLA. Different symbols correspond to the spectral features A, B, C, D, and E, indicated in Table 4.2. (Upper right) Spatial distribution of the centroids of the emission at different velocity channels. The (0,0) position in this map is the position of the reference feature used for self-calibration.

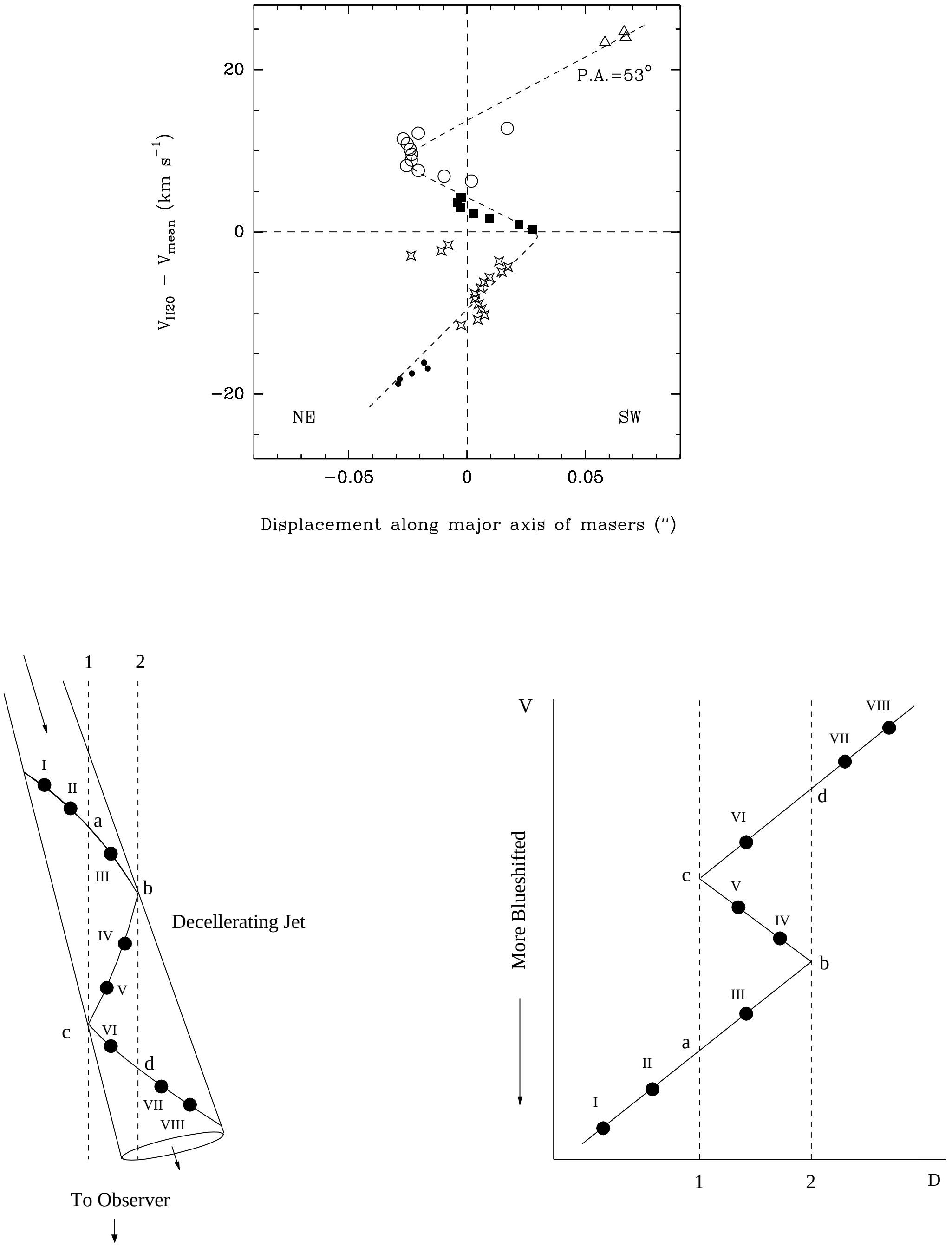

Figure 4.2: (Top) Position-velocity distribution of the water maser emission at different velocity channels in CB 3, along the major axis of the elongated maser distribution shown in Fig. 4.1. The horizontal axis represents the relative position of the emission along the major axis (P.A. = 53 ^{o}) of the distribution with respect to their geometrical center. The vertical axis represents the velocity of each channel after subtracting the mean velocity of the spectrum (-61.0 km s^{-1}). Different symbols correspond to the same spectral features indicated in Fig. 4.1. The dashed line represent the general trend shown by the maser spots in this diagram. We note that points further away from the dashed line are those with the largest positional uncertainty. (Bottom left) Model of a decelerating and precessing jet proposed for CB 3. Filled circles represent hypothetical parcels of gas moving in the direction of the arrow. Dashed lines represent two lines of sight through the jet. (Bottom right) Position-velocity distribution for the proposed model. Filled circles and dashed lines correspond to their equivalent in the left panel masers along the projected main axis of the jet. Four particular points (a to d) are marked in both bottom panels.

The position-velocity diagram of the maser emission along the major axis of the maser structure (Fig. 4.2) shows an interesting wave-like distribution. We note that a similar distribution was observed in AFGL 2591 (Trinidad et al. 2003). We suggest that this position-velocity distribution is compatible with a precessing jet at scales of $\simeq$ 250 AU. The possible presence of a precessing jet was already suggested by the relative spatial distribution of H_2 knots with respect to the powering source (Massi et al. 2004). In the lower panels of Fig. 4.2, we show a sketch illustrating the model we propose. We approximated the precessing jet with a narrow cone on whose surface discrete ejections of material are located. If we assume that the ejected material is being decelerated, we can reproduce a wave-like distribution similar to the one observed (upper panel of Fig. 4.2).

Given the large number of different velocity components, and their time variation (see section 3.4.2.1), it would be interesting to carry out a VLBI monitoring of this source, to trace the spacial distribution and proper motions of these different components, to test the proposed scenario of a precessing jet at these small scales (250 AU), and to ascertain whether the maser variability is related to the presence of episodic mass-loss phenomena.

4.3.2 CB 54

This Bok globule hosts a multiple system of YSOs towards CB54 YC1 (IRAS 07020-1618), with the presence of two bright near-infrared (K band, 2.2 μm) objects (CB54 YC1-I, YC1-II, which are probably class I protostars), plus a bright elongated feature (hereafter CB54 YC1-SW) mainly seen in H_2 [v = 1–0 S(1), 2.121 μm] (Yun & Clemens 1994b, 1995; Yun et al. 1996; see Fig. 4.3). In addition, Yun et al. (1996) and Moreira et al. (1997) reported a radio-continuum source (CB 54 VLA1)[1] at 3.6 and 6 cm located $\simeq 5''$ to the NE of the nominal position of the IRAS source (see Fig. 4.3). These sources are located near the center of a bipolar CO outflow that is oriented in the northeast-southwest direction and probably moves close to the plane of the sky (Yun & Clemens 1994a).

Our VLA observations (Fig. 4.3) reveal water maser emission with two distinct spectral features, at $\simeq$ 15.8 and 17.8 km s^{-1}. These velocities are blueshifted with respect to the velocity of the cloud (V_{LSR}=19.5 km s^{-1}; Clemens & Barvainis 1988). The maser emission in this source is highly variable. No maser emission was detected with the Robledo antenna at the velocities reported here (Chapter 3, figure 3.3), which is understandable since the flux density reported here is below the sensitivity threshold of those single-dish observations. However, with the Robledo-70m antenna we detected a component at $\simeq$ 8 km s^{-1} (see Section 3.4.2.3), which reached a flux density of up to $\simeq$ 45 Jy, and another one of up to $\simeq$ 1 Jy at $\simeq$ 14 km s^{-1}. Neither of these is evident in the VLA spectrum (Fig. 4.3), although the component at $\simeq$ 14 km s^{-1} might be present at a very low level,

---

[1] Named as [YMT96] CB 54 2, in SIMBAD and Chapter 3 of this thesis

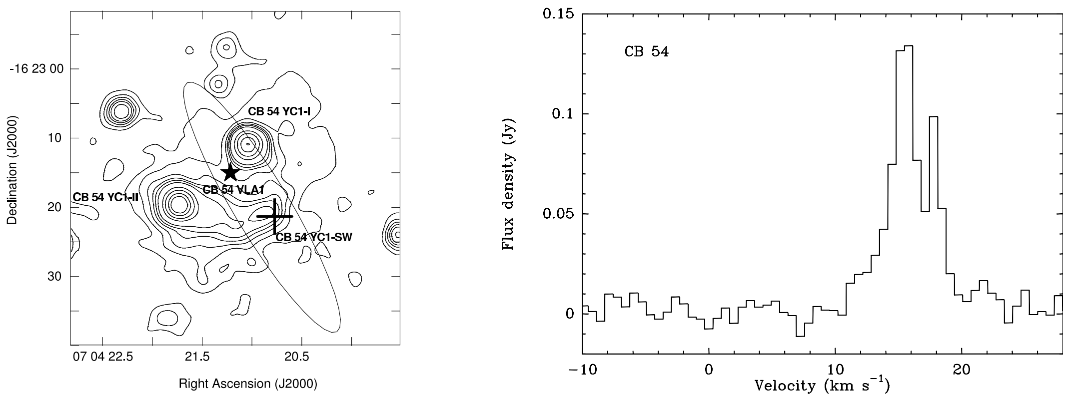

Figure 4.3: (Left panel) Contour map of the 2MASS K-band emission (positional error $\simeq 0''.2$) surrounding IRAS 07020−1618 in CB 54. The ellipse is the position error of the IRAS source. The cross indicates the centroid position of the waters masers observed with the VLA. The star is the position of CB 54 VLA1, the radio-continuum source at 3.6 cm reported by Yun et al. (1996; positional error $\simeq 2''$). (Right panel) Water maser spectrum of CB 54 obtained with the VLA.

and blended with the one at $\simeq$ 15.8 km s^{-1}.

The maser emission is located at the position of the elongated feature CB54 YC1-SW (see Fig. 4.3). Yun (1996), on the basis that the elongated feature appears brighter in H_2 than in the K-band, proposed that it could trace shocked material, such as a knot in a near-infrared jet. However, given its association with the water masers, we suggest that they could mark the position of another embedded YSO and that this object is probably the powering source of the observed molecular outflow in the region. In fact, masers are located $\simeq$ 18000-20000 AU (at a distance of 1.5 Kpc; Launhardt & Henning 1997) from both CB 54 YC1-I and CB 54 YC1-II, which make these objects less likely candidates for pumping the maser emission, since masers in low-mass star-forming regions tend to be within several hundred AU from the powering source (Chernin 1995; Claussen et al. 1998; Furuya et al. 2000, 2003). We did not detect 1.3 cm continuum emission with the VLA either at the position of CB54 YC1-SW or toward the other proposed YSOs in the region, with a 3σ upper limit of 0.4 mJy. Deeper radio continuum measurements in this region could help to confirm whether CB54 YC1-SW is indeed a YSO.

4.3.3 CB 65

Our single dish survey with the Robledo de Chavela antenna revealed water maser emission in IRAS 16277−2332, near the the CB 65 cloud velocity (V_{LSR} = 2.3 km s^{-1}; Clemens & Barvainis 1988), with a peak flux density of 0.3 Jy on 2002 June 16 (see 3.4.2.4). However, no water maser emission was detected with the VLA ($\leq$ 40 mJy,

3σ upper limit), which is not surprising given the time variability of these masers (Reid & Moran 1981). No 1.3 cm continuum emission was detected, with a 3σ upper limit of 2.7 mJy. On the other hand, the observations performed with the IRAM-30m antenna in the CO(1$-$0) and (2$-$1) transitions, showed no high-velocity wings in the spectra, with an rms of 0.03 K and 0.3 K respectively. This indicates the absence of any significant mass-loss activity.

Unfortunately, there are not enough studies in the literature about IRAS 16277$-$2332 that may help us to clarify the real nature of this source. For instance, IRAS data show emission at 60 μm, but only upper limits at 12, 25, and 100 μm. There are no Midcourse Space Experiment (MSX) infrared data nor emission in the 2MASS K, H, or J bands, from which to obtain information about its spectral energy distribution. Deeper infrared observations are needed to reveal the nature of this source.

4.3.4 CB 101

This Bok globule hosts two IRAS sources, IRAS 17503$-$0833 and IRAS 17505$-$0828. Our water maser single-dish survey revealed water maser emission towards IRAS 17503-0833 (see Section 3.4.2.5). This source is located $\simeq 9'$ south of the globule center.

4.3.4.1 Water masers and radio continuum emission

We have detected with the VLA water maser emission toward IRAS 17503$-$0833 at $V_{LSR} \sim 29.5$ km s^{-1} (see Table 4.2 and Fig. 4.4), which is redshifted with respect to the velocity of the molecular cloud ($V_{LSR} = 6.7$ kms^{-1}; Clemens & Barvainis 1988).

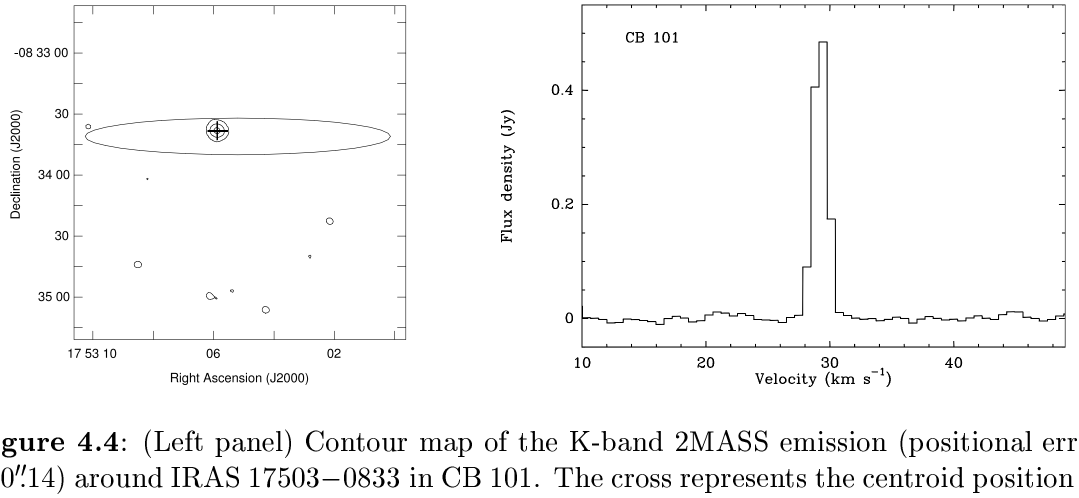

Figure 4.4: (Left panel) Contour map of the K-band 2MASS emission (positional error $\simeq 0''.14$) around IRAS 17503$-$0833 in CB 101. The cross represents the centroid position of the water maser emission. The ellipse represents the position error of IRAS 17503$-$0833. (Right panel) Water maser spectrum toward IRAS 17503$-$0833 in CB101, obtained with the VLA.

The flux density and velocity of the water maser emission are similar to those found with the Robledo antenna. The water maser emission coincides with a point source observed in the 2MASS K-band, which is probably the near-IR counterpart of IRAS 17503−0833 (see Fig. 4.4). We did not detect VLA radiocontinuum emission at 1.3 cm, with a 3σ upper limit of 0.4 mJy.

4.3.4.2 Millimeter and centimeter single-dish observations

Our aim was to search for any sign of star formation activity toward IRAS 17503−0833 (e.g., presence of molecular outflows, high density molecular gas, and/or shocked material). We mapped the CO(1-0) and (2-1) transitions over an area of 40"×40" in order to detect a possible molecular outflow in the region. No high-velocity emission was detected in the spectra of any of these transitions, with a rms of 0.012 K per channel (channel width $\simeq$ 0.8 km s^{-1}) and 0.026 K per channel (channel width $\simeq$ 0.4 km s^{-1}), respectively. Moreover, as for the general distribution of the molecular gas, Fig. 4.5 shows the map of ^{13}CO(1-0) integrated intensity in a region of $2' \times 2'$. It reveals more intense emission towards the northwest of the IRAS source, which is probably originated by the molecular gas contained in the Bok globule, but there is no obvious local maximum of molecular gas towards the source. In Table 4.4 we summarized the single dish observations performed in the rest of molecular transitions, as well as the emission of the CO(1-0), CO(2-1), and ^{13}CO(1-0) lines centered at the IRAS source and used to derive the physical parameters exposed below.

The ^{13}CO(2-1) emission is weak, and barely detectable in the region (Fig. 4.5). We did not detect emission of high-density molecular gas tracers such as the CCS(2_1-1_0), NH$_3$(1,1), CS(2-1) and CS(5-4) lines. No emission of the SiO(2-1) transition was detected either. This transition is usually associated with shocked regions around young stellar objects (Harju et al. 1998; Gibb et al. 2004).

We derived the physical conditions of the region surrounding the IRAS source, from the CO isotopes, under the following three assumptions (Estalella & Anglada 1996): (1) local thermal equilibrium, (2) the CO emission is optically thick, and (3) ^{13}CO emission is optically thin. The CO(1-0) emission at the IRAS position was used to obtain the excitation temperature (T$_{\rm ex}$) from:

$$T_{ex} = 5.53 \left[\ln \left(1 + \frac{5.53}{T_{\rm CO} + 0.82} \right) \right]^{-1}$$

where T$_{\rm CO}$ is the main beam brightness temperature of the CO(1-0) emission, in K.

For the ^{13}CO (1-0) we derived its optical depth ($\tau_{^{13}\rm CO}$) and its column density N$_{^{13}\rm CO}$ as:

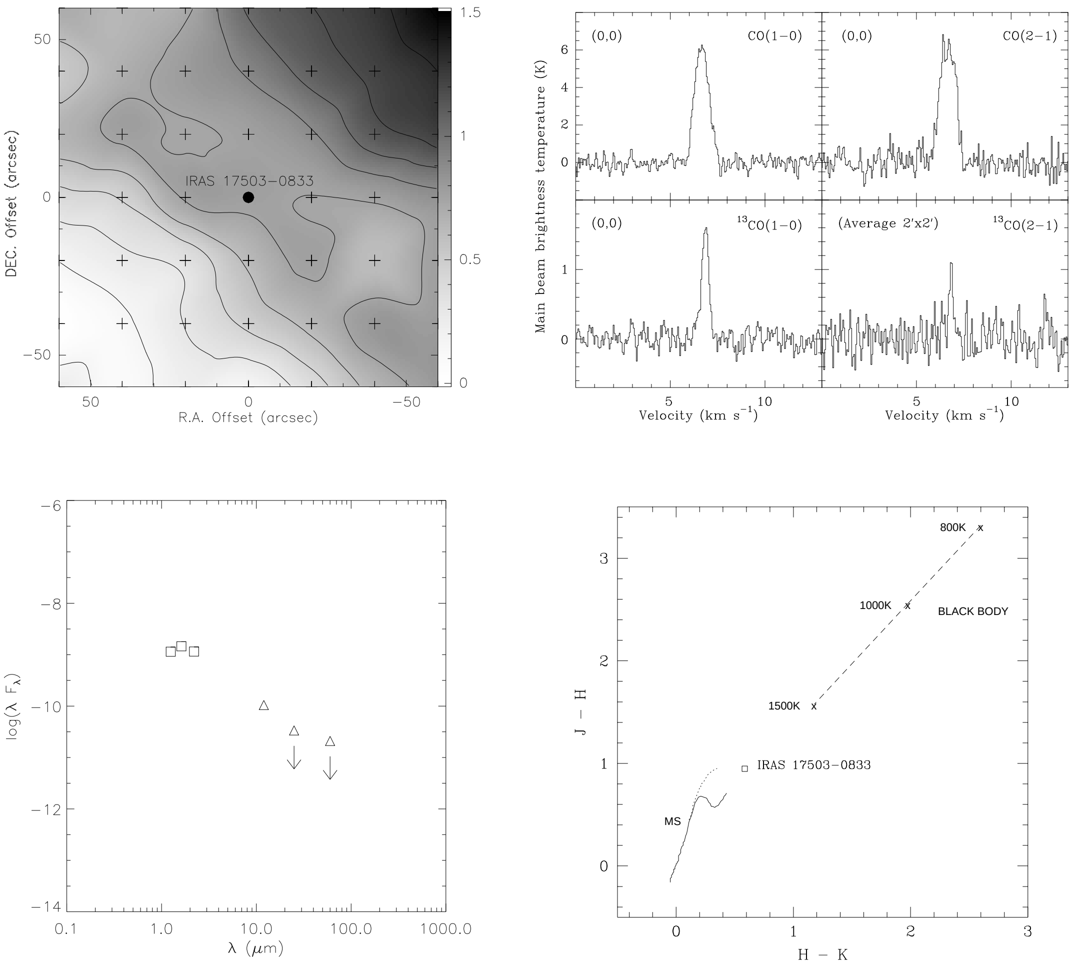

Figure 4.5: (Upper left) Map of the ^{13}CO(1-0) integrated emission in CB 101. The reference position (filled circle) is that of IRAS 17503-0833. Contour levels are represented from 0.15 to 1.5 K km s^{-1} in steps of 0.15 K km s^{-1}. Crosses mark the observed positions. (Upper right) Spectra of CO(1-0), CO(2-1), ^{13}CO(1-0), and ^{13}CO(2-1) at the position of IRAS 17503-0833 in CB 101. The ^{13}CO(2-1) spectrum (lower right) is the average over an area of $\simeq$ 2' × 2' centered at the position of the IRAS source. (Lower left) Infrared spectral energy distribution of IRAS 17503-0833 in CB 101. The squares represent the 2MASS measurements in the H, J, and K band and the triangles represent the IRAS measurements at 12, 25, and 60 μm (see table 4.5). (Lower right) Location of IRAS 17503−0833 in an (H-K)-(J-H) color diagram. The square represents the dereddened infrared color of IRAS 17503−0833. The solid line represents the main sequence, the dotted line represents the Red Giant Branch, and dashed line is a black body at different effective temperatures.

$$\tau_{^{13}\mathrm{CO}} = -\ln\left[1 - T_{^{13}\mathrm{CO}}\left(\frac{5.29}{\exp{(5.29/T_{ex})} - 1} - 0.87\right)^{-1}\right]$$

$$N(^{13}\mathrm{CO}) = 2.42 \times 10^{14}\frac{T_{ex}\Delta v(\tau_{^{13}\mathrm{CO}})}{1 - \exp{(-5.29/T_{ex})}}$$

where $\mathrm{T}_{^{13}\mathrm{CO}}$ is the main beam brightness temperature of the ^{13}CO (1-0) emission in K, and Δv is the line width at half maximum, in km s^{-1}.

The physical parameters (derived from the spectra shown in Fig. 4.5 and their corresponding values in Table 4.4), are T_{ex}=9.6±0.3 K, $\tau_{^{13}\mathrm{CO}}$=0.27±0.07, and N(^{13}CO) = (6.6±2.6)×10^{14} cm^{-2} at the position of the IRAS source. The value of N(H_2) is (3.3±1.2)×10^{20} cm^{-2}, derived from the relative abundance of ^{13}CO with respect to H_2, proposed by Dickman (1978), [H_2/^{13}CO]=5×10^5. Kim & Hong (2002) reported a value of N(^{13}CO)=3.7×10^{15} cm $^{-2}$ towards the central peak position of CB 101 (located $\simeq 9'$ north). This value is $\simeq$ 6 times higher than the value derived by us at the position of IRAS 17503−0833.

4.3.4.3 The nature of IRAS 17503−0833

The absence of any signpost of star formation activity associated with the water maser emission, suggests that the water maser in CB 101 may not be associated with a young object but with an evolved star, since water maser emission is also known to be associated with circumstellar envelopes of late-type stars (Bowers & Hagen 1984; Engels et al. 1986, 1988; Habing 1996). Moreover, the difference between the centroid velocity of the detected water maser and the cloud velocity is $\simeq$ 23 km s^{-1}, whereas this difference is usually $\leq$ 15 km s^{-1} in the case of YSOs (Wilking et al 1994; Anglada et al. 1996a; Brand et al. 2003). To determine the true nature of IRAS 17503−0833, we have studied the data available in the literature.

The IRAS flux density at 12 μm is well determined, but the values for 25, 60, and 100 μm are only upper limits. The near-infrared flux densities were retrieved from the 2MASS catalog, and they are shown, together with the IRAS flux densities, in Table 4.5. We have dereddened the near-IR flux densities with a value for E(B−V) = 0.21, taken from Whitelock et al. (1986) for stars with galactic latitude b = 8 deg. The corrected J, H, and K magnitudes are: 8.643, 7.690, and 7.100, respectively.

In Fig. 4.5 we have plotted the spectral energy distribution (SED) of IRAS 17503−0833, including the upper limits for the IRAS flux densities. The SED is compatible with a blackbody distribution, with its maximum in the near infrared. If this is an evolved object, the presence of only one maximum suggests that no disk or circumstellar envelope is detached from the central star. This would restrict the evolutionary stage of the star to the phase between Red Giant and the Asymptotic Giant Branch (AGB),

Table 4.5: Infrared data for IRAS 17503−0833

λ (μm)	Flux density (Jy)
1.25	0.48
1.65	0.82
2.17	0.82
12	0.42
25	<0.28
60	<0.42

since after the AGB the SEDs usually show two maxima, one belonging to the central star and the other to the circumstellar envelope (Kwok 1993). In Fig. 4.5, we have plotted the dereddened IR colours of the object in an IR color-color diagram, to further check its evolutionary stage. IRAS 17503−0833 is located to the right and above the Main Sequence and the Red Giant Branch, which is typical of Mira stars (see Whitelock et al. 1994, 1995). Moreover, water maser emission is very frequent in Mira-type stars (Bowers & Hagen 1984). Therefore, we suggest that the CO emission found belongs to the cloud CB 101, and IRAS 17503−0833 is a field star, not associated with the cloud. In any case, we think that optical spectra revealing the effective temperature of the star, together with a light curve to perform variability studies of this source are needed to confirm its identification as a Mira star.

4.3.5 CB 205

CB 205 is a very active star formation region containing several YSOs (Herbst & Turner 1976; Neckel et al. 1985; Neckel & Staude 1990; Huard et al. 2000; Massi et al. 2004), and a weakly collimated bipolar molecular outflow with a significant overlapping of the redshifted and blueshifted emission (Xie & Goldsmith 1990).

CB 205 was one of the few Bok globules in the CB catalog where water maser emission was known (Neckel et al. 1985) before the survey we undertook in this thesis (Chapter 3). The maser, located near IRAS 19433+2743, showed a peak flux density of $\simeq$ 4.8 Jy on May-October 1983. This emission was detected again by Brand et al. (1994) on 1992 January 18, with a peak flux density of 0.7 Jy and located $\simeq 40''$ west of our phase center, although inside the $2'$ VLA primary beam at 22 GHz. However, as we mentioned in Chapter 3, we did not detect the maser with the Robledo antenna, with a 3σ upper limit of 0.75 Jy on 2003 July 11 and of 0.15 Jy on 2004 July 22 and 2005 June 16. Our VLA observations also failed to detect any water maser emission on 2004 February 3, at a level of $\gtrsim 7$ mJy (3σ). In our VLA observations, we did not detect any radio continuum emission at 1.3 cm, with a 3σ upper limit of 0.5 mJy.

4.3.6 CB 232

This Bok globule contains a CO bipolar molecular outflow centered near CB 232 YC1 (IRAS 21352+4307), whose lobes are slightly overlapped and exhibit a poor degree of collimation (Yun & Clemens 1994a). Near-infrared maps reveal a single source, the possible counterpart of IRAS 21352+4307 (Yun & Clemens 1994b) which was designated as CB 232 YC1-I and classified as a class I object (Yun & Clemens 1995). Huard et al. (1999) detected two submillimeter sources, SMM1 (the westernmost one) and SMM2 (the easternmost one), located $\simeq 10''$ west and $\simeq 5''$ south-east from CB 232 YC1-I respectively, with a positional error of $\simeq 4''$. SMM1 was classified as a Class 0 source while SMM2 was proposed to be either the submillimeter counterpart of CB 232 YC1-I, or another Class 0 source without infrared counterpart (Huard et al. 1999).

Our VLA observations show water maser emission with velocity $V_{LSR} \sim 10.1$ km s^{-1} (see Table 4.2 and Fig. 4.6), close to the cloud velocity (V_{LSR}=12.6 km s^{-1}; Clemens & Barvainis 1988), and located, within the positional errors, at the position of the near-infrared source (see Fig. 4.6). This gives support to CB 232 YC1-I as the powering source of the outflow. The velocity of the maser is consistent with that found in our single-dish detection (Chapter 3), although the flux density was a factor of ~ 50 larger in the epoch in which we took the interferometer observations. We did not detect radiocontinuum emission at 1.3 cm, with a 3σ upper limit of 0.5 mJy.

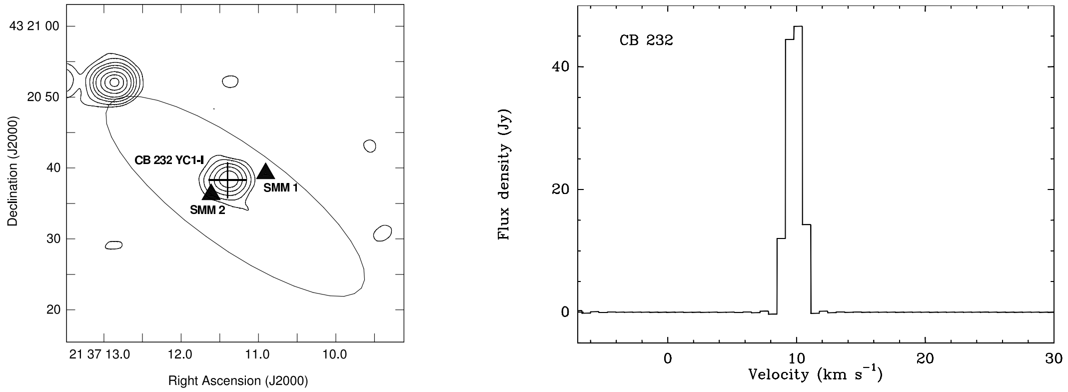

Figure 4.6: (Left panel) Contour map of the near-infrared emission in K-band (positional error $\simeq 0\farcs12$) around IRAS 21352+4307. The ellipse represents the error in the position of the IRAS source. The cross represents the position of the water maser emission, and the triangles mark the position of the submillimeter sources reported by Huard et al. (1999; positional error $\simeq 4''$). (Right panel) Water maser spectrum of CB 232, obtained with the VLA.

4.4 Conclusions

In this chapter we have presented interferometric observations using the VLA, of several sources of water maser emission detected as a follow-up of our single-dish survey performed with the Robledo-70m antenna towards Bok globules. We also presented single-dish observations of several molecular transitions to try to ascertain the nature of the sources that pump water masers in CB 65 and CB 101. The general conclusions we have obtained are the following:

- We have detected water maser emission with the VLA in CB 3, CB 54, CB 101, and CB 232. No detection was observed towards CB 65 or CB 205.
- These water masers are associated with star forming regions showing bipolar molecular outflows, except for CB 101 (IRAS 17503−0833), which we propose is an evolved object, possibly a Mira star, and CB 65 (IRAS 16277−2332), whose nature is unknown.
- All of the Bok globules associated with star formation present multiple stellar systems in different evolutionary stages. Accurate positions of water masers has helped us to get information about their powering sources in the case of CB 3, CB 54, CB 101, and CB 232. We confirm the millimeter source CB 3-mm as the power source in the case of CB 3, and we propose the near-IR source CB 232 YC1-I is the best candidate for pumping the maser emission and probably the outflow observed in CB 232. In the case of CB 54, we propose a new young object (CB 54 YC1-SW), seen as an elongated feature in near-infrared images, as the powering source of the masers and probably of the molecular outflow. In the CB 101 region, the masers are associated with a near-IR point source observed in the 2MASS K-band, which is the possible counterpart of IRAS 17503−0833.
- The maser emission in CB 3 is distributed in the direction of the molecular outflow, and seem to be tracing the inner part of a collimated jet. In the case of CB 54 and CB 232, with our positional accuracy it is not possible to ascertain whether masers are associated with either a jet or a disk.
- The position-velocity distribution of the maser emission in CB 3 shows a wave-like structure, which is consistent with a precessing jet.

4.4.1 Conclusiones

En este capítulo se han presentado observaciones interferométricas con el VLA de diversos glóbulos de Bok con detección de máser de agua, a modo de complemento de la búsqueda realizada en estas regiones con la antena Robledo-70m. También se presentan observaciones de antena única de varias transiciones moleculares, para intentar discernir la naturaleza de las fuentes que provocan la emisión máser en CB 65 y CB 101. Las conclusiones obtenidas son:

- Se ha detectado emisión de máser de agua con el VLA en CB 3, CB 54, CB 101 y CB 232. No se ha observado detección ni en CB 65 ni en CB 205.
- Estos máseres de agua están asociados con regiones de formación estelar que presentan flujos moleculares bipolares, excepto en CB 101 (IRAS 17503−0833), la cual proponemos ser un objeto evolucionado, posiblemente una estrella tipo Mira, y CB 65 (IRAS 16277−2332), cuya naturaleza es desconocida.
- Todos los máseres de agua asociados a formación estelar presentan sistemas estelares múltiples en diferentes fases evolutivas. Las posiciones precisas de los máseres de agua han ayudado a obtener información sobre las fuentes que los producen en el caso de CB 3, CB 54, CB 101 y CB 232. Confirmamos la fuente milimétrica CB 3-mm como la fuente excitadora en el caso de CB 3 y proponemos a la fuente en el infrarrojo cercano CB 232 YC1-I como mejor candidata a fuente inductora de la emisión máser y probablemente del flujo molecular observado en CB 232. En el caso de CB 54, proponemos a un nuevo objeto joven (CB 54 YC1-SW), observado como una estructura alargada en imágenes de infrarrojo cercano, como la fuente de energía de los máseres y probablemente del flujo molecular. En la región de CB 101, los máseres están asociados con una fuente puntual en el infrarrojo cercano observada en la banda K del 2MASS, posible contrapartida de IRAS 17503−0833.
- La emisión máser en CB 3 está distribuida en la dirección del flujo molecular y parece trazar la parte más interna de un jet colimado. En el caso de CB 54 y CB 232, con nuestra resolución espacial no es posible saber si los máseres están asociados a un jet o a un disco.
- La distribución de los máseres de agua de CB 3 en un diagrama de posición-velocidad, muestra una estructura ondulada consistente con un jet en precesión.

Chapter 5

CCS and NH_3 emission associated with low-mass young stellar objects

In this chapter we present a single-dish survey of CCS emission (complemented with ammonia observations) at 1 cm, toward a sample of low- and intermediate-mass young star forming regions known to harbor water maser emission, made with NASA's 70 m antenna at Robledo de Chavela, Spain. This work has a double aim: search for the youngest protostars and find the best candidates for future CCS interferometric observations. We also study the relationship between the presence of CCS and the physical characteristics of the star forming regions of this survey.

5.1 Motivation

The lines of the CCS molecule are a powerful tool for studying the physical conditions and the structure of dark molecular clouds, because they are intense, abundant and not very opaque in these regions. In addition, CCS is very useful for performing dynamical studies, since it is heavier than other high density gas tracers (and therefore, its lines are narrower) and it has no hyperfine structure (Saito et al. 1987; Suzuki et al. 1992).

Moreover, CCS is useful for obtaining information about the age of molecular clouds. Previous single-dish observations show that CCS lines are intense in starless, cold, quiescent cores, while ammonia tends to be abundant in star forming regions (Suzuki et al. 1992). It has been suggested that CCS is present in the first stages of molecular cloud evolution, but it is soon destroyed (on a timescale of $\simeq 10^5$ years, Millar & Herbst 1990; Suzuki et al. 1992) after the formation of a dense core. This destruction process is induced by the core contraction (Suzuki et al. 1992) that initiates star formation. On the other hand, when the molecular cloud evolves, the physical conditions and the chemical evolution in molecular cores favor the formation of other molecules like NH_3 (Suzuki et al. 1992). For this reason the abundance ratio $[NH_3]/[CCS]$ has been considered as an indicator of the evolution of molecular cores. This time-dependent chemistry is responsible for the pronounced spatial anticorrelation observed in the emission from these two species, where ammonia tends to trace the inner regions and the CCS is found to be located outside, surrounding ammonia cores, in a clumpy distribution (Hirahara et al. 1992; Kuiper et al. 1996; Lai et al. 2003).

If this evolutionary trend (CCS more abundant in starless cores and NH_3 in more evolved, active star forming regions) is correct, any chance to use CCS as a tool to study star-formation processes will necessarily happen during the very first stages of the stellar evolution, i.e., Class 0 protostars. Interestingly, in these young protostars some of the key phenomena characteristic of the star formation (infall, disk formation and powerful mass-loss phenomena) are especially prominent and coeval, and have their own kinematical signature, which make kinematical studies of their environment especially interesting. In this early stage of stellar evolution, the presence of water maser emission at 22 GHz is rather common. This emission is considered a good tracer of mass-loss activity in young stellar objects (YSOs) in general (Rodríguez et al. 1980b; De Buizer et al. 2005), and a good indicator of the age of low-mass YSOs, since they tend to be excited preferentially in the Class 0 stage (Furuya et al. 2001).

The critical scales for these star formation processes are of the order of $\simeq 100-1000$ AU in the case of low mass stars ($\leq 1''-10''$ for nearby molecular clouds; Beltrán et al. 2001; Chen et al. 1995; Claussen et al. 1998). In order to study these phenomena with high enough resolution, it is necessary to carry out interferometric observations. This is feasible for strong maser lines, but very difficult for thermal emission (like CCS and ammonia) since it is usually weak and therefore high sensitivity is needed. At wavelengths of ~ 1 cm an instrument like the VLA provides high angular resolution, but at the expense of worse atmospheric phases that blur the emission. Weak sources, in which self-calibration is not possible, would not be detected, or the quality of their maps would be poor. Nevertheless, these kinds of problems have been addressed, in the case of continuum emission, by using the cross-calibration technique. This method involves the simultaneous observation of 1 cm continuum and strong water masers, and the use of the self-calibration solutions of the latter to correct phase and amplitude errors in the weaker continuum (Torrelles et al. 1996, 1997, 1998b). This technique of cross-calibration using water masers has never been applied to spectral lines. The $CCS(2_1-1_0)$ transition at $\sim$22 GHz is probably the best candidate to perform it, since it is only 110 MHz away from the H_2O $(6_{16}-5_{23})$ maser line.

In this chapter we present a sensitive and systematic single-dish survey of CCS emission (complemented with NH_3 observations) at 1 cm wavelength, toward low- and intermediate-mass star forming regions that are known to harbor water maser emission, using the NASA's 70 m antenna at Robledo de Chavela, Spain. One of our main aims is to find the best candidates to make interferometric CCS studies with the VLA, but applying the cross-calibration technique for obtaining high-quality maps. Interferometric maps of CCS, ammonia, and water masers would allow us to study kinematical and physical properties of star forming regions at high resolution. Another purpose of the present survey is the search for the youngest star forming regions, assuming that the presence of water masers and CCS emission are signs of youth in low-mass star-forming regions. Moreover, we present a search for the relation between the CCS emission and the physical characteristics of the star forming regions of the survey.

This Chapter is structured as follows: in section §5.2 we describe our observations and data reduction. In section §5.3 we show the survey results, as well as a short description of the sources detected. We discuss the results in §5.4 and, finally, we summarize our conclusions in §5.5.

5.2 Observations

Observations were carried out in different periods between 2002 April and 2005 March, using the NASA's 70 m antenna (DSS-63) at Robledo de Chavela, Spain. The total telescope time was $\simeq$ 50 hours (without including calibration or pointing checks). We observed the CCS J_N=2_1-1_0 transition (rest frequency = 22344.033 MHz) and the NH_3(1,1) inversion transition (rest frequency = 23694.496 MHz) toward a sample of star forming regions.

The sample surveyed (Table 5.1) consists of 40 low-mass ($L_{\rm bol} < 100$ $L_\odot$) and intermediate-mass ($100 < L_{\rm bol} < 10^4$ $L_\odot$) star-forming regions associated with water maser emission, as a sign of youth and ongoing star formation processes. Most of the sources are low-mass star forming regions, although we have included 12 intermediate-luminosity star forming regions as a control sample, in order to test any possible relation between the CCS emission and the mass of the sources. Observations were centered at positions where water maser emission has been reported in the literature.

Most of the CCS observations were performed in frequency-switching mode. We used the SDS 256-channel digital autocorrelator spectrometer with a bandwidth of 1 MHz, centered at the V_{LSR} of each cloud (see Table 5.1), which provides a velocity resolution of 0.05 km s^{-1}. Seven sources (see Table 5.2) were observed in position-switching mode, with the SPB500 384-channel digital autocorrelator spectrometer with a bandwidth of 2 MHz (velocity resolution of 0.07 km s^{-1}). The system temperature varied from 44 to 135

K, depending on weather conditions and elevation, with a mean system temperature of 76 K.

The ammonia observations were also made in position-switching mode, using SPB500 spectrometer. We used a bandwidth of 16 MHz, centered at the V_{LSR} of each cloud, which provides a velocity resolution of 0.5 km s^{-1}. NGC 2071-North and AFGL 5157 were observed using a bandwidth of 4 MHz, with a velocity resolution of 0.13 km s^{-1}, but the spectra were smoothed to a final resolution of 0.5 km s^{-1}. The system temperature varied from 52 to 99 K, with a mean system temperature of 78 K. The rms pointing accuracy of the data presented here was better than $10''$.

Table 5.1: Observed Sources

Source	Alternative name	Right Ascension[1] (J2000)	Declination[1] (J2000)	V_{LSR}[2] (km s^{-1})	L_{bol}[3] ($L_\odot$)	D[4] (pc)	References[5]
L1287[6]	IRAS 00338+6312	00 36 47.5	+63 29 02	−18.0	1000	850	11,67,42
L1448−IRS3	IRAS 03225+3034	03 25 36.4	+30 45 20	4.5	10	300	12,5,8
L1448C	LDN 1448-mm	03 25 38.7	+30 44 05	4.5	9	300	12,5,8
RNO 15 FIR	IRAS 03245+3002	03 27 39.0	+30 12 59	5.2	16	350	12,63,60
IRAS 2A	IRAS 03258+3104	03 28 55.4	+31 14 35	7.0	43	350	24,41,23
HH 6	IRAS 7	03 29 11.2	+31 18 31	7.0	18	350	33,19,39
B1−IRS	IRAS 03301+3057	03 33 16.3	+31 07 51	6.3	2.8	350	24,36
T TAU−South	IRAS 04190+1924	04 21 59.4	+19 32 06	8.2	10	160	12,46,10
L1534B	IRAS 04361+2547	04 39 13.9	+25 53 21	6.2	3.8	140	12,35,8
L1641−North[6]	IRAS 05338−0624	05 36 18.7	−06 22 09	7.4	120	500	12,61,22
HH 1	IRAS 05339−0647	05 36 19.1	−06 45 01	9.3	50	500	16,57,32
AFGL 5157[6]	IRAS 05345+3157	05 37 47.8	+31 59 24	−18.0	5000	1800	34,48,52
Haro4−255	IRAS 05369−0728	05 39 22.3	−07 26 45	4.8	13	480	12,2,21
L1641−S3	IRAS 05375−0731	05 39 56.0	−07 30 18	5.1	70	450	12,61,53
NGC 2024 FIR 5	Orion B	05 41 44.5	−01 55 43	11.0	$\gtrsim$10	450	24,29,1
HH 212	IRAS 05413−0104	05 43 51.1	−01 03 01	1.7	14	500	12,30,68
B35A	IRAS 05417+0907	05 44 29.8	+09 08 54	11.8	15	460	12,7,6
HH 19−27	NGC 2068 H_2O maser	05 46 31.2	−00 02 35	9.9	1.7	400	3,48,25
NGC 2071[6]	IRAS 05445+0020	05 47 04.8	+00 21 43	9.4	750	500	56,64,31
NGC 2071−North	IRAS 05451+0037	05 47 42.3	+00 38 40	9.0	40	500	12,64,38
IRAS 06291+0421[6]		06 31 48.1	+04 19 31	13.7	1882	1600	9,66,65
NGC 2264 IRS[6]	IRAS 06384+0932	06 41 10.3	+09 29 19	8.7	2300	800	22,64,43
IRAS 06584−0852[6]		07 00 51.5	−08 56 29	40.5	5670	4480	49,66,45
CB 54	IRAS 07020-1618	07 04 21.2	−16 23 15	19.5	55	600	27,13,58
L260	IRAS 16442-0930	16 46 58.6	−09 35 23	3.5	0.97	160	22,28,47
IRAS 18265+0028[6]		18 29 05.8	+00 30 36	5.3	347	440	14,49
Serpens FIRS 1	IRAS 18273+0113	18 29 49.8	+01 15 21	8.0	46	310	12,20,37
LDN 723−mm	IRAS 19156+1906	19 17 53.9	+19 12 25	10.5	3	300	24,26,17

Table 5.1: (continued).

IRAS 20050+2720[6]	IRAS 20050+2720 MMS 1	20 07 06.7	+27 28 53	6.0	260	700	9,4,61
S106 FIR[f]	IRAS 20255+3712	20 27 25.5	+37 22 49	−1.0	<1000	600	24,63,50
L1157-mm	IRAS 20386+6751	20 39 06.5	+68 02 13	2.7	11	440	12,44,18
GF9−2		20 51 30.1	+60 18 39	−2.7	0.3	200	24,59
B361	IRAS 21106+4712	21 12 26.1	+47 24 24	2.7	4.7	350	12,28,6
CB 232	IRAS 21352+4307	21 37 11.3	+43 20 36	12.6	3.9	350	27,13,15
IC 1369N[6]	IRAS 21391+5802	21 40 42.4	+58 16 10	0.2	500	750	9,62,54
L1204A[6]	IRAS 22198+6336	22 21 27.6	+63 51 42	−10.5	367	900	24,63,22
L1204B	IRAS 22199+6322	22 21 33.3	+63 37 21	−10.3	52	900	14,55,22
L1251A	IRAS 22343+7501	22 35 24.3	+75 17 06	−4.0	27	300	12,28,51
L1251B	IRAS 22376+7455	22 38 47.1	+75 11 29	−4.0	14	300	12,51
Cepheus E	IRAS 23011+6126	23 03 13.1	+61 42 26	−10.4	50	730	24,64,40

Notes to Table 5.1

[1] Observed position, coincident with reported water maser position. Units of right ascension are hours, minutes, and seconds. Units of declination are degrees, arcminutes, and arcseconds

[2] Velocity of the cloud with respect to the local standard of rest.

[3] Bolometric luminosity of the source.

[4] Distance to the source.

[5] REFERENCES:(1)André et al. 2000, (2)Anglada et al. 1989, (3)Anglada et al. 1996a, (4)Bachiller et al. 1995, (5)Bachiller et al. 1990b, (6)Beichman et al. 1986, (7)Benson & Myers 1989, (8)Bontemps et al. 1996, (9)Brand et al. 1994, (10)Cabrit & Bertout 1992, (11)Cesaroni et al. 1988, (12)Claussen et al. 1996, (13)Clemens & Barvainis 1988, (14)Codella & Felli 1995, (15)Codella & Muders 1997, (16)Comoretto et al. 1990, (17)Davidson 1987, (18)Davis & Eisloeffel 1995, (19)Edwards & Snell 1983, (20)Eiroa et al. 1992, (21)Evans et al. 1986, (22)Felli et al. 1992, (23)Froebrich 2005, (24)Furuya et al. 2003, (25)Gibb & Little 2000, (26)Goldsmith et al. 1984, (27)Gómez et al. submitted, (28)Goodman et al. 1993, (29)Graf et al. 1993, (30)Harju et al. 1993, (31)Harvey et al. 1979, (32)Harvey et al. 1986, (33)Henkel et al. 1986, (34)Henning et al. 1992, (35)Heyer et al. 1987, (36)Hirano et al. 1997, (37)Hurt & Barsony 1996, (38)Iwata et al. 1988, (39)Jennings et al. 1987, (40)Ladd & Hodapp 1997, (41)Langer et al. 1996, (42)Lorenzetti et al. 2000, (43)Margulis et al. 1989, (44)Mikami et al. 1992, (45)Molinari et al. 2000, (46)Momose et al. 1996, (47)Myers et al. 1987, (48)Pastor et al. 1991, (49)Persi et al. 1994, (50)Richer et al. 1993, (51)Sato et al. 1994, (52)Snell et al. 1988, (53)Stanke et al. 2000, (54)Sugitani et al. 1989, (55)Tafalla et al. 1993, (56)Tofani et al. 1995, (57)Torrelles et al. 1993a, (58)Wang et al. 1995, (59)Wiesemeyer et al. 1999, (60)Wilking et al. 1994b, (61)Wilking et al. 1989a, (62)Wouterloot & Brand 1989, (63)Wouterloot et al. 1993, (64)Wouterloot et al. 1988, (65)Wu et al. 2004, (66)Wu et al. 2001, (67)Yang et al. 1995, (68)Zinnecker et al. 1992

[6] Intermediate-luminosity ($L_{bol} > 100\ L_\odot$) sources.

5.3 Survey results

In Table 5.2 and Table 5.3 we summarize the results of the survey. Out of the 40 star forming regions surveyed in the CCS (2_1-1_0) line, only 6 low-mass sources show emission, and their spectra are shown in Fig 5.1. We have not detected CCS emission towards any of the 12 intermediate-mass objects. On the other hand, we also observed 36 of the sources in the NH_3(1,1) transition, of which 31 show detectable emission. We note that all sources detected in CCS are associated with ammonia emission. In order to compare our results with the work by Suzuki et al. (1992), who surveyed dark cores mostly in Taurus and Ophiucus, we will consider only the low-mass sources in our sample. We have excluded the source L260 from statistical calculations, since its noise level for CCS is significantly higher than that of the other sources. In fact, several of our CCS detections are below the upper limit given for L260 (Table 5.2). With this exclusion, we have a subset of 27 low-mass sources, among which we can strictly define as sources without detectable CCS emission those with $T_{\rm MB} < 0.3$ K or $N_{\rm CCS} < 2.1 \times 10^{12}$ cm^{-3}. Taking from Suzuki et al. (1992) the star forming regions (considering as such those with presence of outflows and/or IRAS sources), the detection rates obtained for CCS is 23% at 22 GHz. Since their detection limit of the CCS column density is similar to ours, we can meaningfully compare it with our detection rate of 22% for CCS. Using Fisher's exact test, we determined that our detection rates for CCS is statistically compatible with that of Suzuki et al. (1992), at a confidence level of 95%. This compatibility is reasonable, since water maser emission (the selection criterion for our survey) is a good tracer of star formation activity (Furuya et al. 2003; Rodríguez et al. 1980b).

Most of the star forming regions we surveyed have detectable ammonia emission, which suggests that ammonia survives well in the protostar phase, as indicated by the presence of water masers. Few of the regions have CCS emission, but all of these also have NH_3. Therefore, there are no regions associated with both H_2O maser and CCS emission, but without NH_3. Bearing in mind that there are many CCS-emitting clouds without any sign of harboring protostars (Benson et al. 1998; Suzuki et al. 1992), these results support the evolutionary sequence of CCS+NH_3+H_2O → NH_3+H_2O. In particular, it supports the idea that the CCS molecule is destroyed before ammonia.

Table 5.2: CCS (2_1-1_0) line parameters [1]

Source	T$_{\rm MB}$ [2] (K)	V$_{\rm LSR}$ [3] (km s^{-1})	Δv [3] (km s^{-1})	$\int$T$_{\rm MB}$dv [4] (K km s^{-1})	N$_{\rm CCS}$ [5] (10^{12} cm^{-2})
L1287	<0.3	....	....	<0.07	<1.9
L1448−IRS3	0.32±0.11	4.68±0.05	0.36±0.11	0.09±0.03	2.4±0.8
L1448C	0.46±0.07	4.65±0.03	0.58±0.07	0.305±0.024	8.1±0.6
RNO 15 FIR	<0.15	....	....	<0.03	<0.8
IRAS 2A	<0.21	....	....	<0.05	<1.3
HH 6	<0.24	....	....	<0.05	<1.3
B1−IRS	0.70±0.13	6.72±0.04	0.89±0.10	0.57±0.05	15.1±1.3
T TAU−South	<0.22	....	....	<0.05	<1.3
L1534B	<0.20	....	....	<0.04	<1.1
L1641−North[6]	<0.20	....	....	<0.05	<1.3
HH 1[6]	<0.24	....	....	<0.06	<1.6
AFGL 5157	<0.3	....	....	<0.07	<1.9
Haro4−255	<0.3	....	....	<0.07	<1.9
L1641−S3	<0.22	....	....	<0.05	<1.3
NGC 2024 FIR 5	<0.20	....	....	<0.04	<1.1
HH 212	<0.3	....	....	<0.07	<1.9
B35A	<0.23	....	....	<0.05	<1.3
HH 19−27	<0.3	....	....	<0.07	<1.9
NGC 2071[6]	<0.24	....	....	<0.06	<1.6
NGC 2071−North	0.41±0.12	8.54±0.04	0.38±0.08	0.14±0.03	3.7±0.8
IRAS 06291+0421	<0.3	....	....	<0.07	<1.9
NGC 2264 IRS	<0.20	....	....	<0.04	<1.1
IRAS 06584−0852	<0.23	....	....	<0.05	<1.3
CB 54	<0.22	....	....	<0.05	<1.3
L260	<0.5	....	....	<0.11	<3
IRAS 18265+0028	<0.20	....	....	<0.04	<1.1
Serpens FIRS 1	<0.20	....	....	<0.04	<1.1
LDN 723−mm	<0.3	....	....	<0.07	<1.9
IRAS 20050+2720	<0.3	....	....	<0.07	<1.9
S106 FIR	<0.15	....	....	<0.03	<0.8
L1157−mm[6]	<0.18	....	....	<0.05	<1.3
GF9−2[6]	0.90±0.16	−2.415±0.022	0.24±0.05	0.25±0.05	6.6±1.3
B361	<0.16	....	....	<0.04	<1.1
CB 232	<0.24	....	....	<0.05	<1.3
IC 1369N	<0.3	....	....	<0.07	<1.9
L1204A	<0.24	....	....	<0.05	<1.3
L1204B	<0.3	....	....	<0.07	<1.9
L1251A[6]	0.59±0.11	−4.91±0.04	0.47±0.09	0.28±0.04	7.4±1.1
L1251B[6]	<0.3	....	....	<0.08	<2.1
Cepheus E	<0.3	....	....	<0.07	<1.9

Table 5.3: NH$_3$(1,1) line parameters ^{1}

Source	$T_{MB}{}^2$ (K)	$V_{LSR}{}^3$ (km s^{-1})	Δv^3 (km s^{-1})	$\int T_{MB} dv^4$ (K km s^{-1})	$N_{NH3}{}^5$ (10^{15} cm^{-2})
L1287	3.9±0.3	-17.73±0.12	2.2±0.3	9.3±0.5	2.76±0.15
L1448−IRS3	5.7±0.3	4.22±0.07	1.17±0.16	7.7±0.4	1.52±0.08
L1448C	4.97±0.24	4.60±0.03	1.28±0.14	6.8±0.3	1.00±0.04
RNO 15 FIR	2.73±0.21	4.50±0.06	1.00±0.14	3.2±0.3	1.33±0.12
IRAS 2A	1.70±0.13	7.27±0.09	1.69±0.19	3.15±0.17	5.0±0.3
HH 6	1.8±0.3	8.27±0.10	1.1±0.3	2.3±0.5	2.4±0.5
B1−IRS	4.04±0.24	5.95±0.06	1.06±0.14	5.2±0.4	1.79±0.14
T TAU−South	<0.3	....	....	<0.3	<0.09
L1534B	<0.5	....	....	<0.4	<0.12
L1641−North	3.68±0.21	7.11±0.04	1.27±0.18	5.2±0.3	1.25±0.07
HH 1	0.83±0.22	9.02±0.07	2.1±0.5	1.8±0.3	27±5
AFGL 5157^6	<0.3	....	....	<0.3	<0.09
Haro4−255	1.7±0.3	4.44±0.10	1.07±0.24	2.0±0.4	3.2±0.7
L1641−S3	2.6±0.4	5.28±0.12	1.5±0.3	4.0±0.5	3.4±0.4
NGC 2024 FIR 5	1.94±0.22	11.12±0.13	2.5±0.3	4.8±0.4	1.17±0.10
HH 212	1.16±0.21	1.65±0.06	0.8±0.3	1.4±0.3	11.2±2.4
B35A	2.25±0.21	11.88±0.06	1.04±0.17	2.7±0.3	2.05±0.22
HH 19−27	1.57±0.13	10.24±0.06	1.12±0.16	2.34±0.22	4.4±0.4
NGC 2071	3.12±0.24	8.94±0.07	1.44±0.18	5.0±0.4	0.41±0.03
NGC 2071−North^6	1.02±0.07	8.37±0.11	1.03±0.26	0.94±0.13	4.5±0.6
IRAS 06291+0421	<0.3	....	....	<0.3	<0.09
NGC 2264 IRS	5.09±0.23	8.22±0.12	2.7±0.3	13.2±0.4	1.42±0.04
IRAS 06584−0852	<0.3	....	....	<0.3	<0.09
CB 54	0.98±0.13	19.55±0.09	1.3±0.3	1.40±0.21	0.140±0.021
LDN 723−mm	1.63±0.18	10.89±0.06	0.88±0.15	1.63±0.23	0.67±0.09
IRAS 20050+2720	2.27±0.11	5.88±0.11	2.5±0.3	6.19±0.20	3.80±0.12
S106 FIR	0.78±0.19	-1.57±0.16	1.4±0.4	1.0±0.3	0.56±0.18
L1157−mm	2.24±0.17	2.64±0.06	0.84±0.12	2.00±0.21	1.12±0.12
GF9−2	3.32±0.18	-2.49±0.06	0.80±0.11	2.71±0.22	1.36±0.11
B361	2.3±0.3	2.76±0.10	1.5±0.3	3.5±0.4	0.28±0.03
CB 232	1.00±0.11	12.39±0.07	0.99±0.15	1.10±0.15	2.7±0.4
IC 1369N	1.79±0.21	0.50±0.11	2.1±0.3	4.2±0.4	1.79±0.17
L1204A	1.78±0.19	-11.00±0.09	1.44±0.19	2.9±0.3	4.4±0.5
L1204B	1.49±0.22	-10.56±0.10	1.39±0.22	2.2±0.3	2.9±0.4
L1251A	0.75±0.13	-5.33±0.12	1.4±0.3	1.11±0.18	6.5±1.1
Cepheus E	1.03±0.21	-11.05±0.11	1.01±0.24	1.0±0.3	2.2±0.7

Notes to Table 5.2

[1] Uncertainties in this table are 2σ for detections. For nondetections, upper limits are 3σ.

[2] Main beam brightness temperature.

[3] Central $V_{\rm LSR}$ and line width obtained from a Gaussian fit to the CCS line. Uncertainties represent the error in the Gaussian fit.

[4] Integrated intensity. Upper limits were calculated assuming a width equal to the mean value of velocity width for detections ($\Delta v \simeq 0.5$ km s^{-1}).

[5] CCS column density obtained from $N_{\rm mol} = \frac{8\pi\nu^3}{c^3 g_j A_{ji}} \frac{Q(T_{\rm rot}) \int T_{MB} dv}{[B_\nu(T_{\rm ex}) - B_\nu(T_{\rm bg})]} \frac{\exp(E_j/kT_{\rm rot})}{\exp(h\nu/kT_{\rm ex})-1}$ (optically thin approximation), ν is the frequency of the transition, Q is the partition function, E_j is the energy of the upper state (1.61 K; Wolkovitch et al. 1997), $T_{\rm rot}$ is the rotational temperature, g_j is the statistical weight of the upper rotational level. A_{ji} is the Einstein coefficient for the CCS(2_1-1_0) transition (4.33×10^{-7}s^{-1};Wolkovitch et al. 1997), $B(T)$ is the intensity of black-body radiation at temperature T, and $T_{\rm ex}$ is the excitation temperature. Since we only observed one CCS transition, we could not obtain a reliable estimate of $T_{\rm exc}$ and $T_{\rm rot}$; therefore, we assumed $T_{\rm rot}$=$T_{\rm exc}$= 5 K, the mean value assigned by Suzuki et al. (1992) for a large sample of young sources. We assumed these values even for the intermediate-mass sources, since, for instance, an increase of 4 K in both $T_{\rm exc}$ and $T_{\rm rot}$ causes a change in the CCS column density of only $\simeq 45\%$.

[6] Sources observed using the 384 channel spectrometer, with a velocity resolution of 0.07 km s^{-1}. These sources were smoothed to a final velocity resolution of $\simeq$ 0.14 km s^{-1}. The rest of CCS targets (observed with the 256 channel spectrometer with a velocity resolution of 0.05 km s^{-1}) were smoothed to a resolution of 0.10 km s^{-1}.

Notes to Table 5.3

[1] Uncertainties in this table are 2σ for detections. For nondetections, upper limits are 3σ.

[2] Main beam brightness temperature of the main hyperfine component.

[3] Central $V_{\rm LSR}$ and line width obtained from a Gaussian fit to the main line of the NH_3(1,1) transition. Uncertainties represent the error in the Gaussian fit.

[4] Integrated intensity of the main hyperfine component. Upper limits were calculated assuming a width equal to the mean value of velocity width for detections ($\Delta v \simeq 1.4$ km s^{-1}).

[5] Column density obtained from $N_{\rm mol} = \frac{16[1+\exp(h\nu/kT_{\rm ex})]\pi\nu^3}{c^3 g_j A_{ji}} \frac{Q(T_{\rm rot}) \int T_{MB} dv}{[B_\nu(T_{\rm ex}) - B_\nu(T_{\rm bg})]} \frac{\exp(E_j/kT_{\rm rot})}{\exp(h\nu/kT_{ex})-1}$ (optically thin approximation). E_j is the energy of the $J, K = 1, 1$ rotational level (23.4 K; Ho & Townes 1983), g_j is the statistical weight of the upper sublevel involved in the inversion transition, A_{ji} is the Einstein coefficient of the NH_3(1,1) transition (1.67×10^{-7}s^{-1}; Ho & Townes 1983). We calculated the optical depth and the excitation temperature from the relationship between hyperfine components for each source. When no satellite hyperfine line was detected, we adopted $T_{\rm ex} = 7.8$ K, the mean $T_{\rm ex}$ of all the sources. We assumed $T_{\rm rot} = T_{\rm ex}$.

[6] Sources observed with a velocity resolution of 0.13 km s^{-1}. These sources were smoothed to a final velocity resolution of 0.5 km s^{-1}. The rest of the ammonia targets were observed with a velocity resolution of 0.5 km s^{-1}.

5.3.1 Notes on the sources detected in CCS

5.3.1.1 L1448 Region

L1448 is a dense globule located in Perseus. This cloud contains numerous signatures of mass-loss activity (Bachiller et al. 1990b, 1995; Curiel et al. 1999) and it is an interesting environment for studying the possibility that outflows from YSOs may induce new star formation in other regions of the parental cloud. Single-dish ammonia observations reveal two peaks located at the center and at the north-east of the cloud, associated with L1448C and L1448-IRS3 respectively (Anglada et al. 1989; Bachiller et al. 1990b).

L1448C (Curiel et al. 1990) is catalogued as a Class 0 source (André et al. 1993; Barsony 1994) that drives one of the most energetic and highly collimated molecular outflows ever seen in a low-mass star forming region (Bachiller et al. 1990b). This outflow reveals a strong interaction with the northern material of the cloud, associated with L1448-IRS3, the brightest far-infrared source of the region.

L1448-IRS3 is known to consist of three individual Class 0 sources: a close proto-binary system [L1448N(A) and L1448N(B)], in which each component powers its own outflow, and a third source, L1448 NW (Curiel et al. 1990; Terebey & Padgett 1997; Barsony et al. 1998). Barsony et al. (1998) suggested that the outflow powered by L1448C was responsible for the formation of the proto-binary system, whose outflows may, in their turn, have produced the NW source.

We detected CCS emission towards both L1448-IRS3 and L1448C. This is the first detection of emission from this molecule reported for either of them.

5.3.1.2 B1-IRS

B1-IRS (IRAS 03301+3057) is a far-infrared source located in the Perseus OB2 complex (Bachiller et al. 1990c). This source is classified as a Class 0 source (Hirano et al. 1997), and it is associated with a CO molecular outflow that displays a strong blueshifted emission (Bachiller et al. 1990c; Hirano et al. 1997).

CCS emission at 22 GHz was detected for the first time in this region by Suzuki et al. (1992). Later, Lai & Crutcher (2000) observed CCS at 33.8 GHz with the BIMA interferometer, and their maps showed a clumpy distribution surrounding B1-IRS.

5.3.1.3 NGC2071-North

NGC2071 North is located at $20'$ north of the reflection nebula NGC2071 (Fukui et al. 1986). This region hosts a CO molecular outflow that lies near the source IRAS 05451+0037. Maps of the outflow at different angular resolution display very different geometries: a bent-U shaped outflow at $17''$ resolution, which suggests strong interaction with the ambient material (Iwata et al. 1988), and overlapping blue- and redshifted emission at $\gtrsim 50''$ resolution (Iwata et al. 1988; Goldsmith et al. 1992), which is compatible with a bipolar outflow whose axis lies very near the plane of the sky. IRAS 05451+0037 is coincident with a CS and a NH_3 peak (Goldsmith et al. 1992), and it shows the far-infrared spectrum of a T Tauri star (Iwata et al. 1988). This source was suggested to be the central engine of the molecular outflow (Iwata et al. 1988), although this is somewhat uncertain due to the complicated geometry of the outflow.

Suzuki et al. (1992) detected CCS at 45 GHz toward this source. In our survey, we report CCS emission at 22 GHz for the first time.

5.3.1.4 GF9-2

This source is located in the filamentary quiescent dark cloud GF-9 (LDN 1082), without any associated IRAS point sources or radio continuum emission (Ciardi et al. 1998; Wiesemeyer et al. 1999). It was catalogued as a transitional object between pre-stellar and proto-stellar Class 0 phase (Wiesemeyer et al. 1999), which would turn GF-9 to be the youngest source in our survey. Furuya et al. (2003) detected the presence of weak redshifted CO wing emission, and a weak H_2O maser (0.3 Jy). These authors pointed out that GF9-2 was the lowest-luminosity (0.3 $L_\odot$) object known to harbor H_2O masers. We have detected both CCS and ammonia emission lines toward this source for the first time.

5.3.1.5 L1251A

L1251A (IRAS 22343+7501) is located at the northern part of L1251, a small elongated cloud located in Cepheus. This source has been classified as a Class I object (Mardones et al. 1997; Nikolić et al. 2003) and appears to be powering the extended CO outflow seen in this region (Sato & Fukui 1989), as well as an optical jet (Balazs et al. 1992). Several radio continuum sources were discovered near IRAS 22343+7501 (Meehan et al. 1998). Recent VLA centimeter observations, reveal that this IRAS source may consist of two protostellar objects, with spectral indices consistent with thermal emission, and either of them could be the driving source of the CO outflow (Beltrán et al. 2001). We report CCS emission toward this source for the first time.

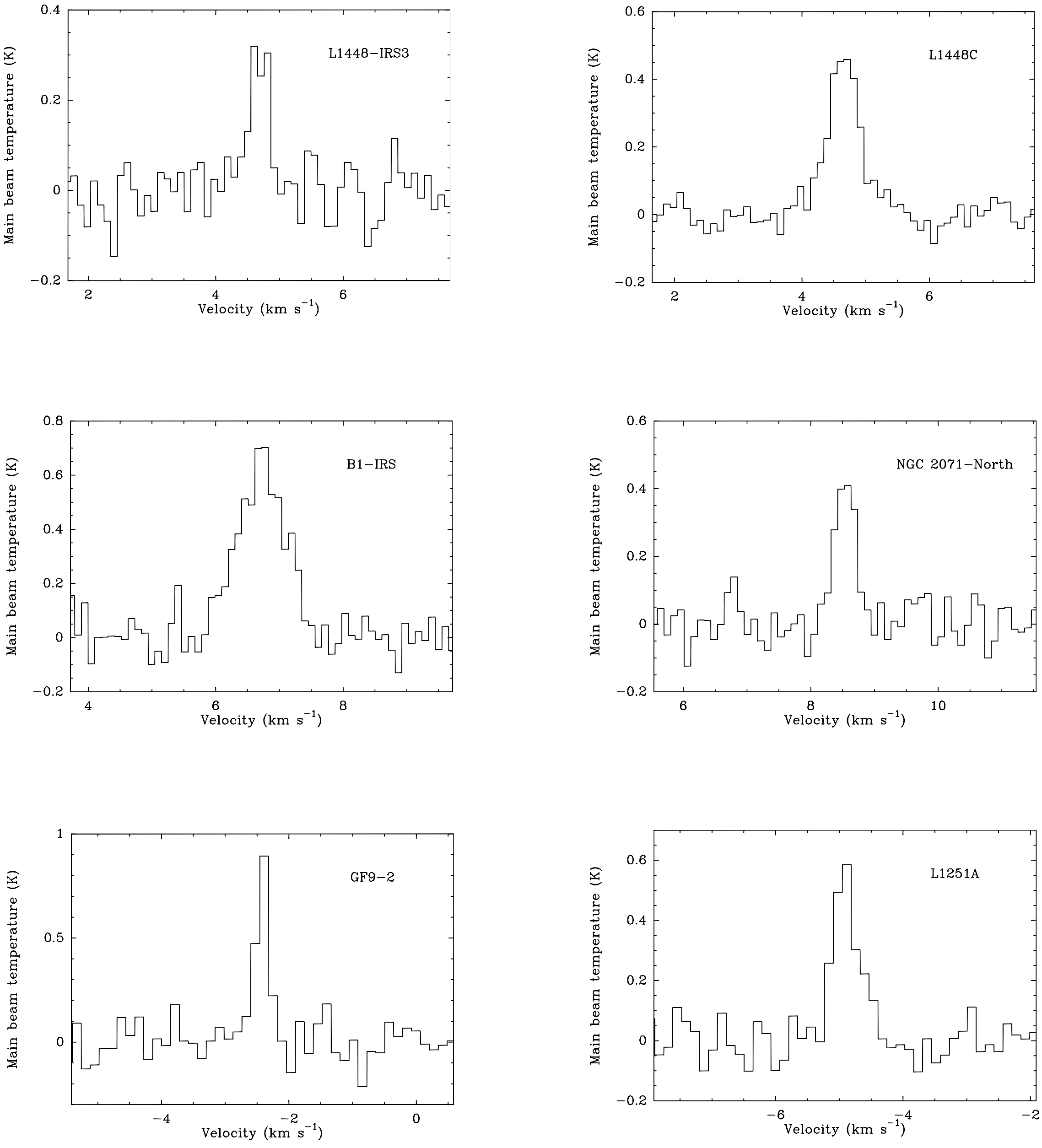

Figure 5.1: Spectra of CCS(2_1-1_0) transition detected with the Robledo-70m antenna.

5.4 Discussion

5.4.1 The lifetime of CCS in star forming regions

The detection rate obtained in our survey for CCS (22% of the low-mass sources show CCS emission) is similar to the results of Suzuki et al. (1992) in star forming regions (23% detections). The low rate of detection of CCS emission in star forming regions seems to indicate that this molecule is soon destroyed after the processes associated with star formation begin. This result, together with the presence of water maser emission, allows us to roughly estimate the lifetime of CCS in low-mass star forming regions. The association of a low-mass central source with water maser emission typically lasts for one third of the duration of the embedded state (Wilking et al. 1994a; Claussen et al. 1996). This embedded phase is estimated to last for $\simeq (1-4) \times 10^5$ yr (Wilking et al. 1989b; André & Montmerle 1994; Chen et al. 1995). Therefore, the water maser emission lasts for $\simeq (0.3-1.3) \times 10^5$ yr in low-mass star forming objects. If we assume that the regions of our sample are homogeneously distributed in age along the $\simeq (0.3-1.3) \times 10^5$ yr in which water maser emission is observed, our detection rate of 6 out of 27, would indicate that the CCS emission lasts for $\simeq (0.7-3) \times 10^4$ yr after the beginning of the embedded phase.

5.4.2 Evolutionary stage of the SFRs associated with CCS emission

As we mentioned in the introduction, since the CCS molecule has been considered in previous works as a youth tracer of molecular cores, the star forming regions associated with this emission should contain some of the youngest YSOs. This evolutionary trend for the CCS chemistry must be valid as a general, qualitative trend when we compare large groups of molecular cores, although it may not stand in a quantitative way in the comparison of particular sources. In particular, the results of our survey do not totally agree with the first statement, since four of the sources that host CCS emission are catalogued as young Class 0 sources (GF9-2, L1448-IRS3, L1448C, B1-IRS), but L1251A and NGC2071-North are catalogued as more evolved YSOs. There are two possible explanations for these results: either the classification of the evolutionary stage of L1251A and NGC2071-North should be revised, or the particular physical conditions and processes of each source affect the production and destruction of CCS.

NGC2071-North (IRAS 05451+0037) shows a far-infrared spectrum of a T Tauri star (Iwata et al. 1988). Nevertheless, there is no optical counterpart in the POSSM prints, and no near-infrared emission in the 2MASS catalog at the position of IRAS 05451+0037, which suggests a more embedded nature of this source. The complicated geometry of the molecular outflow of the region (see subsection 5.3.1), makes it difficult to reliably know whether IRAS 05451+0037 is the real engine of the outflow. In order to clarify the real geometry of the outflow, the power source, and its evolutionary stage, more accurate and extended observations of CO, together with submillimeter observations, are needed. In particular, the study of possible peaks at submillimeter frequencies (typical of Class 0 objects) and the measurement of the relation L_{smm}/L_{bol} (André et al. 1993), are especially important to elucidate the possible existence of other embedded sources in the region, and to determine their evolutionary stage.

In the case of L1251A (IRAS 22343+7501), it is associated with a nebulosity visible at J, H, and K 2MASS-bands, and it is visible in POSSM plates. This source has been classified as a Class I YSO (Mardones et al. 1997; Nikolić et al. 2003). Nevertheless, Meehan et al. (1998) discovered several radio continuum sources in the region near the IRAS source, candidates to YSOs, and the CCS emission could be associated with any of these embedded sources. In this case, higher resolution observations of CCS emission would be useful to study its association with those sources.

The second possible explanation would be to accept that, in some cases, CCS could be associated with sources in a more evolved stage. This could be the case if CCS emission depends not only on age, but also on the particular phenomena related to the star formation of each cloud. This possibility will be further pursued in Chapter 6, where a high resolution CCS study of B1-IRS is presented. As we will see there, the CCS emission could be enhanced in the region where the outflow interacts with the surrounding cloud medium. The outflow interaction with fresh low-density gaseous material that exists around dense cores, could squeeze this low-density gas to the higher densities needed ($\simeq 10^5$ cm^{-3}) to form this molecule and excite its line emission. This phenomenon could explain the detection of this molecule in stages more evolved than Class 0 sources. The possible dependence of CCS on parameters different from age is discussed in next section.

5.4.3 Search for dependencies of CCS emission on source and cloud parameters

The abundance ratio [NH_3]/[CCS] was proposed by Suzuki et al. (1992) to be a good indicator of cloud evolution. This conclusion was based on theoretical pseudo-time-dependent calculations of the fractional abundance of CCS and NH_3, under conditions of constant H_2 density and constant gas kinetic temperature. The variation of the fractional abundances in both molecules was explained as an effect of the evolution of the molecular clouds, with CCS more abundant in starless cores, and ammonia more abundant in regions with signs of star formation activity. Moreover, Suzuki et al. (1992) pointed out that this chemical evolutionary track was insensitive to the density of H_2.

Nevertheless, when the column densities of both molecules (N_{NH_3} and N_{CCS}) are compared among different clouds, the proposed anticorrelation disappears (Suzuki et al. 1992). In our case, if we order the sources in which we detected CCS by their ratio of derived column densities N_{NH_3}/N_{CCS}, they are, from lowest to highest ratio: B1−IRS, L1448C, GF9−2, L1448−IRS3, L1251A, and NGC2071−North. If the N_{NH_3}/N_{CCS} ratio were dependent on the age of cloud cores only, B1−IRS would then be the youngest source, and NGC2071−North the oldest one, but our ordering does not exactly conform to an evolutionary scheme. L1251A and NGC 2071-North have indeed been proposed to be the more evolved of these six sources, but most of the CCS non-detections seem to be younger than these two objects. On the other hand, we would expect GF9−2 to show the lowest N_{NH_3}/N_{CCS} ratio, given its classification as a transitional object between pre-stellar and protostellar phase (Wiesemeyer et al. 1999). These discrepancies are understandable if, as Suzuki et al. (1992) suggest, the evolutionary NH_3−CCS anticorrelation fades out when using data from different sources.

The absence of anticorrelation among different clouds was explained by Suzuki et al. (1992) as the effect of the overlapping of individual evolutionary tracks for the chemistry of clouds with different H_2 column densities. For this reason, the relationship between column densities of CCS and ammonia may not be a good quantitative indicator of cloud evolution even assuming a common start time. This statement has also been suggested by Benson et al. (1998), who did not find statistically significant differences between star forming regions and starless cores in their CCS column density.

Furthermore, even the abundance of CCS alone has been questioned as a good quantitative tracer of cloud evolution. Lai & Crutcher (2000) suggested that the abundance of CCS is not likely to trace the age of contracting cores very sensitively. Moreover, in Chapter 6 we propose that CCS abundance could be enhanced through interaction with a molecular outflow, which suggests that the local conditions and processes within each cloud could also influence the CCS emission. Being evident that CCS emission does not depend on the age of the clouds only, we have searched for other possible dependences on different parameters. To do this, we have compiled from the literature several parameters of the observed sources (luminosity, radio continuum and water maser flux densities; see Tables 5.1 and 5.4) and of their associated molecular outflows (degree of collimation, mass, dynamical age, mechanical luminosity, kinetic energy, momentum, and momentum rate; see Table 5.4). For consistency, we obtained the outflow parameters from single-dish observations of the CO(2-1) line, when available. Otherwise, we made use of interferometric and/or data from other CO transitions.

To check whether any of these parameters of sources and outflows is related in any way with the presence of detectable CCS emission, we have tried to determine whether the parameters show different distributions in the groups of sources with and without CCS emission. The application of a Kolmogorov-Smirnov test did not find any significant difference in distribution of the source or outflow parameters.

However, when we apply the same test to the characteristics of the ammonia emission we measured, we find that the distribution of the peak ammonia intensity significantly depends on CCS detectability. Interestingly, we found no significant difference in the distribution of integrated intensity (column density) of ammonia among sources with and without CCS. In a more quantitative way, the mean peak intensity of NH_3 in the group of sources detected in CCS is 3.3 K, while that in the group of undetected sources is 2.1 K. We found that these two means are significantly different, using a T-test (and first applying a Lilliefors test to check that the involved variables follow a normal distribution, which is a prerequisite for the use of the T-test).

We have to be cautious in interpreting this result that sources with detectable CCS emission show significantly brighter NH_3 emission. We have assumed in our calculations that the filling factor of both emissions has a value of one, which is likely not to be true, at least in the case of CCS, since interferometric maps in several regions show its emission to be significantly clumpy (Velusamy et al. 1995; Lai & Crutcher 2000). Therefore, the trend we have found could be just a distance effect since, if the molecular emission does not fill the Robledo beam, sources closer to us would tend to be brighter in both CCS and NH_3. However, we think that the observed trend of higher peak NH_3 intensity in sources with CCS is due to intrinsic characteristics of the sources, rather than to a filling factor/distance effect. The most important argument is that, if it were due to a distance bias, we would expect exactly the same trend for the NH_3 integrated intensity but, as mentioned above, we saw no significant difference for this quantity between sources with and without detectable CCS emission. On the other hand, it is not obvious that the subset of low-mass sources with CCS emission are significantly closer to us than those without emission (see Table 5.1).

A possible effect of different filling factors could be to hide real correlations between source and cloud parameters and those of the molecular line emission. However, we do not think it likely that it is showing a spurious correlation in this case. In any case, the impact of source distance on filling factors is probably not very strong, if the whole extent of the molecular emission is larger than the telescope beam. If this is the case, the filling factor of a clumpy distribution, albeit lower than 1, would not change much with distance if clumps were more or less uniformly distributed within the total spatial extent of the emission. In the case of B1$-$IRS (see Chapter 6), CCS and NH_3 VLA maps show emission $\simeq 3$ times more extended than the Robledo beam ($\simeq 40''$). Ammonia maps of the sources sampled here are also typically larger than this beam (Jijina et al. 1999). The lack of CCS maps in the star forming regions in which we detected this emission makes the quantification of their filling factor difficult.

The fact that we find differences in peak intensity, but not in integrated intensity can be explained if the significant decrease of NH_3 peak intensity between sources with and without detectable CCS emission is somewhat compensated by a corresponding increase in the NH_3 line width, resulting in small differences in integrated intensities. This could be interpreted in evolutionary terms, since mass-loss phenomena related to active star forming processes would increase the turbulence of the surrounding interstellar medium, thus broadening the line width as these processes progress. Therefore, younger regions would tend to show detectable CCS emission and narrower NH_3 lines. However, with our data we cannot confirm such a trend for ammonia linewidths. A Kolmogorov-Smirnov test did not find any significant difference in those linewidths between sources with and without detected CCS. It may still be possible that there is a difference, too small to be detected by the Kolmogorov-Smirnov test, but enough to blur the differences in integrated intensity between sources with or without CCS.

It is also of interest to consider the different widths of the CCS and NH_3 lines for the 6 sources detected in the former (see Tables 5.2 and 5.3). Ammonia thermal linewidths are a factor of $\simeq 1.8$ intrinsically broader than those of CCS, due to the different masses of these molecules, but this thermal broadening alone cannot explain the observed differences. In the most extreme cases, L1448−IRS3 and GF9−2, the NH_3 line is more than 3 times broader than the CCS one. This is consistent with both lines tracing different regions of gas, with different kinematics. The narrower CCS lines would trace more quiescent gas, with less turbulence or velocity gradients. B1-IRS is the source in which both linewidths are more similar, but, as we will see in Chapter 6, the CCS-emitting gas shows in this source evidence of interaction with the molecular outflow, with clear velocity gradients, which makes CCS lines wider. Apart from B1-IRS, the source with the most similar linewidths is L1448C, a source with an energetic molecular outflow. This could suggest that the gas traced by CCS in this region may also be significantly interacting with the molecular outflow. In this context, the source GF9-2 would be the youngest source, in agreement with the transitional prestellar-protostellar classification made by Wiesemeyer et al. (1999).

We point out that these results must be considered carefully, since they are based on a small sample of regions showing CCS emission. The lack of statistically significant results for the source and outflow parameters indicates that CCS emission could be sensitive to the local temperature and density conditions of each cloud, or to filling factor/distance effects. Moreover, we must take into account that the outflow and source parameters were obtained from different instruments, and that on the other hand, the number of CCS detections is small, which would mask possible correlations. We obviously need to widen this study to include more star forming regions associated with CCS emission. Moreover, obtaining a homogeneous set of observations of outflows and source parameters (obtained with the same telescope for all sources) would be useful for improving our statistical study. While such studies will require a large amount of telescope time, it is not possible to circumvent the fact that gas and dust in SFRs have very low surface brightness.

Table 5.4: Parameters of outflows and sources

Source	R_c [1]	M_{out} [2] ($M_\odot$)	t^3 (10^4 yr)	L_{CO} [4] ($L_\odot$)	P^5 ($M_\odot$km s^{-1})	F^6 (10^{-4})	E_{kin} [7] (10^{38}J)	S_{6cm} [8] (mJy)	$S_{3.6cm}$ [9] (mJy)	S_{H_2O} [10] (Jy)	References[11]
L1287	2.00	2.5	11.0	0.06	13.20	1.2	0.79	<0.3	0.35	26.6	87,78,58,80,33
L1448−IRS3	2.00	0.013	0.26	0.32	0.3	1.2	0.1	0.92	1.19	729	6,12,70,23,84,3
L1448C	5.40	0.059	0.36	1.3	1.6	4.5	0.56	0.062-0.17	0.23	≃120	6,12,70,23,14,84,17
RNO 15 FIR	....	0.027	3.1	0.0029	0.124	0.04	0.013	<0.24	<0.12	202.4	27,57,84,100
IRAS 2A	....	0.0287	0.9	0.0157	0.1650	0.24	0.0129	0.06	0.25	10.5	49,75,79,33
HH 6	....	0.038	0.57	0.0162	0.173	0.31	0.0105	0.48	0.83	70	49,47,75,46,41
B1−IRS	....	0.0007	∼0.1	0.016	0.01	∼0.1	0.0018	....	....	20	7,42,33
T TAU−South	1.00	0.44	0.98	0.17	1.7	1.7	0.2	4.7	4.8	25	14,85,48
L1534B	2.30	0.008	0.6	0.001	0.024	0.04	0.0007	0.23	0.14	444.2	92,54,93,103,100
L1641-North	2.00	1.6	1.4	0.15	9.3	6.6	0.57	0.48	0.6	66	102,32,4,19
HH 1	5.20	0.0011	0.1	0.17	0.0458	0.5	0.01994	0.55	0.53	5.3	39,22,76,18,33
AFGL 5157	2.60	7.6	19	0.09	37.1	2	2	1.0	0.80	115	88,87,62,15,68
Haro4−255	2.10	0.72	5.0	0.12	....	....	....	<0.32	0.43	15	56,31,4,19
L1641−S3	2.00	0.38	0.99	1.1	7.0	7	1.3	1.23	0.80	8.9	99,64,65,46,33
NGC 2024 FIR 5	15	1.6	1.4	2.0	20.00	14	3.4	....	0.11	26.6	73,72,16,77,33
HH 212	7.00	0.2	....	....	....	....	....	....	0.04	300	53,34,19
B35A	2.30	0.86	18.0	0.0029	2.0	0.11	0.064	0.2	....	62	67,9,93,19
HH 19−27	....	2.1	20.0	0.021	6.90	0.35	0.5	....	....	40	29,35,69,40
NGC 2071	3.70	9.7	1.6	4.0	81.4	51.0	8.0	7.9	12.33	6521	89,38,86,94,59,30
NGC 2071−North	2.30	5.0	17	0.2	45	2.6	3	....	....	2.5	45,33
IRAS 06291+0421	1.20	13.0	7.3	0.78	103.0	17.0	7.0	....	....	12.9	102,100
NGC 2264 IRS	1.00	7.20	1.1	25.0	150.0	....	....	1.4	0.62	44.18	55,56,71,98,94
IRAS 06584−0852	....	....	....	....	....	....	....	<0.45	....	14.4	60,61,68
CB 54	5.00	0.75	2.8	0.077	4.4	1.6	0.26	0.2	0.2	49.3	104,96,63,105,Table 3.2
L260	....	....	....	....	....	0.003	....	....	....	199.5	66,12,37
IRAS 18265+0028	....	....	....	....	....	....	....	....	....	60	68,13
Serpens FIRS 1	....	1.8	3	0.6	9	3	2.17	2.7	2.8	54	28,44,24,33
LDN 723−mm	4.10	0.5	3	0.1	5.0	1.6	0.53	0.28	0.36	75.1	36,25,2,84,33
IRAS 20050+2720	....	1.7	4.5	16.0	25.4	50.0	7.65	....	1.4	37.7	98,5,18,33
S106 FIR	....	....	....	....	....	....	....	4.8	14.9	20.7	74,8,50,33
L1157−mm	....	0.18	2.1	0.03	1.1	0.5	0.076	0.15	0.18	19.7	26,95,57,84

Table 5.4: (continued).

Source	R_c[1]	M_{out}[2] ($M_\odot$)	t[3] (10^4 yr)	L_{CO}[4] ($L_\odot$)	P[5] ($M_\odot$km s^{-1})	F[6] (10^{-4})	E_{kin}[7] (10^{38}J)	S_{6cm}[8] (mJy)	$S_{3.6cm}$[9] (mJy)	S_{H_2O}[10] (Jy)	References[11]
GF9−2	....	....	....	....	....	....	....	....	<0.1	0.3	33,97
B361	....	>0.025	2.4	>0.00043	>0.055	>0.024	>0.0013	<0.09	<0.06	14	9,101,57,19
CB 232	2.80	0.44	3.4	0.026	2.2	0.7	0.11	....	....	46.6	104,21,43,Table 4.2
IC 1369N	2.90	0.3	3.0	0.02	1.2	0.4	0.05	<0.5	0.27	139.4	91,10,98,13
L1204A	....	0.5	....	....	3.2	....	0.2	<0.45	<0.2	262.7	102,61,94,46,100
L1204B	....	....	....	....	....	....	....	....	....	22.2	30,13
L1251A	1.60	1.95	13.6	0.042	11.7	0.86	0.69	0.22	0.24	22	81,11,19
L1251B	....	0.116	2.3	0.039	1.14	0.50	0.111	0.84	1.34	72.13	81,4,103,33
Cepheus E	3.80	0.21	4.0	....	1.74	....	....	....	....	14.6	51,18,33

Notes to Table 5.4

[1] Collimation factor of the molecular outflow (see e.g., Wu et al. 2004 and references therein for a definition of this and the rest of outflow parameters).

[2] Mass of the outflow.

[3] Dynamical time of the outflow.

[4] Mechanical luminosity of the outflow.

[5] Momentum of the outflow.

[6] Driving force or momentum rate of the outflow, in $M_\odot$ km s^{-1}year^{-1}.

[7] Kinetic energy of the outflow.

[8] Radio continuum flux density at 6 cm.

[9] Radio continuum flux density at 3.6 cm.

[10] Maximum water maser flux density reported in the literature.

[11] REFERENCES:

(1) Anglada & Rodríguez 2002; (2) Anglada et al. 1996b; (3) Anglada et al. 1989; (4) Anglada et al. 1998 (5) Bachiller et al. 1995; (6) Bachiller et al. 1990b; (7) Bachiller et al. 1990c; (8) Bally & Predmore 1983; (9) Beichman et al. 1986; (10) Beltrán et al. 2002; (11) Beltrán et al. 2001; (12) Bontemps et al. 1996; (13) Brand et al. 1994; (14) Cabrit & Bertout 1992; (15) Carpenter et al. 1990; (16) Chandler & Carlstrom 1996; (17) Chernin 1995; (18) Chini et al. 2001; (19) Claussen et al. 1996; (20) Codella & Bachiller 1999; (21) Codella & Muders 1997; (22) Correia et al. 1997; (23) Curiel et al. 1990; (24) Curiel et al. 1993; (25) Davidson 1987; (26) Davis & Eisloeffel 1995; (27) Davis et al. 1997a; (28) Davis et al. 1999; (29) Edwards & Snell 1984; (30) Felli et al. 1992; (31) Fukui et al. 1989; (32) Fukui et al. 1988; (33) Furuya et al. 2003; (34) Galván-Madrid et al. 2004; (35) Gibb & Little 2000; (36) Goldsmith et al. 1984; (37) Han et al. 1998; (38) Harvey et al. 1979; (39) Harvey et al. 1986; (40) Haschick et al. 1983; (41) Henkel et al. 1986; (42) Hirano et al. 1997; (43) Huard et al. 1999; (44) Hurt & Barsony 1996; (45) Iwata et al. 1988; (46) Jenness et al. 1995; (47) Jennings et al. 1987; (48) Knapp & Morris 1976; (49) Knee & Sandell 2000; (50) Kurtz et al. 1994; (51) Ladd & Hodapp 1997; (52) Launhardt et al. 1997; (53) Lee et al. 2000; (54) Lucas et al. 2000; (55) Margulis et al. 1988; (56) Margulis et al. 1989; (57) Meehan et al. 1998; (58) McCutcheon et al. 1991; (59) Mitchell et al. 2001; (60) Molinari et al. 2000; (61) Molinari et al. 1998; (62) Molinari et al. 2002; (63) Moreira et al. 1997; (64) Morgan et al. 1990; (65) Mundy et al. 1993; (66) Myers et al. 1987; (67) Myers et al. 1988; (68) Persi et al. 1994; (69) Phillips et al. 2001; (70) Reipurth et al. 2002; (71) Reipurth et al. 2004; (72) Richer et al. 1992; (73) Richer et al. 1989; (74) Richer et al. 1993; (75) Rodríguez et al. 1999; (76) Rodríguez et al. 2000; (77) Rodríguez et al. 2003; (78) Rodríguez et al. 2002; (79) Sandell & Knee 2001; (80) Sandell & Weintraub 2001; (81) Sato et al. 1994; (82) Scappini et al. 1991; (83) Schwartz et al. 1988; (84) Shirley et al. 2000; (85) Skinner & Brown 1994; (86) Snell & Bally 1986; (87) Snell et al. 1990; (88) Snell et al. 1988; (89) Snell et al. 1984; (90) Su et al. 2004; (91) Sugitani et al. 1989; (92) Terebey et al. 1990; (93) Terebey et al. 1992; (94) Tofani et al. 1995; (95) Umemoto et al. 1992; (96) Wang et al. 1995; (97) Wiesemeyer et al. 1999; (98) Wilking et al. 1989a; (99) Wilking et al. 1990; (100) Wouterloot et al. 1993; (101) Wu et al. 1992; (102) Wu et al. 2004; (103) Young et al. 2003; (104) Yun & Clemens 1994a; (105) Yun et al. 1996

5.4.4 Prospects for future interferometric observations

There is not yet a theoretical chemical model that includes the effects of a central protostar and explains how they affect CCS and ammonia formation and destruction. High resolution observations of CCS and ammonia in star forming regions can provide the data against which such models could be tested.

All of these six sources are intrinsically interesting for detailed interferometric observations, although B1-IRS seemed, in principle, the most interesting candidate to perform interferometric observations with the VLA, since a cumply distributions has already been observed with high-resolution observations at 33.8 GHz (Lai & Crutcher 2000), and it is the most intense detection of our survey. Such interferometric observations have been carried out in this thesis, and will be presented in next chapter.

We propose that the rest of the detections in this survey are good candidates for high angular resolution observations, to compare with and to understand better the results obtained in B1-IRS. Also, L1448C and L1448-IRS3 are especially appropriate for studying the suggested association between the CCS and the molecular outflow, since this region hosts energetic and collimated molecular outflows. Moreover, this region is a good environment for studying outflow-induced star formation. In GF9-2, it would be interesting to study the CCS and the ammonia distribution in a young object transitional between pre-stellar and protostellar Class 0 source. NGC2071-North and L1251A are good prospective sites for making high-resolution observations of CCS in regions classified as more evolved (in which very few such observations have been made), or to try to reveal whether there is a younger object driving their respective molecular outflows.

5.5 Conclusions

We presented a single-dish survey of CCS and NH_3 emission at 1 cm, carried out with NASA's 70 m antenna at Robledo, toward a sample of low- and intermediate-mass young star forming regions that are known to harbor water maser emission. Our aim was to find the best candidates for a VLA high resolution study of the kinematical and physical properties of young Class 0 objects, to search for the youngest protostars, and to determine the relationship between CCS and NH_3 in star forming regions. Our general conclusions are the following:

- We have detected six low-mass sources that show CCS emission, out of a sample of 40 star forming regions associated with water maser emission. Four of these (L1448C, L1448-IRS3, GF9-2, and L1251A) had not been previously detected in any CCS transition, another one (NGC 2071-North) has been detected for the first time with the CCS line at 1 cm, while the other one (B1-IRS) had already been reported to show CCS emission in this and other transitions. All our CCS detections also show ammonia emission.

- From the CCS detection rate, and the duration of the water maser emission in low-mass star forming regions, we derive a lifetime of this molecule of $\simeq (0.7-3) \times 10^4$ yr in these regions, after the beginning of the embedded phase.

- Three of the six sources detected in CCS are catalogued as Class 0 protostars (L1448-IRS3, L1448C and B1-IRS), one could be a transitional object between pre-stellar and protostellar Class 0 stage (GF9-2), and the last two sources (NGC2071-North and L1251A) are catalogued as more evolved, a young T Tauri and a Class I source, respectively. Since CCS is considered an early-time molecule, to explain the CCS detections in more evolved objects, we speculate with two possibilities: either the classification of NGC2071-North and L1251A should be revised, or the star formation activity and the physical properties of each cloud could influence in the production and destruction of the CCS molecules.

- We did not find any statistically significant trend that may relate the presence of CCS emission with different parameters of the molecular outflows or the central sources of these star forming regions.

- We found that the distribution and mean of the peak intensity of NH_3 in the group of sources detected in CCS are significantly different from those in the group of undetected ones, with the ammonia mean peak intensity higher in regions with CCS. However, no significant difference is found with respect to the integrated intensity of NH_3. Stronger NH_3 peak line intensities with indistinguishable integrated intensities suggests that the lines are narrower and the emitting regions less turbulent (i.e. younger), although this remains to be confirmed observationally.

- The linewidths of the CCS and NH_3 lines are noticeably different, with CCS being three times narrower in some cases. This suggest that emission from these lines arises from gas with different kinematical properties within the telescope beam. The cases with more similar widths (B1-IRS and L1448C) may trace strong interactions between molecular outflows and the CCS-emitting gas.

5.5.1 Conclusiones

Se presenta una búsqueda de emisión de CCS y NH_3 a 1 cm con antena única, llevada a cabo con la antena de 70 m de NASA situada en Robledo, sobre una muestra de regiones de formación estelar jóvenes de masa baja o intermedia con emisión conocida de máseres de agua. Nuestro objetivo principal ha sido encontrar a los mejores candidatos para realizar un estudio de alta resolución con el VLA de las propiedades cinemáticas y físicas de objetos de clase 0 jóvenes, buscar las protoestrellas más jóvenes y determinar la relación entre el CCS y el NH_3 en regiones de formación estelar. Las conclusiones generales son las siguientes:

- Se han detectado seis regiones de masa baja que muestran emisión en CCS, dentro de una muestra de 40 regiones de formación estelar con presencia de máser de agua. Cuatro de ellas (L1448C, L1448-IRS3, GF9-2 y L1251A) no habían sido detectadas previamente en ninguna transición de CCS, otra (NGC 2071-North) ha sido detectada aquí por primera vez a 1 cm, mientras que B1-IRS había sido publicada como emisora de CCS en esta y otras transiciones. Todas nuestras detecciones en CCS muestran también emisión en amoniaco.

- A partir de la tasa de detección de CCS y de la fase de duración de la emisión de máseres de agua en regiones de formación estelar de masa baja, inferimos un tiempo de vida de esta molécula de $\simeq (0.7-3) \times 10^4$ años en este tipo de regiones, tras el comienzo de la fase embebida.

- Tres de las seis fuentes detectadas en CCS están catalogadas como protoestrellas de clase 0 (L1448-IRS3, L1448C y B1-IRS), otra podría ser un objeto de transición entre un estado pre-estelar y una protoestella de clase 0 (GF9-2), y las dos fuentes restantes (NGC2071-North y L1251A) están catalogadas como más evolucionadas, como una joven estrella T Tauri y una fuente de clase I respectivamente. Ya que el CCS está considerado como una molécula temprana, para explicar la asociación de CCS con objetos más evolucionados proponemos dos posibilidades: o bien la clasificación de NGC2071-North y L1251A debería ser revisada, o bien la actividad de la formación estelar y las propiedades físicas de cada fuente podrían influir en la producción y destrucción de las moléculas de CCS.

- No se encuentra ninguna tendencia estadísticamente significativa que relacione la presencia de emisión de CCS con distintos parámetros de los flujos moleculares o de las fuentes centrales de estas regiones de formación estelar.

- Encontramos que la distribución y la media de los máximos de intensidad de amoníaco en el grupo de fuentes detectadas en CCS son significativamente diferentes comparadas con las del grupo de no detecciones, con una media de intensidad máxima de amoniaco mayor en regiones con CCS. Sin embargo, no se encuentra ninguna diferencia significativa en los valores de intensidades integradas del amoníaco. Intensidades máximas de amoniaco más intensas con intensidades integradas similares sugieren líneas de emisión más estrechas y regiones emisoras menos turbulentas (es decir, más jóvenes), aunque esto necesita ser confirmado observacionalmente.

- La anchura de las líneas de CCS y NH_3 son notablemente diferentes, siendo las de CCS tres veces más estrechas en algunos casos. Esto sugiere que la emisión de estas líneas proviene de gas con diferentes propiedades cinemáticas dentro del haz del telescopio. Los casos con anchuras más parecidas (B1-IRS and L1448C) podrían trazar una interacción fuerte entre los flujos moleculares y el gas emisor en CCS.

Chapter 6

Study of the molecular environment of the class 0 source B1-IRS

In this chapter we present VLA observations of NH_3 and CCS thermal lines, as well as H_2O maser emission at 1 cm from the star-forming region B1-IRS with $\simeq 5"$ (=1750 AU) of angular resolution. We have carried out these observations to derive information about the spatial distribution and kinematics of the processes taking place in the vicinity of this star forming region, as well as the time-dependent chemistry. We reported for the first time a spatial anticorrelation between CCS and ammonia emission at such a high-angular resolution. We also suggest for the first time the possibility that CCS abundance is enhanced via shock-induced chemistry.

6.1 B1-IRS: Our best candidate for high-resolution studies

The far-infrared source B1-IRS (IRAS 03301+3057) is one of the few sources known to exhibit both CCS and water maser emission in the studies by Suzuki et al. (1992), Furuya et al. (2001), and Chapter 5 of this thesis. This is a Class 0 source (Hirano et al. 1997) located in the Perseus OB2 complex at a distance of 350 pc (Bachiller et al. 1990c). The B1 cloud contains a large amount of molecular gas, as shown by the strong $C^{18}O(1–0)$ emission detected by Bachiller & Cernicharo (1984). There is no optically visible counterpart of B1-IRS, but 850 micron dust continuum emission has been detected by Matthews & Wilson (2002) using SCUBA. There are two compact SiO clumps in the vicinity of B1-IRS (Yamamoto et al. 1992), and blueshifted CO(1–0) emission observed by Hirano et al. (1997), who suggested the presence of a pole-on molecular outflow. The SiO clumps are located at the interface between the CO outflow and the dense gas traced by the $C^{18}O$, suggesting that the outflow, probably driven by the IRAS source, is interacting with the surrounding medium, thus yielding the SiO emission through shocks.

In Chapter 5, we proposed this source as the most interesting candidate to be studied at high-resolution, since it showed the most intense CCS emission, and the clumpy distribution of this molecule was already detected at 33.8 GHz with BIMA (Lai & Crutcher 2000). In this work, we have used the VLA to study the properties of the CCS, NH_3, and water maser emission from B1-IRS, in order to obtain information about its circumstellar dynamics and stage of evolution. The rest frequencies of the CCS and H_2O transitions are sufficiently close together that they can be observed simultaneously with the VLA, also offering the possibility of using the water masers to track tropospheric phase fluctuations, if the masers are strong enough. Unfortunately this was not the case at the time of the observations presented here, but the atmosphere was in any case very stable.

This chapter is structured as follows: in §6.2 we describe our observations and data reduction procedure, as well as the analysis of VLA archive data. In §6.3 we present our observational results (morphology and physical parameters), which are then discussed in §6.4. We summarize our conclusions in §6.5.

6.2 Observations and data processing

Simultaneous observations of the $J_N=2_1$-1_0 transition of CCS and the 6_{16}-5_{23} transition of H_2O were carried out on 2003 April 4 using the VLA in its D configuration. The phase center of these observations was R.A.(J2000) = $03^h33^m16\overset{s}{.}3$, Dec(J2000) = $31°07'51''$. We used the four IF spectral line mode, with two IFs for each molecular transition, one in each of right and left circular polarizations. For the CCS observations we sampled 128 channels over a bandwidth of 0.781 MHz centered at $V_{\rm LSR}$ = 6.8 km s^{-1}, with a velocity resolution of 0.082 km s^{-1}. Water maser observations were obtained using 64 channels over a 3.125 MHz bandwidth centered at $V_{\rm LSR}$ = 15.7 km s^{-1}, with 0.66 km s^{-1} velocity resolution. The total on-source integration time was $\simeq$ 7.5 hours. Our primary calibrator was 3C48, for which we adopted a flux density of 1.1253 Jy (at the CCS frequency) and 1.1315 Jy (at the H_2O frequency) using the latest VLA values (1999.2). The source 3C84 was used as phase and bandpass calibrator (bootstrapped flux density = 11.80±0.14 Jy at the CCS frequency and 11.65±0.14 Jy at the H_2O frequency). Calibration and data reduction were performed with AIPS.

CCS data were reduced applying spectral Hanning smoothing and natural weighting of the visibilities, to improve the signal-to-noise ratio. The final velocity resolution is 0.16 km s^{-1} and the synthesized beam is $4\overset{''}{.}33 \times 3\overset{''}{.}30$ (P.A = $-79\overset{\circ}{.}2$). Water maser maps were produced using a "robust" weighting (Briggs 1995) of 0, to optimize a combination of both angular resolution and sensitivity. The synthesized beam obtained was $3\overset{''}{.}29$ ×

$2''.73$ (P.A = $87^\circ.9$).

In order to compare our water maser results with those at other epochs, we also retrieved earlier H_2O data from the VLA archive. These observations were carried out on 1998 October 24 and 1999 February 26, in CnB and CD configuration respectively, for project AF354. These data have been published by Furuya et al. (2003). Both sets of observations were made in the 1IF spectral line mode, in right circular polarization only, with a bandwidth of 3.125 MHz centered at $V_{\rm LSR}$ = 0 km s^{-1}, and sampled over 128 channels, thus providing a velocity resolution of 0.33 km s^{-1}. The phase center of these observations was R.A.(J2000) = $03^h33^m16^s.030$, Dec(J2000) = $31^\circ07'34''.05$. The time on source was $\simeq$ 3 minutes in 1998 and $\simeq$ 13 minutes in 1999. In both epochs 3C48 was used as primary flux calibrator, with an assumed flux density of 1.1313 Jy and 1.1315 Jy for the 1998 and 1999 observations respectively (adopting the latest 1999.2 VLA values). The secondary calibrator was 0333+321, with a bootstrapped flux density of 1.66±0.10 Jy for the 1998 observations and 1.67±0.03 Jy for the 1999 observations. The water masers were strong enough during these earlier observations to enable self-calibration, after referencing the maser positions to 0333+321. Images were made with the robust parameter set to 0, giving synthesized beams of $0''.91 \times 0''.38$ (P.A. = $81^\circ.7$) and $3''.05 \times 1''.16$ (P.A. = $68^\circ.8$) for the 1998 and 1999 data respectively.

We have also processed VLA archive data of the $NH_3(1,1)$ inversion transition. The observations were made on 1988 August 13 for project AG265, in the D configuration. The total bandwidth was 3.125 MHz, centered at $V_{\rm LSR} = 6.1$ km s^{-1} and sampled by 128 channels, which provided a velocity resolution of 0.33 km s^{-1}. Both right and left circular polarizations were obtained. The phase center of these observations was R.A.(J2000) = $03^h33^m16^s.337$, Dec(J2000) = $31^\circ07'51''.03$. The total time on source was $\simeq$ 2 h. The source 3C48 was used as the primary flux calibrator, with an adopted flux density of 1.0542 Jy (1999.2 values). The phase calibrator was 3C84 (bootstrapped flux density = 38.0±1.5 Jy). Since the NH_3 emission was faint and extended, we processed the data using natural weights and a *uv*-taper of 20 kλ, to improve the sensitivity to the extended emission. The resulting synthesized beam is $8''.62 \times 7''.76$ (P.A. = $-75^\circ.5$). The size of the VLA primary beam at the frequencies corresponding to the CCS, H_2O, and NH_3 transitions ($\simeq$22-24 GHz) is $\simeq 2'$.

To have an estimate of the missing flux density due to the lack of short spacings of the VLA, we have obtained single-dish spectra of both CCS and NH_3 towards the position R.A.(J2000) = $03^h33^m16^s.3$, Dec(J2000) = $31^\circ07'51''$, with the NASA's 70 m antenna (DSS-63) at Robledo de Chavela, Spain, at the same frequencies as the VLA. Observations were made in frequency switching mode, using the SDS 256-channel autocorrelator spectrometer. The CCS observations (already presented as part of the survey in Chapter 5) were performed in six time slots between 2002 August and 2003 July with a total integration time of 60 minutes and an average system temperature of $\simeq$ 80 K. We used a bandwidth of 1 MHz (velocity resolution = 0.05 km s^{-1}). The NH_3 observations were carried out during 2003 July, with an average system temperature of $\simeq$ 60 K. The on-source integration time was 40 minutes. To detect all the hyperfine lines we used a bandwidth of 10 MHz (velocity resolution = 0.5 km s^{-1}). The rms pointing accuracy of the telescope was better than $9''$. All the single-dish data reduction was carried out using the CLASS package.

In addition to the radio data, we have retrieved a K-band image from the Two Micron All Sky Survey (2MASS), to obtain a better position for the infrared source. This image was smoothed with a $5''$ Gaussian (FWHM), to search for low surface-brightness, extended emission.

6.3 Results

6.3.1 The infrared source

The 2-μm map obtained from the 2MASS archive, and convolved with a $5''$ Gaussian (Fig. 6.1), shows a point source, designated 2MASS J03331667+3107548, at R.A.(J2000) = $03^h33^m16\overset{s}{.}678$, Dec(J2000) = $31^o07'54\overset{''}{.}88$ (2σ absolute position error $\simeq$ $0\overset{''}{.}22$). This position is $\simeq$ $6''$ away from the IRAS catalog position, R.A.(J2000) = $03^h33^m16\overset{s}{.}3$, Dec(J2000) = $31^o07'51''$, but well within the error ellipsoid (2σ error axes = $48''\times14''$) of the latter. In what follows, we will consider the position of the 2MASS point source as the location of the central source of B1-IRS. We also find extended 2 μm infrared emission elongated to the south west of the point source, with position angle $\simeq -120^o$, suggestive of a reflection nebula.

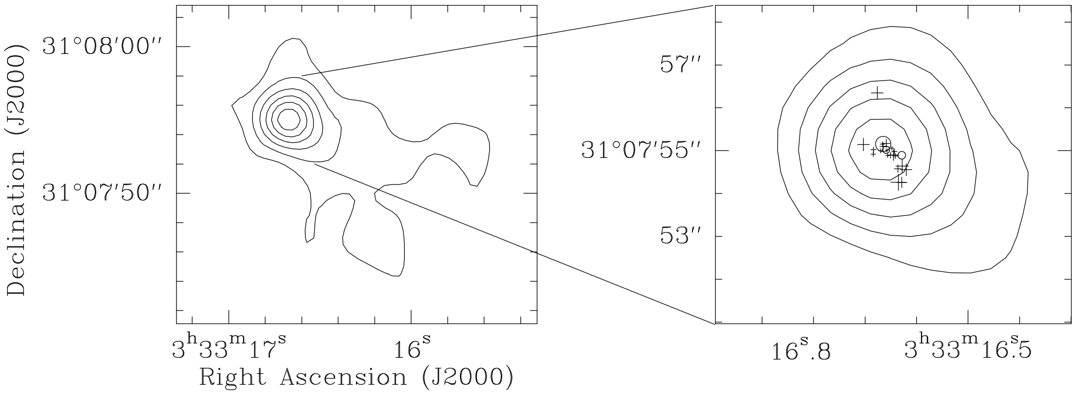

Figure 6.1: 2MASS K-band image convolved with a $5''$ Gaussian. Contours represent 90%, 75%, 60%, 45%, 30%, and 15% of the peak emission (the source magnitude is K = 14.208±0.122, measured by 2MASS). Crosses and open circles in the close-up of the infrared emission (right panel) represent the structure of red and blueshifted water masers respectively, obtained in the April 2003 observations and scaled by their relative position uncertainty.

6.3.2 The water masers

Our water maser observation on April 2003 shows a complex spectral pattern in which it is difficult to single out different emission features. Our analysis of morphology and kinematics of the emission is based on its location at the different velocity channels sampled. The positions shown in Table 6.1 were determined by fitting two-dimensional Gaussian to the maser emission detected at each channel. Most of the emission is redshifted with respect to the cloud velocity ($V_{\rm LSR}$ = 6.3 km s^{-1}; Hirano et al. 1997) with LSR velocities between 9.1 and 23.6 km s^{-1}, although three channels are blueshifted, with LSR velocities between 2.5 and 3.8 km s^{-1}. The maximum flux density was $\simeq$ 15.4±1.6 mJy at $V_{\rm LSR}$ = 17.7 km s^{-1}, two orders of magnitude weaker than in the earlier epochs reported by Furuya et al. (2003). The maser emission at each velocity channel is spatially unresolved, but when we plot the position of the emission for all of them (see Fig. 6.2), an elongated structure can be seen, with a length of $\simeq 1''\!.3$ ($\simeq$455 AU) and P.A. $\simeq -120^{\rm o}$. Since the size of the structure is larger than the typical positional accuracy for each individual channel (Table 6.1), we believe that the overall morphology is real.

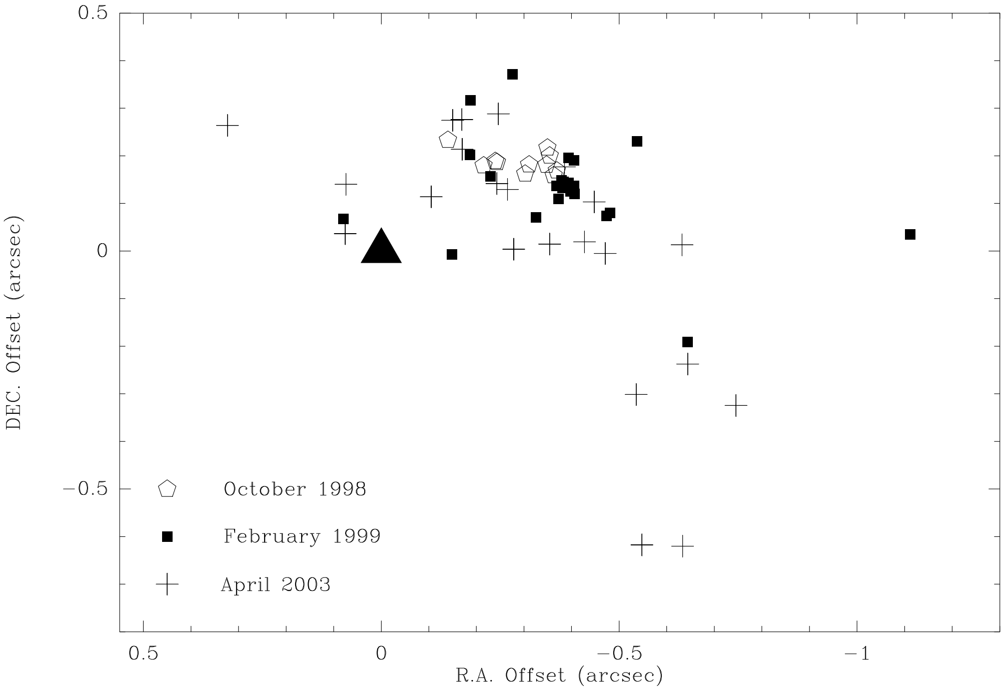

Figure 6.2: Positions of water maser emission for all velocity channels observed towards B1-IRS at different epochs. Open pentagons, filled squares, and crosses represent the maser emission at each different channel, observed in October 1998, February 1999, and April 2003, respectively. The position offsets are relative to the 2 micron point source, which is represented by a filled triangle. The northernmost maser spot shown in Fig. 6.1 is out of the scale in this plot.

We have compared our new data with those obtained in 1998 October and 1999 February by Furuya et al. (2003). The maser positions for those epochs are shown in Fig. 6.2, and in Tables 6.2 and 6.3. The same elongated distribution is evident. In these earlier data sets all maser emission is redshifted with respect to the cloud velocity. We note that there is a discrepancy of $\simeq 23''$ between the positions of the 1998 October masers presented here and the positions reported in Table 3 of Furuya et al. (2003) using the same data. The location of the emission is similar for all three epochs, taking into account their mean absolute positional uncertainties ($\simeq 0\rlap{.}''3$, $0\rlap{.}''16$, and $0\rlap{.}''04$ for 2003 April, 1999 February and 1998 October respectively). Therefore we are confident that our positions are correct.

The water maser emission is located at a distance $\leq 1''$ (350 AU) from the 2μm source, suggesting that this is the center of activity of the region. Considering an average LSR velocity of $\simeq 14.0$ km s^{-1} of the maser emission, i.e., $\simeq 7.7$ km s^{-1} redshifted with respect to the cloud velocity (6.3 km s^{-1}), and a mean distance of $0\rlap{.}''5$ from the central source, the central mass needed for the water masers to be gravitationally bound is $\simeq 12$ M$_\odot$. However, B1-IRS is a low luminosity protostar ($L \simeq 2.8$ L$_\odot$, Hirano et al. 1997), and it is unlikely to be much more massive than $\simeq 1$ M$_\odot$. These results strongly suggest that the masers are tracing mass loss motions rather than bound motions in a circumstellar disk.

Table 6.1: Water maser emission on 2003 April 04

Right Ascension[1] (J2000)	Declination[1] (J2000)	Position [2,3] uncertainty ($''$)	Flux density [2] (mJy)	$V_{\rm LSR}$[4] (km s^{-1})
03 33 16.62	31 07 54.6	0.3	4.3±1.6	9.1
03 33 16.629	31 07 54.89	0.17	7.3±1.7	3.8
03 33 16.63	31 07 54.3	0.3	4.9±1.7	19.0
03 33 16.63	31 07 54.6	0.3	3.9±1.7	22.3
03 33 16.636	31 07 54.58	0.17	7.1±1.7	10.4
03 33 16.64	31 07 54.3	0.4	3.2±1.7	22.9
03 33 16.641	31 07 54.88	0.13	9.7±1.6	14.4
03 33 16.643	31 07 54.98	0.13	9.3±1.6	11.7
03 33 16.648	31 07 55.06	0.09	13.1±1.6	15.0
03 33 16.650	31 07 54.89	0.14	8.6±1.6	18.3
03 33 16.65	31 07 54.9	0.3	4.7±1.7	16.4
03 33 16.656	31 07 54.88	0.09	14.7±1.7	12.4
03 33 16.657	31 07 55.01	0.08	15.4±1.6	17.7
03 33 16.659	31 07 55.02	0.16	7.8±1.7	3.2
03 33 16.659	31 07 55.17	0.19	6.4±1.6	11.1

Table 6.1: (continued)

Right Ascension[1] (J2000)	Declination[1] (J2000)	Position [2,3] uncertainty ($''$)	Flux density [2] (mJy)	V_{LSR}[4] (km s^{-1})
03 33 16.665	31 07 55.09	0.17	6.9±1.6	9.8
03 33 16.666	31 07 55.15	0.12	10.6±1.6	13.7
03 33 16.670	31 07 54.99	0.10	12.3±1.7	13.1
03 33 16.67	31 07 55.2	0.3	3.6±1.7	2.5
03 33 16.68	31 07 56.3	0.3	4.0±1.6	23.6
03 33 16.684	31 07 54.92	0.12	7.1±1.7	17.0
03 33 16.684	31 07 55.02	0.13	9.2±1.6	15.7
03 33 16.70	31 07 55.1	0.3	4.1±1.6	19.7

Notes to Table 6.1

[1] Units of right ascension are hours, minutes, and seconds. Units of declination are degrees, arcminutes, and arcseconds.

[2] Uncertainties are 2σ.

[3] Relative position uncertainties with respect to the phase center. The absolute position error of the phase center is $\sim 0''.28$.

[4] Velocity of maser emission.

Table 6.2: Water maser emission on 1998 October 24

Right Ascension[1] (J2000)	Declination[1] (J2000)	Position [2,3] uncertainty ($''$)	Flux density [2] (mJy)	V_{LSR}[4] (km s^{-1})
03 33 16.6493	31 07 55.049	0.024	440±80	15.1
03 33 16.6498	31 07 55.039	0.020	570±90	14.8
03 33 16.6504	31 07 55.080	0.017	750±100	14.5
03 33 16.6509	31 07 55.061	0.019	560±80	14.2
03 33 16.651	31 07 55.10	0.03	610±90	13.8
03 33 16.6538	31 07 55.062	0.009	2300±300	16.1
03 33 16.654	31 07 55.04	0.03	360±70	13.5
03 33 16.6591	31 07 55.067	....[5]	2800±300	15.8
03 33 16.6593	31 07 55.069	0.011	970±130	15.5
03 33 16.661	31 07 55.06	0.15	1050±140	16.5
03 33 16.667	31 07 55.11	0.07	130±60	16.8

Notes to Table 6.2

[1] Units of right ascension are hours, minutes, and seconds. Units of declination are degrees, arcminutes, and arcseconds.

[2] Uncertainties are 2σ.

[3] Relative position uncertainties with respect to the reference feature used for self-calibration

[4] Velocity of maser emission.

[5] Reference feature. Absolute position error $\sim 0''.021$

Table 6.3: Water maser emission on 1999 February 25

Right Ascension[1] (J2000)	Declination[1] (J2000)	Position [2,3] uncertainty ($''$)	Flux density [2] (mJy)	$V_{\rm LSR}$[4] (km s^{-1})
03 33 16.591	31 07 54.91	0.16	137±23	19.1
03 33 16.628	31 07 54.69	0.14	118±20	12.8
03 33 16.636	31 07 55.11	0.25	57±27	20.1
03 33 16.641	31 07 54.95	0.04	352±24	15.1
03 33 16.641	31 07 54.96	0.04	362±21	13.2
03 33 16.646	31 07 55.00	0.05	36±30	17.4
03 33 16.646	31 07 55.07	0.13	142±22	18.1
03 33 16.6465	31 07 55.017	0.014	1180±50	17.1
03 33 16.647	31 07 55.02	0.16	152±23	18.4
03 33 16.6470	31 07 55.006	....[5]	6500±230	15.8
03 33 16.6481	31 07 55.021	0.003	6010±220	16.1
03 33 16.6481	31 07 55.026	0.007	2090±80	15.5
03 33 16.6483	31 07 55.013	0.006	2810±100	16.5
03 33 16.649	31 07 54.99	0.04	410±30	13.5
03 33 16.649	31 07 55.03	0.06	236±23	13.8
03 33 16.6493	31 07 55.017	0.008	1810±70	16.8
03 33 16.65	31 07 55.1	0.3	45±24	19.8
03 33 16.653	31 07 54.95	0.17	98±23	17.8
03 33 16.660	31 07 55.04	0.10	169±23	14.2
03 33 16.66	31 07 55.3	0.4	27±20	11.2
03 33 16.663	31 07 55.08	0.13	17±30	19.4
03 33 16.663	31 07 55.20	0.14	111±22	18.8
03 33 16.666	31 07 54.87	0.11	108±21	14.8
03 33 16.684	31 07 54.95	0.14	104±20	14.5

Notes to Table 6.3

[1] Units of right ascension are hours, minutes, and seconds. Units of declination are degrees, arcminutes, and arcseconds.

[2] Uncertainties are 2σ.

[3] Relative position uncertainties with respect to the reference feature used for self-calibration

[4] Velocity of maser emission.

[5] Reference feature. Absolute position error $\sim 0''.12$.

6.3.3 CCS and NH_3 emission

6.3.3.1 CCS emission

The integrated emission from the CCS molecule is distributed in three clumps (Fig. 6.3). The clump centers are located $\simeq 25''$ (9000 AU) south-west (SW clump), $\simeq 50''$ (17000 AU) north-east (NE clump), and $\simeq 15''$ (5000 AU) north-west (NW clump) from the central source. Fig. 6.4 shows the CCS emission integrated over different velocity intervals. All clumps are redshifted with respect to the systemic velocity of the B1 core ($V_{\rm LSR} = 6.3$ km s^{-1}). Moreover, the SW, NE and NW CCS clumps show clear velocity gradients of $\simeq 23$, $\simeq 10$, and $\simeq 12$ km s^{-1} pc^{-1} respectively (see Figs. 6.5 and 6.6) over the whole size of the clumps, with velocities closer to that of the ambient cloud near the central object.

Clump SW has the most redshifted velocities ($V_{\rm LSR}$ from 6.6 km s^{-1} to 7.6 km s^{-1}). It has an ellipsoidal shape, elongated perpendicularly to the direction of the velocity gradient, with two emission peaks. Clump NE shows emission from $V_{\rm LSR}$ = 6.6 km s^{-1} to 7.1 km s^{-1}, and it is divided into three "fingers" that point towards the north-west. Clump NW has a velocity gradient from $V_{\rm LSR}$ = 6.3 to 6.8 km s^{-1} (i.e., closer to the mean cloud velocity), and its morphology is elongated, with its major axis pointing towards the central source.

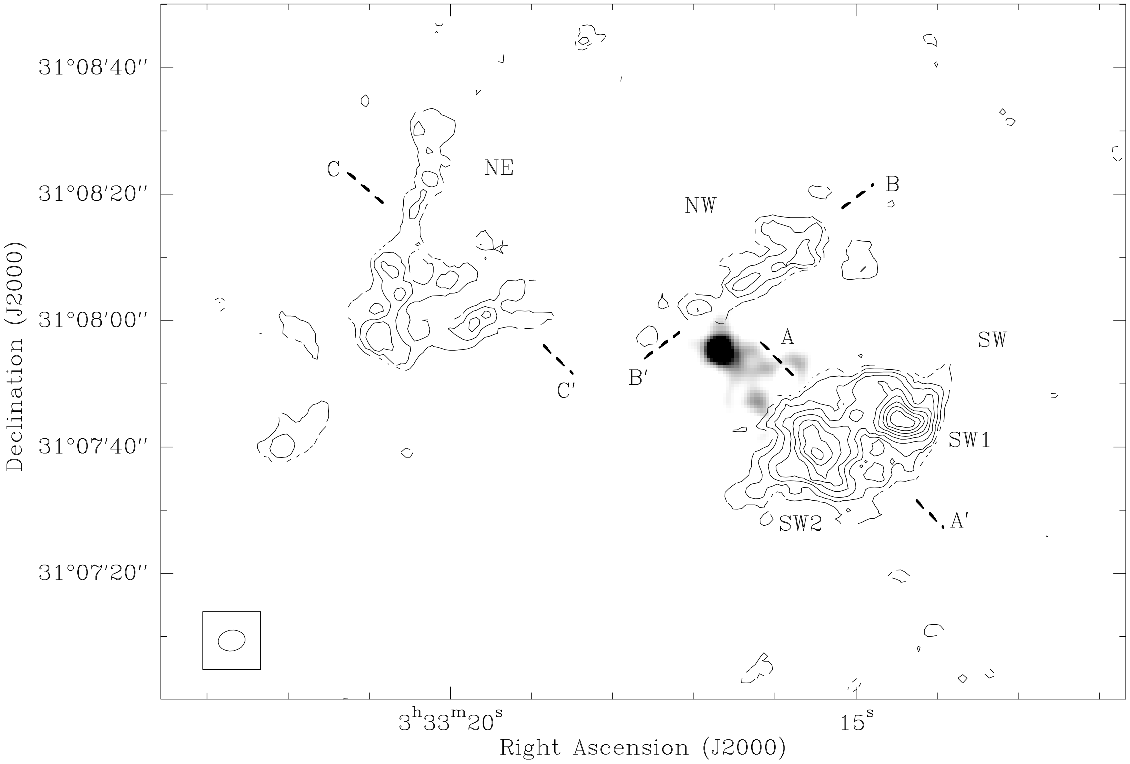

Figure 6.3: CCS integrated emission (contours) not corrected for the response of the VLA primary beam, overlaid on the 2MASS K-band emission (grey scale). Contour levels range from 0.66 to 5.94 mJy beam^{-1} km s^{-1} in intervals of 0.66 mJy beam^{-1} km s^{-1}. Grey scale ranges between 10% and 45% of the peak emission (the source magnitude is K = 14.208 ± 0.122 measured by 2MASS). The south-west (SW), north-west (NW) and north-east (NE) CCS clumps are labeled. Dashed lines represent the axes where position-velocity diagrams have been obtained (Fig. 6.6) .

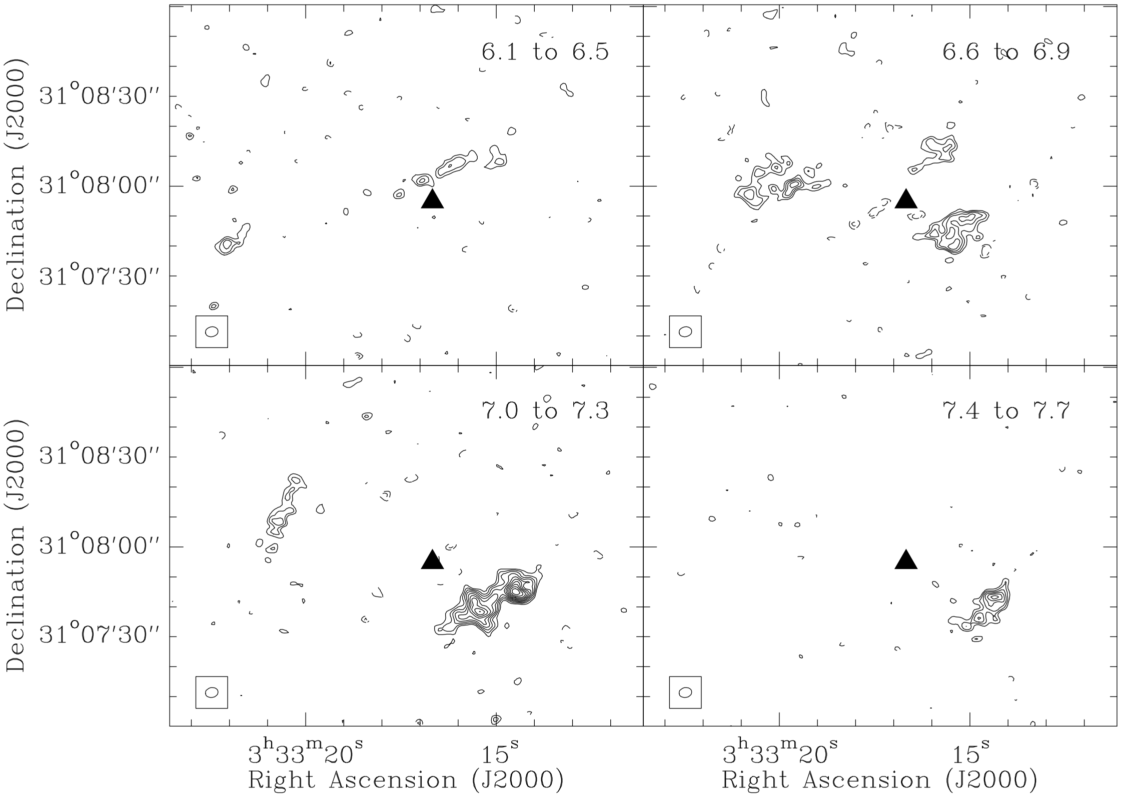

Figure 6.4: Contour maps of the CCS integrated emission over the LSR velocity ranges (in km s^{-1}) indicated in the top right corner of each panel. Contour levels are at -2.56, -1.92, and from 1.92 to 7.68 at steps of 0.64 mJy beam^{-1} km s^{-1} (the rms of the maps). Filled triangle indicates the 2 μm point source position. No primary beam correction has been applied to these figures.

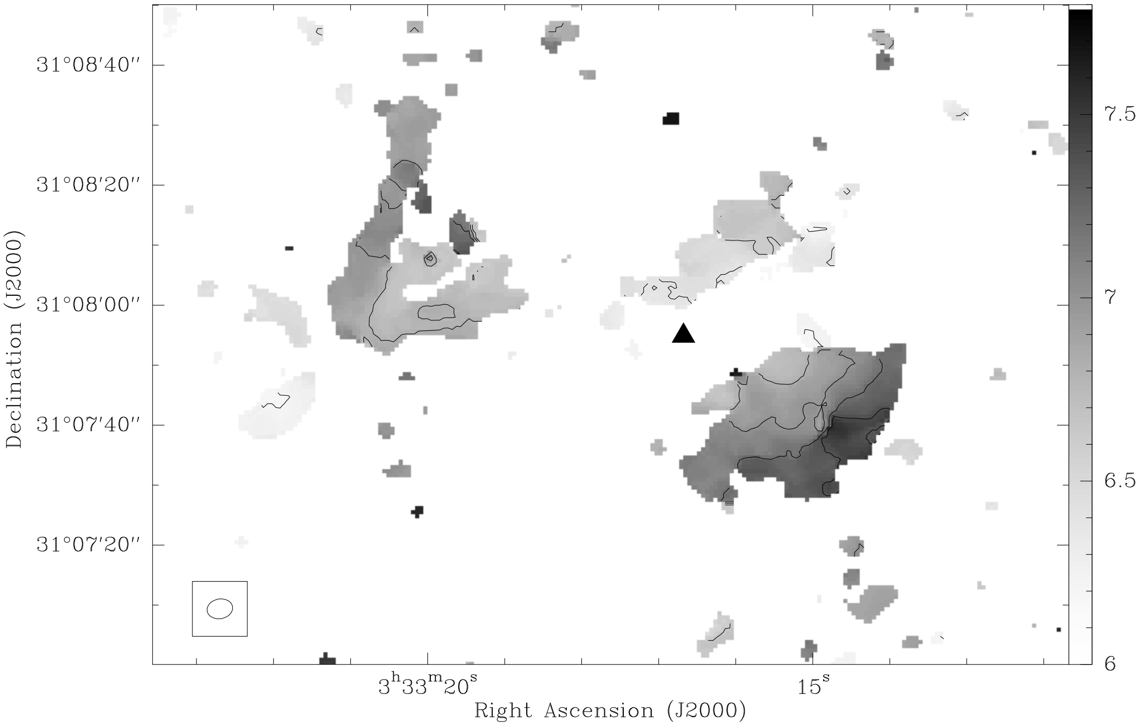

Figure 6.5: Map of CCS intensity-weighted mean velocity (first-order moment). Contour levels range from 6.0 to 7.8 km s^{-1} at steps of 0.2 km s^{-1}. The grayscale is also from 6.0 to 7.8 km s^{-1}. The filled triangle represents the position of the 2 μm source.

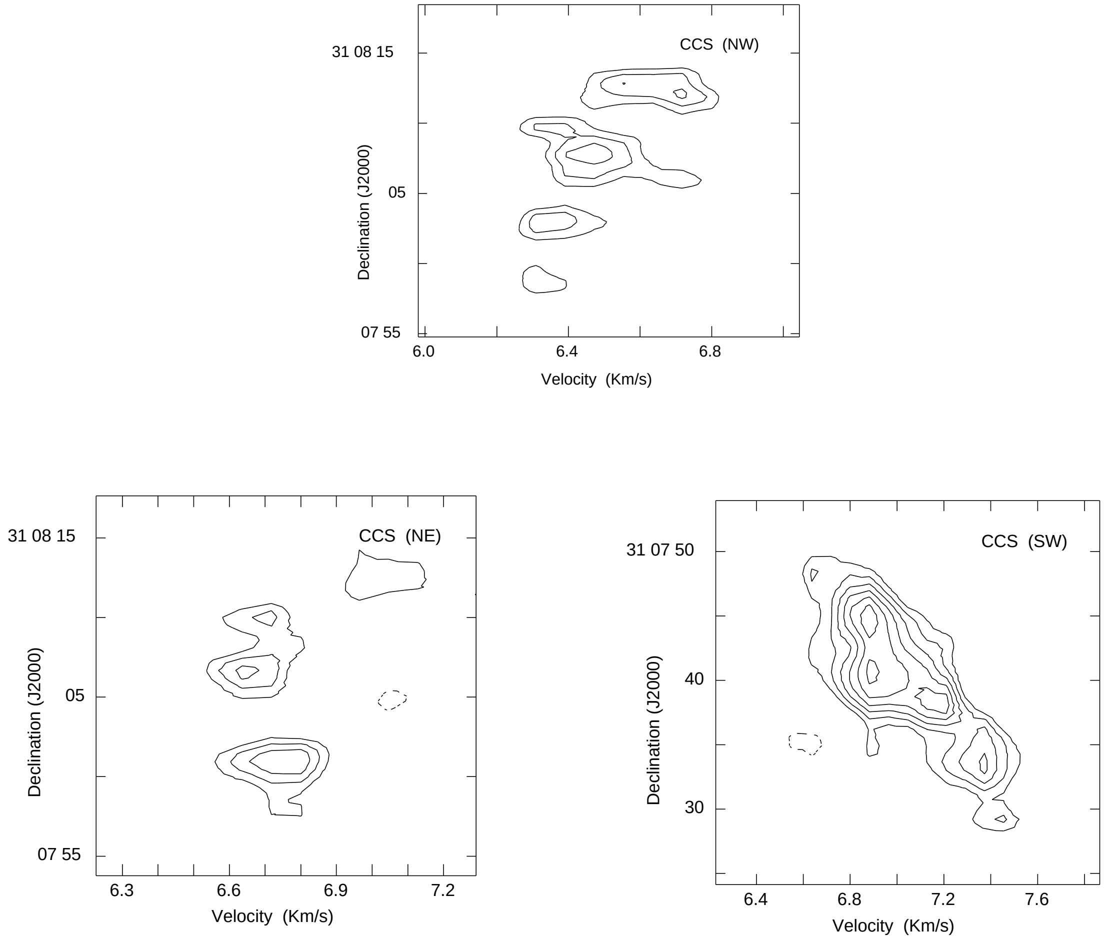

Figure 6.6: Position-velocity diagrams of the CCS clumps. The upper panel represents the position-velocity diagram of the NW clump through axis B-B' (see Fig. 6.3), the lower-left one corresponds to the NE clump through axis C-C', and the lower-right one the SW clump through axis A-A'. Contours are at -3.6, and from 3.6 to 9.6 mJy beam^{-1} with steps of 1.2 mJy beam^{-1}, the rms of the maps. These plots have not been corrected from the response of the VLA primary beam.

6.3.3.2 NH_3 emission

Ammonia emission is very extended and clumpy (Fig. 6.7). Most clumps are distributed in two strips, with NW-SE orientation. The general trend, however, as illustrated by Fig. 6.7, is that CCS and NH_3 emissions are spatially anticorrelated. Such an anticorrelation has been observed in other sources (Hirahara et al. 1992; Willacy et al. 1998; Lai et al. 2003), but this is the first time that it has been detected with such a high angular resolution ($\simeq 5''$).

We have to note, however, that there is considerable extended $NH_3(1,1)$ and CCS ($J_N=2_1$-1_0) emission in the B1-IRS region to which the VLA is not sensitive. Indeed, from our single-dish observations of these transitions (Fig. 6.8) we estimate that $\simeq$ 90% of the ammonia and CCS emission is missed with the VLA.

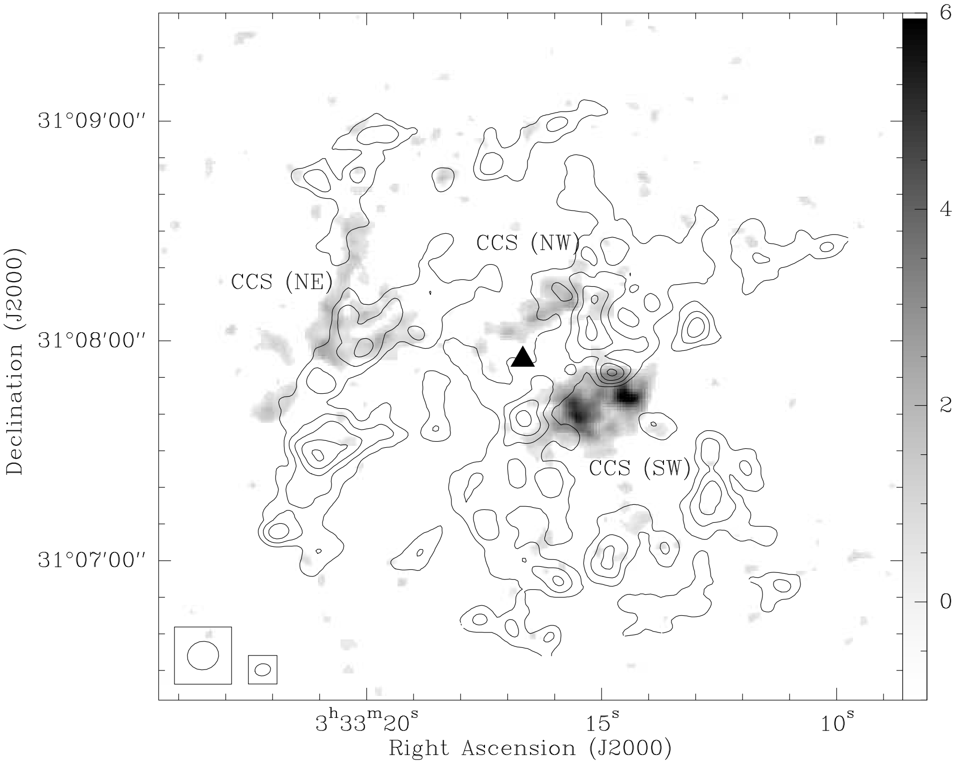

Figure 6.7: CCS (greyscale) and ammonia main line (contours) integrated emission. Greyscale ranges from −1 to 6 mJy beam^{-1} km s^{-1}. Contour levels range from 40 to 120 mJy beam^{-1} km s^{-1} with increment steps of 20 mJy beam^{-1} km s^{-1} , the rms of the map. Filled triangle represents the 2 μm source. The beam on the left correspond to the ammonia observations and the beam on the right corresponds to the CCS observations. No primary beam correction has been applied to these maps. However, given that the phase center was almost the same in the CCS and NH_3 observations, the beam response is similar and does not affect the comparison between both emissions.

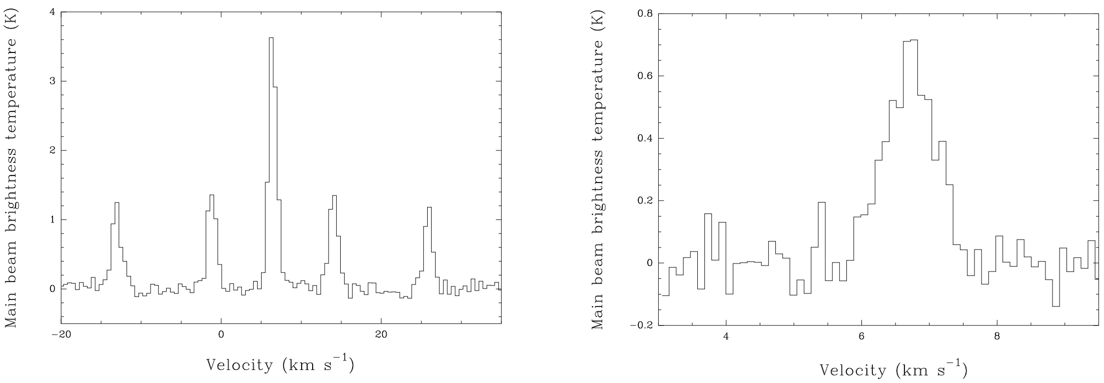

Figure 6.8: Single-dish spectra observed with the Robledo-70m antenna, at the position R.A.(J2000) = $03^{h}33^{m}16^{s}\!.34$, Dec(J2000) = $31^{\circ}07'51''\!.1$. Left panel represents the NH_3(1,1) emission, with rms noise $1\sigma = 0.08$ K. Right panel is the CCS(2_1-1_0) spectrum, with rms noise $1\sigma = 0.13$ K.

6.3.3.3 Physical parameters

Although the maps shown in this Chapter have not been corrected by the primary beam response for display proposes, such a correction has been applied to the data prior to deriving physical parameters. Table 6.4 summarizes the main physical parameters obtained from the CCS and NH_3 lines. For the CCS data, we provide parameters for each individual clump, since they are well defined in the integrated intensity map (Fig. 6.3). For these calculations, we have divided the emission of the SW clump in two different peaks, SW1 (located at lower right ascension), and SW2 (located at the eastern part of the SW clump). The mean clump column density of CCS is $N_{\rm CCS} \simeq (3.0\pm0.8)\times10^{13}\,{\rm cm}^{-2}$, which is similar to the value obtained by Suzuki et al. (1992) for B1 (1.38×10^{13} cm^{-2}). Assuming a relative abundance of CCS with respect to H_2 of 0.9×10^{-10} (mean value reported by Lai & Crutcher 2000 for B1), the resulting mean $N_{\rm H_2}$ is $\simeq (3.3 \pm 0.8) \times 10^{23}$ cm^{-2}.

Given the low signal-to-noise ratio and the clumpy structure of the NH_3 emission, we only give averaged values for this molecule in Table 6.4. The column density of ammonia at each local maximum seen in the integrated intensity map (Fig. 6.7), ranges between $\simeq 6 \times 10^{14}$ and 3×10^{15} cm^{-2}, with a mean clump value of $\simeq (1.4 \pm 0.4) \times 10^{15}$ cm^{-2} , similar to the value of 1×10^{15} cm^{-2} reported by Bachiller & Cernicharo (1986).

Table 6.4: Physical parameters of the clumps observed in NH_3 and CCS[a]

Molecule	Clump	I_ν [b] (mJy beam^{-1})	$\int I_\nu dv$ [b] (mJy beam^{-1} km s^{-1})	$N_{\rm mol}$ [c] (10^{13} cm^{-2})	$N_{\rm H_2}$ [d] (10^{23} cm^{-2})	Sizes[e] (AU× AU)	M_c [f] ($M_\odot$)
NH_3	Mean[g]	170±30	210±30	140±40	1.4±0.4	10700×4600	2.1±0.6
CCS	SW1	14.2±2.8	7.5±1.4	3.7±1.7	4.1±1.9	2900×2900	1.1±0.5
CCS	SW2	10.5±2.8	6.0±1.4	2.9±1.5	3.2±1.7	5000×2900	1.4±0.7
CCS	NW	4.7±2.6	3.4±1.3	1.7±1.1	1.9±1.2	7000×2100	0.8±0.5
CCS	NE	9.3±3.9	7.3±2.0	3.6±1.7	4.0±1.9	12600×2900	4.4±2.0

Notes to Table 6.4

[a] All the uncertainties in this table are 2σ.

[b] Intensity and integrated intensity at the position of the emission peak for each clump (main hyperfine component only for ammonia).

[c] Column density obtained from $N_{\rm mol} = \frac{8\alpha\pi\nu^3}{c^3 g_j A_{ji}} \frac{Q(T_{\rm rot}) \int I_\nu dv}{[B_\nu(T_{\rm ex}) - B_\nu(T_{\rm bg})]} \frac{\exp(E_j/kT_{\rm rot})}{\exp(h\nu/kT_{ex})-1}$ (optically thin approximation), where α is a factor equal to 1 for CCS, and equal to $2[1+\exp(h\nu/kT_{\rm ex})]$ for NH_3, ν is the frequency of the transition, Q is the partition function, $\int I_\nu dv$ is the integrated intensity (referred only to the main line in the case of the ammonia), E_j is the energy of the upper state in the case of the CCS (1.61 K; Wolkovitch et al. 1997) and the energy of the rotational level whose inversion transition is observed in the case of the ammonia (23.4 K; Ho & Townes 1983), $T_{\rm rot}$ is the rotational temperature, g_j is the statistical weight of the upper rotational level in the case of the CCS, and of the upper sublevel involved in the inversion transition in the case of the ammonia. A_{ji} is the Einstein coefficient for the overall transition (1.67 and 4.33×10^{-7}s^{-1} for the NH_3(1,1) and CCS(2_1-1_0) transitions, respectively; Ho & Townes 1983; Wolkovitch et al. 1997), and $T_{\rm ex}$ is the excitation temperature. For the CCS molecule we adopted a $T_{\rm rot} = T_{\rm ex} = 5$ K (Suzuki et al. 1992). For the NH_3 calculations, we have assumed a $T_{\rm rot} = 12$ K derived by Bachiller & Cernicharo (1984) from single-dish observations. From our single dish ammonia spectrum (see Fig. 6.8), we derived an optical depth of $\tau = 0.9 \pm 0.5$, which provides a $T_{\rm ex} = 8.8 \pm 2.4$ K. The final $N_{\rm NH_3}$ was obtained by multiplying the optically thin solution by the factor $(\tau/[1 - e^{-\tau}])$.

[d] Hydrogen column density, obtained assuming a fractional abundance with respect to H_2 of 10^{-8} for NH_3 (Herbst & Klemperer 1973) and 0.9×10^{-10} for CCS (Lai & Crutcher 2000).

[e] FWHM of the clumps. It is an averaged value in the case of the ammonia.

[f] Clump mass, derived from the N_{H_2} and the half-power area. It is an averaged value for ammonia clumps.

[g] Average value for the NH_3 clumps.

6.4 Discussion

6.4.1 The geometry of the molecular outflow

Hirano et al. (1997) detected moderately-high velocity blueshifted CO emission centered close to the position of the IRAS source and consisting of many clumps at different blueshifted velocities. No redshifted emission was obvious in their data. Given the distribution of the blueshifted gas around the IRAS position (Fig. 6.9), Hirano et al. (1997) suggested the existence of a molecular outflow driven by the IRAS source, and oriented pole-on with respect to the observer. In order to explain the absence of the redshifted CO lobe, these authors suggested that higher density material is slowing down that component of the outflow.

Our results, however, do not support the pole-on geometry for the outflow. The 2MASS source, which is within the error box of the IRAS position, is located at the tip of the blueshifted outflow, rather than at its center (see Fig. 6.9). If we assume that the 2MASS source is actually tracing the powering source of the outflow (confirmed by its association with the water masers), its blueshifted lobe would flow towards the southwest from the central source.

The low velocity of the CO blueshifted emission with respect to the $V_{\rm LSR}$ of the cloud ($|V_{\rm CO} - V_{\rm LSR}| < 8$ km s^{-1}), and the lack of a significant amount of redshifted gas, are more compatible with the molecular outflow being close to the plane of the sky. The absence of a coherent velocity gradient of the water masers along their linear structure is also consistent with this geometry.

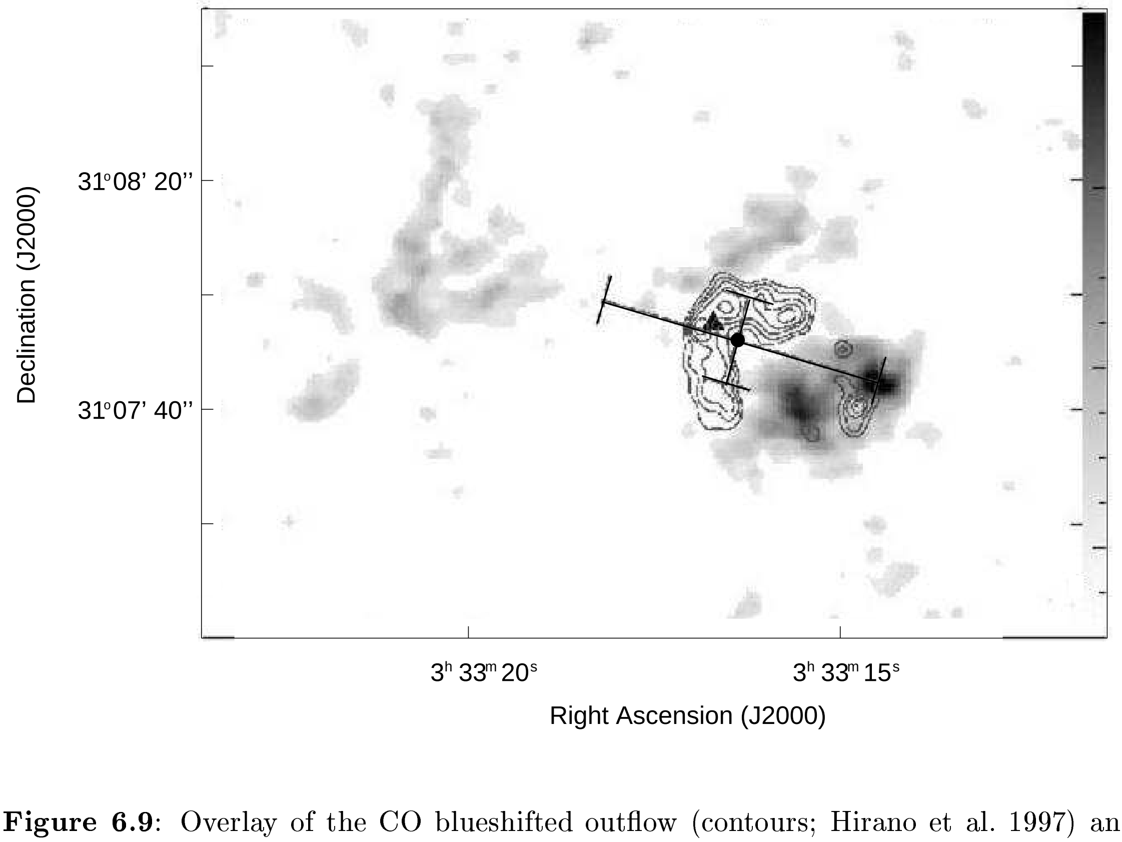

Figure 6.9: Overlay of the CO blueshifted outflow (contours; Hirano et al. 1997) and CCS integrated emission (greyscale; this thesis). The filled circle represents the IRAS source with its error position barrs. The triangle marks the 2 micron point source. The CCS emission is not corrected from the response of the primary beam.

6.4.2 The outflow traced by water masers

The water maser emission is distributed in the direction of the extended infrared nebula, approximately NE-SW. This is the same orientation as the blueshifted CO lobe with respect to the central source, and suggests that the masers are tracing the base of the outflow. Note, however, that most of the maser components are redshifted with respect to the cloud velocity, and yet their location primarily to the south and west of the infrared source means that they coincide with the blueshifted CO lobe. This apparent kinematic discrepancy could be explained if the masers are tracing the background walls of a cavity evacuated in the cloud by a molecular outflow close to the plane of the sky. The existence of such a cavity was suggested by Hirano et al. (1997) form their $C^{18}O$ map. In the proposed geometry of an outflow close to the plane of the sky, the background walls could show redshifted motions, assuming a finite opening angle. The fact that no corresponding blueshifted masers are shown tracing the foreground walls could be due to different physical conditions of the gas, with denser gas in the background (that probably corresponds to the region that goes deeper into the molecular cloud), and would produce a stronger interaction with the outflow in that area. Proper motion measurements of the B1-IRS water masers will help to clarify whether our proposed geometry, with the outflow close to the plane of the sky and evacuating a cavity in the cloud, is correct.

6.4.3 The interaction between the molecular outflow and its surrounding environment

The CCS clumps show a clear velocity gradient, with less redshifted velocities towards the central source (see Fig. 6.5). If we assume that the ambient cloud velocity is 6.3 km s^{-1} (Hirano et al. 1997), these clumps would be redshifted with respect to the cloud velocity. This velocity pattern cannot be explained purely by foreground clumps with infalling motions, for which we would expect more redshifted velocities closer to the source. Nevertheless, if we consider that the CCS clumps may be interacting with the outflowing material, the infalling clumps could be slowed down closer to the central source due to this interaction, explaining in this way the less redshifted velocities at these positions.

An alternative scenario to explain the CCS kinematics is outflowing clumps driven by a wind. If this wind exhibits a Hubble-flow type velocity, that increases with distance from the driving source (as it is observed in other outflows from class 0 protostars, Chandler & Richer 2001), we could explain the velocity pattern by background clumps interacting with, and being accelerated by the outflowing material. In order to have redshifted CCS emission at both to the NE and SW from the central source, the outflow must lie near the plane of the sky, and the CCS clumps should be associated with the back side of the outflow, both for the southwestern blueshifted CO lobe, and the (as yet) undetected northeastern redshifted CO lobe (see an schematic representation of the different models in Figure 6.10).

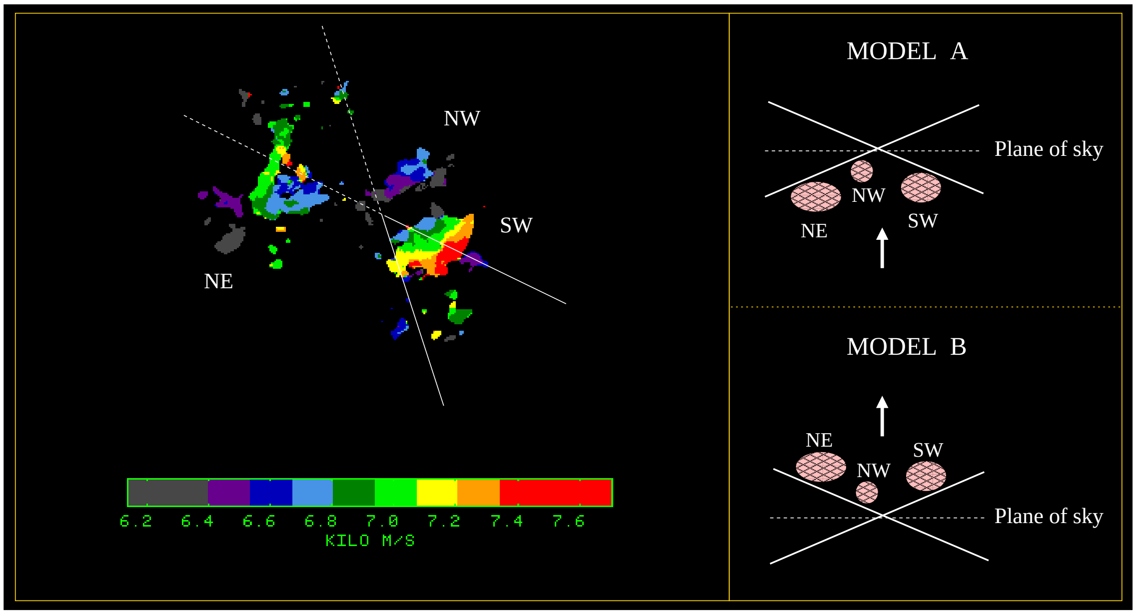

Figure 6.10: (Left panel) Map of CCS intensity-weighted mean velocity (first-order moment). The color scale ranges from 6.0 to 7.8 km s^{-1}. The proposed CO outflow geometry is represented by a cone, with solid lines associated with the blueshifted CO outflow and the dashed lines associated with the redshifted one, with the lobes almost in the plane of the sky. (Right panels) Schematic representation of the proposed models to explain the observed CCS velocity pattern. Hatched ellipses correspond to the different CCS clumps, and the cone represents the molecular outflow. Upper right panel represents foreground infalling clumps decelerated by the molecular outflow (model A), and lower right panel represents background outflowing accelerated clumps (model B). For both right panels, the observer would be located at the bottom of the page.

A way to distinguish between these two models (foreground infalling clumps decelerated by the outflow (model "A") vs. background outflowing accelerated clumps (model "B")), is to ascertain whether the motions observed in the CCS clumps can be gravitationally bound.

There are two main components in the observed motions: the internal velocity gradients within the clumps, and the bulk velocity of the whole clump with respect to the central source. For the first component, the mass M needed to gravitationally bind a cloud of size R with velocity gradient dV/dl is $M = V^2 R G^{-1}$, with $V = (dV/dl)R$. This means that the masses needed to bind the internal gradient within each clump are 1.3, 0.3, and 0.4 $M_\odot$ for clumps SW, NW, and NE, respectively. The masses derived for the clumps (Table 6.4) are of the same order of those necessary for the clumps to be bound, although we must consider this result carefully due to the very large uncertainties involved in these calculations.

On the other hand, if we consider an average velocity of each CCS clump with respect to that of the ambient cloud, and the distance from the infrared source to the center of each clump, the masses needed to bind the motions for SW, NW, and NE CCS clumps as a whole are 6, 0.4, and 6 $M_\odot$, respectively. The mass of gas contained in a region of radius equal to the distance to the central source would be 13-30 $M_\odot$ for the SW clump, 5-11 $M_\odot$ for the NW clump, and 51-120 $M_\odot$ for the NE clump, depending on the values of N_{H_2} obtained from either averaged values for NH_3 or CCS.

Therefore, we see that the observed motions in the CCS clumps can be gravitationally bound, a fact that does not allow us to discard either of the alternative models. Regardless of the real geometry and dynamics of the region, it seems that there is an important interaction of the ambient gas with the molecular outflow.

We must point out that the observed CCS clumps may not really be physical entities. These clumps are likely to represent regions of enhanced abundance of CCS (Suzuki et al. 1992; Ohashi et al. 1999). This chemical gradient of CCS is a result of variations in the local conditions of the cloud (Lai et al. 2003). However, our mass estimates to check if the motions are gravitationally bound are still valid even if the enhanced CCS emission are not physical clumps, given that we are calculating the mass of the region of gas enclosed by the CCS emission. The largest source of uncertainty is the value of the molecular abundance, which is a common problem when deriving column densities using other molecular tracers. In our calculations we consider a fractional abundance of CCS with respect to the H_2 of 0.9×10^{-10}, which is the mean value reported by Lai & Crutcher (2000) for this region.

6.4.4 Chemical evolution: CCS vs. NH_3

In previous single-dish works, a spatial anticorrelation between CCS and ammonia was found, both by comparing detections of those molecules in surveys of sources (Suzuki et al. 1992), and by mapping their emission in the same region (Lai et al. 2003). It is interesting to check whether this anticorrelation still stands when we map a source at high resolution. The overlay of our CCS and ammonia maps (Fig. 6.7) shows a clear anticorrelation between them throughout the B1-IRS region, except $\simeq 30''$ to the north of the ammonia maximum (which coincides with the NE CCS clump), where there is some superposition. This is the first time that this anticorrelation is observed at such a high resolution ($\simeq 5'' = 1750$ AU) in a star-forming region, and illustrates that the chemistry is not only time-dependent, but also exhibits small-scale spatial structure that can potentially seriously affect the interpretation of derived physical and dynamical properties if it is not properly taken into account.

The chemical gradients traced by these molecules may be the result of changing the local conditions. At this moment, most of the theoretical chemical models considering the age and distance to the cloud center, include a large number of physical parameters to study the variation of the column density, the distribution, and the fractional abundance of molecules like CCS and NH_3 among other species. Some of these models include the strength of magnetic fields, initial chemical composition of the cloud, the probability of molecules sticking to dust grains, cosmic-ray ionization rate, and cloud mass (Shematovich et al. 2003), UV photodisociation, cosmic-ray induced photoionization and photodisociation reactions, CO depletion onto grains, and desorption by cosmic-rays (Nejad & Wagenblast 1999), or core geometry and view angles (Aikawa et al. 2003). Until now, these chemical studies focused on starless cores and did not consider the effects of a central star, probably because most of the CCS studies have been made toward starless cores (Kuiper et al. 1996; Ohashi et al. 1999; Lai et al. 2003; Shinnaga et al. 2004).

The way in which all of these factors and the activity of protostars (in the case of star forming regions) can modify the classical ion-molecule or radical/neutral pathways of production of molecules like CCS (Smith 1988; Suzuki et al. 1988; Petrie 1996; Scappini & Codella 1996) needs to be studied in theoretical works to give a better interpretation of our results. The development of models that implement the onset of energetic activity associated with the formation of a star and how this affects the CCS and NH_3 production will be the key to ascertain the evolutionary stage of B1-IRS. Models treating consistently both CCS and NH_3 and considering the effect of young stars could provide more reliable values of the relative abundances and column densities of both molecules as a function of the distance from the source. On the other hand, our data on B1-IRS could be used as a reference work to test the predictions of those calculations in detail. Future comparison with other regions observed with high angular resolution will be vital for understanding the precise meaning of the ratio between CCS and NH_3 abundances in star-forming regions, in terms of chemical evolution.

Moreover, detailed chemistry studies in molecular clouds are an important science driver for the development of new interferometers (e.g. SMA or ALMA, see van Dishoeck & Blake 1998; Phillips & Vastel 2003). Our anticorrelation result at small scale proves that chemistry studies is indeed a promising line of research for these new telescopes.

The clumpy distribution of CCS emission detected in B1-IRS, has already been observed by other authors in several molecular clouds such as B335 (Velusamy et al. 1995), L1498 (Kuiper et al. 1996), and TMC-1 (Langer et al. 1995). In the case of B1-IRS, this clumpy distribution was first detected by Lai & Crutcher (2000) in the CCS $J_N = 3_2$-2_1 transition at 33.8 GHz with the BIMA interferometer with an angular resolution of $\simeq 30''$. In particular, there seems to be a spatial coincidence between BIMA clumps F and B and our VLA clumps SW and NE respectively. Moreover our VLA observations reveal a lack of CCS emission at the position of B1-IRS. This absence of emission has been suggested to be due to a lower abundance of the molecule, rather than to a density decrease, since this molecule needs high density to be excited and the density is expected to be higher towards the center (Velusamy et al. 1995). The clumpy distribution could be due to an episodic infall (as suggested by Velusamy et al. 1995 for B335).

Another possibility that it is worth considering is that CCS might be locally enhanced in shocked regions. In fact, the observed CCS clumps show kinematical signs of interaction with the outflow, which suggests that the CCS emission could be originated from gas affected by the impact of shocks. The outflow could squeeze low density gas to the higher densities ($\simeq 10^5$ cm^{-3}) needed to produce the CCS, and trigger the formation of the molecule. Such low density gas exists around dense clouds like B1, and the outflow associated to B1-IRS could interact with fresh material around the dense core. Although there is currently no chemical model that includes this kind of phenomena related to the star formation, to support the suggested enhancement, observations of other molecules have suggested that their abundance is enhanced in the environment of jets and outflows, by shock-induced chemistry, as in the case of CS (Arce & Sargent 2004), NH_3 (Torrelles et al. 1992, 1993a), or HCO^+ (Girart et al. 2000). Theoretical chemistry models support those findings (Wolfire & Koenigl 1993; Taylor & Williams 1996; Viti et al. 2002). In particular, for HCO^+ it has been proposed that in some cases its abundance may be increased by a fast outflow impinging on fragments of dense gas (Rawlings et al. 2000), and this type of interaction between outflow and dense gas is also suggested by our CCS data, although the chemical reactions involved will certainly be different.

If this abundance enhancement takes place in short timescales ($\simeq 10^5$ yr), one could expect to find clumps of the order of $5''$ at the distance of B1 (350 pc), considering a typical sound speed of $\simeq 0.1$ km s^{-1}.

Clearly, further interferometric CCS observations of the environment of other star forming regions as well as theoretical chemistry models will be useful to determine whether CCS emission tends to selectively trace regions of interaction of the outflow with its surrounding medium. These studies combined with high-resolution data of NH_3 and other molecular tracers will also help to determine the spatial distribution and chemical evolution of these species.

6.5 Conclusions

We have presented high-resolution observations of ammonia, CCS, and water masers toward the Class 0 object B1-IRS (IRAS 03301+3057). Our main conclusions are as follows:

- There is a 2MASS infrared point source located $\sim 6''$ NE from the nominal position of the IRAS source, and at the NE tip of a blueshifted CO outflow lobe. Fainter infrared emission extending towards the SW from the point source is also detected.
- There is a group of water masers associated with the infrared point source. Their elongated distribution (in the NE-SW direction), and their unbound motions suggest that these masers are tracing the base of the outflow.
- The infrared and water maser data suggest that the infrared point source traces the position of the powering source of the mass-loss phenomena in the region, and that mass is ejected along the NE-SW direction.
- We detect three clumps of CCS emission surrounding the infrared source, all redshifted with respect to the systemic cloud velocity. They show clear velocity gradients, with less redshifted gas towards the central source. We interpret these gradients in terms of clumps that are strongly interacting with a molecular outflow that lies almost in the plane of the sky.
- Ammonia emission is weak and extended. It shows a spatial anticorrelation with CCS. Although this kind of anticorrelation is known to be present in other star-forming regions, this is the first time that it has been observed with such a high-angular resolution ($\simeq 5''$).
- We suggest the possibility that CCS abundance is enhanced via shock-induced chemistry. However, theoretical calculations will be needed to confirm this hypothesis.

6.5.1 Conclusiones

Se presentan observaciones a alta resolución en amoniaco, CCS y máseres de agua en torno al objeto de clase 0 B1-IRS (IRAS 0331+3057). Las conclusiones principales son las siguientes:

- Hay una fuente infrarroja puntual de 2MASS situada a $\sim 6''$ NE de la posición nominal de la fuente IRAS y en el extremo NE del lóbulo desplazado al azul del flujo molecular de CO.
- Hay un grupo de máseres de agua asociados con la fuente puntual infrarroja. Su distribución alargada (en la dirección NE-SW) y sus movimientos no ligados, sugieren que estos máseres están trazando la base de un flujo molecular.
- Los datos de infrarrojo y de emisión máser sugieren que la fuente puntual infrarroja traza la posición de la fuente excitadora de los fenómenos de pérdida de masa en la región, y que la masa es expulsada a lo largo de la dirección NE-SW.
- Se detectan tres "grumos" de CCS alrededor de la fuente infrarroja, todos ellos desplazados al rojo con respecto a la velocidad sistémica de la nube. Muestran un claro gradiente de velocidad, con el gas menos enrojecido situado más cerca de la fuente central. Estos gradientes se interpretan en términos de "grumos" que están interaccionando fuertemente con un flujo molecular orientado casi en el plano del cielo.
- La emisión en amoniaco es débil y extendida. Muestra una anticorrelación espacial con el CCS. Aunque este tipo de anticorrelación se sabe que existe en otras regiones de formación estelar, ésta es la primera vez que se observa con alta resolución angular ($\simeq 5''$).
- Se sugiere la posibilidad de que la abundancia de CCS aumente por medio de una química inducida por choques. Sin embargo, son necesarios los cálculos teóricos pertinentes que confirmen esta hipótesis.

Chapter 7

Study of the multiple system IRAS 16293−2422: testing the cross-calibration technique for molecular lines

In this chapter we present another attempt to simultaneously detect CCS and water maser emission at 1 cm, this time towards the Class 0 protostar IRAS 16293−2422, using the VLA in its D configuration. Although these observations failed to detect CCS emission at high-resolution, we could test for the first time that the cross-calibration technique using water masers to trace atmospheric variation is feasible to improve the quality of the thermal spectral line data. We checked this by comparing radiocontinuum emission (at the frequency of the thermal CCS transition) before and after applying such a cross-calibration.

7.1 Motivation

CCS has proven to be an excellent kinematic tracer, as shown in our previous VLA study towards B1-IRS (see chapter 6), which illustrates the usefulness of interferometric CCS observations for kinematic and morphological studies. Regarding the interesting results obtained for B1-IRS with the CCS observations, we have performed similar observations in H_2O masers and CCS towards the multiple protostellar system IRAS 16293−2422. Moreover, these observations represent a new attempt to test the cross-calibration technique that failed in B1-IRS observations, due to the low flux density of its maser emission at the epoch of our observations.

IRAS 16293−2422 is a low-luminosity protostar located in the small L1689 N molecular cloud in the ρ Ophiuchus complex, at a distance of 120 pc (Knude & Hog 1998). This source is a multiple system comprising two sources, A and B, separated by $\simeq 5''$ (750 AU) along P.A. $\simeq -50^o$ (Wootten 1989). IRAS 16293−2422B seems to be a single object, while interferometric observations reveal that the object A is in its turn composed of two radio continuum sources (A1 and A2; Wootten 1989) and a possible third submillimeter companion (A_b; Chandler et al. 2005). This region hosts multiple molecular outflows (Mizuno et al. 1990; Stark et al. 2004), which seem to be powered by the different components of the protobinary system (Chandler et al. 2005). Strong water maser emission has also been observed towards this source (up to $\simeq$ 6000 Jy, Claussen et al. 1986).

Our scientific aim in this work was to study differences in morphology (fragmentation at small scales, disruption of the cloud by the outflow) and kinematics (interaction between outflowing and infalling gas) of the cloud, and compare our results in IRAS 16293−2422 (a multiple protostellar system) with the results obtained for B1−IRS (probably a single object).

From a technical point of view, with this, and the work presented in chapter 6 for B1-IRS, we tried to push to the limits the capabilities of the VLA, by using water masers to track atmospheric phase and amplitude variations. The self-calibration solutions of the strong water masers are then applied to weaker emission. It is important to point out that this cross-calibration technique has already been successfully applied to greatly improve the quality of radio-continuum maps, but this thesis represent the first attempt to use this technique for a thermal spectral line (the CCS transition at 1 cm).

CCS emission towards IRAS 16293−2422 was detected by Hirota et al. (2001) in single-dish observations at 45 GHz, reporting a main beam brightness temperature of 0.42 K with a beam of $40''$. Sources in the sample of Suzuki et al. (1992) show a mean ratio between CCS transitions at 45 and 22 GHz of 2. CCS emission is typically clumpy, and the peak intensity can be significantly higher in VLA maps that in single-dish ones. For instance, spectra of B335 taken with the Goldstone antenna (beam $45''$) and the VLA in its D configuration, show a brightness temperature 10 times higher for the latter (Velusamy et al. 1995). Moreover, the cross calibration technique using the water maser could enhance brightness by a further factor of 2. With all these considerations, the peak intensity expected for CCS emission at 22 GHz in IRAS 16293−2422 was $\sim$14 mJy beam^{-1}.

This chapter is structured as follows: in §7.2 we describe the observations and data reduction procedure. In §7.3 we show the observational and technical results of this work. In §7.4 we dicuss the cross-calibration technique problems and we summarize our conclusions in §7.5.

7.2 Observations

Simultaneous observations of the $J_N=2_1$-1_0 transition of CCS and the 6_{16}-5_{23} transition of H_2O were carried out on 2005 August 2, 3, and 6 using the VLA in its D configuration. The phase center of these observations was R.A.(J2000) = $16^h32^m22\overset{s}{.}862$, Dec(J2000) = $-24^{\circ}28'44\overset{''}{.}10$. We used the four IF spectral line mode, with two IFs for each molecular transition, one in each of right and left circular polarizations. For the CCS observations we sampled 128 channels over a bandwidth of 0.781 MHz centered at $V_{\rm LSR}$ = 4.0 km s^{-1}, with a velocity resolution of 0.082 km s^{-1}. Water maser observations were obtained using 64 channels over a 3.125 MHz bandwidth centered at $V_{\rm LSR}$ = 5.1 km s^{-1}, with 0.66 km s^{-1} velocity resolution. Our primary calibrator was J1331+305, for which we adopted a flux density of 2.5297 Jy (at the CCS frequency) and 2.5396 Jy (at the H_2O frequency) using the latest VLA values (1999.2). The source J1626-298 was used as phase calibrator (bootstrapped flux density = 2.03±0.04 Jy at the CCS frequency and 1.92±0.04 Jy at the H_2O frequency). As bandpass calibrators, we used the primary calibrator on the first and third days, and the secondary calibrator on the second day. Calibration and data reduction were performed with the Astronomical Image Processing System (AIPS) of NRAO.

The detected water maser emission was strong enough to enable self-calibration in all three observing sessions. Water maser maps were made setting the robust parameter to 0, and they were smoothed to a final velocity resolution of $\simeq$ 1.3 km s^{-1}, to mitigate the Gibbs ringing. The cross calibration technique was applied to CCS, by applying the self-calibration solutions for each data set of water maser observations, to the CCS data. Finally, we combined the CCS data for all three days with DBCON. Images of CCS emission were made with natural weighting, providing a synthesized beam of $6\overset{''}{.}0 \times 2\overset{''}{.}8$ (P.A. = 6°).

7.3 Results

7.3.1 Water masers and CCS

Our observations reveal strong water maser emission, as reported elsewhere (Wilking & Claussen 1987; Comoretto et al. 1990; Terebey et al. 1992; Claussen et al. 1996; Imai et al. 1999; Furuya et al. 2003). The spectra show three different components at $\sim$5.1, $\sim$2.5, and $\sim$0.5 km s^{-1} (see Fig. 7.1), similar in the three days of observations. We selected the day with the best signal to noise ratio (2005 August 3) in order to illustrate the shape of the spectrum and the location of the masers. Flux densities and positions of the different maser components are shown in Table 7.1.

Our results are in agreement with those reported by other authors, which show water maser spectra rich in components, most of them in the velocity coverage of -8 km s^{-1} $<$ V$_{LSR}$ $<$ 8 km s^{-1} (e.g. Claussen et al. 1996; Imai et al. 1999; Furuya et al. 2003) with different flux densities from a few Jy (e.g. Claussen et al. 1996) to more than 2000 Jy (e.g. Comoretto et al. 1990) variable in time.

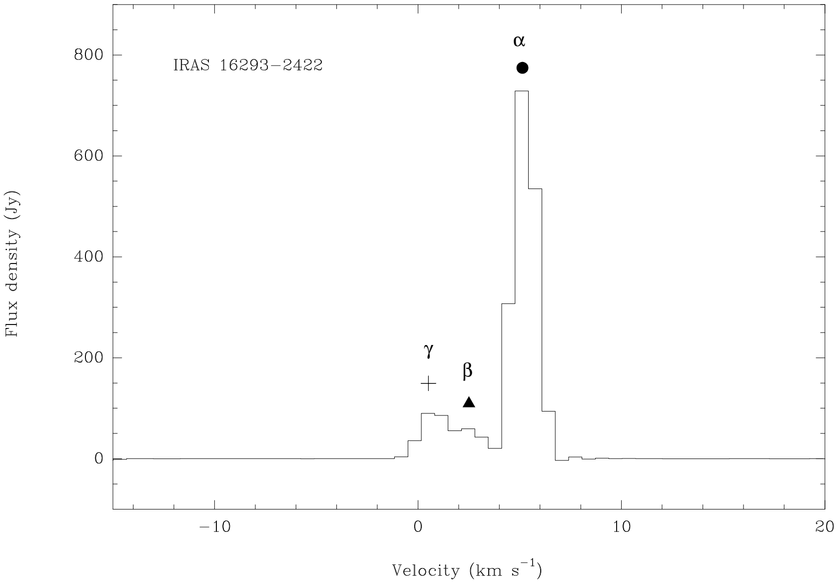

Figure 7.1: Integrated water maser spectrum obtained with the VLA toward IRAS 16293−2422, on 2005 August 3.

Table 7.1: Detected water maser components

Component	R.A. Offset [1] (″)	Dec Offset[1] (″)	Position [2,3] uncertainty (″)	Flux density [2] (Jy)	$V_{\rm LSR}$[4] (km s^{-1})
α	0	0	... [5]	730±30	5.1
β	0.594	0.251	0.003	59±3	2.5
γ	0.860	0.232	0.003	89±4	0.5

Notes to Table 7.1

[1] Position offsets of the peak of each distinct water maser feature with respect to the reference feature used for self-calibration. $(\alpha,\delta)_{J2000.0} = (16^h 32^m 22^s.825, -24^o 28' 36''.74)$.

[2] Uncertainties are 2σ.

[3] Relative position errors with respect to the reference positions

[4] LSR velocity of the spectral channel where the peak of the maser feature is detected. Velocity resolution $\sim$1.3 km s^{-1}.

[5] Reference feature. Absolute position error $\sim 0''.28$.

Water maser emission was used to apply the cross-calibration technique to CCS data, but we did not detect any CCS emission towards IRAS 16293−2422, obtaining a 3σ upper limit of $\simeq$ 28 mJy. In order to improve the signal-to-noise ratio we smoothed the CCS data up to a resolution of $\simeq$ 0.3 km s^{-1}, and we tapered the uv data to obtain a synthesized beam of $\simeq$10$''$. Nevertheless we still failed to detect the CCS emission.

The obtained CCS upper limit is higher than the estimated peak intensity (i.e. $\sim$14 mJy beam^{-1}; see section 7.1). Probably, the bad weather conditions during the observations, and the atmospheric phase fluctuations for the low elevation at which this source is visible from the VLA (less than 30°), are responsible for the non-detection.

With this negative result for the detection of CCS, we can estimate upper limits to the column density of the CCS molecule. We follow the method and the assumptions described in chapter 5, Table 5.2 to calculate the CCS column density. The estimation of the upper limit of the integrated intensity, is obtained assuming a peak intensity equal to 28 mJy, which is the upper limit derived from our observations. We calculate the corresponding peak brightness temperature from the Rayleigh-Jeans Law:

$$\left(\frac{T_b}{K}\right) = 13.6 \left(\frac{I_\nu}{\text{Jy beam}^{-1}}\right) \left(\frac{\lambda}{mm}\right)^2 \left(\frac{\theta_a\ \theta_b}{arcsec^2}\right)^{-1}$$

where I_ν is the observed peak intensity, and θ_a and θ_b are the dimensions of the synthesized beam ($6''\!.0 \times 2''\!.8$). As we did to estimate upper limits of CCS column density in Chapter 5, Table 5.2, we assumed a mean value of velocity width for the line of $\Delta V \simeq 0.5$ km s^{-1}, an excitation temperature was fixed to 5 K and $T_{ex} = T_{rot}$. With these assumptions, we obtained an upper limit of N(CCS) $\leq 2.2 \times 10^{13}$ cm^{-2}.

7.3.2 Radio continuum emission and the feasibility of cross-calibration for CCS spectral lines

Although we did not detect any CCS emission, we averaged the central 93 velocity channels of the data set for this molecule, which allowed us to study the radio continuum emission at 22.34 GHz.

We detected two radio continuum sources (see Fig. 7.2), which are unresolved by our beam. They are located at R.A.(J2000) = $16^h32^m22^s\!.86$, Dec(J2000) = $-24^\circ28'36''\!.6$ (absolute positional error $\simeq1''\!.4$), with a flux density of 3.6±2.3 mJy, and at R.A.(J2000) = $16^h32^m22^s\!.68$, Dec(J2000) = $-24^\circ28'32''\!.7$ (absolute positional error $\simeq 1''\!.2$), with a flux density of 3.8±2.3 mJy. These sources correspond to the location of the protobinary system IRAS 16293−2422 A and B reported by Wootten (1989), and their flux densities are in agreement with the fluxes reported by Chandler et al. (2005). Our angular resolution did not allow us to separate the multiple sources within component A. The water masers are associated with the A component, in agreement with Wootten (1989), see Fig. 7.2.

In order to test if the cross-calibration technique may work for spectral line data, we compared continuum maps (at the frequency of the CCS line) with and without applying the technique, and we observed an improvement in the signal-to-noise ratio of the continuum emission (see Fig. 7.2). By applying this technique we obtained an improvement of ∼4% in the rms, ∼18% in the peak intensity, and ∼25% in the signal-to-noise ratio, which changes from 4σ to 5σ. With these results, we confirm for that cross-calibration technique works and can eventually be applied to improve maps in CCS line observations.

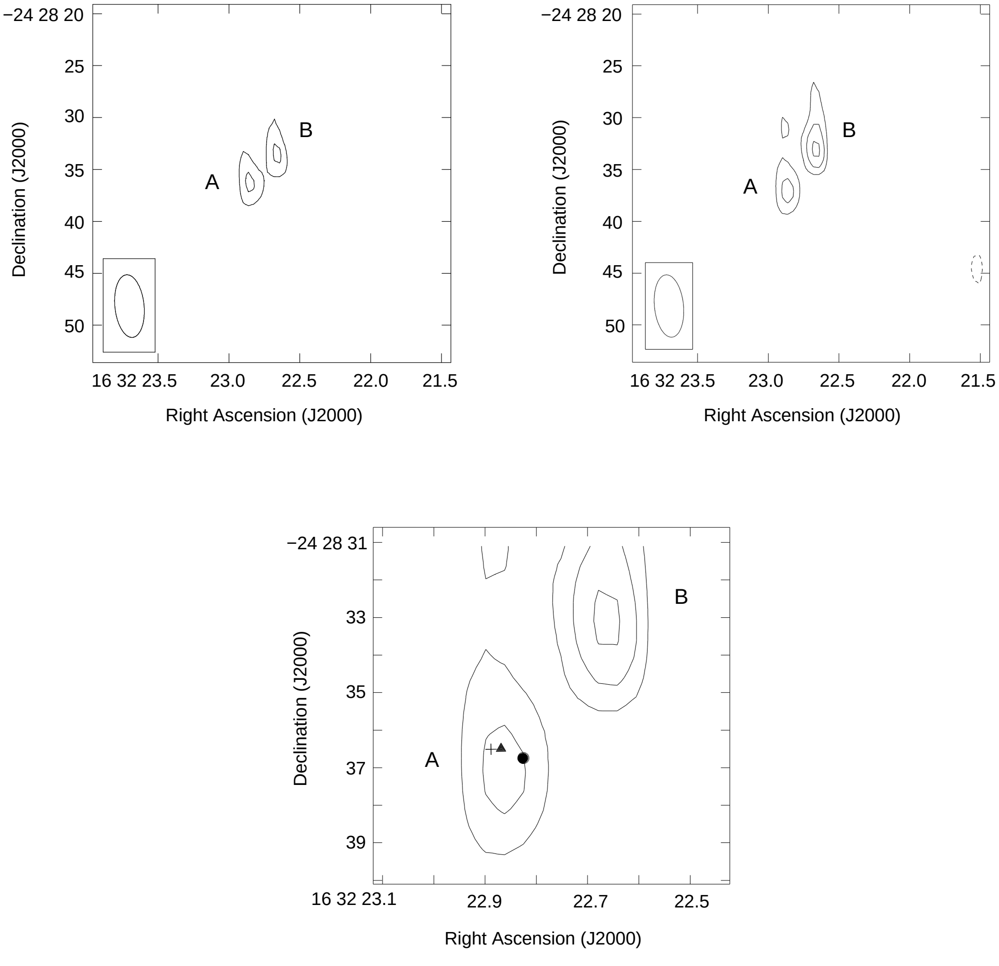

Figure 7.2: Contour maps of the continuum emission from IRAS 16293−2422. Top Left: Map from data reduced without applying the cross-calibration technique. Contour levels are at −0.96 mJy beam^{-1}, and from 2.9 to 3.8 mJy beam^{-1}, at steps of 0.96 mJy beam^{-1}. Top Right: Map from data with the cross-calibration technique applied. Contour levels are at −0.93 mJy beam^{-1}, and from 2.8 to 4.6 mJy beam^{-1}, at steps of 0.93 mJy beam^{-1}. Bottom: Close-up of the cross-calibrated map. The cross, triangle, and circle represent the position of the water maser components (symbols have the same meaning as in Fig 7.1).

7.4 Comments and prospects for cross-calibration on spectral lines

In this thesis we have tried to apply the cross-calibration technique on spectral thermal lines twice, in the B1-IRS region (chapter 6), and in IRAS 16293−2422 (this chapter). Both attempts illustrate the difficulties of this technique, since two conditions are required for applying the cross-calibration successfully:

1. To observe a strong water maser in order to find the self-calibration solutions that will be applied later to the thermal emission.
2. To have an relatively intense and clumpy distribution of CCS emission and good weather conditions during the observation, to make possible the detection of CCS thermal emission.

The first condition is crucial in the cross-calibration technique, but very unpredictable. It is well known that water maser emission in low-mass young stellar objects shows a strong variability on short timescales ($<$ 1 month, Haschick et al. 1983; Claussen et al. 1996; Wilking et al. 1994a; Furuya et al. 2003). In the case of B1-IRS (Chapter 6), the technique could not be applied because the water maser was not strong enough.

The second condition is important to detect CCS emission with interferometric techniques. If CCS emission would be completely extended without showing any clumpy distribution, interferometers would be "blind" to this emission, due to the lack of short spacings. Another pre-requisit to have success in the observation of CCS is that the clumps must be strong enough and we must observe them under good weather conditions, otherwise the CCS thermal emission lines may not be detected. This part failed in the observations towards IRAS 16293−2422. In addition, no single dish CCS maps were done before towards this cloud and, although previous maps show that the clumpiness is a common characteristic on CCS spacial distribution (Hirahara et al. 1992; Velusamy et al. 1995; Kuiper et al. 1996; Lai & Crutcher 2000; Lai et al. 2003), the degree of clumpiness in our source was unknown.

In this chapter we showed for the first time that this cross-calibration technique may eventually work for CCS lines, although we could not present the "improved" cross-calibrated CCS maps. At the very end of this thesis work, and after we observed a reappearance of the water maser emission in L1448C region (on 2005 March 13 with the Robledo-70m antenna) after more than ten years of non-detections, we observed the L1448 region (one of our regions detected in CCS in chapter 5) in both CCS and water masers using the VLA. These observations will be part of our future work, but a preliminary reduction of the data shows strong water maser emission and a clumpy CCS distribution, thus it seems that we may finally be able to apply this technique for spectral lines and obtain high-quality CCS maps.

7.5 Conclusions

We have performed simultaneous observations of CCS and H_2O masers at 22 GHz towards IRAS 16293−2422, in order to study the morphological and dynamical conditions of the surrounding cloud. The results and conclusions of these observations are the following:

- We detected strong enough water maser emission to self-calibrate the data. Three distinct water maser components are evident.
- We used the self-calibration solutions obtained for the water maser data, to apply for the first time the cross-calibration technique to the CCS spectral line data, but we failed to detect CCS emission. The bad weather conditions during the observations and the atmospheric phase fluctuations at low elevations yielded a final 3σ upper limit above the expected CCS brightness temperature, despite the application of cross-calibration.
- We averaged 93 CCS central channels, and we detected two radio continuum sources, which correspond to the components A and B of the protobinary system that exist in the region. The water maser emission is associated to the southern A component, in agreement with other works.
- We have compared the radio continuum maps with and without applying the cross-calibration technique and we obtained an improvement of $\sim$25% in the signal-to-noise-ratio of the cross-calibrated maps. This indicates that the cross-calibration of thermal lines using water maser is a promising technique. Our work in this thesis represents the first attempt to pursue such a technical development.

7.5.1 Conclusiones

Hemos realizado observaciones simultáneas de CCS y máseres de H_2O a 22 GHz en IRAS 16293−2422 para estudiar las condiciones morfológicas y dinámicas de la nube que la rodea. Los resultados y las conclusiones de estas observaciones son las siguientes:

- Hemos detectado emisión de máser de agua lo suficientemente fuerte como para autocalibrar los datos. Podemos distinguir tres componentes máser distintas.

- Hemos usado las soluciones obtenidas en la autocalibración de los datos de máseres de agua para aplicar por primera vez la técnica de calibración cruzada a los datos de línea espectral de CCS, pero no hemos detectado emisión de CCS. Las malas condiciones atmosféricas durante las observaciones y las fluctuaciones de fase producidas por la atmósfera a elevaciones bajas produjeron un límite superior (3σ) por encima de la temperatura de brillo de CCS esperada, a pesar de la aplicación de la calibración cruzada.

- Hemos promediado 93 canales centrales de CCS y hemos detectado dos fuentes de radio continuo, que se corresponden con las componentes A y B de un sistema protobinario existente en la región. La emisión de los máseres de agua está asociada a la componente del sur (A), en concordancia con otros trabajos.

- Hemos comparado los mapas de radio continuo obtenidos aplicando y sin aplicar la técnica de calibración cruzada y hemos hallado una mejora del $\sim$25% en la relación señal a ruido de los mapas donde la calibración cruzada ha sido aplicada. Ésto indica que la calibración cruzada en líneas térmicas usando máseres de agua es una técnica prometedora. El trabajo de esta tesis presenta el primer intento de aplicación de esta técnica.

Chapter 8

Modeling molecular line emission from accretion irradiated disks

In this chapter we model the expected molecular line emission from protoplanetary disks, modifying different physical parameters to obtain distinctive observational signatures. Our aim is to determine the kind of observations that will allow us to extract information about the physical parameters of disks. With this purpose we perform a statistical analysis of principal components and a multiple linear correlation on our set of results from the models. We also present prospects for future molecular line observations of protoplanetary disks using SMA and ALMA.

8.1 Introduction and motivation

The mass of disks around young stars is $\sim 99\%$ gas and only 1% dust. However, since the dust opacity is large compared to the gas opacity in a wider range of wavelengths (i.e., from near to far IR), the dust component dominates the absorption and reprocessing of stellar radiation and the emergent spectral energy distributions (SEDs) of disks around Classical T Tauri (CTTS) and Herbig Ae stars (HAe). Most of the models constructed to explain observed SEDs have taken into account only the dusty component in the calculation of the disk temperature (Chiang & Goldreich 1997; D'Alessio et al. 1998, 1999, 2001). In spite of this simplification, these models have been successful to explain the observed SEDs. However, SEDs are not sensitive to kinematical information, details of the radial and vertical temperature distribution, the chemistry of the gaseous component (Aikawa et al. 1996, 1997; Aikawa & Herbst 1999; van Zadelhoff et al. 2001), the possibility that the gas in the upper layers is hotter than the dust in lower layers by absorption of UV and X-rays (i.e., Glassgold et al. 2004) and/or photo-electrical effect (i.e., Nomura & Millar 2005), etc.

The study of molecular line emission from disks around young stars is an important tool to infer disks physical properties (e.g., Dartois et al. 2003; Carr et al. 2004). An advantage of a spectral line is that emission at different frequencies/velocities might be probing different disk regions, making lines an important test for disk models. However, this is also a disadvantage in some sense, since one observes intensities convolved with the beam of the telescope and with a finite spectral resolution, and therefore the information of the different regions is mixed up in a complicated way. Thus, the analysis and relationship between observations and model properties might become very complicated and difficult to disentangle. There are some previous works that compare molecular line emission from protoplanetary or circumbinary disks with specific models of such an emission (e.g., Koerner et al. 1993; Guilloteau & Dutrey 1998; Qi et al. 2003, 2004) and, in general, agreement between model and observations is fairly good, at least in the general appearance of the maps. However, given the great deal of physical parameters involved in the resulting molecular line emission, it is not straightforward to determine those parameters from a particular observation just by fitting an emission model.

Our main aim in this chapter is to identify a set of observational characteristics that give most information on the physical properties of the disk. Such observational characteristics should then be given the heaviest weight in a fit between observations and model aiming to determine physical parameters in a disk. In order to achieve this goal, we have developed a grid of molecular line emission models calculated for various mass accretion rates, radius, viscosities and maximum dust grain radius distributions. The small size scale of a protoplanetary disk (∼100 AU) and their low temperatures (∼ 100 K; Beckwith et al. 1990) require observations with high sensitivity and subarsecond high-angular resolution, since 100 AU subtends $0\farcs7$ at 140 pc (the distance to the Taurus cloud). This make interferometric observations necessary to carry out this kind of studies. With the intention of reproduce a real interferometric observation of a protoplanetary disk with different physical parameters, we resolved the transfer equation and convolved each model with a beam of $0\farcs4$, as a compromise between resolution and sensitivity. From each resultant map, we have measured different observational signatures, as if they were data from a real interferometric observation. Finally, in order to obtain the best combinations of such observational parameters that yield more information about the physical characteristics of disks, we have undertook a novel statistical approach to link observational properties of the expected molecular line emission with the underlying physical properties of the disk, by means of a principal component and multiple linear correlation analysis. We will try to show that this is a promising type of analysis to prepare the observations with the new generation of millimeter and submillimeter interferometers.

In this study it is extremely important to choose an appropriated molecular transition sensitive to the physical parameters in which we may be interested. To carry out our study we have selected the $C^{17}O(J=3 \rightarrow 2)$ transition at 337 GHz. This line is a high excitation transition of a CO isotope with very low abundance, which makes it less susceptible to be affected by absorption and/or emission from surrounding cloud material. This transition is also a suitable candidate to be observed in protoplanetary disks using SMA and ALMA, as shown by Gómez & D'Alessio (2000).

This chapter is structured as follows: in §8.2 we describe the assumptions to calculate the disk structure models and the initial input parameters. In §8.3 we explain the radiative transfer and we discuss the selection of the $C^{17}O$ (3-2) as the molecular line to make our study. In §8.4 we outline the network of models and the general trends of the line emission maps. In §8.5 we describe the statistical study that identify the set of observational characteristics that give most information on the physical properties of the disk, and we comment the results derived in §8.6. In §8.7 we perform a study of the detectability of our modeled disks with SMA and ALMA. Finally, in §8.8 we show the comments and prospects for these studies and we summarize the conclusions in §8.9.

8.2 Disk structure models

8.2.1 Assumptions

We base our calculations of molecular line emission, on structure models of accretion disks irradiated by the central star, which have been previously used to explain different observations of classical T Tauri Stars. The assumptions and calculation method of such models are described in D'Alessio et al. (1998, 1999, 2001). In summary, the disk is assumed to be in steady state, with a constant mass accretion rate $\dot{M}$ and an $\alpha-$viscosity (Shakura & Sunyaev 1973), with a constant value of the viscosity parameter α. The disk is in vertical hydrostatic equilibrium in the gravitational potential well of the star, neglecting the disk self-gravity. We assume that gas and dust are thermally coupled, having the same temperature everywhere. This dust/gas temperature enters in the calculation of the disk volumetric density distribution through the integration of the hydrostatic equilibrium equation. The main heating mechanisms considered are viscous dissipation and stellar irradiation. The viscous dissipation is important in heating the inner regions (close to the star and close to the midplane), the direct stellar irradiation heats the disk atmosphere, and the stellar radiation scattered and reprocessed by the disk upper layers heats the whole vertical structure. The transfer of radiation through the disk is calculated taking into account that the dust scatters and absorbs stellar and disk radiation, implying that the temperature structure depends on the dust properties. The viscous irradiated disk models used in the present study show the temperature inversion previously found by Calvet et al. (1991, 1992), i.e., at the outer disk, $R \gtrsim 10$ AU, the upper layers are hotter than the disk midplane, because they are heated by direct stellar irradiation (see also Chiang & Goldreich 1997 and D'Alessio et al. 1998).

The dust opacity is calculated using the Mie theory for compact spherical grains. We consider a distribution of sizes given by $n(a) = n_0 a^{-p}$, where a is the radius of the grains, n_0 is a normalization constant, and p is a free parameter. In this work, we have adopted p = 3.5 from Draine & Lee (1984) and the model of dust composition proposed by Pollack et al. (1994) with the variations introduced by D'Alessio et al. (2001). To account for the possibility of dust growth, we adopt different values of maximum grain sizes. Dust grains of different sizes have different opacity at mm wavelengths, affecting the molecular line emission in different ways. The existence of bigger grains in disks than in the interstellar medium was proposed to explain the observed slope of the continuum SED at millimeter wavelengths (Beckwith & Sargent 1991). Large grains could be depleted from higher layers of the disk, but could be well mixed with gas below a few gas scale heights. For simplicity, the disk models adopted here (from D'Alessio et al. 2001), assume that gas and dust are well mixed. This seems a reasonable assumption if the molecular line is formed closer to the midplane than to the upper layers. This point will be discussed later (subsection 8.3.1).

8.2.2 Input parameters

For the present study we have considered the following input parameters: maximum disk radius (R_d), maximum radius of dust grains (a_{max}), disk mass accretion rates ($\dot{M}$), and viscosity parameter (α) (see values in Table 8.1).

Table 8.1: Initial physical parameters

R_d (1) (AU)	a_{max} (2) (μm)	$\dot{M}$ (3) (M⊙/year)	α (4)
50	1	10^{-9}	0.001
100	10	$3\ 10^{-8}$	0.005
150	10^2	10^{-7}	0.01
	10^3		0.02
	10^4		0.05
	10^5		

Notes to Table 8.1
(1) Disk radius
(2) Maximum radius of dust grains
(3) Mass accretion rate
(4) Viscosity parameter

We have adopted typical parameters of a T Tauri star from Gullbring et al. (1998), i.e., $M_* = 0.5$ M$_\odot$, $R_* = 2$ R$_\odot$, and $T_* = 4\,000$ K for all the models. The disks are assumed to be at 140 pc, the distance of the Taurus molecular cloud (Kenyon, Dobrzycka and Hartmann 1994), with a typical inclination angle i = 60°. It is important to mention that each disk structure is self-consistently calculated given these input parameters. This means that the whole disk structure is affected by all the parameters, consequently affecting the line properties. This might complicate the analysis of the resulting line properties, but we think this gives a more realistic description of the interplay between the different variables.

8.3 Radiative transfer and molecular line emission

The model of the disk structure provides a detailed density and temperature distribution through the disk as a function of the height and the distance to the disk center. To derive the line intensity for a given molecular transition, we must resolve the transfer equation. We have used the same assumptions and formalism that Gómez & D'Alessio (2000), and we summarize them briefly here. We assume local thermal equilibrium for the population of the molecular energy levels and we consider thermal line profiles. We divide the disk in a grid of cells considering isovelocity lines and their perpendicular lines (see Appendix in Gómez & D'Alessio 2000). We integrate the transfer equation $dI_\nu/ds = \kappa_\nu \rho (S_\nu - I_\nu)$ through the line of sight at the center of each cell, where I_ν is the intensity, κ_ν is the absorption coefficient that consider the contributions from the line and continuum, i.e., $\kappa_\nu = \kappa_c + \kappa_l$, ρ is the mass density of the gas, and S_ν the source function. The coefficient κ_c is dominated by dust and we consider pure absorption opacity of each kind of dust grains size. The absorption coefficient for a molecular transition is calculated as:

$$\kappa_l = \frac{A_{ij} c^2}{8\pi\nu^2} \frac{g_i}{g_j} \left[1 - \exp\left(-\frac{h\nu}{kT}\right)\right] \frac{n_j}{\rho} \Phi(v)$$

where A_{ij} is the Einstein coefficient for the i→j transition, ν is the frequency of the transition, g_i and g_j are the statistical weigh t for the upper and lower states respectively, n_j is the density of molecules in the lower energy level, and the $\Phi(v)$ is the thermal line profile.

In order to derive the flux density, we convolved all our models with a beam of $0\farcs4$ of HPBW, as a compromise between resolution and sensitivity. Finally we subtract the continuum emission to isolate the flux density of the molecular line, obtaining a set of model results that reproduce a real observation of a protoplanetary disk with different physical parameters.

8.3.1 Selection of the emission line transition

It is very common that young stellar objects like T Tauri stars are still embedded in the material of the parental cloud. The envelope that surrounds the disk-star system is composed by cold gas and dust that could hide the disk emission.

On one hand, the surrounding material could absorb the emission from the hotter, innermost part of the disk structure. This problem can be solved selecting molecular transition whose energy is high enough to trace the hotter gas from the disk, while few molecules in the colder envelope are in the states involved in this transition, thus avoiding line absorption at the envelope. However, the frequency of the transition must not be too high, because otherwise the dust in the envelope would become optically thick. On the other hand, the molecular line emission from the whole cloud could hide the deeper emission from the disk, as it is usually the case for the more abundant CO isotopes. To make sure that the observed emission comes only from the disk structure, we must select a molecular species of low abundance for which the envelope is optically thin and therefore its emission would be negligible.

In order to fulfill these conditions, we have chosen the ($J=3 \rightarrow 2$) transition of the $C^{17}O$ molecule at 337 GHz. Its molecular abundance relative to H_2 is low, 5.0×10^{-8} (White & Sandell 1995) and the frequency transition at 337 GHz is still low enough to avoid being much absorbed by the dusty envelope.

In a recent work, Dartois et al. (2003) have studied the disk vertical temperature structure using different isotopes of CO. Being characterized by different opacities, different lines trace the gas at distinct depths. Dartois et al. (2003) find a good agreement between the inferred temperature for each transition/isotope and the temperature where $\tau \sim 1$ in irradiated (dusty) disk models. Following Dartois et al. (2003), we have studied the formation region of different molecular lines from different isotopes of CO in our grid of disk models. To illustrate this study, we have selected several disk models with different physical characteristics, represented in Figure 8.1. In that plot, we can see that $C^{17}O$ is formed closer to the midplane than the rest of the isotopes. This fact makes the LTE assumption acceptable, since the region that mainly contribute to the line emission shows higher densities than the critical density of the selected transition ($\simeq 5 \times 10^4$ cm^{-3}).

In addition, given the high gas densities in the disk, we expect that the abundance of this isotope, would be less affected by photodisociation produced by the incident radiation, since it would be shielded against it, specially in the deepest layers. Moreover, theoretical models of the evolution of molecular abundances in protoplanetary disks, predict depletion of CO from the gas phase for temperatures below 20 K (Aikawa et al. 1996) and therefore, depletion is probably not significant for the chosen molecule and for the disk radii we are considering here (< 150 AU), and therefore the assumption that gas and dust are well mixed seems reasonable.

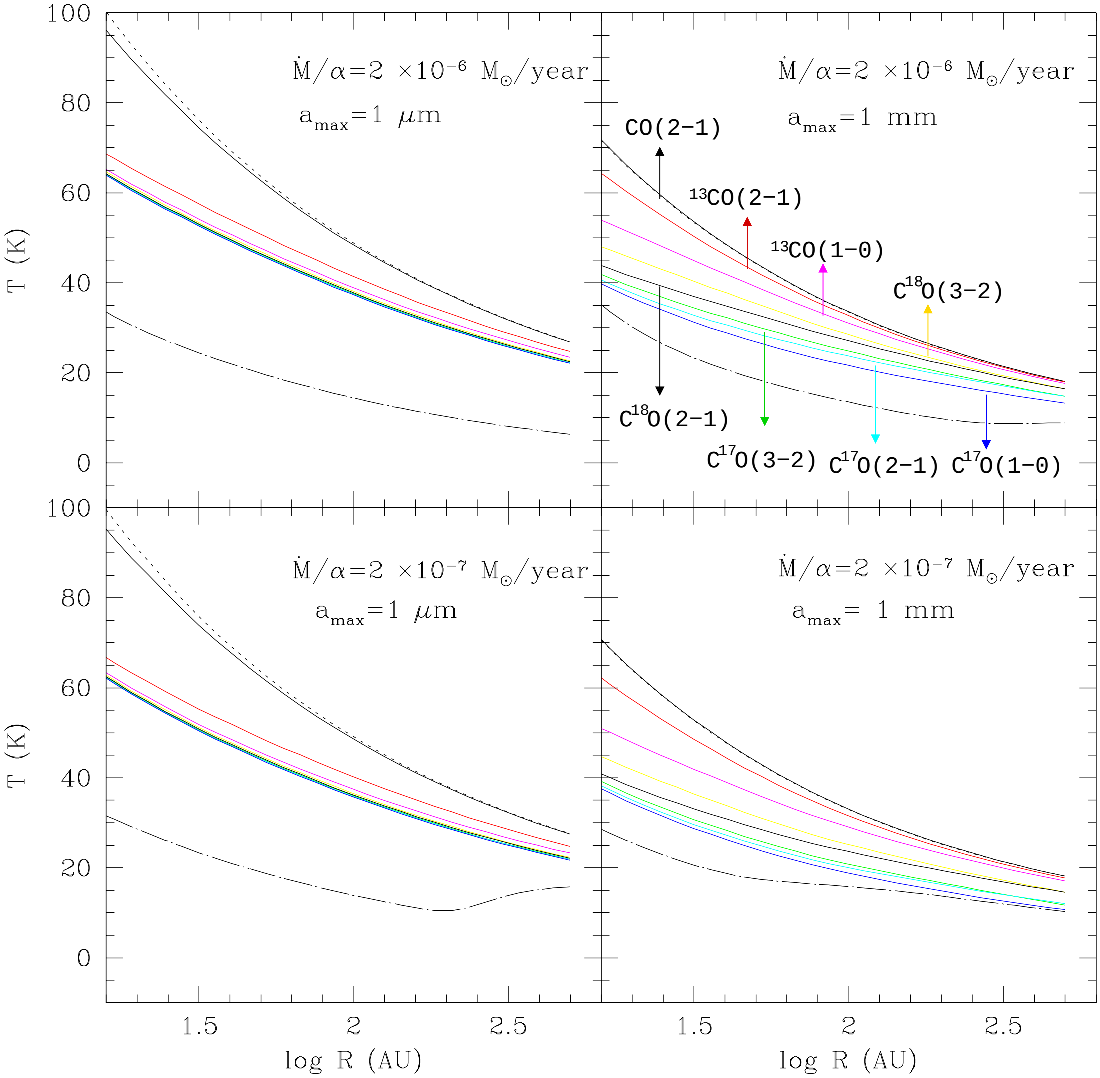

Figure 8.1: Temperature for which $\tau_\nu = 1$ for different transitions of different CO isotopes, versus different values of disk radius. Dotted and line-dotted lines represent the disk surface temperature and the central temperature of the disk, respectively. We show a sample of selected disks models at $v = 0$ km s^{-1}, for different values of maximum grain radius and $\dot{M}/\alpha$.

8.4 Results

We have calculated the expected emission in the $C^{17}O(3\text{-}2)$ transition for a typical T Tauri star with a disk inclination angle of 60°, and for all possible combinations of the physical parameters showed on Table 8.1. We had a total of different 241 models for which we have solved the radiative transfer equation at 12 different velocities, from -2.5 to 2.5 km s^{-1} at steps of 0.5 km s^{-1}. The results are maps as shown in Fig 8.2, in which we only show the positive velocities, since the maps are similar and almost symmetrical in negative velocities to the ones shown here (there are slight differences though, due to the hyperfine structure of the $C^{17}O$ transition). From each map we have measured the following observational signatures as if they were data from a real interferometric observation: intensity of the principal (northern) and secondary (southern) peak at each velocity, distance from disk center to principal peaks, half power sizes of the emission, and velocity at which the maximum intensity is present. These represent a total of 43 different observational parameters for each input model.

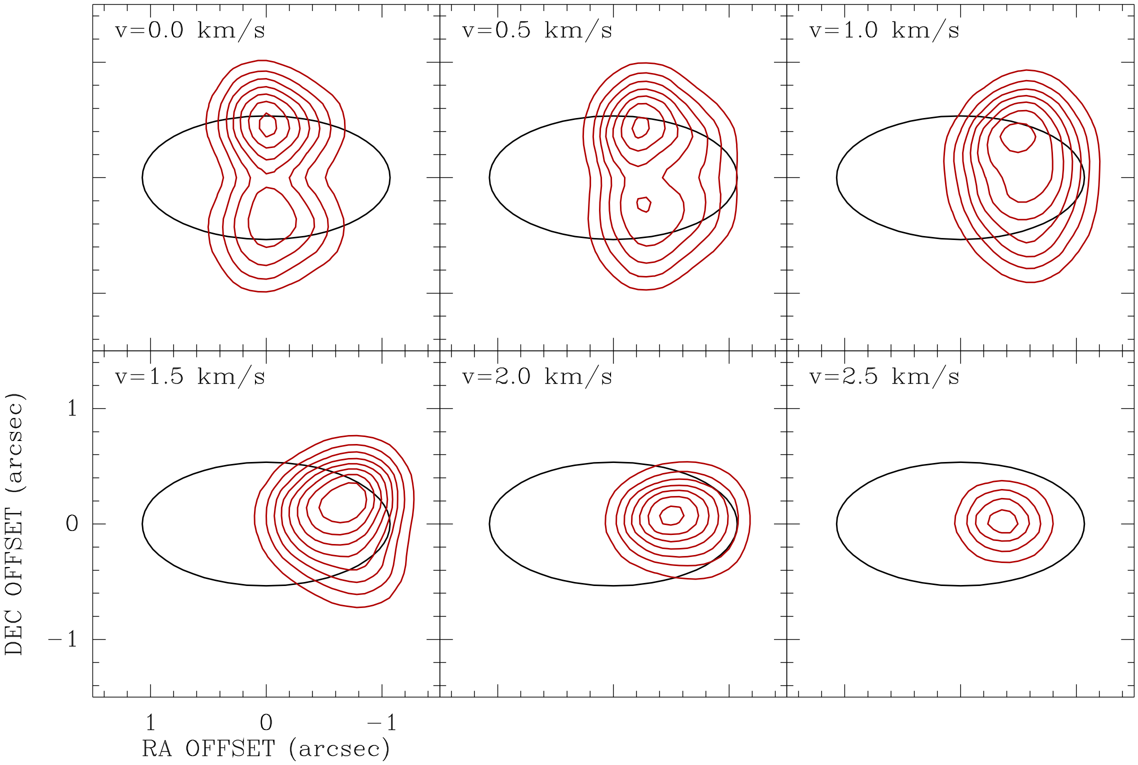

Figure 8.2: Emission maps at different velocities for a disk with radius = 150 AU, a_{max} = 10 μm, i = 60°, α = 0.01 and mass accretion rate = $10^{-7} M_{\odot}$/year. Maps have been convolved with a $0''.4$ beam. The lowest contour and the increment step are 20 mJy/beam. The ellipse traces the outer edge of the disk.

8.4.1 Line emission maps

In all maps obtained from our grid of models we observe the same tendencies as Gómez & D'Alessio (2000). Summarizing, we observe an asymmetry on both sides of the major axis, as expected from optically thick emission. The areas further away from the observer (positive declination in Fig. 8.2) show line emission of higher intensity because the line of sight intercepts areas of the disk closer to the central star, where the gas is warmer. This results is confirmed in DM Tau spectral line observations by Dartois et al. (2003), where an inclination angle $i \simeq -37^{\mathrm{o}}$ was assumed. We notice another asymmetry on both sides of the minor axis, that it is more pronounced when approaching to the velocity of the cloud (v = 0.0 km s^{-1}). It caused by the asymmetry of the hyperfine structure in the C^{17}O molecule.

We find that the maximum intensity of the line at the systemic velocity ($v = 0$ km/s) traces the outer edge of the disk. As previously discussed by Sargent & Beckwith (1991) and Gómez & D'Alessio (2000), this is a consequence of the fact that the effective area emitting at a given velocity within the beam increases with the distance to the central star more steeply than the decrease of brightness temperature with distance.

Moreover, at the center of the disk the emission intensity diminishes, and we can even see absorption lines in some of our maps. The cause is the opacity of the dust continuum emission. High continuum opacities (that are common in the central part of the disks) reduce the contrast between the emission lines and the continuum, and, if it is high enough, lines could show up in absorption.

8.5 Statistical tools

As we mentioned in section 8.4, we chose a set of 43 different observational parameters to characterize the maps resulting from our model calculations. These parameters are, in principle, somewhat arbitrary. If we want to simulate a real observation, in which we would like to extract information about the underlying physical characteristics of disks, it is obvious that some of these 43 parameters will have more informative power, while some may turn out to be irrelevant. Moreover, it is likely that not all the chosen observational parameters will be independent.

Here, we have undertook a statistical analysis to try to identify a set or a combination of observational parameters that could render more information about the disks properties. First, we used a principal component analysis to reduce the number of observational parameters to a small, informative set. Later, we investigate whether we can obtain quantitative values of physical magnitudes from observational parameters, by means of multiple linear regression.

8.5.1 Principal Components

The principal component analysis is a statistical technique that provides a dimensional reduction of a set of variables. In our case, each of the initial 43 observational parameters would be an axis in a system of coordinates in a multidimensional space. The method consists of finding a set of orthogonal axes in which the variance (heterogeneity) of our data is maximum (see Thurstone 1947; Kaiser 1958). This is solved through a linear and orthogonal transformation that corresponds to a rigid rotation of the original data into a new set of coordinates. The eigenvalues obtained provide information about the variances of the data in the new space, and the eigenvectors represent the direction of the axes in the new space of representation of our data. In our study, this analysis reduces the number of observational signatures necessary to derive information about the physical parameters, to a smaller set of linearly independent parameters: the principal components.

8.5.2 Multiple linear correlation

In order to quantitatively estimate each physical parameter from the set of observational variables, we have also carried out a multiple regression analysis (Pearson 1908). In our case, the obtained principal components will be considered the independent variables, and the physical properties of the disk will be the dependent ones. The multiple linear correlation analysis will then try to make the best fit, to derive a linear function of the form:

$$y_i = a_1 x_1 + a_2 x_2 + ... + a_j x_j \ ,$$

where y_i is the dependent variable, and x_j are the independent ones. In an ideal case (correlation coefficient $\simeq 1$), we would obtain a function with a good predictive power for the dependent variable. For our particular problem, we would like to obtain a formula with which, from a set of observational parameters, we could calculate the physical characteristics of the disk.

Moreover, to test the signification of the multiple regression we applied the F-Snedecor test (Snedecor 1934) as hypothesis testing. The ratio of two chi-squares divided by their respective degrees of freedom follows an F distribution. The test consist of comparing the relation between the variance of the predicted values for the dependent valuable and the error variance with the value of the F distribution.

8.6 Observational signatures vs. physical parameters

8.6.1 Eigenvalues and Eigenvectors of Principal Components

To reduce the number of relevant components in the principal component analysis, we adopted the Kaiser criterion (Kaiser 1960), which only retains factors with eigenvalues greater than 1. In our case, the criterion selects four factors, which account for 91% of the total variance of the system. In fact, the first and the second factors alone represent 82% of the total variance. Therefore, most of the following analysis is based on these two first principal components.

We have represented the eigenvectors in Table 8.2, for each principal component. The numerical entries in this table show the linear combination coefficients for each observational parameter, used to build the corresponding principal component. Therefore, they indicate the relative weight of each observational parameter on the components.

Table 8.2: Eigenvectors

Observational Parameters	PC1	PC2	PC3	PC4
$I(v_0)$[1]	-0.0279	0.0020	0.0030	0.0033
$I(v_{0.5})$[1]	-0.0276	0.0019	0.0029	0.0034
$I(v_1)$[1]	-0.0281	0.0007	0.0022	0.0035
$I(v_{1.5})$[1]	-0.0340	-0.0023	0.0024	0.0040
$I(v_2)$[1]	-0.0276	-0.0086	0.0016	0.0040
$I(v_{2.5})$[1]	-0.0118	-0.0082	0.0028	0.0040
$r(v_0)$[2]	-0.1360	0.0388	-0.0072	-0.0137
$r(v_{0.5})$[2]	-0.1462	0.0325	-0.0041	-0.0169
$r(v_1)$[2]	-0.1581	0.0448	-0.0015	-0.0086
$r(v_{1.5})$[2]	-0.1930	0.0100	0.0266	-0.0262
$r(v_2)$[2]	-0.1077	0.0075	-0.0030	-0.0150
$r(v_{2.5})$[2]	-0.0483	0.0310	-0.0094	-0.0062
$I_{sec}(v_0)$[3]	-0.0289	-0.0047	0.0004	0.0019
$I_{sec}(v_{0.5})$[3]	-0.0297	-0.0042	0.0006	0.0022
$I_{sec}(v_1)$[3]	-0.0179	-0.0091	-0.0024	-0.0018
$I_{sec}(v_{1.5})$[3]	-0.0003	0.0007	-0.0009	-0.0004
$I_{sec}(v_2)$[3]	0.0000	0.0000	0.0000	0.0000
$I_{sec}(v_{2.5})$[3]	0.0000	0.0000	0.0000	0.0000
$a(v_0)$[4]	-0.0595	0.0426	0.0316	0.0034
$b(v_0)$[4]	-0.0790	0.0334	0.0272	-0.0184
$a(v_{0.5})$[4]	-0.1615	-0.0309	0.0259	0.0043
$b(v_{0.5})$[4]	-0.1947	-0.0788	0.0523	-0.0076

Table 8.2: (continued).

Observational Parameters	PC1	PC2	PC3	PC4
$a(v_1)^4$	-0.1138	-0.0250	0.0281	-0.0024
$b(v_1)^4$	-0.0388	-0.0024	0.0041	0.0017
$a(v_{1.5})^4$	-0.1777	-0.1926	-0.0350	-0.0615
$b(v_{1.5})^4$	-0.2271	-0.1499	0.0086	0.0743
$a(v_2)^4$	-0.2420	-0.0171	0.0543	-0.0023
$b(v_2)^4$	-0.1181	0.0056	0.0133	-0.0084
$a(v_{2.5})^4$	-0.0286	0.0168	-0.0054	0.0011
$b(v_{2.5})^4$	-0.0028	0.0114	-0.0067	0.0010
$a_{sec}(v_0)^5$	-0.0746	0.1023	0.0703	0.0434
$b_{sec}(v_0)^5$	-0.0436	0.1026	0.0406	-0.0607
$a_{sec}(v_{0.5})^5$	-0.0026	0.0161	-0.0127	-0.0076
$b_{sec}(v_{0.5})^5$	-0.0006	0.0047	-0.0057	-0.0011
$a_{sec}(v_1)^5$	0.0000	0.0000	0.0000	0.0000
$b_{sec}(v_1)^5$	0.0000	0.0000	0.0000	0.0000
$a_{sec}(v_{1.5})^5$	-0.0733	0.0985	0.0683	0.0525
$b_{sec}(v_{1.5})^5$	-0.0398	0.0951	0.0398	-0.0549
$a_{sec}(v_2)^5$	-0.0040	0.0185	-0.0141	-0.0097
$b_{sec}(v_2)^5$	-0.0008	0.0043	-0.0060	-0.0006
$a_{sec}(v_{2.5})^5$	0.0000	0.0000	0.0000	0.0000
$b_{sec}(v_{2.5})^5$	0.0000	0.0000	0.0000	0.0000
${v_{I_{max}}}^6$	0.3176	-0.1431	0.1527	-0.0241

Notes to Table 8.2

[1] Intensity of the principal peak at each velocity (0, 0.5, 1, 1.5, 2, 2.5 km s^{-1})

[2] Distance from disk center to principal peaks

[3] Intensity of the secondary peak at each velocity

[4] Mayor (a) and minor (b) axis of the half power sizes of emission for the principal peak of intensity at each different velocity

[5] Mayor (a) and minor (b) axis of the half power sizes of emission for the secondary peak of intensity at each different velocity

[6] Velocity at which the maximum intensity is present

For the first principal component (PC1) the physical parameters with a larger weight in its definition are (in order of decreasing relative weights) the velocity of the peak emission, the half power sizes for principal peaks at intermediates velocities, and the distance from principal peaks to center. The parameters that define the second principal component (PC2) are the half power sizes of principal peaks at 1.5 km s^{-1}, the velocity of the peak emission, and the half power sizes of secondary peaks at 0.0 and 1.5 km s^{-1}.

The third principal component (PC3) is defined by the velocity of the peak emission and the half power sizes for principal and secondary peaks at 0.0 and 1.5 km s^{-1}. Finally, the physical parameters that define the forth principal component (PC4) are the half power sizes for principal peaks at 1.5 km s^{-1} and for secondary peaks at 0.0 and 1.5 km s^{-1}.

8.6.2 PC1(kinematical component)-PC2(spatial component) diagrams

Due to the fact that the first and the second principal component represent the 82% of the total variance of the system, we have represented all our models in a PC1-PC2 diagram, to check whether such diagrams can be used to discriminate disks with particular physical characteristics, if we see some clustering related to the physical properties. Considering the parameters with the larger weights in each of these principal components, we have named them as "kinematical component" and "spatial component" in the case of PC1 and PC2, respectively.

The most evident result is shown when we represent disks with different radii in the PC1(kinematical)-PC2(spatial) diagram (see Fig 8.3). The disks with radius 50 AU are distributed on the right part of the diagram, the ones with radius 100 AU are located at the central part and the disks with radius 150 AU are located on the left of the plot. This means that the kinematic principal component (x axis) is qualitatively good to discriminate among disks with different radii. This result indicates that we can get information about the radius of a protoplanetary disk (physical parameter) from the velocity of the peak emission, the half power sizes for principal peaks at intermediates velocities and from the distance from principal peaks to center (observational signatures). That the disk radii can be discriminated relatively well by maps of line emission may seem a relatively obvious result, but it illustrates the power of this kind of statistical analysis.

Another interesting trend is seen from the representation in the diagram of disks with different mass accretion rate (see Fig 8.4). Disks with higher mass accretion rates tend to populate the upper parts of the PC1(kinematical)-PC2(spatial) diagram. Therefore, in this case it is the second principal component (y axis) the one that better discriminate among disks with different mass accretion rates. Considering the parameters that give rise to this component, we can say that the half power sizes of principal peaks at 1.5 km s^{-1}, the velocity of the peak emission and the half power sizes of secondary peaks at 0.0 and 1.5 km s^{-1} velocities provide information about the mass accretion rate of the disks.

Other trends relating principal components and the rest of the physical parameters are also present, but qualitatively they are not as clear as these two we have mentioned. In the case of other physical parameters, it is the second principal component the one that provides more information about the α parameter and the maximum radius of dust grains values. Further analysis including models of more molecular transitions will certainly be useful to obtain refined principal components that can better discriminate these physical parameters.

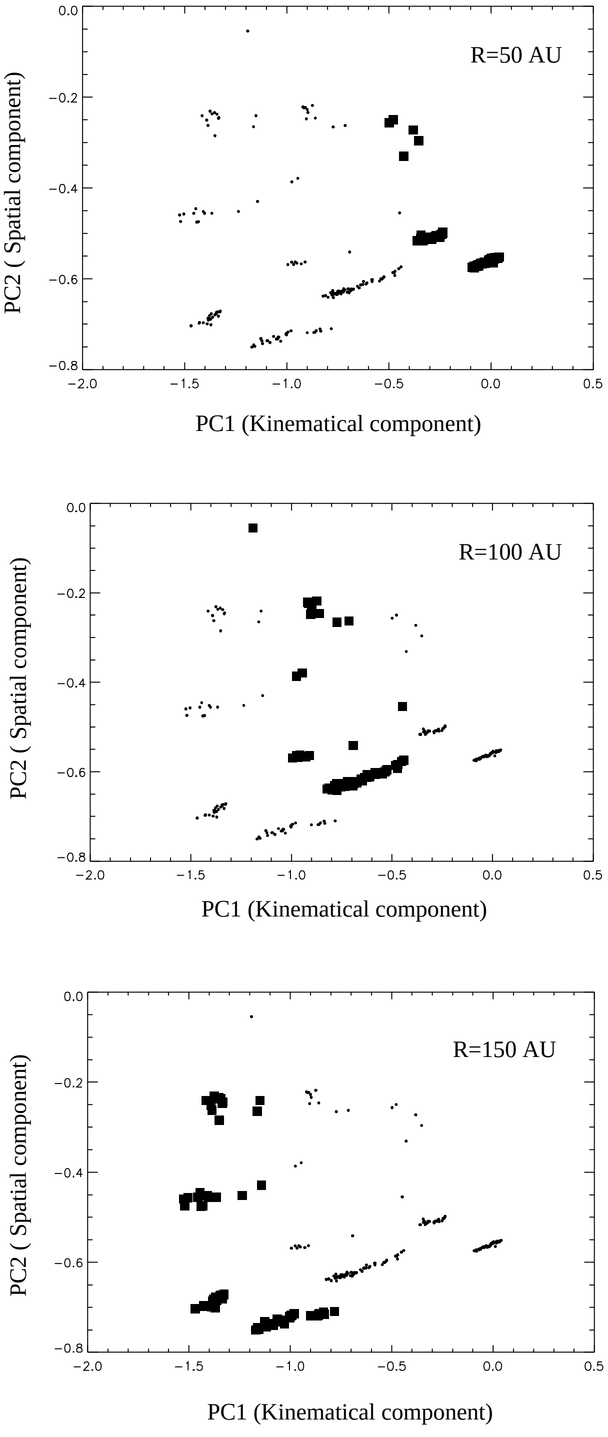

Figure 8.3: Disk radii in the PC1-PC2 diagrams. Dots represent all the modeled disks with different physical parameters. Squares represent disks with radius 50 A.U. (upper), 100 A.U. (central) and 150 A.U. (bottom).

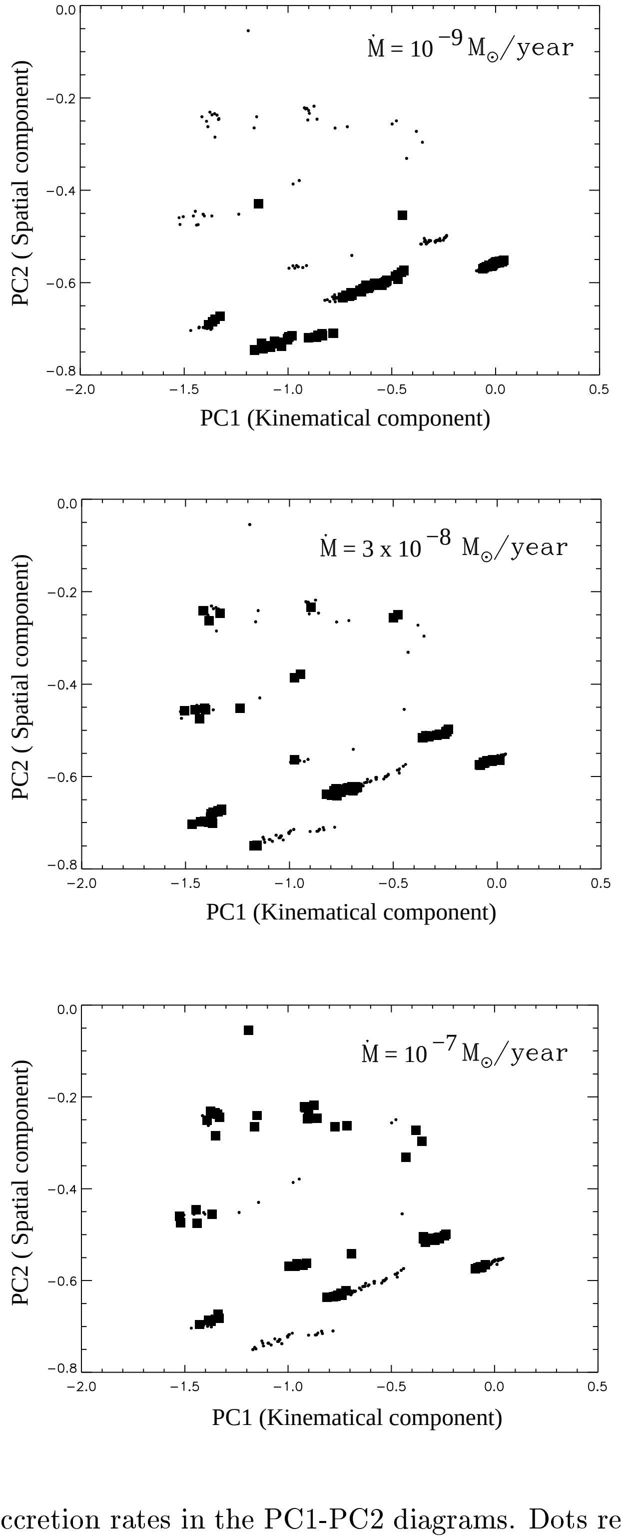

Figure 8.4: Mass accretion rates in the PC1-PC2 diagrams. Dots represent all the modeled disks with different physical parameters. Squares represent disk with mass accretion rate of 10^{-9} $M_\odot$/year (upper), 3×10^{-8} $M_\odot$/year (central) and 10^{-7} $M_\odot$/year (bottom).

8.6.3 Multiple correlation

We have seen in the previous section that diagrams of principal components can be useful to discriminate among disks with different physical characteristics. It would be interesting, however, to have a mathematical tool to easily obtain numerical values for these physical characteristics based on the observed maps. As a first approach, we have here performed a multiple linear correlation with the observational parameters as independent variables, and the physical characteristics as dependent ones. The resulting coefficients for such a fit are shown in Table 8.3.

As it was deduced in the previous subsection, the linear correlation coefficients of each principal component (see r(PC$_i$) values in Table 8.3) show that PC1(kinematical component) is the best one to derive information about the disk radii and PC2(spatial component) provide the most information in the determination of the rest of the physical parameters, $\dot{M}$, α, and maximum radius of dust grains.

Table 8.3: Correlation coefficients and F-Snedecor test values

	r(PC1)^a	r(PC2)^a	r(PC3)^a	r(PC4)^a	R^b	F
Radius	-0.9	-0.19	0.07	-0.001	0.97	951.62
$\dot{M}$	-0.18	0.5	-0.3	-0.16	0.57	26.93
α	0.16	-0.21	0.13	0.07	0.31	5.94
Max. Grain Radius	-0.08	-0.009	-0.012	0.08	0.19	2.07
	$\lambda_0{}^c$	$\lambda_1{}^c$	$\lambda_2{}^c$	$\lambda_3{}^c$	$\lambda_4{}^c$	
Radius	-55.3	-79.4	-54.2	133.3	-137.7	
$\dot{M}$	1.8×10^{-7}	-0.16×10^{-7}	1.4×10^{-7}	-1.7×10^{-7}	-0.15×10^{-7}	
α	-0.0195	0.0024	-0.0349	+0.0465	-0.0091	
Max. Grain Radius	-16943.4	-100.4	-40213.2	+48703.1	+123751.8	

Notes to Table 8.3

[a] r(PCi) are the linear correlation coefficients of each principal component.

[b] Multiple correlation coefficient.

[c] λ_i are the coefficients of the linear combination of principal components obtained from the multiple regression study, to derive the values of the physical parameters in the first column.

The most important piece of information that can be retrieved with this kind of study is the deduction of the linear combination of observational signatures that provide quantitative information about physical characteristics. This linear combination can be derived from λ_i coefficients in table 8.3 as follows:

$$Physical\ \ parameter = \lambda_0\ +\ \lambda_1 PC1\ +\ \lambda_2 PC2\ +\ \lambda_3 PC3\ +\ \lambda_4 PC4$$

As an example, in the case of the radius of the protoplanetary disk, this combination would be the following:

$$R_d = -55.3 - (79.4 \times PC1) - (54.2 \times PC2) + (133.3 \times PC3) - (137.7 \times PC4)$$

With these sets of linear combinations, we could estimate physical parameters from observations, provided that the fit is good enough.

The strongest correlation (see R values in Table 8.3) is obtained for radius (correlation coefficient R = 0.97), followed by mass accretion rate (R = 0.57), viscosity parameter (R = 0.31) and maximum radius of dust grains (R = 0.19). The multiple correlation coefficients alone are not good statistical indicators of the goodness of linear fits. To assess the validity of our fitted functions we carried out an F test to derive the signification of the linear regression. We assume a confident limit of 95%, which means that we could admit as good fits with values $F < 1.44$. However in all our results the values exceeded this critical value (see table 8.3). This result suggests that our variables are far from the linear regime, which is certainly reasonable.

8.7 Detectability of molecular lines with new interferometers

In order to test our predictions observationally, we present a line detectability study with interferometers that will be able to reach subarsecond resolution, e.g., SMA and ALMA.

We have calculated the line intensity expected for all our line models. The lowest peak intensity (∼7 mJy beam^{-1}) corresponds to disks with 50 AU radius, $\dot{M} = 10^{-9}$ M$\odot$ yr^{-1}, $\alpha = 0.05$ and 1 μm maximum grain radius. On the other hand, the highest peak intensity (∼180 mJy beam^{-1}) corresponds to disks with 150 AU radius, $\dot{M} = 10^{-7}$ M$\odot$ yr^{-1}, $\alpha = 0.01$ and 10^5 μm maximum grain radius.

With the SMA (Submillimeter Array), a sensitivity of ∼85 mJy beam^{-1} is expected[1], considering the 8 antennas of the array working at 337 GHz, with 1 km s^{-1} velocity resolution and 10 hours integration time, under standard values of precipitable water vapor (∼2.0 mm for 300−355 GHz).

On the other hand, in the case of ALMA, considering 64 antennas, 1 km s^{-1} velocity resolution, only 1 hour integration time and 1.5 mm of precipitable water vapor (median at the site over all hours and seasons), the sensitivity expected is 1.2 mJy beam^{-1} (Butler & Wooten 1999).

Considering 5σ emission as detections, we conclude that all our disks modeled, even the faintest, will be detected with one hour integration time with ALMA. Neverthe-

---

[1] http://sma1.sma.hawaii.edu/call.html

less, it will be extremely difficult of observe any of our modeled disks with the SMA, at least the ones with the physical characteristics showed in this work (see Table 8.1), since the SNR obtained for the modeled disks with the highest intensities ($\sim$180 mJy beam^{-1}) in 10 hours of integration time, would only be 2σ.

Therefore, ALMA will be a crucial instrument to observationally test the predictions and assumptions of our models.

8.8 Comments and prospects for these statistical studies

The results derived from the statistical study presented in this chapter show that this method could be a powerful tool to obtain information related to the physical characteristics in protoplanetary disks from observational parameters.

The most important information of our study is related to the radius of the disks. This preliminary study results in a way to obtain a first approximation of the disks radii that depends only of the observations, avoiding the application of χ^2 fitting techniques.

Since this is a promising method of study, and considering the future set of observations in protoplanetary disks that will be carried out with the development of ALMA, we plan to complete and improve our models and analysis. First, to easily observe the tendencies in the principal component diagram, we plan to increase the sample, building a more extended set of models with a wider variety of initial physical and observational parameters. Calculations in other molecular transitions or isotopes would further constrain the information on temperature and density. Finally, an update in the calculation of the disk structure models would be done, considering in detail the photodisociation or depletion effects in the line of study, and dust grain growth.

8.9 Conclusions

In this chapter we have presented a statistical method to derive physical parameters from observational characteristics in a protoplanetary disk. To make this study we modeled the expected emission of the $C^{17}O$(3-2) transition from protoplanetary disks with different physical properties. We then applied a principal component and a multiple correlation analysis, to obtain a set of linear combinations of observational parameters that may provide relevant information of the physics of the disks. The main conclusions are the following:

- The most significant results of our analysis are related to disk sizes. We can discriminate among disks with different radii using a principal component composed mainly of the velocity of the peak emission, the half power sizes for principal peaks at intermediates velocities and the distance from principal peaks to center.

- Moreover, some information about the mass accretion rate could be obtained from a principal component made of the half power sizes of principal peaks at 1.5 km s^{-1}, the velocity of the peak emission and the half power sizes of secondary peaks at 0.0 and 1.5 km s^{-1} velocities, although the results are much less significant than in the case of radii.

- We have shown a preliminary but promising and potentially useful statistical method that will be improved and completed in a future with studies in other transitions.

- We have performed a study of detectability with ALMA and SMA. All our modeled disks could be detected with ALMA, using one hour integration time, nevertheless the sensitivity reached by the SMA is not enough to detect our disks with reasonable integration times. We conclude that ALMA will play an important role to test observationally our models and our statistical results.

8.9.1 Conclusiones

En este capítulo hemos presentado un método estadístico para inferir parámetros físicos de discos protoplanetarios a partir de las características observacionales de los mismos. Para realizar este estudio, hemos modelado la emisión esperada de la transición $C^{17}O$(3-2) en discos protoplanetarios con distintas propiedades físicas. Después hemos aplicado un análisis de componentes principales y correlación múltiple para obtener un conjunto de combinaciones lineales de parámetros observacionales que proporcionen información relevante de la física de los discos. Las principales conclusiones son las siguientes:

- Los resultados más significativos de nuestro análisis están relacionados con el tamaño de los discos. Podemos discriminar entre discos con diferentes radios usando una componente principal compuesta principalmente por la velocidad del máximo de emisión, los tamaños de las regiones a mitad de potencia de los máximos principales de emisión a velocidades intermedias y de la distancia de los máximos principales al centro del disco.

- Además, se puede obtener algo de información sobre la tasa de acrecimiento de masa mediante una componente principal compuesta fundamentalmente por los tamaños de las regiones a mitad de potencia de los máximos principales a velocidad de 1.5 km s^{-1}, la velocidad del pico máximo de emisión y los tamaños de la región a mitad de potencia de los máximos secundarios a velocidades de 0.0 km s^{-1} y 1.5 km s^{-1}, aunque los resultados son mucho menos significativos que en el caso de los radios.

- Hemos mostrado un método estadístico preliminar pero prometedor y potencialmente útil, que será mejorado y completado en un futuro con estudios en otras transiciones.

- Hemos realizado un estudio de detectabilidad con ALMA y SMA. Todos nuestros discos modelados podrían ser detectados con ALMA usando una hora de tiempo de integración, sin embargo la sensibilidad alcanzada por el SMA no es suficiente para detectar nuestros discos en tiempos de integración razonables. Concluimos que ALMA representará un papel importante en la comprobación observacional de nuestros modelos y de nuestros resultados estadísticos.

Chapter 9

General conclusions and future work

9.1 General conclusions

In this thesis we have studied several aspects related to age, physical conditions, kinematics, and chemistry of the environment surrounding low-mass young stellar objects, using molecular emission lines as main tools. Most of the work has been done by means of a combination of single-dish observations and higher resolution interferometric data. The conclusions obtained with this work comprise both technical and scientific achievements.

In order to perform the single-dish spectroscopic observations at 1 cm presented in this thesis, we have set-up and calibrated the radio astronomical equipment of NASA's 70 m antenna located at the Madrid Deep Space Communication Complex (Robledo de Chavela, Spain). Thanks to our technical work, nowadays molecular line observations at this wavelength are now being carried out routinely.

We presented the most sensitive and systematic single-dish survey of H_2O maser emission at 22 GHz towards Bok globules. Out of a total of 207 target positions observed, we report six new H_2O maser detections, and we confirm the H_2O maser detection towards CB 3. Thus, we have increased the number of Bok globules in the CB catalog known to emit H_2O masers from three to nine.

The presence of radio continuum emission (from submillimeter to centimeter wavelengths), molecular outflows, and peak in maps of high-density gas tracers (CS or NH_3) have all about the same weight as predictors of the presence of H_2O maser emission. However, the mere presence of IRAS point sources tends to be a somewhat worse predictor. The H_2O masers in Bok globules we found are likely to be associated with YSOs, and tend to be related to large and massive Bok globules, located at distances ≥ 1 kpc, more likely to show multiple star formation. We speculate whether masers with unusually high velocities

($\geq$ 15 km s^{-1} with respect to the cloud velocity) in low-mass star-forming regions, might be related to enhanced mass-loss in close binaries ($\simeq$ 65 AU separations).

Using the first interferometric VLA H_2O maser observations at 22 GHz reported towards Bok globules, we have located the exciting source of the H_2O maser emission in CB 3 (where masers seem to trace the inner part of a jet), CB 54, CB 101, and CB 232. All these objects (except the one in CB 101, probably a Mira star) are also the most likely powering source of the molecular outflows in their regions.

We also report a sensitive single-dish survey (using the Robledo-70m antenna) of CCS and NH_3 emission towards a sample of 40 YSOs with presence of H_2O masers. We have detected six low-mass sources that show CCS emission (L1448C, L1448-IRS3, B1-IRS, NGC2071-North, GF9-2 y L1251A), which also show the presence of NH_3. All of these regions, except B1-IRS, are reported for the first time here as CCS emitters at 1 cm.

Four of them are very young sources, but the CCS is also found in a T Tauri star and a Class I source. Given that CCS is considered to be an "early time" molecule, this result suggests that, if the evolutionary classification reported in the literature for these objects is correct, the production/destruction of the CCS could be affected by the particular physical properties of the clouds, rather than depending on age alone.

No characteristic of the central sources and/or the molecular outflows present in the regions seems to be related to the presence of CCS. Nevertheless, the higher peak intensities, but similar integrated intensities of NH_3 in regions associated with CCS emission compared with those without it, suggest that CCS-emitting regions might be less turbulent (i.e., younger).

We have complemented this survey with VLA observations of CCS, H_2O masers and NH_3 towards one of our detections, the Class 0 region B1-IRS. This study is the second one reported in CCS using the VLA, and the first one using the new VLA K-band receivers. We suggest for the first time that a shocked-induced chemistry could be responsible for a local CCS abundance enhancement, since the kinematical pattern of this molecule suggests a strong interaction between the gas traced by CCS and the molecular outflow present in the region. We also show for the first time a spatial anticorrelation at scales of $\simeq 5''$ between the NH_3 and the CCS, which indicates that a combination of both molecules is needed to fully trace the column density and kinematics of dense material.

We tried for the first time the feasibility of cross-calibration of thermal molecular lines using H_2O masers to correct for atmospheric amplitude and phase fluctuations at $\simeq$ 22 GHz. This was done with VLA simultaneous observations of CCS and H_2O masers at 1 cm towards the star forming region IRAS 16293-2422. Although we failed to detect CCS emission, the radio-continuum emission at the CCS frequency showed a significant improvement in SNR after cross-calibration.

Using theoretical calculations of $C^{17}O(3-2)$ molecular line emission in protoplanetary disks, we show a potentially powerful statistical method to infer which observational characteristics could be more relevant to obtain information about the underlying physical parameters of these disks. As a preliminary result, this method allows us to discriminate between disks with different radii relatively well, and to a lesser degree we could obtain information on mass accretion rates. In addition, our calculations resulted in specific predictions for the detectability of molecular line emission of protoplanetary disks using SMA and ALMA. All the modeled disks would be easily detected with only one hour of integration time with ALMA.

9.1.1 Conclusiones generales

En esta tesis hemos estudiado distintos aspectos relacionados con la edad, las condiciones físicas, la cinemática y la química del entorno que rodea los objetos estelares jóvenes de masa baja, usando las líneas moleculares de emisión como principales herramientas. La mayor parte de este trabajo ha sido realizada mediante una combinación de observaciones de antena única y datos interferométricos en alta resolución. Las conclusiones obtenidas de este trabajo comprenden tanto aspectos técnicos como científicos.

Para realizar las observaciones espectroscópicas con antena única a 1 cm, hemos puesto a punto y hemos calibrado el equipo radioastronómico de la antena de 70 m de NASA situada en el Complejo de Comunicaciones del Espacio Profundo de Madrid (Robledo de Chavela, España). Gracias a nuestro trabajo técnico, hoy día se están realizando de forma rutinaria observaciones de líneas moleculares a esa longitud de onda.

Presentamos la búsqueda más sensible y sistemática de emisión de máseres de H_2O a 22 GHz en glóbulos de Bok. De un total de 207 posiciones observadas, detectamos seis nuevos máseres de H_2O y confirmamos la ya conocida detección de máser de agua en CB 3. Así, hemos incrementado el número de glóbulos de Bok en el catálogo de CB con emisión máser conocida de tres a nueve.

La presencia de emisión de radiocontinuo (de longitudes de onda submilimétricas a centimétricas), flujos moleculares y máximos en mapas de trazadores de gas de alta densidad (CS o NH_3) tienen aproximadamente el mismo peso predictivo de emisión de máseres de agua. Sin embargo, la mera presencia de fuentes puntuales IRAS tiende a predecir algo peor la presencia de estos máseres. Los máseres de H_2O que encontramos en glóbulos de Bok están probablemente asociados con objetos estelares jóvenes y tienden a localizarse en glóbulos de Bok grandes y masivos, situados a distancias $\geq$ 1 kpc, que presentan con mayor probabilidad formación estelar múltiple. Especulamos si los máseres con velocidad inusualmente alta ($\geq$ 15 km s^{-1} con respecto a la velocidad de la nube) en regiones de formación estelar de masa baja, podrían estar relacionados con episodios energéticos de pérdida de masa en binarias cercanas ($\simeq$ 65 UA de separación).

Usando las primeras observaciones interferométricas con el VLA a 22 GHz de máseres de agua en glóbulos de Bok, hemos localizado la fuente excitadora de la emisión máser en CB 3 (donde los máseres parecen trazar la parte interna de un jet), CB 54, CB 101 y CB 232. Todos estos objetos (excepto el de CB 101, posible estrella tipo Mira) también son probablemente las fuentes impulsoras de los flujos moleculares de sus respectivas regiones.

Además, mostramos una búsqueda sensible con antena única (usando la antena Robledo-70m) de emisión de CCS y amoniaco en una muestra de 40 objetos estelares jóvenes con presencia de máseres de agua. Hemos detectado emisión de CCS en seis fuentes de masa baja (L1448C, L1448-IRS3, B1-IRS, NGC2071-North, GF9-2 y L1251A), las cuales muestran también presencia de NH_3. Todas estas regiones, excepto B1-IRS, son mostradas aquí por primera vez emitiendo en CCS a 1 cm. Cuatro de ellas son fuentes muy jóvenes, sin embargo también se encuentra CCS en una estrella T Tauri y una fuente de clase I. Ya que el CCS está considerado como una molécula "temprana", este resultado sugiere que, si la clasificación evolutiva de estos objetos publicada en la literatura es correcta, la producción/destrucción del CCS podría estar afectada por las propiedades físicas particulares de las nubes moleculares, en lugar de depender únicamente de la edad.

Ninguna de las características de las fuentes centrales ni de los flujos moleculares presentes en dichas regiones parecen estar relacionadas con la presencia de CCS. Sin embargo, los picos de intensidad máxima mayores y las intensidades integradas similares de NH_3 en regiones asociadas con emisión de CCS con respecto a aquellas sin emisión, sugieren que las regiones emisoras de CCS podrían ser menos turbulentas (es decir, más jóvenes).

Hemos complementado esta búsqueda con observaciones de VLA en CCS, máseres de H_2O y NH_3 en una de nuestras detecciones, la región de clase 0 B1-IRS. Este estudio es el segundo publicado en CCS usando el VLA y el primero que utiliza los nuevos receptores del VLA en banda K. Sugerimos por primera vez que una química inducida por choque podría ser la responsable de un aumento local de la abundancia de CCS, ya que el patrón cinemático de esta molécula sugiere una fuerte interacción entre el gas trazado por el CCS y el flujo molecular presente en la región. También mostramos por primera vez una anticorrelación espacial a escalas de $\simeq$ 5" entre el NH_3 y el CCS, lo que indica que una combinación de ambas moléculas es necesaria para trazar por completo la densidad de columna y la cinemática del material denso.

Hemos probado por primera vez la viabilidad de la calibración cruzada en líneas moleculares térmicas, usando máseres de H_2O para corregir las fluctuaciones atmosféricas en amplitud y fase a $\simeq$ 22 GHz. Esto fue realizado con observaciones simultáneas con el VLA en CCS y máseres de H_2O a 1 cm en la región de formación estelar IRAS 16293-2422. Aunque no detectamos emisión en CCS, la emisión en radiocontinuo a la frecuencia del CCS mostró una mejora significativa en su relación señal-ruido tras la calibración cruzada.

Usando cálculos teóricos de la línea molecular de emisión $C^{17}O$(3-2) en discos protoplanetarios, mostramos un prometedor método estadístico para inferir qué características observacionales podrían ser más relevantes para obtener información de los parámetros físicos de estos discos. Como resultado preliminar, este método nos permite discriminar entre discos con distintos radios relativamente bien y en grado menor podríamos obtener información sobre las tasas de acrecimiento de masa. Además, nuestros cálculos han resultado en predicciones de detectabilidad de líneas moleculares de emisión en discos protoplanetarios usando SMA y ALMA. Todos los discos modelados podrían ser fácilmente detectados con tan sólo una hora de tiempo de integración con ALMA.

9.2 Future work

The results of this thesis provide new data to understand the physics and the kinematics of the innermost gas around low-mass YSOs and open new (some general and some specific) questions in that framework. My future work will consist of a extension of the study showed in this thesis and a new line of research in the millimeter and submillimeter regimes in star-forming regions. I will detail my future research projects in what follows.

9.2.1 Further water maser studies in Bok globules

In the future, a detailed study will be done towards CB 54 via deep and simultaneous observations in water maser and continuum at 1 cm using the VLA in its A configuration. Our main aim is to detect the radio continuum emission towards the source that we propose to be powering the molecular outflow in the region (CB 54 YC1-SW), applying the cross-calibration technique to improve the SNR. These observations have already been carried out, and a preliminary data reduction shows a radio continuum source very close to the maser emission, as predicted in chapter 4.

In order to trace the spacial distribution and kinematics of the different maser components in CB 3 at milliarcsecond resolution, a proper motion study will be done. The extrapolation back in time of the proper motions of maser emission might clarify the position of the pumping source. We have just performed these observations using the VLBA[1]. This is an interesting opportunity to study the star formation processes in an intermediate-mass star forming region at very small scales.

In addition, and to complete the water maser survey in Bok globules, high-resolution observations using the VLA will be performed towards CB 34 and CB 199, in order to accurately derive the position of the masers, pinpoint the powering source and study the kinematics of the surrounding medium.

9.2.2 Study of high-mass YSOs via millimeter and submillimeter water masers

In chapters 3 and 4 we have shown the usefulness of water maser emission at 22 GHz to probe the dynamics and age of YSOs and their environment. In recent years, various water maser lines at millimeter and submillimeter frequencies have been detected in star forming regions and evolved objects. Different transitions at 96, 183, 321, 325, 471, 437, 439, and 658 GHz have been observed (Menten & Melnick 1989; Menten et al. 1990; Cernicharo et al. 1990; Melnick et al. 1993; Menten & Young 1995), and maser emission at 906 GHz has also been predicted (Melnick 1993). The already observed water maser

---

[1] Very Long Baseline Array

transitions in these ranges are usually related to strong 22 GHz water maser emission, especially in high-mass YSOs. Since the formation of high-mass stars remains poorly understood, and upcoming millimeter and submillimeter telescopes will allow a detailed study of the processes involved in star formation, a search for water masers at millimeter and submillimeter emission in high-mass star forming regions would be useful in several aspects:

1. Study the physics, chemistry, and kinematics of the innermost areas of massive star-forming regions.
2. Infer the presence of high mass protostars, in the cases where the powering sources of outflows are not known.
3. Understand the excitation mechanism of the water molecule. Provide constraints on the models of pumping mechanisms and on the physical conditions of the emitting regions.
4. Study the association of maser emission with either outflowing material or disks and derive the frequency of those jet-disk systems in high-mass YSOs.
5. Study non-collimated or isotropic mass-ejection processes in high-mass YSOs, and possible evolutionary transitions between isotropic and highly-collimated ejections.

In addition, these maser detections would be extremely useful for future calibration techniques of data from millimeter/submillimeter interferometers, in particular for ALMA, since water masers emission has been found in most of the future ALMA bands and they could be used as an useful phase reference for interferometric data.

This study would be made by means of a single-dish survey (e.g., with APEX[2]), searching for millimeter and submillimeter water masers in a large set of high-mass star forming regions associated with strong water maser emission at 22 GHz. The most interesting maser detections would be observed with interferometric techniques to accurately derive the maser positions and their spatial distribution at different frequencies. This study could provide interesting targets for future ALMA observations towards high-mass star forming regions.

9.2.3 Detailed study of CCS and NH_3 emission in the whole set sources detected in this thesis.

As a follow-up of the interesting results we obtained for B1-IRS, a detailed high resolution study would be done in CCS, ammonia, and water masers in the rest of the sources detected in our single-dish CCS survey (see chapter 5). This study would be performed through a combination between single-dish and interferometric maps. The

---

[2] Atacama Pathfinder Experiment

VLA in its D-configuration would be used to carry out the high-resolution observations, while the Robledo-70m antenna would provide zero-spacing fluxes. The main goals of this work would be the following:

1. Study in detail the kinematics of the regions.
2. Study the chemical evolution in star-forming cores.
3. Test whether the spatial anticorrelation between CCS and ammonia observed in B1-IRS stands at small scales (a few arcsec) in the rest of our CCS detections.
4. Study the suggested enhancement of CCS abundance in shocked regions produced by outflowing material (since all our candidates show molecular outflows).
5. Provide the data to test future theoretical chemical models that includes the effects of a central protostar on the destruction/production of CCS and ammonia.

L1448 region is especially appropriate for testing our suggestion of enhancement of CCS abundance in shocked regions, since it hosts energetic and collimated molecular outflows. We have already observed with the VLA in the D configuration both CCS and water masers in L1448C and L1448-IRS3. We will try to observe the rest of sources detected in CCS (GF9-2, L1251A and NGC 2071-North) in the near future.

9.2.4 Future study in protoplanetary disks

As it was mentioned in chapter 8, we plan to increase the sample of physical and observational parameters in order to observe more tendencies in the principal component diagram.

A study of canonical correlation would allow us to find the overall correlation between both sets of variables (i.e., the group of observational characteristics and the group of physical parameters), without restricting to the linear correlation used for this thesis.

An improvement in the disk structure will be made for future studies, trying to build disk structures as realistic as possible. This includes dust grain growth, and possible photodissociation or depletion effects for the studied molecules.

In order to obtain information of temperatures and densities, the calculations would be done for other transitions and molecules (starting with different CO isotopes).

Finally, when ALMA is operative, the results predicted by our models and statistical studies, could be observationally tested.

List of publications

The work presented in this thesis has given rise to the following publications in international journals and contributions to meetings:

Papers in refereed journals

- "*Molecular Line Emission from Accretion Disks Around YSOs* " **de Gregorio-Monsalvo,I.**; Gómez, J. F.; D'Alessio, P., 2004, Ap&SS, 292, 445.
- "*High-Resolution Observations in B1-IRS: Ammonia, CCS and Water Masers*" **Gregorio-Monsalvo, I.**; Chandler, C. J.; Gómez, J. F.; Kuiper, T. B. H.; Torrelles, J. M.; Anglada, G., 2005, Ap&SS, 295, 65.
- "*High-Resolution Molecular Line Observations of the Environment of the Class 0 Source B1-IRS* " **de Gregorio-Monsalvo, I.**; Chandler, C. J.; Gómez, J. F.; Kuiper, T. B. H.; Torrelles, J. M.; Anglada, G., 2005, ApJ, 628, 789.
- "*CCS and NH_3 Emission Associated with Low-mass Young Stellar Objects*" **de Gregorio-Monsalvo, I.**; Gómez, J.F.; Suárez, O.; Kuiper, T.B.H.; Rodríguez, L.F.; Jiménez-Bailón, E., 2006, ApJ, in press. Astroph/0512616.
- "*VLA Observations of Water Masers in Bok Globules* " **de Gregorio-Monsalvo, I.**; Gómez, J.F.; Suárez, O., Kuiper, T.B.H.; Anglada, G., Patel, N.A.; Torrelles, J.M., 2006, Submitted to the Astronomical Journal.
- "*A Sensitive Survey for Water Maser Emission towards Bok Globules Using the Robledo 70m Antenna*" Gómez, J.F.; **de Gregorio-Monsalvo, I.**; Suárez, O.; Kuiper, T.B.H., 2006, Submitted to the Astronomical Journal.

Non-refereed contributions to meetings or published in books.

- "*Protoplanetary Disks: Detectability and Statistical study of $C^{17}O(3-2)$ line* " **de Gregorio-Monsalvo, I.**, Gómez, J.F., D'Alessio P.; V Spanish Astronomical Society Meeting, Toledo (Spain). September 2002. Poster.
  Highlights of Spanish Astrophysics III, 478. 2003 Kluwer Academic Publisher.
- "*Radio Spectroscopy Observations at the Madrid Deep Space Station* " Gómez, J.F., **de Gregorio-Monsalvo, I.**, Jiménez-Bailón, E., García-Miró,C., Suárez, O., Kuiper, T.B.H; V Spanish Astronomical Society Meeting, Toledo (Spain). September 2002. Co-author talk.
  Highlights of Spanish Astrophysics III, 405. 2003 Kluwer Academic Publisher.

- "*Models of Molecular Line Emission from Protoplanetary disks* " **de Gregorio-Monsalvo, I.**, Gómez, J.F., D'Alessio P.; Third IRAM Millimeter Interferometry School, 2002, Grenoble (France). Poster.
- "*Interstellar Spectroscopy at the Madrid DSN Station* " **de Gregorio-Monsalvo, I.**, Suárez, O., Gómez, J.F., Kuiper, T.B.H; NAIC-NRAO School on Single-Dish Radio Astronomy Techniques and Applications, 2003, Greenbank (USA). Poster.
- "*High Resolution Observations in B1-IRS: ammonia vs CCS and water masers* " **de Gregorio-Monsalvo, I.**; Chandler, C. J.; Gómez, J. F.; Kuiper, T. B. H.; Torrelles, J. M.; Anglada, G.; XXXIII Young European Radio Astronomy Conference, 2003, Bonn (Germany). Talk.
- "*A Sensitive Survey of Water Masers towards Bok Globules* " Gómez, J. F.; **de Gregorio-Monsalvo, I.**; Suárez, O.; Kuiper, T.B.H.; Joint European and National Astronomical Meeting, 2004, Granada (Spain). Poster.
- "*CCS in low-mass star forming regions: Radio Astronomy at the MDSCC* " **de Gregorio-Monsalvo, I.**; Gómez, J. F.; Suárez, O.; Kuiper, T.B.H.; Joint European and National Astronomical Meeting, 2004, Granada (Spain). Talk.

Other publications

In addition, there are other publications and contributions to meetings indirectly related to this thesis. The following works have been performed by means of spectroscopic observations with the Robledo-70m antenna, which set-up was exposed in Chap 2.

Papers in refereed journals

- "*A Survey for Water Maser Emission towards Planetary Nebulae: New Detection in IRAS 17347–3139* " **de Gregorio-Monsalvo, I.**; Gómez, Y.; Anglada, G.; Cesaroni, R.; Miranda, L. F.; Gómez, J. F.; Torrelles, J. M., 2004, ApJ, 601, 921.
- "*Spectral index of the H_2O-maser emitting planetary nebula IRAS 17347-3139* " Gómez, J.F.; **de Gregorio-Monsalvo, I.**; Lovell, J. E. J.; Anglada, G.; Miranda, L.F; Suárez, O.; Torrelles, J.M.; Gómez, Y., 2005, MNRAS, 364, 738.
- "*Discovery of Water Maser Emission in Eight AGN with 70-m Antennas of NASA's Deep Space Network*" Kondratko, P.T.; Greenhill, L.J.; Moran, J.M.; Lovell, J.E.J.; Kuiper, T.B.H.; Jauncey, D.L.; Cameron, L.B.; Gómez, J.F.; García-Miró, C.; Moll, E.; **de Gregorio-Monsalvo, I.**; Jiménez-Bailón, E., 2006, ApJ, 638, 100.

IAU Circulars

- "*epsilon Eridani, upsilon Andromedae, 51 Pegasi, HD 209458, HD 196050* " Greenhill, L.; Kondratko, P.; Lovell, J.; Gómez, J. F.; **de Gregorio-Monsalvo, I.**; Kuiper, T, 2002, IAU Circ., 7985, 1

Non-refereed contributions to meetings or published in books.

- "*A survey for Water Maser Emission toward Planetary Nebulae: New Detection in IRAS 17347-3139* " **de Gregorio-Monsalvo, I.**; Gómez, Y.; Anglada, G.; Cesaroni, R.; Miranda, L. F.; Gómez, J. F.; Torrelles, J. M.; XXXIII Young European Radio Astronomy Conference, 2003, Bonn (Germany). Poster.

Bibliography

Aarseth, S. J., Lin, D. N. C., & Palmer, P. L. 1993, ApJ, 403, 351

Adams, F. C., Lada, C. J., & Shu, F. H. 1987, ApJ, 312, 788

Aikawa, Y., & Herbst, E. 1999, A&A, 351, 233

Aikawa, Y., Miyama, S. M., Nakano, T., & Umebayashi, T. 1996, ApJ, 467, 684

Aikawa, Y., Ohashi, N., & Herbst, E. 2003, ApJ, 593, 906

Aikawa, Y., Umebayashi, T., Nakano, T., & Miyama, S. M. 1997, ApJ, 486, L51

Allen, D. A., & Burton, M. G. 1993, Nature, 363, 54

Alves, J. F., & Yun, J. L. 1995, ApJ, 438, L107

André, P. 1994, The Cold Universe, 179

André, P. & Montmerle, T. 1994, ApJ, 420, 837

André, P., Ward-Thompson, D., & Barsony, M. 1993, ApJ, 406, 122

André, P., Ward-Thompson, D., & Barsony, M. 2000, Protostars and Planets IV, 59

Anglada, G. 1995, RevMExAA SC, 1, 67

Anglada, G., Estalella, R., Pastor, J., Rodríguez, L. F., & Haschick, A. D. 1996a, ApJ, 463, 205

Anglada, G. & Rodríguez, L. F. 2002, RevMexAA, 38, 13

Anglada, G., Rodríguez, L. F., Cantó, J., Estalella, R., & Torrelles, J. M. 1992, ApJ, 395, 494

Anglada, G., Rodríguez, L. F., & Torrelles, J. M. 1996b, ApJ, 473, L123

Anglada, G., Rodríguez, L. F., & Torrelles, J. M. 2000, ApJ, 542, L123

Anglada, G., Rodríguez, L. F., Torrelles, J. M., Estalella, R., Ho, P. T. P., Cantó, J., López, R., & Verdes-Montenegro, L. 1989, ApJ, 341, 208

Anglada, G., Villuendas, E., Estalella, R., Beltrán, M. T., Rodríguez, L. F., Torrelles, J. M., & Curiel, S. 1998, AJ, 116, 2953

Anthony-Twarog, B. J. 1982, AJ, 87, 1213

Appenzeller, I., Oestreicher, R., & Jankovics, I. 1984, A&A, 141, 108

Araya, E., Hofner, P., Kurtz, S., Linz, H., Olmi, L., Sewilo, M., Watson, C., & Churchwell, E. 2005, ApJ, 618, 339

Arce, H. G. & Sargent, A. I. 2004, ApJ, 612, 342

Armstrong, J. T., & Winnewisser, G. 1989, A&A, 210, 373

Aspin, C., Sandell, G., & Walther, D. M. 1992, MNRAS, 258, 684

Avila, R., Rodríguez, L. F., & Curiel, S. 2001, RevMexAA, 37, 201

Bacciotti, F., & Eislöffel, J. 1999, A&A, 342, 717

Bachiller, R. 1996, ARA&A, 34, 111

Bachiller, R. & Cernicharo, J. 1984, A&A, 140, 414

Bachiller, R. & Cernicharo, J. 1986, A&A, 166, 283

Bachiller, R., del Río Álvarez, S., & Menten, K. M. 1990a, A&A, 236, 461

Bachiller, R., Fuente, A., & Tafalla, M. 1995, ApJ, 445, L51

Bachiller, R., & Gómez-González, J. 1992, A&A Rev., 3, 257

Bachiller, R., Guilloteau, S., Dutrey, A., Planesas, P., & Martín-Pintado, J. 1995, A&A, 299, 857

Bachiller, R., Martín-Pintado, J., Tafalla, M., Cernicharo, J., & Lazareff, B. 1990b, A&A, 231, 174

Bachiller, R., Menten, K. M., & del Río Álvarez, S. 1990c, A&A, 236, 461

Bachiller, R. & Pérez Gutiérrez, M. 1997, ApJ, 487, L93

Bachiller, R., Pérez Gutiérrez, M., Kumar, M. S. N., & Tafalla, M. 2001, A&A, 372, 899

Balazs, L. G., Eisloeffel, J., Holl, A., Kelemen, J., & Kun, M. 1992, A&A, 255, 281

Bally, J., Heathcote, S., Reipurth, B., Morse, J., Hartigan, P., & Schwartz, R. 2002, AJ, 123, 2627

Bally, J., & Lada, C. J. 1983, ApJ, 265, 824

Bally, J., Lada, E. A., & Lane, A. P. 1993, ApJ, 418, 322

Bally, J., & Predmore, R. 1983, ApJ, 265, 778

Barsony, M. 1994, ASP Conf. Ser. 65: Clouds, Cores, and Low Mass Stars, 197

Barsony, M., Ward-Thompson, D., André, P., & O'Linger, J. 1998, ApJ, 509, 733

Bastien, P., & Menard, F. 1988, ApJ, 326, 334

Bastien, P., & Menard, F. 1990, ApJ, 364, 232

Beckwith, S. V. W., & Sargent, A. I. 1991, ApJ, 381, 250

Beckwith, S. V. W., & Sargent, A. I. 1993, ApJ, 402, 280

Beckwith, S. V. W., Sargent, A. I., Chini, R. S., & Guesten, R. 1990, AJ, 99, 924

Beichman, C. A., Myers, P. C., Emerson, J. P., Harris, S., Mathieu, R., Benson, P. J., & Jennings, R. E. 1986, ApJ, 307, 337

Beltrán, M. T., Estalella, R., Anglada, G., Rodríguez, L. F., & Torrelles, J. M. 2001, AJ, 121, 1556

Beltrán, M. T., Girart, J. M., Estalella, R., Ho, P. T. P., & Palau, A. 2002, ApJ, 573, 246

Bence, S. J., Padman, R., Isaak, K. G., Wiedner, M. C., & Wright, G. S. 1998, MNRAS, 299, 965

Benson, P. J., Caselli, P., & Myers, P. C. 1998, ApJ, 506, 743

Benson, P. J., & Myers, P. C. 1989, ApJS, 71, 89

Benson, P. J., Myers, P. C., & Wright, E. L. 1984, ApJ, 279, L27

Bergin, E. A. & Langer, W. D. 1997, ApJ, 486, 316

Beuther, H., & Shepherd, D. 2005, Cores to Clusters: Star Formation with Next Generation Telescopes. Edited by M.S. Nanda Kumar, CAUP, Porto, Portugal; M. Tafalla, Observatorio Astronomico Nacional, Madrid, Spain; P. Caselli, INAF-Osservatorio Astrofisico di Arcetri, Firenze, Italy Reprinted from Astrophysics and Space Science Library, Vol. 324, pp. 105-119, 2005 Springer New York, 105

Bok, B. J., & Reilly, E. F. 1947, ApJ, 105, 255

Bolton, S. J., Janssen, M., Levin, S., Klein, M., Gulkis, S., Elachi, C., Thorne, R., Bastian, T., Sault, R., Dulk, G., Leblanc, Y., McLeod, R., Roller, J. 2001, Bulletin of the American Astronomical Society, 33, 1029

Bontemps, S., André, P., Terebey, S., & Cabrit, S. 1996, A&A, 311, 858

Booth, R. S., & Diamond, P. J. 2004, The Role of VLBI in Astrophysics, Astrometry and Geodesy. Proceedings of the NATO Advanced Study Institute, held September 17-29, 2001, in Bologna, Italy. Series II, mathematics, physics and chemistry, Vol. 135. Edited by Franco Mantovani and Andrzej Kus. ISBN 1-4020-1875-4: ISBN 1-4020-2406-1 (e-book). Published by Kluwer Academic Publishers, Dordrecht, The Netherlands, 2004, p.257, 257

Boss, A. P. 1998, ApJ, 503, 923

Bottema, R. 2003, MNRAS, 344, 358

Bourke, T. L., Hyland, A. R., & Robinson, G. 1995a, MNRAS, 276, 1052 (BHR)

Bourke, T. L., Hyland, A. R., Robinson, G., James, S. D., & Wright, C. M. 1995b, MNRAS, 276, 1067

Bowers, P. F., & Hagen, W. 1984, ApJ, 285, 637

Brand, J., Cesaroni, R., Caselli, P., Catarzi, M., Codella, C., Comoretto, G., Curioni, G. P., Curioni, P., di Franco, S., Felli, M., Giovanardi, C., Olmi, L., Palagi, F., Palla, F., Panella, D., Pareschi, G., Rossi, E., Speroni, N., & Tofani, G. 1994, A&AS, 103, 541

Brand, J., Cesaroni, R., Comoretto, G., Felli, M., Palagi, F., Palla, F., & Valdettaro, R. 2003, A&A, 407, 573

Briggs, D. 1995, Ph.D. thesis, New Mexico Inst. of Mining and Technology

Buehrke, T., Mundt, R., & Ray, T. P. 1988, A&A, 200, 99

Burrows, C. J., Stapelfeldt, K. R.; Watson, A. M.; Krist, J. E.; Ballester, G. E.; Clarke, J. T.; Crisp, D.; Gallagher, J. S., III; Griffiths, R. E.; Hester, J.J.; Hoessel, J. G.; Holtzman, J. A.; Mould, J. R.; Scowen, P. A.; Trauger, J. T.; Westphal, J. A. 1996, ApJ, 473, 437

Butler, B., & Wooten, A. 1999, ALMA Memo 276

Butner, H. M., Evans, N. J., Harvey, P. M., Mundy, L. G., Natta, A., & Randich, M. S. 1990, ApJ, 364, 164

Cabrit, S., & Bertout, C. 1992, A&A, 261, 274

Calvet, N., Magris, G. C., Patino, A., & D'Alessio, P. 1992, RevMexAA, 24, 27

Calvet, N., Patino, A., Magris, G. C., & D'Alessio, P. 1991, ApJ, 380, 617

Carpenter, J. M., Snell, R. L., & Schloerb, F. P. 1990, ApJ, 362, 147

Carr, J. S., Tokunaga, A. T., & Najita, J. 2004, ApJ, 603, 213

Cattell, R. B., 1966, Multivariate Behavioral Research, 1, 245

Cernicharo, J., Thum, C., Hein, H., John, D., García, P., & Mattioco, F. 1990, A&A, 231, L15

Cesaroni, R., Palagi, F., Felli, M., Catarzi, M., Comoretto, G., di Francos, Giovanardi, C., & Palla, F. 1988, A&AS, 76, 445

Chandler, C. J., Brogan, C. L., Shirley, Y. L., & Loinard, L. 2005, ApJ, 632, 371

Chandler, C. J., & Carlstrom, J. E. 1996, ApJ, 466, 338

Chandler, C. J., Gear, W. K., Sandell, G., Hayashi, S., Duncan, W. D., Griffin, M. J., & Hazell, A. S. 1990, MNRAS, 243, 330

Chandler, C. J. & Richer, J. S. 2001, ApJ, 555, 139

Chandler, C. J. & Sargent, A. I. 1993, ApJ, 414, L29

Chen, H., Myers, P. C., Ladd, E. F., & Wood, D. O. S. 1995, ApJ, 445, 377

Chen, H., Tafalla, M., Greene, T. P., Myers, P. C., & Wilner, D. J. 1997, ApJ, 475, 163

Chernin, L. M. 1995, ApJ, 440, L97

Chernin, L. M. & Masson, C. R. 1992, ApJ, 396, L35

Chiang, E. I., & Goldreich, P. 1997, ApJ, 490, 368

Chini, R., Ward-Thompson, D., Kirk, J. M., Nielbock, M., Reipurth, B., & Sievers, A. 2001, A&A, 369, 155

Choi, M., Evans, N. J., II, Gregerson, E. M., & Wang, Y. 1995, ApJ, 448, 742

Choi, M., Panis, J., & Evans, N. J. 1999, ApJS, 122, 519

Ciardi, D. R., Woodward, C. E., Clemens, D. P., Harker, D. E., & Rudy, R. J. 1998, AJ, 116, 349

Clark, J. S., & Porter, J. M. 2004, A&A, 427, 839

Clarke, C., Reipurth, B., & Delgado-Donate, E. 2004, RevMexAA SC, 21, 184

Claussen, M. J., Marvel, K. B., Wootten, A., & Wilking, B. A. 1998, ApJ, 507, L79

Claussen, M. J., Wilking, B. A., Benson, P. J., Wootten, A., Myers, P. C., & Terebey, S. 1996, ApJS, 106, 111

Clemens, D. P., & Barvainis, R. 1988, ApJS, 68, 257 (CB)

Clemens, D. P., Yun, J. L., & Heyer, M. H. 1991, ApJS, 75, 877

Codella, C., & Bachiller, R. 1999, A&A, 350, 659

Codella, C., & Felli, M. 1995, A&A, 302, 521

Codella, C., & Muders, D. 1997, MNRAS, 291, 337

Codella, C., Palumbo, G. G. C., Pareschi, G., Scappini, F., Caselli, P., & Attolini, M. R. 1995, MNRAS, 276, 57

Codella, C., & Scappini, F. 1998, MNRAS, 298, 1092

Comoretto, G., Palagi, F., Cesaroni, R., Felli, M., Bettarini, A., Catarzi, M., Curioni, G. P., Curioni, P., di Franco, S., Giovanardi, C., Massi, M., Palla, F., Panella, D., Rossi, E., Speroni, N., Tofani, G. 1990, A&AS, 84, 179

Correia, J. C., Griffin, M., & Saraceno, P. 1997, A&A, 322, L25

Curiel, S., Raymond, J. C., Moran, J. M., Rodríguez, L. F., & Cantó, J. 1990, ApJ, 365, L85

Curiel, S., Rodríguez, L. F., Gómez, J. F., Torrelles, J. M., Ho, P. T. P., & Eiroa, C. 1996, ApJ, 456, 677

Curiel, S., Rodríguez, L. F., Moran, J. M., & Cantó, J. 1993, ApJ, 415, 191

Curiel, S., Torrelles, J. M., Rodríguez, L. F., Gómez, J. F., & Anglada, G. 1999, ApJ, 527, 310

D'Alessio, P., Calvet, N., & Hartmann, L. 1997, ApJ, 474, 397

D'Alessio, P., Calvet, N., & Hartmann, L. 2001, ApJ, 553, 321

D'Alessio, P., Calvet, N., Hartmann, L., Lizano, S., & Cantó, J. 1999, ApJ, 527, 893

D'Alessio, P., Cantó, J., Calvet, N., & Lizano, S. 1998, ApJ, 500, 411

Dartois, E., Dutrey, A., & Guilloteau, S. 2003, A&A, 399, 773

Davidson, J. A. 1987, ApJ, 315, 602

Davis, C. J., & Eisloeffel, J. 1995, A&A, 300, 851

Davis, C. J., Eisloeffel, J., Ray, T. P., & Jenness, T. 1997a, A&A, 324, 1013

Davis, C. J., Matthews, H. E., Ray, T. P., Dent, W. R. F., & Richer, J. S. 1999, MNRAS, 309, 141

Davis, C. J., Ray, T. P., Eisloeffel, J., & Corcoran, D. 1997b, A&A, 324, 263

De Buizer, J. M., Radomski, J. T., Telesco, C. M., & Piña, R. K. 2005, ApJS, 156, 179

de Gregorio-Monsalvo, I., Chandler, C. J., Gómez, J. F., Kuiper, T. B. H., Torrelles, J. M., & Anglada, G. 2005a, Ap&SS, 295, 65

de Gregorio-Monsalvo, I., Chandler, C. J., Gómez, J. F., Kuiper, T. B. H., Torrelles, J. M., & Anglada, G. 2005b, ApJ, 628, 789.

de Gregorio-Monsalvo, I., Gómez, Y., Anglada, G., Cesaroni, R., Miranda, L. F., Gómez, J. F., Torrelles, J. M. 2004, ApJ, 601, 921

de Gregorio-Monsalvo, I., Gómez, J. F., Suárez, O., Kuiper, T. B. H., Rodríguez, L. F., & Jiménez-Bailón, E. 2006, ApJ, 642, in press. Astro-ph/0512616

Dickman, R. L. 1978, ApJS, 37, 407

Doeleman, S. S., Lonsdale, C. J., & Pelkey, S. 1999, ApJ, 510, L55

Draine, B. T. & Lee, H. M. 1984, ApJ, 285, 89

Edwards, S., Cabrit, S., Strom, S. E., Heyer, I., Strom, K. M., & Anderson, E. 1987, ApJ, 321, 473

Edwards, S., & Snell, R. L. 1983, ApJ, 270, 605

Edwards, S., & Snell, R. L. 1984, ApJ, 281, 237

Eiroa, C., Torrelles, J. M., Gómez, J. F., Sakamoto, S., Hasegawa, T., Kawabe, R., Hayashi, M., & Casali, M. M. 1992, PASJ, 44, 155

Eislöffel, J., Smith, M. D., Davis, C. J., & Ray, T. P. 1996, AJ, 112, 2086

Elitzur, M. 1992, ARA&A, 30, 75.

Elitzur, M., Hollenbach, D. J., & McKee, C. F. 1989, ApJ, 346, 983

Elitzur, M., Hollenbach, D. J., & McKee, C. F. 1992, ApJ, 394, 221

Ellingsen, S. P. 2006, ApJ, 638, 241

Elmegreen, B. G., & Lada, C. J. 1977, ApJ, 214, 725

Engels, D., Schmid-Burgk, J., & Walmsley, C. M. 1986, A&A, 167, 129

Engels, D., Schmid-Burgk, J., & Walmsley, C. M. 1988, A&A, 191, 283

Estalella, R., & Anglada, G. 1996, Introducción a la Física del Medio Interestelar. Textos docentes, 50 (Edicions de la Universitat de Barcelona; Barcelona)

Estalella, R., Mauersberger, R., Torrelles, J. M., Anglada, G., Gómez, J. F., López, R., & Muders, D. 1993, ApJ, 419, 698

Estalella, R., Paredes, J. M., & Rius, A. 1983, A&A, 124, 309

Evans, N. J., Levreault, R. M., & Harvey, P. M. 1986, ApJ, 301, 894

Felli, M., Palagi, F., & Tofani, G. 1992, A&A, 255, 293

Fiebig, D., Duschl, W. J., Menten, K. M., & Tscharnuter, W. M. 1996, A&A, 310, 199

Forster, J. R. & Caswell, J. L. 1989, A&A, 213, 339

Frank, A., Gardiner, T. A., Delemarter, G., Lery, T., & Betti, R. 1999, ApJ, 524, 947

Frerking, M. A. & Langer, W. D. 1982, ApJ, 256, 523

Froebrich, D. 2005, ApJS, 156, 169

Froebrich, D., Smith, M. D., Hodapp, K.-W., & Eislöffel, J. 2003, MNRAS, 346, 163

Fukui, Y. 1988, Vistas in Astronomy, 31, 217

Fukui, Y., Iwata, T., Mizuno, A., Ogawa, H., & Takaba, H. 1989, Nature, 342, 161

Fukui, Y., Sugitani, K., Takaba, H., Iwata, T., Mizuno, A., Ogawa, H., & Kawabata, K. 1986, ApJ, 311, L85

Fukui, Y., Takaba, H., Iwata, T., & Mizuno, A. 1988, ApJ, 325, L13

Furuya, R. S., Kitamura, Y., Wootten, H. A., Claussen, M. J., & Kawabe, R. 2001, ApJ, 559, L143

Furuya, R. S., Kitamura, Y., Wootten, A., Claussen, M. J., & Kawabe, R. 2003, ApJS, 144, 71

Furuya, R. S., Kitamura, Y., Wootten, H. A., Claussen, M. J., Saito, M., Marvel, K. B., & Kawabe, R. 2000, ApJ, 542, L135

Galván-Madrid, R., Avila, R., & Rodríguez, L. F. 2004, RevMexAA, 40, 31

Garay, G., Mardones, D., & Rodríguez, L. F. 2000, ApJ, 545, 861

Garden, R., Geballe, T. R., Gatley, I., & Nadeau, D. 1986, MNRAS, 220, 203

Gibb, A. G., & Little, L. T. 2000, MNRAS, 313, 663

Gibb, A. G., Richer, J. S., Chandler, C. J., & Davis, C. J. 2004, ApJ, 603, 198

Girart, J. M., Estalella, R., Ho, P. T. P., & Rudolph, A. L. 2000, ApJ, 539, 763

Girart, J. M., Ho, P. T. P., Rudolph, A. L., Estalella, R., Wilner, D. J., & Chernin, L. M. 1999, ApJ, 522, 921

Glassgold, A. E., Najita, J., & Igea, J. 2004, ApJ, 615, 972

Goddi, C., Moscadelli, L., Alef, W., Tarchi, A., Brand, J., & Pani, M. 2005, A&A, 432, 161

Goldreich, P. & Kwan, J. 1974, ApJ, 191, 93

Goldsmith, P. F., Margulis, M., Snell, R. L., & Fukui, Y. 1992, ApJ, 385, 522

Goldsmith, P. F., Snell, R. L., Hemeon-Heyer, M., & Langer, W. D. 1984, 286, 599

Gómez, J. F., Curiel, S., Torrelles, J. M., Rodríguez, L. F., Anglada, G., & Girart, J. M. 1994, ApJ, 436, 749

Gómez, J. F., & D'Alessio, P. 2000, ApJ, 535, 943

Gómez, J. F., de Gregorio-Monsalvo, I., Lovell, J. E. J., Anglada, G., Miranda, L. F., Suárez, O., Torrelles, J. M., & Gómez, Y. 2005, MNRAS, 364, 738

Gómez, M., Stark, D. P., Whitney, B. A., & Churchwell, E. 2003, AJ, 126, 863

Goodman, A. A., Benson, P. J., Fuller, G. A., & Myers, P. C. 1993, ApJ, 406, 528

Graf, U. U., Eckart, A., Genzel, R., Harris, A. I., Poglitsch, A., Russell, A. P. G., & Stutzki, J. 1993, ApJ, 405, 249

Greaves, J. S. 2004, MNRAS, 351, L99

Greenhill, L. J., Kondratko, P. T., Lovell, J. E. J., Kuiper, T. B. H., Moran, J. M., Jauncey, D. L., & Baines, G. P. 2003, ApJ, 582, L11

Gueth, F., & Guilloteau, S. 1999, A&A, 343, 571

Gueth, F., Guilloteau, S., & Bachiller, R. 1998, A&A, 333, 287

Gueth, F., Guilloteau, S., Dutrey, A., & Bachiller, R. 1997, A&A, 323, 943

Guilloteau, S., Bachiller, R., Fuente, A., & Lucas, R. 1992, A&A, 265, L49

Guilloteau, S., & Dutrey, A. 1998, A&A, 339, 467

Gullbring, E., Hartmann, L., Briceno, C., & Calvet, N. 1998, ApJ, 492, 323

Habing, H. J. 1996, A&A Rev., 7, 97

Han, F., et al. 1998, A&AS, 127, 181

Harju, J., Lehtinen, K., Booth, R. S., & Zinchenko, I. 1998, A&AS, 132, 211

Harju, J., Walmsley, C. M., & Wouterloot, J. G. A. 1993, A&AS, 98, 51

Haro, G. 1952, ApJ, 115, 572 .

Harris, S. 1985, (Sub)Millimeter Astronomy, 527

Hartigan, P., Heathcote, S., Morse, J. A., Reipurth, B., & Bally, J. 2005, AJ, 130, 2197

Hartigan, P., & Kenyon, S. J. 2003, ApJ, 583, 334

Harvey, P. M., Campbell, M. F., Hoffmann, W. F., Thronson, H. A., & Gatley, I. 1979, ApJ, 229, 990

Harvey, P. M., Joy, M., Lester, D. F., & Wilking, B. A. 1986, ApJ, 301, 346

Harvey, D. W. A., Wilner, D. J., Di Francesco, J., Lee, C. W., Myers, P. C., & Williams, J. P. 2002, AJ, 123, 3325

Haschick, A. D., Moran, J. M., Rodríguez, L. F., & Ho, P. T. P. 1983, ApJ, 265, 281

Henkel, C., Guesten, R., & Haschick, A. D. 1986, A&A, 165, 197

Henning, T., Cesaroni, R., Walmsley, M., & Pfau, W. 1992, A&AS, 93, 525

Herbig, G. H. 1951, ApJ, 113, 697

Herbig, G. H. & Kuhi, L. V. 1963, ApJ, 137, 398

Herbst, E. & Klemperer, W., 1973, ApJ, 185, 505

Herbst, W. & Turner, D. G. 1976, PASP, 88, 308

Herbst, W. & Warner, J. W. 1981, AJ, 86, 885

Hester, J. J., & Desch, S. J. 2005, ASP Conf. Ser. 341: Chondrites and the Protoplanetary Disk, 341, 107

Heyer, M. H., Ladd, E. F., Myers, P. C., & Campbell, B. 1990, AJ, 99, 1585

Heyer, M. H., Snell, R. L., Goldsmith, P. F., & Myers, P. C. 1987, ApJ, 321, 370

Hirabayashi, H., & Hirosawa, H. 2000, Advances in Space Research, 26, 589

Hirabayashi, H.; Hirosawa, H.; Kobayashi, H.; Murata, Y.; Asaki, Y.; Avruch, I. M.; Edwards, P. G.; Fomalont, E. B.; Ichikawa, T.; Kii, T.; Okayasu, R.; Wajima, K.; Inoue, M.; Kawaguchi, N.; Chikada, Y.; Bushimata, T.; Fujisawa, K.; Horiuchi, S.; Kameno, S.; Miyaji, T.; Shibata, K. M.; Shen, Z.; Umemoto, T.; Kasuga, T.; Nakajima, J.; Takahashi, Y.; Enome, S.; Morimoto, M.; Ellis, J.; Meier, D. L.; Murphy, D. W.; Preston, R. A.; Smith, J. G.; Wietfeldt, R. D.; Benson, J. M.; Claussen, M. J.; Flatters, C.; Moellenbrock, G. A.; Romney, J. D.; Ulvestad, J. S.; Langston, G. I.; Minter, A. H.; D'Addario, L. R.; Dewdney, P. E.; Dougherty, S. M.; Jauncey, D. L.; Lovell, J. E. J.; Tingay, S. J.; Tzioumis, A. K.; Taylor, A. R.; Cannon, W. H.; Gurvits, L. I.; Schilizzi, R. T.; Booth, R. S.; Popov, M. V. 2000, PASJ, 52, 955

Hirahara, Y., Suzuki, H., Yamamoto, S., Kawaguchi, K., Kaifu, N., Ohishi, M., Takano, S., Ishikawa, S., Masuda, A. 1992, ApJ, 394, 539

Hirano, N., Kameya, O., Mikami, H., Saito, S., Umemoto, T., & Yamamoto, S. 1997, ApJ, 478, 631

Hirano, N., Liu, S.-Y., Shang, H., Ho, P. T. P., Huang, H.-C., Kuan, Y.-J., McCaughrean, M. J., & Zhang, Q. 2006, ApJ, 636, L141

Hirota, T., Ikeda, M., & Yamamoto, S. 2001, ApJ, 547, 814

Hirota, T., Ito, T., & Yamamoto, S. 2002, ApJ, 565, 359

Ho, P. T. P. & Townes, C. H. 1983, ARA&A, 21, 239

Hofner, P., Kurtz, S., Churchwell, E., Walmsley, C. M., & Cesaroni, R. 1994, ApJ, 429, L85

Hogerheijde, M. 1998, Ph.D. Thesis,

Hosking, J. G., & Whitworth, A. P. 2004, MNRAS, 347, 1001

Huard, T. L., Sandell, G., & Weintraub, D. A., 1999, ApJ, 526, 833

Huard, T. L., Weintraub, D. A., & Sandell, G. 2000, A&A, 362, 635

Hunter, T. R., Neugebauer, G., Benford, D. J., Matthews, K., Lis, D. C., Serabyn, E., & Phillips, T. G. 1998, ApJ, 493, L97

Hurt, R. L., & Barsony, M. 1996, ApJ, 460, L45

Hurt, R. L., Barsony, M., & Wootten, A. 1996, ApJ, 456, 686

Imai, H., Iwata, T., & Miyoshi, M. 1999, PASJ, 51, 473

Iwata, T., Fukui, Y., & Ogawa, H. 1988, ApJ, 325, 372

Jayawardhana, R., Hartmann, L., & Calvet, N. 2001, ApJ, 548, 310

Jenness, T., Scott, P. F., & Padman, R. 1995, MNRAS, 276, 1024

Jennings, R. E., Cameron, D. H. M., Cudlip, W., & Hirst, C. J. 1987, MNRAS, 226, 461

Jijina, J., Myers, P. C., & Adams, F. C. 1999, ApJS, 125, 161

Jørgensen, J. K., Bourke, T. L., Myers, P. C., Schöier, F. L., van Dishoeck, E. F., & Wilner, D. J. 2005, ApJ, 632, 973

Jungwiert, B., & Palous, J. 1994, A&A, 287, 55

Kaiser, H.F. 1958, Psychometrika, 23, 187

Kaiser, H.F. 1960, Educational and Psychological Measurement, 20, 141

Kane, B. D., & Clemens, D. P. 1997, AJ, 113, 1799

Keene, J., Davidson, J. A., Harper, D. A., Hildebrand, R. H., Jaffe, D. T., Loewenstein, R. F., Low, F. J., & Pernic, R. 1983, ApJ, 274, L43

Kenyon, S. J., Dobrzycka, D., & Hartmann, L. 1994, AJ, 108, 1872

Kenyon, S. J., & Hartmann, L. 1987, ApJ, 323, 714

Kepner, J., Hartigan, P., Yang, C., & Strom, S. 1993, ApJ, 415, L119

Khanzadyan, T. 2003, in Communications of the Konkoly Observatory 103, The interaction of stars with their environment II, eds. C. Kiss, M. Kun, & V. Könyves (Konkoly Observatory: Budapest), 31

Khanzadyan, T., Smith, M. D., Gredel, R., Stanke, T., & Davis, C. J. 2002, A&A, 383, 502

Kim, H. G., & Hong, S. S. 2002, ApJ, 567, 376

Knapp, G. R., & Morris, M. 1976, ApJ, 206, 713

Knee, L. B. G., & Sandell, G. 2000, A&A, 361, 671

Knude, J., & Hog, E. 1998, A&A, 338, 897

Koerner, D. W., & Sargent, A. I. 1995, AJ, 109, 2138

Koerner, D. W., Sargent, A. I., & Beckwith, S. V. W. 1993, ApJ, 408, L93

Kondratko, P. T., Greenhill, L. J.; Moran, J. M.; Lovell, J. E. J.; Kuiper, T. B. H.; Jauncey, D. L.; Cameron, L. B.; Gómez, J. F.; García-Miró, C.; Moll, E.; de Gregorio-Monsalvo, I.; Jiménez-Bailón, E. 2006, ApJ, 638, 100

Konigl, A., & Pudritz, R. E. 2000, Protostars and Planets IV, 759

Kraemer, K. E., & Jackson, J. M. 1995, ApJ, 439, L9

Kuiper, G. P. 1951, Proceedings of a topical symposium, commemorating the 50th anniversary of the Yerkes Observatory and half a century of progress in astrophysics, New York: McGraw-Hill, 1951, edited by Hynek, J.A., p.357, 357

Kuiper, T. B. H., Langer, W. D., & Velusamy, T. 1996, ApJ, 468, 761

Kumar, M. S. N., Anandarao, B. G., & Davis, C. J. 1999, A&A, 344, L9

Kurtz, S., Churchwell, E., & Wood, D. O. S. 1994, ApJS, 91, 659

Kwan, J., & Scoville, N. 1976, ApJ, 210, L39

Kwok, S. 1993, ARA&A, 31, 63

Lada, C. J. 1985, ARA&A, 23, 267

Lada, C. J. 1987, IAU Symp. 115: Star Forming Regions, 115, 1

Lada, E. A. 1992, ApJ, 393, L25

Ladd, E. F., & Hodapp, K.-W. 1997, ApJ, 474, 749

Lada, C. J., & Lada, E. A. 2003, ARA&A, 41, 57

Lai, S. & Crutcher, R. M. 2000, ApJS, 128, 271

Lai, S., Velusamy, T., Langer, W. D., & Kuiper, T. B. H. 2003, AJ, 126, 311

Langer, W. D., Castets, A., & Lefloch, B. 1996, ApJ, 471, L111

Langer, W. D., Velusamy, T., Kuiper, T. B. H., Levin, S., Olsen, E., & Migenes, V. 1995, ApJ, 453, 293

Larson, R. B. 1985, MNRAS, 214, 379

Launhardt, R. Evans, N. J., II., Wang, Y., Clemens, D. P., Henning, Th., & Yun, J. L. 1998, ApJS, 119, 59

Launhardt, R., & Henning, T. 1997, A&A, 326, 329

Launhardt, R., Ward-Thompson, D., & Henning, Th. 1997, MNRAS, 288, L45

Lee, C. W., & Myers, P. C. 1999, ApJS, 123, 233

Lee, C. W., Myers, P. C., & Tafalla, M. 1999, ApJ, 526, 788

Lee, C., Mundy, L. G., Reipurth, B., Ostriker, E. C., & Stone, J. M. 2000, ApJ, 542, 925

Lee, C.-F., Mundy, L. G., Stone, J. M., & Ostriker, E. C. 2002, ApJ, 576, 294

Lemme, C., Wilson, T. L., Tieftrunk, A. R., & Henkel, C. 1996, A&A, 312, 585

Leverault, R.M. 1988, ApJ, 330, 897

Lissauer, J. J. 1993, ARA&A, 31, 129

Loren, R. B. 1976, ApJ, 209, 466

Lorenzetti, D.; Giannini, T.; Nisini, B.; Benedettini, M.; Creech-Eakman, M.; Blake, G. A.; van Dishoeck, E. F.; Cohen, M.; Liseau, R.; Molinari, S.; Pezzuto, S.; Saraceno, P.; Smith, H. A.; Spinoglio, L.; White, G. J. 2000, A&A, 357, 1035

Lorenzetti, D., Giannini, T., Vitali, F., Massi, F., & Nisini, B. 2002, ApJ, 564, 839

Lucas, P. W., Blundell, K. M., & Roche, P. F. 2000, MNRAS, 318, 526

Lyo, A.-R., Lawson, W. A., Mamajek, E. E., Feigelson, E. D., Sung, E.-C., & Crause, L. A. 2003, MNRAS, 338, 616

Mardones, D., Myers, P. C., Tafalla, M., Wilner, D. J., Bachiller, R., & Garay, G. 1997, ApJ, 489, 719

Margulis, M., Lada, C. J., & Young, E. T. 1989, ApJ, 345, 906

Margulis, M., Lada, C. J., & Snell, R. L. 1988, ApJ, 333, 316

Margulis, M., & Snell, R. L. 1989, ApJ, 343, 779

Martin, R. N. & Barrett, A. H. 1978, ApJS, 36, 1

Marvel, K. B. 2005, AJ, 130, 2732

Massi, F., Codella, C., & Brand, J. 2004, A&A, 419, 241

Masunaga, H., & Inutsuka, S.-i. 2000, ApJ, 531, 350

Mathieu, R. D., Myers, P. C., Schild, R. E., Benson, P. J., & Fuller, G. A. 1988, ApJ, 330, 385

Matthews, B. C. & Wilson, C. D. 2002, ApJ, 574, 822

McCaughrean, M. J., & Stauffer, J. R. 1994, AJ, 108, 1382

McCutcheon, W. H., Sato, T., Dewdney, P. E., & Purton, C. R. 1991, AJ, 101, 1435

Meehan, L. S. G., Wilking, B. A., Claussen, M. J., Mundy, L. G., & Wootten, A. 1998, AJ, 115, 1599

Melnick, G. J. 1993, LNP Vol. 412: Astrophysical Masers, 412, 41

Melnick, G. J., Menten, K. M., Phillips, T. G., & Hunter, T. 1993, ApJ, 416, L37

Menten, K. M., Krügel, E., & Walmsley, C. M. 1983, Mitteilungen der Astronomischen Gesellschaft Hamburg, 60, 409

Menten, K. M., & Melnick, G. J. 1989, ApJ, 341, L91

Menten, K. M., Melnick, G. J., & Phillips, T. G. 1990, ApJ, 350, L41

Menten, K. M., & van der Tak, F. F. S. 2004, A&A, 414, 289

Menten, K. M., & Young, K. 1995, ApJ, 450, L67

Mikami, H., Umemoto, T., Yamamoto, S., & Saito, S. 1992, ApJ, 392, L87

Millar, T. J. & Herbst, E. 1990, A&A, 231, 466

Mitchell, G. F., Johnstone, D., Moriarty-Schieven, G., Fich, M., & Tothill, N. F. H. 2001, ApJ, 556, 215

Mizuno, H. 1980, Progress of Theoretical Physics, 64, 544

Mizuno, A., Fukui, Y., Iwata, T., Nozawa, S., & Takano, T. 1990, ApJ, 356, 184

Molinari, S., Brand, J., Cesaroni, R., & Palla, F. 2000, A&A, 355, 617

Molinari, S., Brand, J., Cesaroni, R., Palla, F., & Palumbo, G. G. C. 1998, A&A, 336, 339

Molinari, S., Testi, L., Rodríguez, L. F., & Zhang, Q. 2002, ApJ, 570, 758

Momose, M., Ohashi, N., Kawabe, R., Hayashi, M., & Nakano, T. 1996, ApJ, 470, 1001

Moreira, M. C., & Yun, J. L. 1995, ApJ, 454, 850

Moreira, M. C., Yun, J. L., Torrelles, J. M., Afonso, J. M., & Santos, C. A. 1999, AJ, 118, 1315

Moreira, M. C., Yun, J. L., Vázquez, R. Torrelles, J. M., 1997, AJ, 113, 1371

Morgan, J. A., Snell, R. L., & Strom, K. M. 1990, ApJ, 362, 274

Morita, K.-I., Hasegawa, T., Ukita, N., Okumura, S. K., & Ishiguro, M. 1992, PASJ, 44, 373

Moro-Martín, A., Noriega-Crespo, A., Molinari, S., Testi, L., Cernicharo, J., & Sargent, A. 2001, ApJ, 555, 146

Moscadelli, L., Cesaroni, R., & Rioja, M. J. 2000, A&A, 360, 663

Mouschovias, T. C. 1991, NATO ASIC Proc. 342: The Physics of Star Formation and Early Stellar Evolution, 449

Mueller, M. W., & Arnett, W. D. 1976, ApJ, 210, 670

Mundy, L. G., McMullin, J. P., Grossman, A. W., & Sandell, G. 1993, Icarus, 106, 11

Myers, P. C. 1999, The Physics and Chemistry of the Interstellar Medium, Proceedings of the 3rd Cologne-Zermatt Symposium, held in Zermatt, September 22-25, 1998, Eds.: V. Ossenkopf, J. Stutzki, and G. Winnewisser, GCA-Verlag Herdecke, ISBN 3-928973-95-9, 227

Myers, P. C., Fuller, G. A., Mathieu, R. D., Beichman, C. A., Benson, P. J., Schild, R. E., & Emerson, J. P. 1987, ApJ, 319, 340

Myers, P. C., Heyer, M., Snell, R. L., & Goldsmith, P. F. 1988, ApJ, 324, 907

Myers, P. C., & Ladd, E. F. 1993, ApJ, 413, L47

Nakano, T. 1998, ApJ, 494, 587

Neckel, T., Chini, R., Güsten, R., & Wink, J. E. 1985, A&A, 153, 253

Neckel, T. & Staude, H. J. 1990, A&A, 231, 165

Nejad, L. A. M. & Wagenblast, R. 1999, A&A, 350, 204

Nikolić, S., Johansson, L. E. B., & Harju, J. 2003, A&A, 409, 941

Nisini, B., Bacciotti, F., Giannini, T., Massi, F., Eislöffel, J., Podio, L., & Ray, T. P. 2005, A&A, 441, 159

Nomura, H., & Millar, T. J. 2005, A&A, 438, 923

Nyquist, H. 1928, Physical Review , 32, 110

O'Dell, C. R., & Wen, Z. 1994, ApJ, 436, 194

O'Dell, C. R., Wen, Z., & Hu, X. 1993, ApJ, 410, 696

Ohashi, N., Lee, S. W., Wilner, D. J., & Hayashi, M. 1999, ApJ, 518, L41

Palla, F., & Prusti, T. 1993, A&A, 272, 249 A&A, 39,1

Pankonin, V., Winnberg, A., & Booth, R. S. 1977, A&A, 58, L25

Paredes, J. M., Estalella, R., & Rius, A. 1987, A&A, 186, 177

Paredes, J. M., Estalella, R., & Rius, A. 1990, A&A, 232, 377

Parker, N. D. 1989, MNRAS, 235, 139

Pastor, J., Buj, J., Estalella, R., López, R., Anglada, G., & Planesas, P. 1991, A&A, 252, 320

Patel, N. A.; Curiel, S.; Sridharan, T. K.; Zhang, Q.; Hunter, T. R.; Ho, P. T. P.; Torrelles, J. M.; Moran, J. M.; Gómez, J. F.; Anglada, G. 2005, Nature, 437, 109

Patel, N. A., Greenhill, L. J., Herrnstein, J., Zhang, Q., Moran, J. M., Ho, P. T. P., & Goldsmith, P. F. 2000, ApJ, 538, 268

Pearson, K. 1908, Biometrika, 6, 59

Persi, P., Palagi, F., & Felli, M. 1994, A&A, 291, 577P

Persson, S. E., Geballe, T. R., Simon, T., Lonsdale, C. J., & Baas, F. 1981, ApJ, 251, L85

Petrie, S. 1996, MNRAS, 281, 666

Phillips, R. R., Gibb, A. G., & Little, L. T. 2001, MNRAS, 326, 927

Phillips, T. G., & Vastel, C. 2003, SFChem 2002: Chemistry as a Diagnostic of Star Formation, proceedings of a conference held August 21-23, 2002 at University of Waterloo, Waterloo, Ontario, Canada N2L 3G1. Edited by Charles L. Curry and Michel Fich. NRC Press, Ottawa, Canada, 2003, p. 3., 3

Pollack, J. B., Hollenbach, D., Beckwith, S., Simonelli, D. P., Roush, T., & Fong, W. 1994, ApJ, 421, 615

Pollack, J. B., Hubickyj, O., Bodenheimer, P., Lissauer, J. J., Podolak, M., & Greenzweig, Y. 1996, Icarus, 124, 62

Pudritz, R. E., & Norman, C. A. 1983, ApJ, 274, 677

Pudritz, R. E., & Norman, C. A. 1986, ApJ, 301, 571

Qi, C., Ho, Paul T. P., Wilner, David J., Takakuwa, S., Hirano, N., Ohashi, N., Bourke, T.L., Zhang, Q., Blake, G. A., Hogerheijde, M., Saito, M., Choi, M., Yang, Ji. 2004, ApJ, 616, L11

Qi, C., Kessler, J. E., Koerner, D. W., Sargent, A. I., & Blake, G. A. 2003, ApJ, 597, 986

Qi, C., Wilner, D. J., Calvet, N., Bourke, T. L., Blake, G. A., Hogerheijde, M. R., Ho, P. T. P., & Bergin, E. 2006, ApJ, 636, L157

Raga, A. C., Cantó, J., Calvet, N., Rodríguez, L. F., & Torrelles, J. M. 1993, A&A, 276, 539

Rawlings, J. M. C., Taylor, S. D., & Williams, D. A. 2000, MNRAS, 313, 461

Reid, M. J. & Moran, J. M. 1981, ARA&A, 19, 231

Reipurth, B. 2000, AJ, 120, 3177

Reipurth, B., & Aspin, C. 2004, ApJ, 608, L65

Reipurth, B., & Bally, J. 2001, ARA&A, 39, 403

Reipurth, B., Heathcote, S., & Vrba, F. 1992, ApJ, 256, 225

Reipurth, B., Rodríguez, L. F., Anglada, G., & Bally, J. 2002, AJ, 124, 1045

Reipurth, B., Rodríguez, L. F., Anglada, G., & Bally, J. 2004, AJ, 127, 1736

Reipurth, B., Yu, K. C., Heathcote, S., Bally, J., & Rodríguez, L. F. 2000, AJ, 120, 1449

Reynolds, S. P. 1986, ApJ, 304, 713

Richer, J. S., Hills, R. E., & Padman, R. 1992, MNRAS, 254, 525

Richer, J. S., Hills, R. E., Padman, R., & Russell, A. P. G. 1989, MNRAS, 241, 231

Richer, J. S., Padman, R., Ward-Thompson, D., Hills, R. E., & Harris, A. I. 1993, MNRAS, 262, 839

Rohlfs, K., & Wilson, T. L. 2000, Tools of Radio Astronomy (Berlin:Springer)

Rodríguez, L. F., Anglada, G., & Curiel, S. 1999, ApJS, 125, 427

Rodríguez, L. F., Anglada, G., & Raga, A. 1995, ApJ, 454, L149

Rodríguez, L. F., Anglada, G., Torrelles, J. M., Mendoza-Torres, J. E., Haschick, A. D., & Ho, P. T. P. 2002, A&A, 389, 572

Rodríguez, L. F., Curiel, S., Moran, J. M., Mirabel, I. F., Roth, M., & Garay, G. 1989, ApJ, 346, L85

Rodríguez, L. F., Delgado-Arellano, V. G., Gómez, Y., Reipurth, B., Torrelles, J. M., Noriega-Crespo, A., Raga, A. C., & Cantó, J. 2000, AJ, 119, 882

Rodríguez, L. F., Gómez, Y., & Reipurth, B. 2003, ApJ, 598, 1100

Rodríguez, L. F., Ho, P. T. P., & Moran, J. M. 1980a, ApJ, 240, L149

Rodríguez, L. F., Moran, J. M., Dickinson, D. F., & Gyulbudaghian, A. L. 1978, ApJ, 226, 115

Rodríguez, L. F., Moran, J. M., Gottlieb, E. W., & Ho, P. T. P. 1980b, ApJ, 235, 845

Rodríguez, L. F., Porras, A., Claussen, M. J., Curiel, S., Wilner, D. J., & Ho, P. T. P. 2003, ApJ, 586, L137

Rodríguez, L. F., & Reipurth, B. 1989, RevMexAA, 17, 59

Rodríguez, L. F. & Reipurth, B. 1998, RevMexAA, 34, 13

Rodríguez, M., Rodríguez, L. F., Gyulbudaghian, A. L., & May, J. 2002, RevMexAA, 38, 161

Rosvick, J. M., & Davidge, T. J. 1995, PASP, 107, 49

Ruden, S. P., & Lin, D. N. C. 1986, ApJ, 308, 883

Saito, S., Kawaguchi, K., Yamamoto, S., Ohishi, M., Suzuki, H., & Kaifu, N. 1987, ApJ, 317, L115

Sandell, G., & Knee, L. B. G. 2001, ApJ, 546, L49

Sandell, G., & Weintraub, D. A. 2001, ApJS, 134, 115

Sargent, A. I., & Beckwith, S. V. W. 1991, ApJ, 382, L31

Sato, F., & Fukui, Y. 1989, ApJ, 343, 773

Sato, F., Mizuno, A., Nagahama, T., Onishi, T., Yonekura, Y., & Fukui, Y. 1994, ApJ, 435, 279

Saraceno, P., André, P., Ceccarelli, C., Griffin, M., & Molinari, S. 1996, A&A, 309, 827

Scappini, F., Caselli, P., & Palumbo, G. G. C. 1991, MNRAS, 249, 763

Scappini, F. & Codella, C. 1996, MNRAS, 282, 587

Schwartz, P. R. & Buhl, D. 1975, ApJ, 201, L27

Schwartz, P. R., Gee, G., & Huang, Y.-L. 1988, ApJ, 327, 350

Scoville, N. Z., Sargent, A. I., Sanders, D. B., Claussen, M. J., Masson, C. R., Lo, K. Y., & Phillips, T. G. 1986, ApJ, 303, 416

Seth, A. C., Greenhill, L. J., & Holder, B. P. 2002, ApJ, 581, 325

Shakura, N. I., & Sunyaev, R. A. 1973, A&A, 24, 337

Shematovich, V. I., Wiebe, D. S., Shustov, B. M., & Li, Z. 2003, ApJ, 588, 894

Shinnaga, H., Ohashi, N., Lee, S., & Moriarty-Schieven, G. H. 2004, ApJ, 601, 962

Shirley, Y. L., Evans, N. J., Rawlings, J. M. C., & Gregersen, E. M. 2000, ApJS, 131, 249

Shu, F. H., Adams, F. C., & Lizano, S. 1987, ARA&A, 25, 23

Shu, F. H., Johnstone, D., & Hollenbach, D. 1993, Icarus, 106, 92

Shu, F., Najita, J., Ostriker, E., Wilkin, F., Ruden, S., & Lizano, S. 1994, ApJ, 429, 781

Skinner, S. L., & Brown, A. 1994, AJ, 107, 1461

Smith, I. W. M. 1988, ASSL Vol. 146: Rate Coefficients in Astrochemistry, 106

Smith, J. G., Meier, D. L., Murphy, D. W., Preston, R. A., Tingay, S. J., Traub, D. L., & Wietfeldt, R. D. 2000, Advances in Space Research, 26, 637

Snedecor, G.W. 1934, Calculation and Interpretation of Analysis of Variance and Covariance (Ames, Iowa:Collegiate Press).

Snell, R. L. & Bally, J. 1986, ApJ, 303, 683

Snell, R. L., Dickman, R. L., & Huang, Y.-L. 1990, ApJ, 352, 139

Snell, R. L., Huang, Y.-L., Dickman, R. L., & Claussen, M. J. 1988, ApJ, 325, 853

Snell, R. L., Loren, R. B., & Plambeck, R. L. 1980, ApJ, 239, L17

Snell, R. L., Scoville, N. Z., Sanders, D. B., & Erickson, N. R. 1984, ApJ, 284, 176

Stanimirovic, S., Altschuler, D., Goldsmith, P., & Salter, C. 2002, ASP Conf. Ser. 278: Single-Dish Radio Astronomy: Techniques and Applications, 278

Stanke, T., McCaughrean, M. J., & Zinnecker, H. 2000, A&A, 355, 639

Stark, R., et al. 2004, ApJ, 608, 341

Strom, S. E. 1995, RevMexAA SC, 1, 317

Strom, K. M., Strom, S. E., Edwards, S., Cabrit, S., & Skrutskie, M. F. 1989, AJ, 97, 1451

Su, Y., Zhang, Q., & Lim, J. 2004, ApJ, 604, 258

Sugitani, K., Fukui, Y., Mizuni, A., & Ohashi, N. 1989, ApJ, 342, L87

Suzuki, H., Ohishi, M., Kaifu, N., Kasuga, T., Ishikawa, S., & Miyaji, T. 1988, Vistas in Astronomy, 31, 459

Suzuki, H., Yamamoto, S., Ohishi, M., Kaifu, N., Ishikawa, S., Hirahara, Y., & Takano, S. 1992, ApJ, 392, 551

Szymczak, M., & Gérard, E. 2004, A&A, 414, 235

Szymczak, M., Pillai, T., & Menten, K. M. 2005, A&A, 434, 613

Tafalla, M. & Bachiller, R. 1995, ApJ, 443, L37

Tafalla, M., Bachiller, R., & Martín-Pintado, J. 1993, ApJ, 403, 175

Takano, T., Stutzki, J., Winnewisser, G., & Fukui, Y. 1986, A&A, 167, 333

Taylor, S. D., & Williams, D. A. 1996, MNRAS, 282, 1343

Terebey, S., Beichman, C. A., Gautier, T. N., & Hester, J. J. 1990, ApJ, 362, L63

Terebey, S., Chandler, C. J., & André, P. 1993, ApJ, 414, 759

Terebey, S. & Padgett, D. L. 1997, IAU Symp. 182: Herbig-Haro Flows and the Birth of Stars, 182, 507

Terebey, S., Shu, F. H., & Cassen, P. 1984, ApJ, 286, 529

Terebey, S., Vogel, S. N., & Myers, P. C. 1992, ApJ, 390, 181

Thurstone, L.L. 1947, Multiple Factor Analysis (Chicago:University of Chicago Press).

Tofani, G., Felli, M., Taylor, G. B., & Hunter, T. R. 1995, A&AS, 112, 299

Tomita, Y., Saito, T., & Ohtani, H. 1979, PASJ, 31, 407

Torrelles, J. M. 1991, ASP Conf. Ser. 16: Atoms, Ions and Molecules: New Results in Spectral Line Astrophysics, 16, 257

Torrelles, J. M., Gómez, J. F., Garay, G., Rodríguez, L. F., Curiel, S., Cohen, R. J., & Ho, P. T. P. 1998a, ApJ, 509, 262

Torrelles, J. M., Gómez, J. F., Ho, P. T. P., Anglada, G., Rodríguez, L. F., & Cantó, J. 1993a, ApJ, 417, 655

Torrelles, J. M., Gómez, J. F., Ho, P. T. P., Rodríguez, L. F., Anglada, G., & Cantó, J. 1994, ApJ, 435, 290

Torrelles, J. M., Gómez, J. F., Rodríguez, L. F., Curiel, S., Anglada, G., & Ho, P. T. P. 1998b, ApJ, 505, 756

Torrelles, J. M., Gómez, J. F., Rodríguez, L. F., Curiel, S., Ho, P. T. P., & Garay, G. 1996, ApJ, 457, L107

Torrelles, J. M., Gómez, J. F., Rodríguez, L. F., Ho, P. T. P., Curiel, S., & Vázquez, R. 1997, ApJ, 489, 744

Torrelles, J. M., Patel, N. A., Anglada, G., Gómez, J. F., Ho, P. T. P., Lara, L., Alberdi, A., Cantó, J., Curiel, S., Garay, G., & Rodríguez, L. F. 2003, ApJ, 598, L115

Torrelles, J. M., Patel, N. A., Gómez, J. F., & Anglada, G. 1992, RevMexAA SC, 13, 108

Torrelles, J. M., Patel, N., Gómez, J. F., Anglada, G., & Uscanga, L. 2005, Ap&SS, 295, 53

Torrelles, J. M.; Patel, N. A.; Gómez, J. F.; Ho, Paul T. P.; Rodríguez, L. F.; Anglada, G.; Garay, G.; Greenhill, L.; Curiel, S.; Cantó, J. 2001a, ApJ, 560, 853

Torrelles, J. M.; Patel, N. A.; Gómez, J. F.; Ho, Paul T. P.; Rodríguez, L. F.; Anglada, G.; Garay, G.; Greenhill, L.; Curiel, S.; Cantó, J. 2001b, Nature, 411, 277

Torrelles, J. M., Rodríguez, L. F., Cantó, J., Anglada, G., Gómez, J. F., Curiel, S., & Ho, P. T. P. 1992, ApJ, 396, L95

Torrelles, J. M., Rodríguez, L. F., Cantó, J., Carral, P., Marcaide, J., Moran, J. M., & Ho, P. T. P. 1983, ApJ, 274, 214

Torrelles, J. M., Verdes-Montenegro, L., Ho, P. T. P., Rodríguez, L. F., & Cantó, J. 1993b, ApJ, 410, 202

Townes, C. H., & Schawlow, A. L. 1975, Microwave Spectroscopy, (New York: Dover publications)

Trinidad, M. A., Curiel, S., Cantó, J., D'Alessio, P., Rodríguez, L. F., Torrelles, J. M., Gómez, J.F., Patel, N., Ho, P. T. P. 2003, ApJ, 589, 386

Umemoto, T., Iwata, T., Fukui, Y., Mikami, H., Yamamoto, S., Kameya, O., & Hirano, N. 1992, ApJ, 392, L83

Vallée, J. P. 1995, AJ, 110, 2256

Vallée, J. P., Bastien, P., & Greaves, J. S. 2000, ApJ, 542, 352

van Dishoeck, E. F. & Blake, G. A. 1998, ARA&A, 36, 317

van Zadelhoff, G.-J., van Dishoeck, E. F., Thi, W.-F., & Blake, G. A. 2001, A&A, 377, 566

Velusamy, T., Kuiper, T. B. H., & Langer, W. D. 1995, ApJ, 451, L75

Visser, A. E., Richer, J. S., & Chandler, C. J. 2001, MNRAS, 323, 257

Visser, A. E., Richer, J. S., & Chandler, C. J. 2002, AJ, 124, 2756

Viti, S., Natarajan, S., & Williams, D. A. 2002, MNRAS, 336, 797

Vlemmings, W. H. T., Diamond, P., van Langevelde, H. J., Torrelles, J, M. 2006, A&A, in press

Vrba, F. J., Luginbuhl, C. B., Strom, S. E., Strom, K. M., & Heyer, M. H. 1986, AJ, 92, 633

Wang, J.-J., Chen, W.-P., Miller, M., Qin, S.-L., & Wu, Y.-F. 2004, ApJ, 614, L105

Wang, Y., Evans, N. J., Zhou, S., & Clemens, D. P. 1995, ApJ, 454, 217

Wang, H., Stecklum, B., & Henning, T. 2005, A&A, 437, 169

Weintraub, D. A., Tegler, S. C., Kastner, J. H., & Rettig, T. 1994, ApJ, 423, 674

Wetherill, G. W., & Stewart, G. R. 1989, Icarus, 77, 330

White, G. J. & Sandell, G. 1995, A&A, 299, 179

Whitelock, P., Feast, M., & Catchpole, R. 1986, MNRAS, 222, 1

Whitelock, P., Menzies, J., Feast, M., Catchpole, R., Marang, F., & Carter, B. 1995, MNRAS, 276, 219

Whitelock, P., Menzies, J., Feast, M., Marang, F., Carter, B., Roberts, G., Catchpole, R., & Chapman, J. 1994, MNRAS, 267, 711

Wiesemeyer, H., Cox, P., Gusten, R., & Zylka, R. 1999, ESA SP-427: The Universe as Seen by ISO, 533

Wiesemeyer, H., Gusten, R., & Wright, M. C. H. 1997, IAU Symp. 182: Herbig-Haro Flows and the Birth of Stars, 182, 260P

Wilking, B. A., Blackwell, J. H., Mundy, L. G., & Howe, J. E. 1989a, ApJ, 345, 257

Wilking, B. A. & Claussen, M. J. 1987, ApJ, 320, L133

Wilking, B. A., Claussen, M. J., Benson, P. J., Myers, P. C., Terebey, S., & Wootten, A. 1994, ApJ, 431, L119

Wilking, B. A., Lada, C. J., & Young, E. T. 1989b, ApJ, 340, 823

Wilking, B. A., Blackwell, J. H., & Mundy, L. G. 1990, AJ, 100, 758

Wilking, B. A., Claussen, M. J., Benson, P. J., Myers, P. C., Terebey, S., & Wootten, A. 1994a, ApJ, 431, L119

Wilking, B. A., Claussen, M. J., Benson, P. J., Myers, P. C., Terebey, S., & Wootten, A. 1994b, ASP Conf. Ser. 65: Clouds, Cores, and Low Mass Stars, 65, 299

Willacy, K., Langer, W. D., & Velusamy, T. 1998, ApJ, 507, L171

Wolfire, M. G., & Koenigl, A. 1993, ApJ, 415, 204

Wolkovitch, D., Langer, W. D., Goldsmith, P. F., & Heyer, M. 1997, ApJ, 477, 241

Wootten, A. 1989, ApJ, 337, 858

Wouterloot, J. G. A., & Brand, J. 1989, A&AS, 80, 149

Wouterloot, J. G. A., Brand, J., & Fiegle, K. 1993, A&AS, 98, 589

Wouterloot, J. G. A., Walmsley, C. M., & Henkel, C. 1988, A&A, 203, 367

Wu, Y., Wei, Y., Zhao, M., Shi, Y., Yu, W., Qin, S., & Huang, M. 2004, A&A, 426, 503

Wu, Y., Wu, J., & Wang, J. 2001, A&A, 380, 665

Wu, Y., Zhou, S., & Evans, N. J. 1992, ApJ, 394, 196

Xiang, D. & Turner, B. E. 1995, ApJS, 99, 121

Xie, T. & Goldsmith, P. F. 1990, ApJ, 359, 378

Yamamoto, S., Mikami, H., Saito, S., Kaifu, N., Ohishi, M., & Kawaguchi, K. 1992, PASJ, 44, 459

Yang, J., Ohashi, N., & Fukui, Y. 1995, ApJ, 455, 175

Young, C. H., Shirley, Y. L., Evans, N. J., & Rawlings, J. M. C. 2003, ApJS, 145, 111

Yun, J. L. 1996, AJ, 111, 930

Yun, J. L., & Clemens, D. P. 1990, ApJ, 365, L73

Yun, J. L. & Clemens, D. P. 1991, ApJ, 365, L73

Yun, J. L., & Clemens, D. P. 1992, ApJ, 385, L21

Yun, J. L., & Clemens, D. P. 1994a, ApJS, 92, 145

Yun, J. L., & Clemens, D. P. 1994b, AJ, 108, 612

Yun, J. L., & Clemens, D. P. 1995, AJ, 109, 742

Yun, J. L., Moreira, M. C., Torrelles, J. M., Afonso, J. M., & Santos, N. C. 1996, AJ, 111, 841

Yusef-Zadeh, F., Biretta, J., & Wardle, M. 2005, ApJ, 624, 246

Zapata, L. A., Rodríguez, L. F., Ho, P. T. P., Zhang, Q., Qi, C., & Kurtz, S. E. 2005, ApJ, 630, L85

Zhang, Q., & Ho, P. T. P. 1995, ApJ, 450, L63

Zhang, Q., Ho, P. T. P., & Wright, M. C. H. 2000, AJ, 119, 1345

Zhang, Q., Ho, P. T. P., Wright, M. C. H., & Wilner, D. J. 1995, ApJ, 451, L71

Zhou, S., Evans, N. J., II, Kömpe, C., & Walmsley, C. M. 1993, ApJ, 404, 232

Zinnecker, H., Bastien, P., Arcoragi, J.-P., & Yorke, H. W. 1992, A&A, 265, 726

Zuckerman, B., Kuiper, T. B. H., & Rodriguez Kuiper, E. N. 1976, ApJ, 209, L137

EN MEMORIA DE
Lucía Hernández Balado,
mi querida abuela